Bridging the gap between industry and academics to develop sample-to-answer methods for advancement towards personalized medicine

By

David “John” Guckenberger Jr.

A dissertation submitted in partial fulfillment of

the requirements for the degree of

Doctor of Philosophy

(Biomedical Engineering)

at the

UNIVERSITY OF WISCONSIN-MADISON

2016

Date of final oral examination: 10/24/2016

The dissertation is approved by the following members of the Final Oral Committee:
David J. Beebe, Professor, Biomedical Engineering
Joshua M. Lang, Assistant Professor, Medicine
Miriam A. Shelef, Assistant Professor, Medicine
Sameer K. Mathur, Associate Professor, Medicine
Anna Huttenlocher, Professor, Medical Microbiology and Immunology

Acknowledgements

Achievements of this magnitude are not accomplished independently. Friends, family, colleagues, and peers have contributed in various ways to shape me into the person I am today. Their nurture, encouragement, motivation, training, and support has given the ability to succeed. I am forever grateful to those who have stayed in my life and contributed to who I am today. The list of people I would like to thank is endless, but there are some key people who have supported me throughout my education and to whom I would like to give recognition:

First and foremost, I would like to thank my family – my parents, Dave and Debra, and my two brothers, Mac and Alex. They have supported me every step of the way.

I would like to thank Dr. Bidhan Roy, associate professor at University of Wiscsonsin – Platteville. Dr. Roy initiated my opportunity in the Microtechnology, Medicine, and Biology (MMB) Lab by facilitating an introduction with Dr. Beebe.

I would like to thank Dr. Edmond W. K. Young and Dr. Erwin Berthier. They volunteered to take me on as an undergraduate student and have acted as mentors and role models ever since. Together, their love for science, dedication, motivation, and hard work has encouraged me to do the best that I can and dedicate myself to science. Both of them have gone out of their way to educate me, and have done so without hesitation. Dr. Young and Dr. Berthier are two people I continually idolize. I can only hope that I am able to mentor others the way the Dr. Young and Dr. Berthier have mentored me.

I would like to thank Dr. David J. Beebe. He has been more than an academic advisor to me; since I transferred to UW-Madison, Dr. Beebe has guided me through every step of my education, both in and out of the lab. He has continually looked out for me and guided me both academically and personally.

I would like to thank Hannah Pezzi: my colleague and closest friend. She has been with me and helped me through every step.

I would like to thank Dr. Josh Lang. His drive and dedication to his field and his patients constantly motivates me as a researcher. He has acted as a role model for and is someone that I look up to.

I would like to Alice Puchalski. When it comes down to it, her hard work and dedication made my research possible.

I would like to thank Emily Junger, Jake Kanack, and Jacob Rothbauer. Their strong work ethics and dedication made these projects possible.

I would like to give a shout out and thanks to Dr. Ben Casavant and Dr. Erwin Berthier who were always willing to try new crazy ideas. Nothing was out of the question and nothing was impossible, worst case improbable.

Finally, I would like to thank my committee for guiding my research and members of the MMB Lab for all of their help and support.

Abstract

Diseases are inherently difficult to diagnose, treat, and monitor. Microfluidic technologies have the potential revolutionize the biotech space, providing new biological insights, and allowing researchers to discover and monitor new biomarkers. Despite the potential that microfluidics has to offer, there is a disconnection between academics and industry that severely limits widespread implementation of microfluidic technologies. This disconnection, largely attributed to the differencing backgrounds of industry and academics, will need to be bridged for microfluidic technologies to become ubiquitous. Here, the source of this disconnection is assessed and fabrications techniques for academics are introduced, which are designed to help bridge the gap between industry and academics. The fabrication techniques include milling, bonding, and surface treatment for thermoplastics, including: wax, polystyrene, polypropylene, and cyclic olefin copolymer. We then apply these techniques to develop new, simple technologies categorized by three topic areas, namely: isolation of circulating tumor cells, in vivo microsampling and drug delivery, and neutrophil migration assays. Together, these topic areas and these technologies demonstrate how simple, manufacturable, and transferable microfluidic technologies can be used to solve complex biological problems.

Contents

Table of Figures:

Chapter 1 Introduction

1.1 Overview

Continuous advancement in the field of biotechnology has brought opportunities and tools with which to diagnose, treat, and monitor patients. Yet, additional action will be required to overcome a disconnection that is limiting the clinical implementation of these technologies. There are several diseases - including asthma and obstructive sleep apnea (OSA) - for which predictive clinical diagnosis is severly limited.[1-3] Lacking tools and biomarkers, clinicians must rely on either the medical history of the patient or the patient's family or wait for physical symptoms to occur; both of which are subject to interpretation. As a result, many people – especially children – go undiagnosed, which can have severe repercussions. For example, studies have shown that OSA effects 2-5% of children between 2-8 years of age[4], leading to cardiovascular, metabolic, and central nervous system diseases[5]; yet, the current success rates of diagnosis is comparable to a coin flip.[5, 6] Similarly, asthma causes over 3300 deaths/year, roughly half of which are children (Centers for Diseases Control), highlighting the need for methods capable of diagnosing diseases pre-symptomatically.

Disease diagnosis is only part of the battle; even for diagnosable diseases, such as cancer, identifying the most effective treatment remains an issue. Cancer lacks a 'one size fits all' treatment (even within a cancer type) where treatment effectiveness is not easily predicted and only a fraction of the treatments administered are successfully.[7] Treatment is complicated by severe patient-to-patient heterogeneity - a treatment that works for one patient may not work for another.[7, 8] As such, a clinician's only approach to treatment selection (e.g., chemotherapies, immune therapies) is to reference similar cases – looking at patient progression, treatment history, and the outcome of the treatment – to then make a "best guess" as to which treatment to select.[8] Though clinician's are incredibly proficient at selecting treatment strategies, a failed treatment has a huge burden on the patient; chemo-therapy is associated with high-costs, terrible side effects, large time commitments, and poor quality of life.[9] More importantly, during the course of a failed treatment, the cancer is allotted time to progress and expand to other organs.

Accordingly, the cancer becomes more difficult to treat, the therapeutic options narrow, and the patient must endure another round of therapy without a guaranteed outcome. From asthma to cancer, the need exists for further technological development to enable new diagnostics, predict treatment efficacy, and monitor treatment responses; the challenge is finding and developing solutions that can be transferred to and implemented in the clinics.

Microfluidic technologies have shown promise in their potential to enable new diagnostic capabilities and allow access to biology that may facilitate unique solutions.[10] Microfluidic technologies possess several key traits. First, the sub millimeter scale of microfluidic technologies gives access to phenomena not accessible at the macro scale,[11, 12]; specific traits include: laminar flow, gradient generation,[13] and surface tension driven flow.[14, 15] Second, the scale of microfluidic technologies enables us to perform *in vitro* assays at physiologically relevant scales.[16, 17] As a result, we can investigate biological interactions including: paracrine signaling through co-cultures,[18] cell migration in response to gradient generation,[19, 20] and more easily interrogate single cell dynamics.[21, 22] Microfluidic technologies have been used to create *in vivo*-like models *in vitro*, including: 3D cultures to mimic tissues,[23, 24] lumens,[25-27], and in vitro organ models.[28] Lastly, due to the small volume requirements of microfluidic technologies, reagent costs are minimized. These benefits and applications have made microfluidic technologies well suited for clinical and point-of-care applications,[29, 30] For example, researchers have demonstrate the potential of using cell response (e.g., neutrophil) as a method of diagnosis.[19, 20] Yet, despite the potential of microfluidic technologies, only few have become commercially available. A potentially key challenge limiting the ubiquity of microdevices is a disconnection that exists between academic institutions and industry.[31]

Academic institutions are innovation powerhouses, but have limited need to design assays compatible with high throughput production. On the other hand, industry and commercialization are the keys to technological success and widespread utility.[32] In order for the microfluidics field to move forward, both academic innovation and commercialization techniques must merge. Over the past decade

the number of new or modified microfluidic technologies has increased exponentially[10, 33] with most of the development happening in academia. Yet, many of these technologies only exist academically and are not commercially available. In fact, after only a few publications (in some cases only one publication) most technologies go dormant never finding widespread use. Though there are several reasons as to why a technology may go dormant, two reasons are prominent. First, researchers and biologists are generally resistant to change; researchers want something that has been *proven* to work which ultimately dissuades them from trying new, unfamiliar technologies.[32, 33] Second, despite the fact that many microfluidic devices are pitched as user friendly, simple, and low cost (from a reagent standpoint), they are often perceived as complex and have unique manufacturing requirements (tight tolerances, specific materials, specific processes), which can make the devices themselves costly. Together, these reasons hinder distribution of microfluidic technologies.

Microfluidics stems from the field of microelectromechanical system (MEMs), which relies heavily on silicon masters to achieve repeatable manufacturing and high resolution.[34] Techniques such as soft lithography (i.e., elastomeric feature replication via polydimethylsiloxane (PDMS)) are then used to replicated the high-resolution features and make microfluidic devices.[35, 36] Though effective, these methods are costly and time consuming – not ideal for large scale or low-cost manufacturing.[33] Conversely, industry relies heavily on manufacturing techniques like injection molding[34] (a high throughput technique), CNC milling[37] (medium throughput), and hot-embossing[38] (medium to low-throughput). Many of these techniques are capable of manufacturing microfluidic devices, but are not currently compatible with PDMS, the material utilized ubiquitously for academic microfluidic technologies. Instead, industrial techniques rely on thermoplastics, such as polystyrene (PS), poplypropylene (PP), and cyclic olefin copolymer (COC). Berthier et al. performed a thorough investigation on the differences between these materials (PDMS vs Thermoplastics) highlighting a disconnection between engineers, who have traditionally relied on PDMS, and biologists, who generally prefer thermoplastics.[33] Because thermoplastics were introduced to biologists in 1965 (used for petri

dishes), biologist have had half of a century to get accustomed to thermoplastics. Due to the consumer's familiarity with thermoplastics, a transition to thermoplastics in the microfluidic community will be imperative to expanding the user-base for microfluidic technologies. Thus, in order to bridge the gap, microfluidic researchers and academic institutions must transition to manufacturing directly in thermoplastics, using methods (like milling or hot embossing) that are directly transferrable to commercial manufacturing. Else, microfluidic technologies – despite being uniquely poised to answer biological questions and meet existing clinical needs – will never see the consumer demand necessary to drive the technologies into clinics.

The first several chapters (Chapters 1-7) are dedicated to towards bringing thermoplastic manufacturing capabilities to academic institutions. Following these fabrication techniques, we layout three case studies aimed at covering three technology portfolios, including: (Case Study 1) exclusion-based sample preparation technologies geared toward isolation of circulating tumor cells; (Case Study 2) Kit-on-a-lid-assays for simplified microfluidic assays; (Case Study 3) Implantable microdevices to assess cancer therapy. Through these case studies, we demonstrate (1) the use of thermoplastics to make simple microfluidic technologies and (2) how microfluidic technologies can answer existing clinical problems while meeting clinical needs and maintaining commercial potential. A detailed overview for each case study is provided below to help set the stage for each of the following chapters.

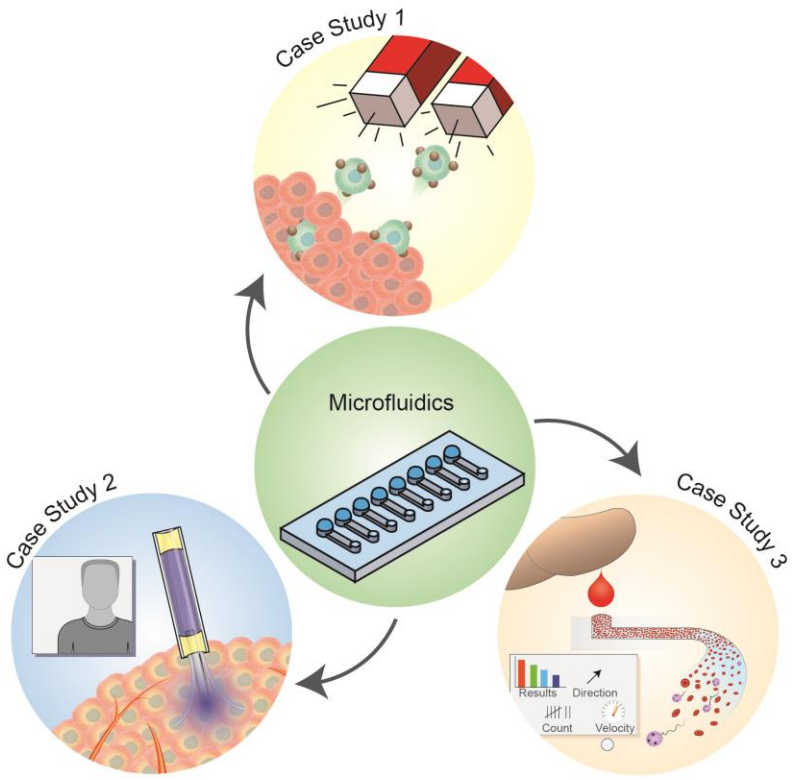

Fig. 1.1 A graphical representation of the following case studies.

1.1.1 Case Study 1: Isolation of Circulating Tumor Cells

Circulating tumor cells (CTCs), often present in late-stage metastatic patients, are cancerous cells that detach from primary tumors or metastases and circulate the bloodstream.[39] Due to their circulation, CTCs are easy to access (via a blood draw) and pose potential as prognostic or predictive biomarkers for several diseases. [8] The Veridex CELLSEARCH system identifies and enumerates CTCs and has become the first commercially available CTC isolation technology approved by the FDA.[40] However, in pushing the field forward, researchers want access to the molecular information (biomarkers) within these cells to enabling further insight into the disease.[8] In light of this, several new technologies and companies have emerged with technologies capable of isolating CTCs for downstream analysis. Some of the technologies include the CTC ichip[41] and the herringbone chip.[42] Additional commercial products related to CTC isolation have also spun out of the field including IsoFlux by Fluidigm,[43] MACs system by Miltenyis Biotec,[44], and the CTC platfrom by Epic Sciences.[45] With all these new developments, there are three key

challenges in the fields of CTCs. The first is to develop technologies that enable numerous endpoints. The second is to achieve higher capture sensitivity and specificity, which will be necessary for more advance endpoints such as DNA sequencing. The third challenge is to determine which biomarkers are pertinent and what information we can get from the CTCs.[46] However, to address the third challenge, we must first address challenges 1 and 2. In this section, we describe three new sample preparation technologies – the Vertical Immiscible filtration assisted by surface tenstion (VerIFAST, Chapter X), the Sliding Lid for Immobilized Droplet Extractions (SLIDE, Chapter X), and the multiplexed platform for automated extraction (mTAE, Chapter X) – that facilitate rare cell capture and numerous endpoints (RNA, DNA, Proteins, Immunostaining) for CTC evaluation.

1.1.2 Case 2: Implantable Microdevices to assess cancer therapy

As previously described, cancers are heterogeneous, thus cancer patients variable response to therapy.[7, 8] Without tools to inform efficacy of drug prior to treatment, predicting patient responses and selecting the proper therapeutic option becomes difficult. Traditionally, the approach has been to immediately administer the drug systemically to the patient. During the treatment period, which is often several weeks and comprised of several treatments, the tumor burden is monitored to assess the efficacy of the treatment. During this time, the patient must endure all of the associated treatment side effects [9], with no guarantee that their cancer will respond. Recently, a new class of technologies has been developed that allows clinicians to pre-screen drug efficacy through localized treatment, directly in the tumor.[47, 48] In addition to evaluating drug efficacy is that during the pre-screen only small doses of drug are delivered, resulting in minimal to no systemic effects for the patients. Further, numerous drugs can be delivered simultaneously, permitting the assessment of individual and combinatorial effects of multiple drugs. However, there are two challenges with these technologies. First, the delivery time is relatively short (<72 hours), which limits the types of drugs that can be tested. Second, these technologies rely on histology to quantify a therapeutic response, which limits the number of analytes that can be assessed. In this Case Study, we demonstrate an implantable technology that enables localized drug delivery in

addition to direct sampling of the tumor microenvironment. This technology is capable of delivering drug for up to two weeks, and enables sampling of nearly one hundred cytokines simultaneously.

1.1.3 Case 3: Kit-On-A-Lid-Assays

Though natural and necessary, inflammation contributes to many (if not most) diseases. Asthma, for example, is the result of an innate immune response to an allergen introduced in the bronchial airways. In this case, inflammation constricts the airway, which can impair breathing and, in severe cases, be fatal if left untreated. Cancer is another example, wherein genetic mutations to immune cells can elicit perpetual, uncontrollable replication and the release of pro-inflammatory chemokines.[49] Other specific examples of a role of inflammation in diseases include: atherosclerosis,[50] anaphylaxis, and rheumatoid arthritis.[51]

Due to the complex role of inflammation, its varied impact, and patient-to-patient heterogeneity, disease prediction, diagnosis, and patient care are ongoing challenges. For example, diagnosis of asthma is based on a combination of lung tests, medical history, previously observed symptoms, and a physical examination. For young children (<5 years), however, lung tests are difficult to administer[52]; thus clinicians must solely rely on medical and family histories or wait for noticeable symptoms to occur. Once a patient is diagnosed with asthma, treatment presents further obstacles. The two leading medical treatments for asthma are Montelukast Sodium (Singular®) and inhaled corticosteroids.[53] In several cases, only one or the other will work on a patient. As such, the clinician must make an educated guess – based on previous cases – as to which drug to prescribe. When the wrong drug is selected, patients incur medical charges and side effects, but see little (if any) benefit. Thus, methods to enable pre-symptomatic diagnosis or to test drug efficacy prior to treatment would improve current treatment procedures.

Recent studies have placed impetus on utilizing neutrophils as predictive biomarkers for inflammatory diseases.[19, 20, 51] For decades, researchers have been mimicking the chemotactic response of neutrophils in vitro. Two of the most highly cited assays for assessing neutrophil response are the Boyden

chamber[54, 55] and migration monitoring under agarose.[56, 57] To perform these assays, however, several milliliters of blood and extensive purification protocols – involving centrifugation, erythrocyte lysing, and neutrophil re-suspension – are required.[58] During these prolonged purification protocols, release of platelet activating factors prime the neutrophils accelerate chemotactic response and increase production of superoxide masking true neutrophil response.[59] Furthermore, the need for several milliliters of blood limits the utility of these assays for pediatric studies (do to the inherently low blood volumes) and high frequency measurements (a 24 hr wait period between blood draws is standard). These limitations motivate the development of new assays that are can be performed as quickly as possible (to minimize extraneous effects from whole blood) and with as little blood as possible (to facilitate broader studies).

Microfluidic assays provide straightforward processes to characterize neutrophil chemotactic response. In a microfluidic protocol proposed by Agrawal et al., neutrophils are captured by passing 10 μL of whole blood (less than a drop of blood) over a protein coated surface (e.g. P-selectin). The erythrocytes are then washed away leaving behind the purified neutrophils.[60] Sackmann et al. took significant measures to further reduce the demand on blood volume and simplify the assay, developing what they termed the Kit-On-A-Lid-Assay (KOALA). Like Agrawal's assay, KOALA leverages protein coated surfaces to capture neutrophils, but relies on passive fluid handling mechanisms to eliminate the need for pumps.[19] Furthermore, by pre-filling lids with chemotaxis factor, creating a chemotactic gradient is as simple as applying a lid to base. Using this platform, neutrophils can be captured within minutes, requiring <3 μL of whole blood. As a result, several technical replicates can be performed from a single droplet of blood. And, because only a single drop of blood is necessary, assays can be performed more frequently (in the order of minutes or hours as opposed to days), enabling temporal assessment of immune response.

In this section, we present a modified version and protocol of the technology originally presented by Sackmann et al.[19] We also demonstrate new analytic techniques that will advance the currents state of migrational analysis, leading to new metrics and higher accuracy. Lastly, we present two "easy-to-use"

forms of KOALA. Fundamentally, this a fluid handling mechanism that enables fluid exchanges, reagent storage, and cell-cryopreservation. Going forward, the KOALA fluid handling technology will play a key role in making these neutrophil assays user-friendly to facilitate use by other labs.

Chapter 2 Micromilling: a method for ultra-rapid prototyping of plastic microfluidic devices[1]

2.1 Introduction

The microfluidics community now has an enormous selection of materials, methods, and techniques for developing microfluidic systems. Many different techniques and methods are now readily available, and are becoming increasingly accessible as a result of heightened research efforts and growing interest in the field. Such a diverse repertoire of methods and tools increases the potential for the advancement, adoption, and proliferation of microfluidic technologies, and opens new avenues for research and development in both academia and industry.

Of all the materials commonly used in microfluidics, plastics remain a primary option due to their many favorable properties and their compatibility for biology applications (e.g., polystyrene is commonly used for mammalian cell culture).[17] Plastics are low cost and highly amenable to high-volume manufacturing processes, making them particularly suitable for those who are developing technologies for commercialization and mass production.[61] For these reasons, plastics have been considered a reliable and robust material since the early years of microfluidics,[62] even as other materials such as PDMS and paper have become increasingly popular.[33,63] With microfluidics entering its third decade, and garnering heightened interest from industry, plastics – and their related fabrication processes – will likely play a major role in translating microfluidics research into commercialized technologies.[10]

Many fabrication methods for plastics are available to researchers, with each fabrication method offering different advantages and limitations.[62] Some methods such as injection molding have existed for decades[64] and are well studied, but have high start-up costs that limit their utility for low-volume production. Other methods such as laser micromachining[65-67] and stereolithography[68, 69] are rapidly evolving due to ongoing advancements in technology, and are thus not as well studied as other traditional methods.[68] While the

1 This chapter has been adapted from the following publication: "Micromilling: a method for ultra-rapid prototyping of plastic microfluidic devices" David J. Guckenberger, Theodorus E. de Groot, Alwin M. D. Wan, David J. Beebe, and Edmond W. K. Young. Lab on a Chip 2015.

current collection of fabrication methods can meet a wide range of technical needs, various gaps still exist within the area of microfabrication that are difficult to address with only these most common methods.

Micromilling is an alternative method that has the potential to address some of the challenges in microfabrication. Micromilling is a fabrication method that creates microscale features via cutting tools that remove bulk material. While many other methods have been discussed previously for microfluidics applications,[70,71] micromilling has received much less attention. Recent work has shown micromilling to be effective for microfluidic devices.[72,73] For example, Kit-On-A-Lid-Assays (KOALA), designed to deliver fluid by assembling multiple slides that can be clipped together, have been used for a variety of assays,[74, 75] and are fabricated by micromilling. Micromilled devices have also been used to create oil and aqueous interfaces for cell capture and RNA, DNA, and protein isolation.[76, 77] Bischel and co-workers utilized milled devices to capture and orient zebrafish for imaging and drug testing.[78] Carney and co-workers cultured primary fetal testis cells in mixed and compartmentalized co-culture to study microenvironmental factors regulating steroid production and organ co-culture assays.[79] However, the method remains underutilized as a microfabrication method compared to other methods. This is largely because of presumed high start-up costs, the need for large equipment and lab space, and the need for unique technical expertise. However, recent developments in machining technology have alleviated many of these drawbacks, making micromilling a potentially important option in microfluidics.

In this tutorial, we present micromilling as a microfabrication method for plastics, and provide practical tips and strategies for achieving ultra-rapid prototyping of microfluidic devices. First, we compare costs and capabilities between micromilling and other common plastic microfabrication methods, allowing the practitioner to determine whether micromilling is suitable for the target application. Second, we present an operational guide to provide insights on how to best set up the machine and tooling, and to select appropriate parameters to enable optimal, reliable, and precise fabrication of microfluidic devices. Third, we address questions related to the quality of micromilled devices by measuring and comparing surface roughness, precision, and repeatability, as produced by micromilling (with a low cost milling system), and by other methods. As a demonstration of the utility of

micromilled plastic devices, we culture mammalian cells in milled microchannels to characterize cell viability and image quality under typical conditions required for conducting cell-based experiments. Lastly, we discuss the advantages, limitations, and overall potential of micromilling as a useful fabrication method. This tutorial will serve as a guide for practitioners who are considering using micromilling in their fabrication repertoire.

2.1.1 Fabrication Overview

A critical step in developing microfluidic systems is choosing the proper microfabrication method. In this section, we provide the microfluidics practitioner with a basis for considering micromilling as a useful fabrication method, particularly for ultra-rapid prototyping of microfluidic devices in plastics (and potentially other materials). First, background and fundamental aspects of micromilling are described. The strengths and limitations are then summarized and compared (in terms of technical capabilities and affordability) to three other common plastic microfabrication techniques: hot embossing, injection molding, and 3D-printing via stereolithography.

2.1.2 Micromilling

Milling is a subtractive manufacturing process that uses rotating cutting tools to remove material from a starting stock piece, commonly referred to as the *workpiece*. The basic milling system, or mill, consists of (1) a *worktable* for positioning the workpiece, (2) a cutting tool (most commonly an *endmill*), and (3) an overhead spindle for securing and rotating the cutting tool (**Fig. 2.1)**. Milling, which has origins dating back to 1818,[80] has undergone significant advances, and now represents a major tool in a machinist's repertoire. The positions of the worktable (X and Y-axis) and spindle (Z-axis) are traditionally adjusted by hand with mechanical levers and cranks, but modern mills now employ *computer numerical control (CNC)* that automates the process, thereby improving repeatability and precision, reducing human error, and adding advanced capabilities (e.g., the direct conversion of computer-aided design (CAD) models to finished parts).

Milling machines with CNC capability (i.e., *CNC mills*) are available with a wide range of technical specifications, encompassing varying levels of stage precision, spindle speeds, and automation. Modern CNC mills are versatile and capable of fabricating devices with features ranging in size from several microns to several meters.[81] The wide availability of cutting tool shapes, materials, and sizes[82] makes the mill amenable to fabricating many types of features in many different materials. Perhaps the most enabling aspect of using a CNC mill is the ability to fabricate a part directly from a three-dimensional (3D) CAD model, making it easier and faster to convert design concepts to working prototypes. Latest advances in technical features have enabled improved precision and resolution down to the micron scale, leading to the use of the term *micromilling* to describe fabrication of increasingly more intricate parts with microscale resolution.[83]

Micromilling can be useful in microfluidics applications: for two main functions (1) machining the mold used in subsequent fabrication steps (e.g., embossing or injection molds)[73, 84] or (2) machining microchannels and features directly into the final part. In the latter case, micromilling offers a key advantage: a plastic workpiece can be milled into a device in less than 30 min, significantly reducing turnaround time from design to prototype.

Milling is well characterized for producing large features in common machining materials such as steel and aluminum. Thus, technical information is available from machining handbooks, shop technicians, and online resources.[85] In addition, comprehensive reviews are available on multi-functional machine tools for metal cutting.[86] In contrast, milling of microscale features in non-traditional milling materials such as plastics is much less characterized, especially in the context of microfluidic devices.[87] Thus, there is a need to fill this gap in technical knowledge to determine the usefulness of micromilling in microfluidics.

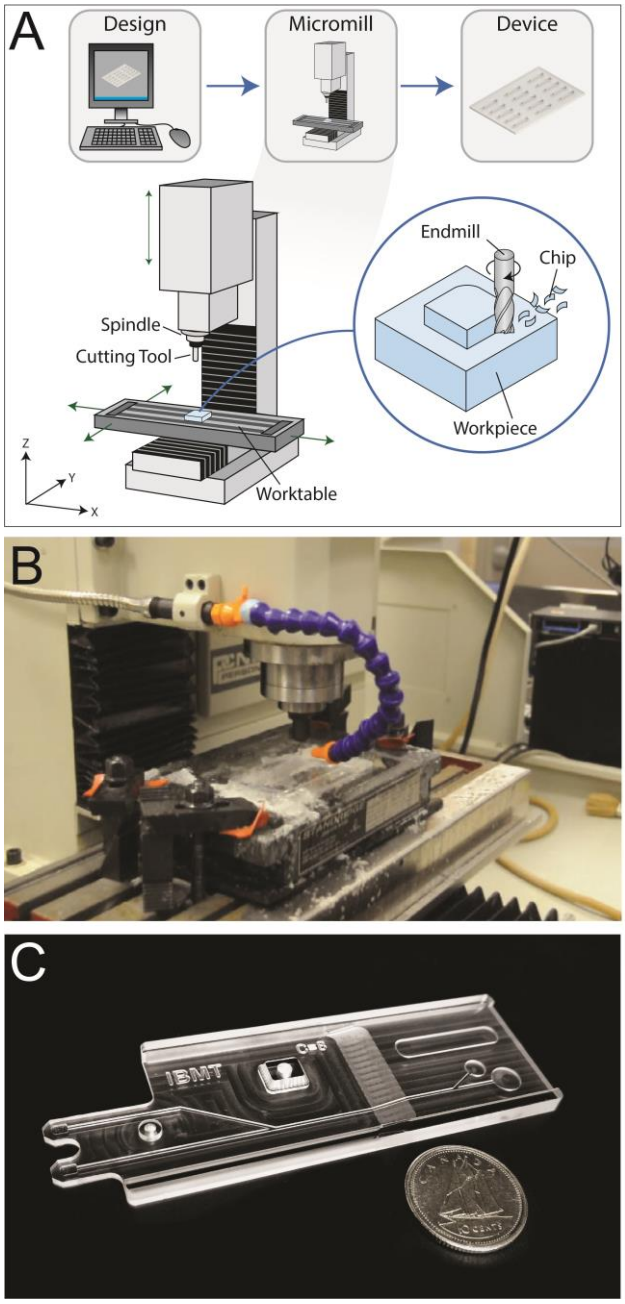

Fig. 2.1 Micromilling basics. (A) A schematic showing the basic components of a CNC mill, which can use computer-aided design (CAD) models to produce finished devices. The mill consists of a worktable (to provide motion in the XY-plane), a cutting tool (to remove material from the workpiece), and a spindle (to hold the cutting tool, spin the cutting tool, and provide motion along the Z-axis). (B) Picture of the milling machine and setup. (C) Picture of a micromilled device.

2.1.3 Other Fabrication Methods for Plastics

To facilitate the discussion of micromilling in the context of microfluidics, we compared it to three of the most commonly discussed microfabrication methods for plastics: (1) injection molding,[88,89] (2) hot

embossing,[90-91] and (3) stereolithography.[68, 69] All three methods have been reviewed elsewhere.[64,92] For convenience, key aspects of these methods are summarized here.

Injection molding is a process in which molten polymer is injected into a mold cavity (often made of steel or aluminum) that contains the template for the features desired on the finished part. The molten polymer conforms to the features within the cavity, hardens during cooling, and is then ejected from the mold to yield a finished part. *Hot embossing* also involves conforming molten polymer to a mold, but instead of injecting the polymer into a cavity, the polymer is pressed against the mold at high temperature and pressure to transfer the desired features from the mold to the softened polymer. While injection molding and hot embossing are indirect fabrication methods that create parts using molds (i.e., intermediary parts that require their own fabrication), other methods can offer more direct approaches that do not require molds or other ancillary components. *Stereolithography*, for example, is an additive manufacturing process that builds 3D parts one layer at a time by curing photosensitive polymeric materials with a laser or other light source, and thus does not require a mold. Classified as a 3D printing method, along with stereolaser sintering and extrusion deposition modelling,[69] stereolithography is rapidly gaining in popularity, and has demonstrated potential for significant utility in microfluidic applications.[68, 93, 94] Note that while milling and stereolithography are both direct fabrication methods, they differ in that milling is a subtractive process, whereas stereolithography is an additive process.

2.1.4 Technical Comparison

A fabrication method must first and foremost offer the technical capabilities required to create the part. Three main technical factors need to be considered: (1) compatibility of that method with the material of choice, (2) ability to achieve the desired features, and (3) quality of the finished part. Since some methods are only compatible with certain materials, the method and the material must be chosen together to achieve optimal quality in the finished product. Since micromilling offers some unique technical capabilities, we were interested in comparing it to other common microfabrication methods to see whether its strengths could be leveraged for microfluidics. Technical capabilities of micromilling and

three other microfabrication methods were tabulated, along with their compatibility with different materials and their ability to achieve certain geometric features **(Fig. 2.2A)**.

Material Compatibility: Hot embossing and injection molding are suitable for polymeric materials, but are impractical for more brittle, rigid materials like glass and metal because both methods create significant stress on the material that often leads to cracks and other defects. Hot embossing can be applied to glass if the temperature is high enough, or to metals if conformable thin films are used.[95, 96] In contrast, stereolithography uses photo-curable polymeric resins, which have similar properties to various common polymers, but also have important differences. For example, Accura 60 (3D Systems Inc, Rock Hill, SC) is marketed as an analogue to polycarbonate in terms of transparency and stiffness, but it differs in terms of hydrophilicity.[69] Micromilling is a primary method for machining metals,[97] and also commonly used for machining plastics. Milling of elastomers, while possible, can be difficult due to large elastic deformation that prevents effective material removal.[98] In addition, glass and ceramics, which are generally difficult to fabricate, are difficult to mill because their brittleness leads to chipping, cracking, and other defects.

Feature Capability. Micromilling and stereolithography provide the widest range of feature capabilities with the least added process complexity. Stereolithography is capable of making complex 3D features that may be impractical or unfeasible with other methods. Complex features such as undercuts, rounded surfaces, and sharp internal corners (see section appendix for more details) can be achieved by micromilling using appropriate tooling and extended process times. Tooling for undercuts and internal corners are not readily available for micro-milling. However, techniques to circumvent the need for internal corners has been provided in the supplementary information **(Fig. A.3)**. Since hot embossing and injection molding both rely on molds for processing, the aspect ratios and feature resolutions are determined by the quality of the molds themselves. Because the molds are often fabricated by milling, the part is no more complex than that achieved by direct milling. Mold quality can, however, be improved through downstream processing of the mold by alternative fabrication methods, such as soft lithography

replication.[38] For injection molding, complex features (e.g., overhangs) are enabled via additional molding mechanisms (e.g., cams). Note that feature capabilities, especially aspect ratios, certainly depend on the properties of the materials used (e.g., melt flow, ductility, and toughness), and thus, feature capability and material choice go hand in hand.

Quality of Finished Part: Quality of the finished part may be assessed by surface roughness, replication fidelity of features, and optical characteristics after fabrication. Surface roughness from hot embossing or injection molding originates from the mold itself, and, if necessary, can be improved significantly through mold polishing. This can be costly and time consuming, especially if multiple designs are being tested. Surface roughness from stereolithography, in contrast, depends on voxel (i.e., 3D-pixel) size and scanning resolution, and often differs significantly depending on orientation of the device within the printer. For micromilling, surface roughness depends on the cutting tool (e.g., tool features, profile, and wear), and the operational parameters chosen for the tool. These parameters can be optimized to reduce surface roughness, as described below.

Besides surface roughness, feature transfer fidelity is another important metric of quality. To ensure that the final part has dimensions that match the original design, one must account for mold shrinkage, a known effect where parts thermally "shrink" as a result of cooling. When milling, friction from the cutting tool can cause temperature increases – affecting feature tolerance and surface quality. However, in plastics, these temperature fluctuations are generally localized around the cutting tool and are mitigated through proper selection of cutting parameters (i.e., feeds and speeds) and adequate use of coolant. Thus, thermal effects, when milling plastics, are not as significant to feature fidelity and tolerances as the tool alignment and the workholding method.

Finally, in terms of optical characteristics, hot embossing of optically transparent polymers can increase autofluorescence of the material;[99] this is a result of the rearrangement of polymer chains. The increased autofluorescence becomes important for applications involving fluorescence detection and microscopy. Interestingly, milling does not change the bulk molecular orientation of polymer chains

within the plastic material the way it would change under high temperature processes like hot embossing, and as such, increased autofluorescence is avoided.

A. Technical Capabilities

Categories	Milling	Embossing	Stereolithography	Injection Molding
Material Capabilities				
Thermoplastics	●●●	●●●	●●○*	●●●
Thermosets	●●○*	●●○*	●●○*	●●●
Elastomers	●○○	●●○†	●●○*	●●●
Metals	●●●	●○○‡	●○○†	●○○*
Glass/Ceramics	●○○†	●○○§	●○○†	○○○*
Wax	●●●	●●●	○○○	●●●
Feature Capabilities				
Additional Heights	No added complexity	Additional layer per height	No added complexity	No added complexity
Aspect Ratio	8:1	2:1	Method dependent	8:1
Contoured 3D Features	Continuous	Layered	Layered	Continuous
Sharp Corners	External Only	Internal / External	Internal / External	Internal / External
Undercuts	Special tooling	Impractical	Yes	Special tooling
Results				
Surface Roughness	0.4 - 2 µm	Replicates mold roughness	0.4 - 6 µm	Replications mold roughness
Autofluorescence	Not affected	Increased by processing	Material dependent	Not affected
Legend	* *Only cured thermosets* † *Poor consistency and characterization*	* *Only uncured thermosets* † *Only thermoplastic elastomers* ‡ *Limited to specific features and thin sheets* § *Layered mix with polymer*	* *Uses resins, that when cured have similar properties to desired polymer* † *Requires polymer/wax addative*	* *Requires polymer/wax addative*

●●● **Excellent**
●●○ **Most conditions**
●○○ **Specific conditions**
○○○ **Impractical**

B. Cost Comparison

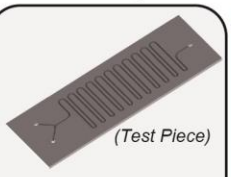

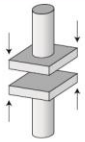

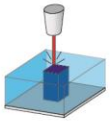

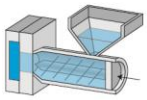

	Milling				Embossing		Stereolithography		Injection Molding	
Setup Costs	*(On-site)*		*(Outsourced)*		*(On-site)*		*(Outsourced)*		*(Outsourced)*	
Equipment	$15k <		*N/A*		$15k <		*N/A*		*N/A*	
Tooling / Supplies	$500		*N/A*		$50		*N/A*		*N/A*	
Process Times and Costs										
Outsourced Expenses	Time	Cost	Time	Cost	Time	Cost	Time	Cost	Time	Cost
Mold / Tooling	*N/A*	*N/A*	*N/A*	*N/A*	4 - 15 d	$ 55 - 321	*N/A*	*N/A*	*N/A*	$ 2255
Device Fabrication	*N/A*	*N/A*	11 - 15 d	$ 137	*N/A*	*N/A*	4 - 6 d	$ 33	11 - 15 d	$ 2
On-site Expenses										
Machine Setup	10 m	*N/A*	*N/A*	*N/A*	5 m	*N/A*	*N/A*	*N/A*	*N/A*	*N/A*
Material Setup	< 5 m	$ 1	*N/A*	*N/A*	< 5 m	$ 1	*N/A*	*N/A*	*N/A*	*N/A*
Device Fabrication	10 m	*N/A*	*N/A*	*N/A*	30 m	*N/A*	*N/A*	*N/A*	*N/A*	*N/A*
Subtotal:	25 m	$ 1	*N/A*	*N/A*	40 m	$ 1	*N/A*	*N/A*	*N/A*	*N/A*
Expenses (per device)										
1 Devices	< 1 h	$ 1	11 - 15 d	$ 137	4 - 15 d	$ 56 - 322	4 - 6 d	$ 33	11 - 15 d	$ 2257
25 Devices	1 d	$ 1	11 - 15 d	$ 137	6 - 17 d	$ 3 - 14	4 - 6 d	$ 33	11 - 15 d	$ 92
50 Devices	3 d	$ 1	11 - 15 d	$ 137	8 - 19 d	$ 2 - 7	4 - 6 d	$ 33	11 - 15 d	$ 47

Fig. 2.2 Fabrication method comparison. A comparison between milling and other microfabrication methods for plastics, in terms of: (A) material compatibility, feature capability, and quality; and (B) cost. In (A), three filled circles = "excellent", three open circles = "impractical" or "inadequate"; see legend (bottom left of A). In (B), for process times, "Time" represents the time of fabrication for one device for both on-site and outsourced devices. "Cost" (in USD) is an estimate, where on-site fabrication is calculated based on cost of goods (not including labor) used

(estimated from the labs of the authors), and outsourced fabrication is based on the lowest quoted price we obtained for the different quantities. N/A = not applicable.

2.1.5 Cost Comparison

A second major consideration when choosing the appropriate fabrication method is the overall cost of employing the method, including equipment, operational, and production costs **(Fig. 2.2B)**. In both academia and industry, the operational cost and potential return on investment eventually become key factors in determining the choice of method, as long as the final part is fabricated to the desired specifications and with sufficient quality to ensure functionality.

First, the required equipment and infrastructure costs for the process will determine the feasibility of simply acquiring the equipment and fabricating the parts in-house. In the case of soft lithography, for example, many universities already have central clean-room facilities that were previously established for research in fields such as microelectronics and micro-electro-mechanical systems (MEMS). This infrastructure provides microfluidics researchers access to the required equipment for lithographic processes, which enabled rapid adoption of soft lithography without the need for new infrastructure.

Injection molding has the highest start-up cost based on infrastructure, equipment setup, and technical know-how for producing quality parts. For this reason, injection molding is commonly outsourced, with a growing number of companies providing injection molding services tailored for microfluidics (e.g., Microfluidic ChipShop, Micronit, SimTech, thinXXS, Symbient). Even if one chooses to outsource, there remains the cost of expensive molds that must be made specifically for each design. This quickly becomes costly during design iterations, and thus, injection molding is typically reserved for mass production of the finalized design. In contrast, start-up costs for hot embossing, milling, and stereolithography processes can be much lower than for injection molding. Entry-level heated presses, milling machines, and stereolithography printers can cost less than $15,000, which helps those working with a tight budget. However, as is often the case, low cost usually means fewer technical features, and greater limitations on spatial resolution, size of workspace, printing speed, material compatibility, and automatic control.

In addition to the cost of the main equipment, accessories can add significantly to operational and maintenance costs of a fabrication method. Milling requires purchasing tooling in the form of endmills that need to be periodically replaced due to damage or wear. While this adds to the list of regular supplies needed for milling, this cost is still significantly lower than the cost of molds required for each design when either injection molding or hot embossing are employed. Furthermore, molds are not only expensive, but require long lead times for their own fabrication. When both the costs of parts and labor are considered, it is understandable that both hot embossing and injection molding are reserved for medium- to high-volume production, respectively. In contrast, operational costs associated with stereolithography and other 3D-printing methods correlate to the material volume of the part (i.e., the amount of material used), as opposed to the design complexity. Thus, stereolithography, because it is an additive process, becomes highly attractive for complex and intricate objects; it is specifically advantageous for parts that use little material or are otherwise difficult to manipulate with other processes, such as micromilling.

A crucial factor that justifies the equipment and operational costs of more expensive methods is the required quantity of production. If higher-volume production is required, injection molding and hot embossing become increasingly more cost effective per part, particularly since these processes can often be parallelized to further increase throughput. In contrast, direct fabrication methods like milling and stereolithography are generally serial fabrication processes, and therefore the cost per part remains fairly constant, independent of the quantity produced. As a result, milling and stereolithography become economical for rapid design iterations, because there is no need for molds or other intermediate production steps.

2.1.6 Summary

We compared micromilling to three other fabrication methods – stereolithography, hot embossing, and injection molding – and assessed their technical capabilities and overall costs. Each method has advantages and limitations, but micromilling offers unique advantages when it comes to ultra-rapid

prototyping because of its low start-up cost, high resolution, and versatility regarding feature geometries and material choices. While there may be challenges with employing this method, these can be overcome with proper selection of equipment, setup, and alignment. To this end, the following sections discuss in detail how these challenges can be addressed so that the benefits of micromilling can be leveraged for microfluidics applications.

2.1.7 Equipment

Once the fabrication method has been chosen, the next step involves selection of the appropriate equipment to meet the needs of the user. For micromilling, choosing the appropriate equipment is critical to ensuring the desired quality of the end product. Milling equipment can be divided into two major categories: (1) the CNC vertical machining center (the central unit that drives the milling process), and (2) the tooling, which comprises the interchangeable parts and accessories that are attached to the central unit. In this section, we discuss the main criteria for selecting an appropriate mill system and associated tooling, with a particular emphasis on microfluidics applications.

2.1.8 CNC Mill Systems

CNC vertical machining centers, more commonly referred to as *mills*, are available in a wide range of configurations that vary in their technical specifications and cost **(Fig. 2.3A)**. With many available options ranging from affordable entry-level systems to advanced, high-precision systems, choosing the right mill for an application can be complicated. Most CNC mills are defined by the following features: (1) *work envelope*, the region of space defined by the allowable motion in the X, Y, and Z directions; (2) *feed rate*, the translational speed of the stage; (3) *spindle speed*, the rotational speed of the spindle that holds the cutting tool; (4) *power* provided by the motor, which often depends on speed and is used to determine appropriate spindle speeds and feed rates for a machining process; (5) the *automatic tool changer (ATC),* a mechanism that automatically changes cutting tools during a milling process, thus eliminating user intervention; and (6) *precision,* or the minimum cutting tolerance achieved by the mill. The *accuracy* of the mill depends on several factors categorized by geometrical errors and wear,

kinematic errors, thermal errors, and stiffness errors.[100] Amongst these mill characteristics, accuracy and speed usually impact cost the most. For example, a basic CNC-milling machine (with accuracy of <25 μm) can be obtained for ~$15,000, whereas, a milling machine with automated tool alignment (with accuracy of <3 μm) may cost over $200,000. In general, CNC-mills can be customized with features that increase throughput and accuracy, albeit at a higher cost. CNC mills that cost over $100,000 often have integrated systems to align and position the workpiece and cutting tool. Thus, different systems and options are available for almost any budget.

2.1.9 Endmills

The most common tool for milling is the endmill. Endmills remove material by cutting along any axis (i.e., X, Y, or Z), and are commercially available in various sizes, shapes (also called *profiles*), and materials **(Fig. 2.3B)**.[101] Endmills have helical grooves, or *flutes*, that wind from the tip of the endmill toward the shaft. The appropriate number of flutes and their helical angles should be selected based on application and the material to be cut. Selecting endmill size is straightforward, and depends largely on the desired feature dimensions and their desired resolution. Selecting the appropriate profile and material can be more challenging, however, because of the vast array of available options. The combination of size, shape, and profile significantly affects the dynamics and potential errors at cutting edges.[102] Square (cylindrical) and ball endmills are "workhorse" profiles that can be used for nearly all applications. Square endmills can be used to mill simple flat features, while ball endmills can be used to mill additional 3D features, including filleted corners, tapered edges, and contoured features.[73] Bull-nose and tapered endmills can also be used to create filleted corners and tapered edges, respectively, and reduce the required cutting time compared to a ball endmill. Many other profiles can be purchased or custom-manufactured for specific applications. Hole machining can be easily performed with square endmills, but drill bits (which only cut in the vertical Z-direction, unlike endmills) are often preferred for holes with a depth-to-diameter ratio greater than 3:1. Undercut features can be produced with woodruff cutters in a secondary machining process, after a slot or edge has first been created with one of the previous tools.

Certain geometries, such as undercuts and threads, remain challenging even with micromilling, but overall, the wide variety of available endmill profiles allows 3D surface contours to be produced more directly, enabling the creation of microfluidic features with complex topography that would otherwise be costly, time consuming, or even impossible to produce with other microfabrication techniques.

High-speed steel and carbide are the most common endmill materials, with carbide more commonly used for micro-endmills. Various endmill coatings are available to increase strength and lubricity, promote the removal of chips (i.e., the small pieces of material cut from the workpiece), and increase resistance to both heat and wear, in order to extend the life of the tool. Thus, coatings should be carefully considered and selected when machining tough materials,[103] such as stainless steel,[104] but are less critical for softer materials, such as plastics, where heat and wear are less likely produced..

Endmills have several dimensional and physical characteristics that should be considered beyond profile and material **(Fig. 2.3C)**. Flute length and cutting diameter directly determine the maximum cutting depth and minimum width of a microchannel, respectively. Though it is possible, it is generally not advisable to mill deeper than the flute length of a given endmill (often three times the diameter); special extended-reach endmills are available if deeper channels or taller features are necessary, but they are generally more expensive, and flex more due to their length, increasing their likelihood of breaking. The shank is the part of the endmill that is inserted into the milling machine; thus, the shank diameter must match the size of the tool holder or *collet*. The helix angle facilitates removal of chips. Insufficient chip removal will lead to clogging of the flutes, which will create heat, and ultimately damage the device, endmill, or both. When milling plastics and other soft materials, heat build-up can be particularly problematic, so lower helix angles are preferred (30° is the industry standard)[105] because they provide more space between flutes, thereby improving chip removal. Additionally, the number of flutes can affect chip removal. For most plastics, two-flute micro-endmills can be operated at faster cutting speeds than four-flute endmills because they allow for better chip removal. On the other hand, four-flute endmills yield lower surface roughness than two-flute endmills. Lastly, the *center-cutting* classification of endmills

indicates whether the endmill is capable of cutting (plunging) in the Z-direction, like a drill bit. Non-center-cutting endmills maintain the capability of cutting in the Z-direction, but must simultaneously move in the XY-plane. This is most often achieved by cutting with a spiral or ramp-like motion. Overall, careful consideration of the endmill characteristics discussed above, including size, material, and profile, will enable the user to select appropriate endmills, and produce high quality parts.

A. CNC Mill Comparison

	Manufacturer	Model	Cost (USD)	Work Envelope (X,Y,Z) in	Work Envelope (X,Y,Z) mm	Feed ipm	Speed RPM	Power HP	ATC tools	Accuracy µin	Accuracy µm
< $50k	Tormach	PCNC 770	$ 15,500	14.0 7.5 13.3	356 191 337	135	10,000	1	10	600	15
	Minitech Machinery	Mini-Mill/GX	$ 21,750	12.0 9.0 9.0	305 229 229	40	25,000	-	N/A	-	-
	Haas	Minimill	$ 34,000	16.0 12.0 10.0	406 305 254	600	6,000	7.5	10	-	-
$50k - $100k	Mill Tronics	RW15	$ 63,000	25.0 25.0 20.5	635 635 521	800	8,000	12	16	400	10
	Bridgeport	GX 480	$ 68,000	19.0 16.0 17.0	483 406 432	590	10,000	20	20	40	1
	DMG Mori Ellison	Milltap 700	$ 70,000	27.6 16.5 15.0	700 420 380	590	10,000	7.5	15	400	10
	DMG Mori Ellison	DMC 635 V	$ 80,000	25.0 20.1 18.1	635 511 460	1181	8,000	17.4	20	40	1
$100k <	Microlution	363-S	$ 100,000	2.5 2.5 2.5	63 63 63	-	50,000	-	36	40	1
	Atometric	G4-Ultra CNC	$ 130,000	4.0 4.0 3.0	102 102 76	1181	100,000	-	14	20	.6
	Datron	Datron M7	$ 150,000	20.0 20.0 9.0	508 508 229	639	48,000	2.6	15	-	-
	Sodick	TT1-400A	$ 220,000	15.8 9.8 11.8	400 250 300	1440	40,000	-	N/A	120	3

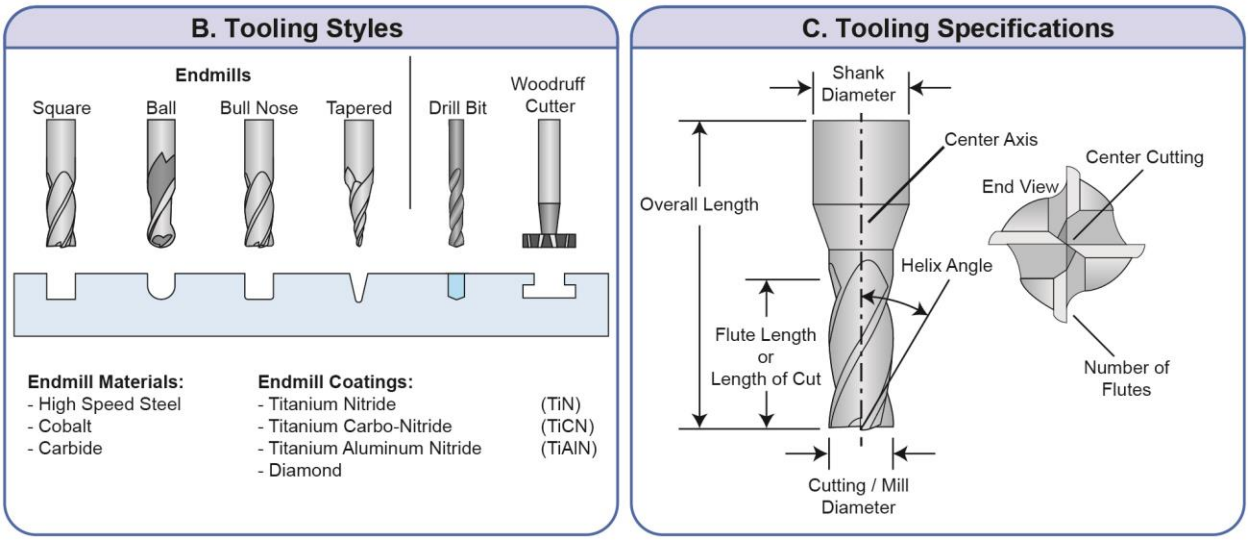

Fig. 2.3 Micromill costs, capabilities, and tooling. (A) CNC mills from several manufacturers are compared and categorized into price ranges. Costs were assessed based on quotes of the lowest level mill from each manufacturer, except for the Tormach mill, which was quoted to be comparable in terms of capabilities to the other CNCs. Unlisted specifications were not given by the manufacturer. (B) Endmills – the most common cutting tool for milling – are available in many profiles, in a variety of materials, and with a variety of coatings. Mills are also compatible with a variety of other cutting tools, some of which are shown. (C) Endmills are defined by several characteristics, each of which contributes to the endmill capabilities and feature quality.

2.1.10 Quality Comparison

When considering micromilling for fabricating microfluidic devices, an obvious concern is how the quality of milled parts compares with parts fabricated via other methods, given the surface roughness that typically results from the milling process. With the proper CNC mill setup and operation, however, it is possible to achieve sufficient resolution and surface roughness to enable practical use of micromilled devices for certain applications. In this section, we provide an evaluation of the quality of microdevices milled with an entry-level CNC milling machine. Specifically, we (1) detail the setup and procedures that we utilize to mill high-precision microdevices; (2) assess the resolution and surface roughness that are achieved with our milling process; and (3) assess the utility of milled channels for cell culture studies. For comparison, we assess the quality of hot-embossed microchannels fabricated using methods described by Young *et al*.[38] Hot embossing was chosen for comparison based on our previous observations of low surface roughness, and based on cost, turnaround time, convenience, and direct compatibility with cell culture, which are all more comparable to micromilling than for injection molding or stereolithography.

2.1.11 Setup and Procedures

Proper setup of milling steps can contribute significantly to improving the quality of the milled part. In particular, workpiece fastening and tool alignment are perhaps the two most influential factors on quality[106] (see **Appendix** for tips on setup and mill operation). For workpiece setup, we have achieved the best final quality by using adhesive tape to secure the plastic sheets to a flat granite block **(Fig. A.1c)**. We recommend securing the block to the worktable using strap clamps located at each of the four corners, or two corners and an opposing center (triangular setup). These clamps are then adjusted to level the block, using a drop test indicator for verification. For our study, the block was levelled to ±0.00025” (6.4 μm) across a span of 10” (254 mm) along the X-axis and 5” (125 mm) along the Y-axis. Plastic sheets are secured to the block using an adhesive. If the adhesive is difficult to remove from the workpiece, a protective sacrificial (easy to remove) tape can be applied to the workpiece. The flatness of the plastic

ideally mimics that of the block. However, unwanted debris, and air bubbles must be avoided, as these artifacts lead to localized height variations in the plastic sheet.

2.1.12 Surface Roughness and Resolution

Surface roughness and resolution are important metrics for assessing the quality of microfluidic devices, particularly for cell biology studies that require microscopy, or that utilize surface interactions (e.g., microfluidic ELISAs with substrate-bound antibodies), where roughness can impact proper operation and control. To this end, we measured the surface roughness of microchannels milled into PS,[38, 107] PMMA, [108, 109] and cyclic olefin copolymer (COC),[110] three transparent polymers commonly used for microdevice fabrication **(Fig. 2.4A)**.[69] In general, the surface roughness is proportional to the feed rate (i.e., surface roughness decreases as feed rate decreases) **(Fig. A.2c-d)**. We expected surface roughness to vary inversely with spindle speed based on other studies.[111] Instead, we observed the lowest surface roughness at a spindle speed of ~ 5000 rpm in our experiments. We believe that this may be due to limits of our particular CNC mill, and that system-specific vibrations[112] may influence the optimal spindle speed for minimizing surface roughness. It is therefore likely that the surface roughness data will be different on mills from other manufacturers, and practitioners should be careful to conduct their own tests to determine optimal spindle speeds. We found that the depth of cut (up to 300%) had minimal effects on surface roughness.

A second major concern associated with surface roughness is the presence of *burrs* – small chips of plastic that remain attached to the workpiece after machining.[113] Burrs occur most commonly in ductile plastics (e.g., COC or polypropylene) and are often prevalent along faces and edges. Occasionally, burrs will form in brittle plastics (e.g., PS or PMMA), but are often limited to edges, as opposed to faces. There are several simple considerations for reducing the likelihood of burrs.[114] The first consideration is to properly choose one of two opposing directions of cutting, referred to as *conventional (up) milling* and *climb (down) milling*.[115] Conventional milling is characterized by the workpiece moving *directly against* the cutting teeth of the endmill at the point of contact, such that the endmill adds resistance to the

workpiece motion **(Fig. A.3a)**. In contrast, climb milling represents the workpiece moving in the *same direction* as the rotating cutting teeth at the point of contact, as if the endmill was reducing resistance to the workpiece motion, and "climbing" along the workpiece surface in the direction of travel. For non-brittle plastics (e.g., polypropylene), conventional milling is recommended to minimize burrs. However, it should be noted that climb milling can also produce high quality finishes for metals[116] and more brittle plastics like PS and PMMA. The second approach is to ensure that the tool is sharp. Dull tools, especially when used with low chip loads (i.e., high spindle speed or low feed rate), cause high levels of friction and generate heat. Heat, in turn, increases material ductility resulting in burrs, or in the worst case, can lead to melted plastic and tool breakage. For these reasons, it is important not to use feed rates that are too low, or spindle speeds that are too high, especially with dull endmills.[117] The third approach, especially if burrs are present on vertical corners, is to adjust the toolpath to avoid tool exits.[118] Many of these factors are changeable settings in the computer aided modelling (CAM) software packages **(Fig. A.6)** and should be tailored to achieve the best quality possible.

When considering milling resolution, it is important to note that while mill tolerances are often specified by the manufacturer, they can also depend on setup and operational parameters. For this reason, we assessed resolution in terms of both accuracy (i.e., ability to achieve a target dimension) and precision (i.e., consistency across features, or low variability) using our mill and workholding techniques, and compared the results from milling to those from hot embossing. Resolution in the XY-plane is unaffected by misalignment, and dependent only on the technical capabilities of the mill **(Fig. 2.4B)**. Using our CNC mill with parameters that yielded the lowest surface roughness **(Fig. 2.4A)**, we consistently achieved <0.001" (<25 μm) accuracy, as expected, based on manufacturer specifications. Importantly, tool flexion induced through factors such as higher chip loads, increased depths of cut, and direction of cut, can lower accuracy. Experienced machinists often employ a final (low chip load) finishing cut to improve accuracy and further reduce surface roughness. In the Z-axis direction (i.e., for feature heights), the milling is repeatable between each separate channel **(Fig. 2.4C)**. The large variation (~.001") observed between the

target height and the measured height was a result of tool alignment, in the Z-axis, to the workpiece. While accuracy in the Z-axis can be effected by tool alignment, the precision is independent. This variation can be reduced by using smaller step distances, by using magnifying optics to better observe tool contact, or alternative (e.g., automated/electronic) approaches for tool alignment.

These results demonstrate that with the appropriate setup and operation, the surface roughness, accuracy, and precision achieved by micromilling are in fact comparable to those achieved by hot embossing **(Fig. 2.4B-C)**. One important difference between milling and embossing, however, is that sharp internal corners are difficult to fabricate via milling because the endmill inherently creates an internal radius of curvature **(Fig. 2.4D)**. However, this may not be an issue for many applications.

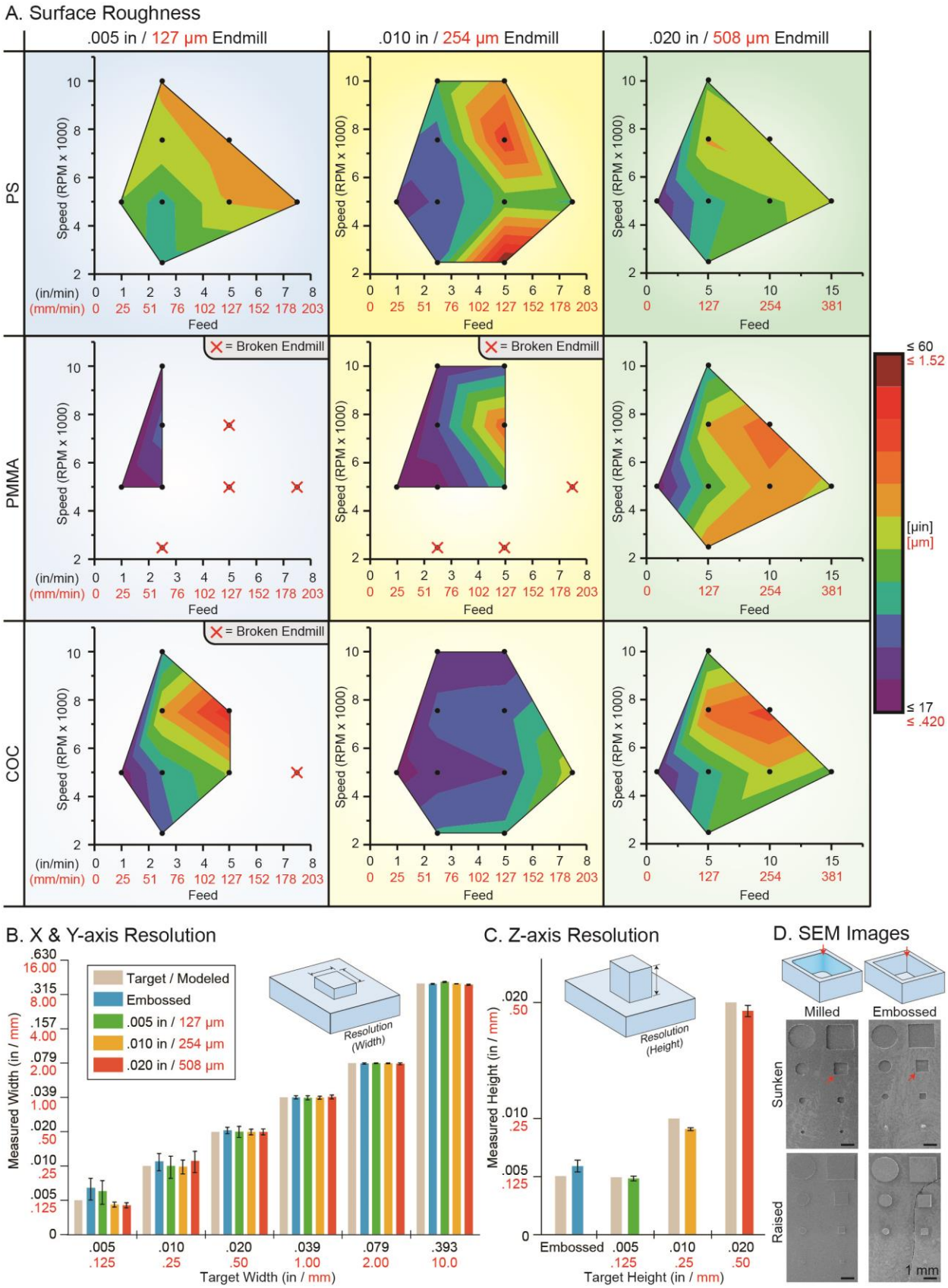
A. Surface Roughness
.005 in / 127 µm Endmill
.010 in / 254 µm Endmill
.020 in / 508 µm Endmill
PS
PMMA
COC
Speed (RPM x 1000)
(in/min)
(mm/min)
Feed
= Broken Endmill
≤ 60
≤ 1.52
[µin]
[µm]
≤ 17
≤ .420
B. X & Y-axis Resolution
Measured Width (in / mm)
Target / Modeled
Embossed
.005 in / 127 µm
.010 in / 254 µm
.020 in / 508 µm
Resolution (Width)
Target Width (in / mm)
C. Z-axis Resolution
Measured Height (in / mm)
Resolution (Height)
Embossed
Target Height (in / mm)
D. SEM Images
Milled
Embossed
Sunken
Raised
1 mm

Fig. 2.4 Surface roughness and resolution using an entry-level CNC mill. (A) Colored contour plots showing surface roughness as a function of spindle speed (y-axis) and feed rate (x-axis). Surface roughness was measured by interferometry (see Appendix), and ranged from 0.420 to 1.52 μm (root-mean-squared averages, color legend, right). Black dots are speed and feed conditions tested (n = 3 samples per dot), while colored contours are interpolated data. Speed and feed conditions that resulted in broken endmills are marked with a red "X". Graphs are arranged in a 3x3 matrix representing data for three different plastics (PS, PMMA, COC), each tested with three different endmill sizes (127, 254, 508-μm diameters). Resolution in the (B) XY-plane and (C) the vertical z-axis were assessed by comparing the actual size of a fabricated feature to its target "nominal" size (i.e., tolerance or accuracy). (n = 3 samples for all conditions; error bars = standard deviation, represents precision; p = 0.79 via Bartlett test for (B)). (D) SEM micrographs of the features used to characterize the resolution. Red arrows point out the ability to make sharp internal corners via embossing, while rounded fillets form for a pocket made via micromilling.

2.1.13 Cell Culture

To test the compatibility of microfabricated devices with cell based experiments, we cultured cells in: (1) micromilled PS devices with two different configurations (one with a flat bottom and one with a milled bottom), (2) a hot-embossed device, and (3) a microtiter plate as a control. PS was selected for its easy machinability and its frequent use in microfluidic cell-based applications.[33,74] For a variety of mammalian cell types (endothelial, prostate cancer stromal, and bone marrow stromal), we found cell viability was unaffected by the method of device fabrication **(Fig. 2.5A)**, suggesting that microfabricated devices are indeed compatible with cell culture experiments. Notably, cells have previously been reported to respond to surface roughness.[119-127] We noticed that cells cultured on the milled surface would occasionally orient along the circular pattern resultant from the milling operation. However, this was not evident in all cases. Furthermore, this issue can easily be avoided by bonding a milled channel to a flat (non-milled) substrate, and culturing the cells on the flat substrate rather than the milled channel. While cell viability was confirmed on milled surfaces, more research is needed to study the effects of milling on cell morphology, proliferation, protein expression, and differentiation. These types of cell studies will be aided by the fact that important factors like protein adsorption and plasma treatment do not appear to be adversely affected by the roughness of the milled surfaces. For microscopy imaging, we found that the roughness of micromilled surfaces could impede phase contrast imaging of cells, particularly when cells were cultured directly on the micromilled surfaces **(Fig. 2.5B and Fig. A.4)**. However, micromilled surface roughness had no observed effect on fluorescent imaging, where image quality was comparable to that obtained with standard microtiter plates **(Fig. 2.5B, control)**.

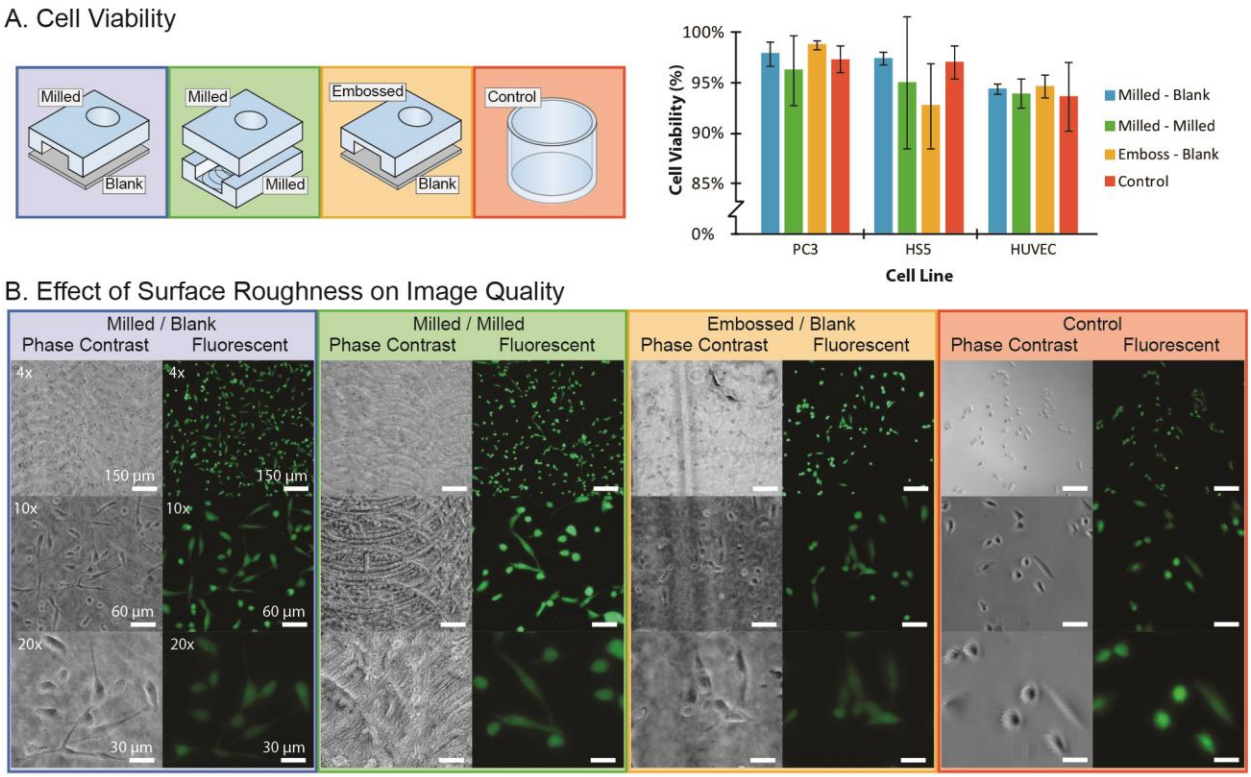

Fig. 2.5 Cell culture and image analysis in milled microchannels. (A) Channels are assembled in three configurations: (1) A milled channel with ports is bonded to a cover layer, (2) a milled port layer is bonded to a milled channel, and (3) an embossed channel with ports is bonded to a cover layer. A microtiter plate is used as a control. Mammalian cell lines are cultured for 48 hours in each configuration, then assayed for cell viability (error bars represent one standard deviation, N=3). No statistically significant difference was observed between culture methods ($p > 0.14$ in all cases, Students T-test). (B) Phase contrast and fluorescent images were taken of HS-5 stromal cells in each channel configuration using 4, 10, and 20× magnifications. (cell culture described in Appendix).

2.5.0 Discussion

This tutorial demonstrates that micromilling has important utility that enables it to fill several gaps in our current microfabrication repertoire. Micromilling offers excellent versatility across various materials, allowing either the creation of molds for subsequent device production (i.e., hot embossing), or the creation of microchannels and other features directly in devices. Most importantly, micromilling provides design-to-prototype turnaround times on the order of *minutes and hours* instead of days, weeks, or even months. In this day and age of fast-paced innovation, the ability to prototype a design at this rate can perhaps be the difference between commercializing a product in a year, and being stuck in "development limbo" for much longer.[30] It is clear that for high-volume production, micromilling cannot compete with the low cost and fast production rates of injection molding and hot embossing. Rather,

micromilling excels in the early development stage where frequent design iterations are required in conjunction with the use of conceptualized models, numerical simulations, and other design tools, to converge on an optimal functional design. During this stage, it is both unnecessary and impractical to invest in a series of costly, high-quality molds for high-volume production methods, when the design has not yet been finalized. Another alternative gaining in popularity is to outsource the fabrication to prototyping firms, which promise to work closely and efficiently with their clients during the crucial design phase to generate molds, produce parts, expedite optimization of the design, and ultimately minimize development costs. Outsourcing is available for injection molding, hot embossing, stereolithography, as well as micromilling (e.g., z-microsystems), and thus is feasible and appropriate in many cases. It does, however, require the client to sacrifice some freedom and control on how and when the device is fabricated and delivered.

Like all fabrication methods, micromilling has advantages and limitations. The main discussion focused on increasing quality of the part in terms of uniformity, accuracy, precision, resolution, and surface roughness. With only an entry-level milling system, we were able to achieve surface roughness of <17 μin (0.42 μm), and similar resolution to hot embossing **(Fig. 2.4D).** The surface roughness can be minimized with the techniques described above, but for applications where optical clarity is critical, such as for phase contrast cell microscopy and imaging, the roughness created from the milling process may not be acceptable. These effects are mitigated by bonding transparent PS cover layers, as opposed to imaging directly on a milled surface. Additionally, the roughness of milled surfaces can be reduced afterward with techniques such as solvent vapor polishing **(Fig. A.5)**, which can in some cases yield surfaces with optical quality.[128]

Besides imaging concerns, a common fear is that surface roughness will promote bubble formation, perhaps due to heterogeneities in the surface that perturb the advancing contact line and lead to trapped pockets of air. In our observations over various designs, geometries, and materials, bubble formation has not been an issue in plastic micromilled devices any more than it is an issue for PDMS

micromolded devices. If the geometry is not inherently prone to bubble formation, then surface roughness does not promote bubble formation within PMMA, PS, or PC devices. This is likely due to the Wenzel condition for rough surfaces,[129, 130] i.e., $\cos\theta_w = r\cos\theta_e$, where $r\cos\theta_e$ is the Young Law contact angle, θ_w is the Wenzel contact angle, and r is the ratio between the true contact surface area and projected planar surface area (i.e., $r = 1$ for smooth surfaces and $r > 1$ for rough surfaces). The Wenzel condition states that roughness enhances hydrophobicity if the surface is naturally hydrophobic (θ \> 90° on a smooth surface of the same material), but also enhances hydrophilicity if the surface is naturally hydrophilic (θ < 90° on a smooth surface of the same material). Since aqueous solutions are the most common priming fluids, and the contact angle of water on PMMA, PS, and PC are all < 90° (reported to be 64°, 87°, and 77°, respectively)[131] surface roughness will tend to enhance hydrophilicity and promote wetting in devices made from these plastics, and this in turn will reduce the chance of bubble formation. Thus far, our observations have consistently confirmed this prediction.

With regard to production rates, experience combined with strong machining skills can help reduce fabrication time for one device to less than 30 minutes for simple geometries. For more complex designs, fabrication time can range anywhere from 30 min to more than an hour. While the operator is free to perform other tasks once the run has been initiated, it is recommended that the operator continue to monitor progress of the run to ensure that it completes without failure.

Fabrication runs do fail occasionally, but most of these failures are caused by common avoidable operational issues. First, endmills will break during a run if there is inadequate chip removal or excessive chip loads (particularly for sub-millimeter diameter endmills). To reduce the frequency of endmill breakage, one can either remove chips efficiently with flood coolant, or use endmills with fewer flutes, which are less likely to trap chips. During the transition from plunge cutting to side milling (i.e., from the Z-axis to milling along the XY-plane) chips often get stuck in the flutes, leading to endmill breakage. This issue can be avoided by using alternative entry methods – such as a spiral or ramped entry – wherein the endmill progressively lowers into the material while simultaneously side milling, as opposed to

strictly plunging into the material. If endmills are breaking due to excessive chip loads, one can simply reduce feed rate or increase spindle speed. While machining handbooks are excellent resources for finding proper feed rates and speeds for conventional tooling and materials, these parameters may need to be tested for micromilling operations, either through trial and error, or with guidance through calculations based on chip load (i.e., the thickness of the chip that will be removed from each flute). Finally, other possible issues, such as machine vibrations, workpiece vibrations, or offsets in height and setup of the workpiece, should all be carefully examined to help troubleshoot failures.

Even with these considerations, we argue that the usefulness of micromilling outweighs its limitations. Indeed, the most significant limitations commonly stated in criticism of micromilling (aside from technical issues) involve its affordability, ease of operation, and suitability for emergent microfluidic applications like cell culture. This review has provided supporting data and evidence to dispel these misconceptions about the challenges of micromilling. First, the capabilities and availability of milling machines are expanding, with a wide selection of equipment to choose from, ranging from high-end advanced systems to affordable systems for the hobbyist. This increases accessibility of the technique to novice machinists and do-it-yourself enthusiasts, which in turn accelerates research, discovery, and innovation. Second, while some mechanical aptitude is necessary to get up and running and to troubleshoot through technical issues, this tutorial guide will hopefully serve as a quick reference to expedite the learning process, and circumvent common pitfalls. Third, cell culture appears to be feasible given our results, although further efforts will be needed to verify specific applications, and further dispel remaining concerns regarding the suitability of milled devices for cell-based studies. Thus, while micromilling has its limitations, the savings it offers in development time and effort during design iterations should alone be worth the investment.

Various other advancements and considerations in the micromilling field are worth noting. First, several manufacturers (e.g., Harvey Tool and Performance Micro Tool) offer endmills with diameters of 0.001 in (25 μm) and smaller. Together with high-end, advanced milling systems, the cutting resolution

that can be achieved with such tools will likely reach new limits. While endmills are the workhorse cutters, other more obscure tools such as dragknives can enable cutting 2D contours and small features from thin plastics that would otherwise be difficult to achieve with conventional endmills. For more advanced applications, many 3-axis CNC milling machines can accommodate a fourth axis (i.e., rotation of the workpiece), adding yet another dimension to microfluidic devices that may be impractical with other microfabrication methods.

As a microfabrication method, micromilling will provide an additional technique that supplements our current repertoire of methods, with specific advantages for handling plastics and other rigid materials. The key advantage of micromilling is its ability to translate designs to prototypes in a matter of minutes and hours, enabling ultra-rapid turnaround times while offering high-quality devices that are suitable for preliminary testing. In addition, complex features can be readily achieved with micromilling, which might otherwise be difficult or impossible to achieve with lithography or embossing. Thus, micromilling can accelerate research and discovery, facilitate innovation, and importantly, contribute to reducing the high costs and long development times that are common to the crucial design phase of technology development. Given these advantages, as well as the available optional accessories and ongoing advancements in technical specifications, micromilling has the potential to play an increased and important role in microfluidics, as well as in other engineering fields.

Chapter 3 Rapid prototyping of arrayed microfluidic systems in polystyrene for cell-based assays[2]

3.1 Introduction

The major advances in microfluidics and recent progress in bioMEMS in the last decade can be largely attributed to the emergence of soft lithography as a fast, facile, and cost-effective method for microfabrication.[36, 132] The ability to exploit the properties of elastomeric materials such as poly(dimethylsiloxane) (PDMS) for rapid prototyping of microscale systems has allowed scientists and engineers to employ iterative design processes to efficiently optimize microchannel configurations for diverse applications and across various disciplines **(Fig. 3.1)**.[28, 133-137] The simplicity and accessibility of soft lithography has also enabled a unique design methodology that is both precise and versatile, facilitating novel and creative experimental approaches to current problems in biology. The popularity of PDMS is due not only to its convenient fabrication process, but also to a number of attractive physical and mechanical properties (e.g., optical transparency, permeability, and pliability) that have proven particularly useful for a range of applications. However, growing evidence suggests that the use of PDMS may be unsuitable for extensive biological research, or for certain specialized studies, where the use of PDMS can potentially lead to biased conclusions.[138] Limitations of PDMS include its ability to absorb small hydrophobic molecules,[139, 140] to allow evaporation through the bulk material,[141] and to recover its hydrophobic nature after being subjected to surface treatments.[142] Furthermore, the acceptance of PDMS-based platforms from the biology research community has been partially hindered by the lack of sufficient use and characterization of the material for biological applications, as well as challenges associated with corroborating PDMS-based results with past results obtained from conventional platforms.[16, 143] To assist

2 This chapter has been adapted from the following publication: "Rapid prototyping of arrayed microfluidic systems in polystyrene for cell-based assays" Edmond W.K. Young*, Erwin Berthier*, David J. Guckenberger, Eric Sackmann, Casey Lamers, Ivar Meyvantsson, Anna Huttenlocher, and David J. Beebe. Analytical Chemistry, 2011.

* Authors contributed equally

the adoption of microfluidic technologies in biology laboratories, which is the ultimate goal for researchers developing cell-based assays, we must address these concerns associated with PDMS.

From the perspective of the biologist, the most commonly used material for in vitro cell-based research is polystyrene (PS), due to its commercial availability in tissue culture plasticware. PS is central to mammalian cell culture research and various cell-based assays, and is therefore unlikely to be supplanted in popularity by other materials. Making PS-based microfluidic devices more readily available would thus reduce the barriers that hinder adoption of microfluidics by allowing better transposition of experimental protocols and better comparisons between data. Moreover, PS is amenable to mass manufacturing processes that facilitate the translation of microscale systems from simple laboratory tools to commercially marketable products, further expanding the potential impact in biological research. This trend is highlighted by the emergence of various companies offering specific plastic microfluidic cell based assays (e.g., Bellbrook Labs, Madison, WI, USA; Ibidi, Munich, Germany).

To date, thermoplastic materials as a whole have been used in a relatively small proportion of published work in the area of microfluidics and microscale technologies in comparison to PDMS.[71, 144] Of this work, the main choices of thermoplastic material for microfabrication include poly(methylmethacrylate) (PMMA),[145-147] polycarbonate (PC),[147-149] cyclo-olefin copolymer (COC),[148, 150, 151] and to a lesser extent PS.[150] Several fabrication methods have been employed to produce thermoplastic microfluidic devices.[71] Of these methods, hot embossing is relatively simple and easy to implement, and thus has potential to become a cost-effective technique for producing devices within a laboratory setting in a manner that complements PDMS-based processes.

A major factor for the dominance of PDMS over thermoplastics as the material of choice for microfluidics research, particularly in academic laboratories, is the number of bottlenecks and limitations present in the process workflow for thermoplastic hot embossing microfabrication **(Fig. 3.1)**. First, PDMS allows a cost-effective device optimization process with the ability to vary the design extensively. Thermoplastic fabrication, on the other hand, requires more expensive and labor-intensive processes,

which include the creation of micro-machined metal molds that require polishing to achieve high quality surface finishes. This may be acceptable in a commercial setting once a design has been finalized, but becomes costly for research laboratories involved in early stages of design and development. Second, after a design is chosen, PDMS offers a rapid and repeatable fabrication process for generating a sufficient supply of devices for laboratory use. Whereas PDMS can be readily bonded to glass, plastics, and to itself via plasma treatment or other methods, monolithic devices made entirely of thermoplastics must rely on more challenging techniques.[71] The failure rate of thermoplastic devices at this stage of the fabrication process represents an additional obstacle along the process workflow. To facilitate the use of PS for microfluidic cell biology applications as an alternative material to PDMS in research laboratories, it is necessary to establish a microfabrication process that is accessible, affordable, efficient, and reliable, at a level that can be competitive with the soft lithography process. Doing so will allow biologists to more easily adopt thermoplastic devices in their research and to take advantage of microscale phenomena relevant to cell biology applications, without being concerned about the adverse effects of PDMS.

In this study, we present a streamlined PS microfabrication process for creating arrays of microfluidic systems on a single device, with the primary goal of establishing a set of protocols that are similar in reliability, and in cost and time expenditure compared to the PDMS-based soft lithography process. We hope to provide an alternative fabrication methodology that gives researchers working at the interface between microfluidics and biology a material consistent with existing laboratory cultureware. To achieve this, we developed methods to (1) fabricate inexpensive solid epoxy molds that use the same equipment as traditional SU-8 master fabrication while being able to withstand the high operating temperatures and pressures of hot embossing; (2) quickly generate arrays of access ports via a through-hole embossing technique that eliminates laborious drilling or punching procedures; and (3) thermally bond PS sheets and films over large areas (100 x 100 mm) and with sufficient strength to withstand long-term cell culture applications in humidified environments. For clarity in nomenclature, we refer to each

bonded PS sample as a *device* consisting of an *array of microsystems*. Each microsystem in the array represents an independent experimental condition, and may consist of network(s) of *microchannels*.

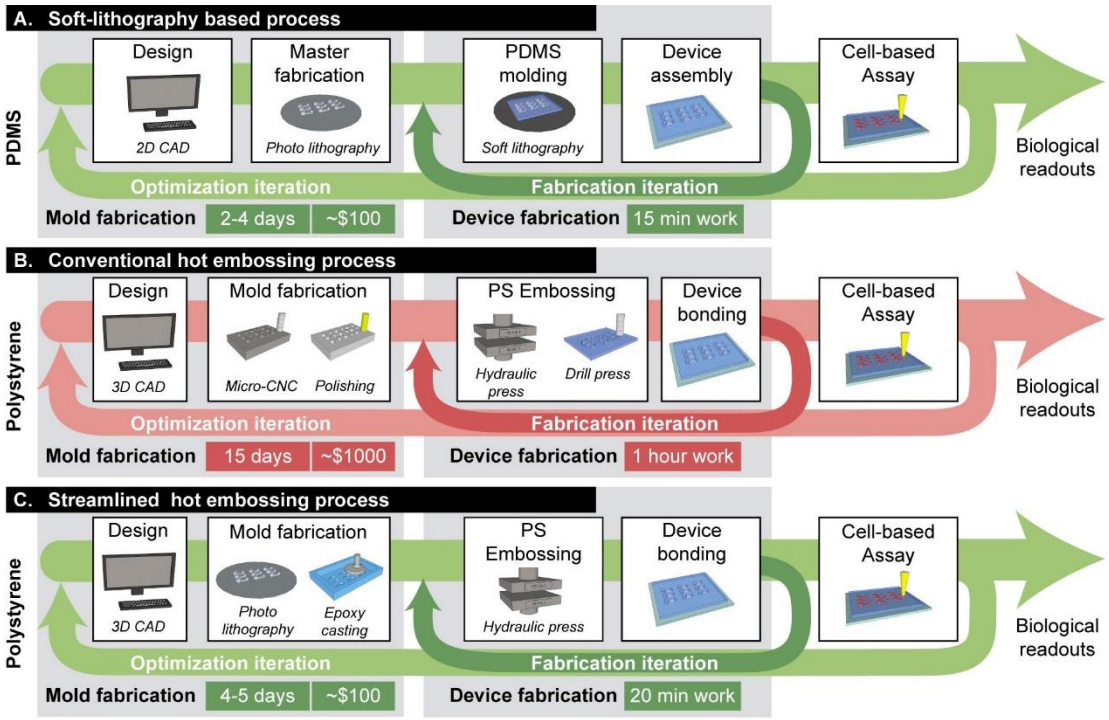

Fig. 3.1 Microfabrication process workflows: comparing PDMS to thermoplastics. (A) PDMS-based soft lithography process. Turnaround time from computer mask design to completed master mold is ~2-4 days. Costs include mask, wafer and SU-8 photoresist. (B) Current thermoplastic-based microfabrication process. ~10-15 days are required from design to usable mold; 1 hour is required for embossing, bonding and drilling access ports (for a platform containing 50-100 ports). Costs include mold machining and polishing. (C) Streamlined thermoplastic-based microfabrication process. Mold fabrication time is similar to (A) with an additional epoxy casting step. Costs are similar to (A) with the additional cost of the epoxy. Devices were fabricated more quickly using a through-hole embossing method that eliminated manual removal of access ports.

3.2 Experimental Section

3.2.1 Epoxy Mold Fabrication

The first two steps in our process were equivalent to those for the soft lithography process currently used in many microfluidics laboratories,[132, 152] namely (1) the design and printing of photomasks, and (2) the fabrication of a master mold using SU-8 photoresist (Microchem, Newton, MA, USA). Briefly, SU-8 photoresist was spincoated on a silicon wafer (WRS Materials, San Jose, CA, USA) to the desired film thickness, pre-baked, exposed to UV light (EXFO, Mississauga, Canada), post-baked, and finally

developed in propylene glycol monomethyl ether acetate (PG-MEA, Sigma, St. Louis, MO, USA). Draft angles on tall features were obtained by aligning the UV light-guide at an angle of 30-35 degrees from normal, and manually rotating the wafer on a turning plate during exposure. Doses were doubled to account for the angled exposure and the rotation.

A negative mold of uniform thickness was made in PDMS (Dow Corning, Midland, MI, USA) from the SU-8 master using typical curing parameters (10:1 mixing ratio of elastomer base and curing agent, 90°C, 1 h) **(Fig. 3.2A)**. Uniformity of the layer thickness was critical, and was achieved by laying a large glass slide on top of two 2.5-mm thick spacers. The PDMS slab was gently demolded from the wafer without detaching from the large glass slide, thereby preventing shrinkage of the features. A 15-mm tall PDMS ring was laid around the features to form a cavity into which a thermocurable epoxy (EC-415, see Materials and Preparation) was poured and allowed to fill the negative-relief features of the PDMS mold **(Fig. 3.2B)**. Air bubbles trapped in the mold features were dislodged manually with a sharp tool. Desiccating the PDMS mold prior to pouring the epoxy reduced the incidence of these bubbles. Following manufacturer's specifications, the epoxy was cured for 24 h on a 40°C hot plate, followed by a four-stage heat treatment (93°C for 2 h; 121°C for 2 h; 149°C for 2 h; 177°C for 2 h) in an oven, and subsequent cooling to ~60°C before removing from the oven. The result was a solid positive-relief epoxy mold that replicated the original SU-8 master **(Fig. 3.2C)**.

3.2.2 Materials and Preparation

PS raw materials were purchased from Goodfellow (Cambridge, MA, USA) in various stock thicknesses, including 1.2 mm-thick stock sheets (#ST313120, amorphous), as well as 50, 125, and 250 μm-thick stock films (#ST311050, ST311125, ST311250, respectively; biaxially oriented). Thick stock sheets can be pre-cut to size using a razor blade or a laser cutting machine (Jinan Artsign Ltd., Jinan City, China) (not required), whereas thinner stock films can be cut to size with scissors. After cutting, PS sample pieces were either used as is, at 1.2 mm thickness, or flattened to other desired thicknesses using a hydraulic heated press (see Hot Embossing). The PS sample was placed between two mirror-finished

stainless steel plates (McMaster-Carr, Elmhurst, IL, USA) to ensure optical transparency. Two metal shims (feeler gauge set, Grainger, Chicago, IL, USA) were used as spacers on opposite sides of the PS part to ensure uniform desired thickness **(Fig. 3.2D)**. Parameters used in the PS flattening protocol are listed as part of **Fig. 3.2G**. As an alternative method to flattening PS sheets, desired thicknesses were also attained by stacking the appropriate PS films together (e.g., a 475 μm-thick PS layer could be achieved by stacking one 250-μm, one 125-μm, and two 50-μm layers together).

Cyclo-olefin polymer (COP) sheets were purchased from Ajedium Films (Ajedium, Solvay Solexis Inc., Newark, DE, USA) as 610-μm thick sheets made from Zeonor COP (1420R grade).

We tested three different epoxies to determine the material most suitable for our applications and our processing requirements: (1) Conapoxy FR-1080 (Cytec Industries Inc., Olean, NY, USA); (2) RenCast 4037 (Freeman Manufacturing, Avon, OH, USA); and (3) EC-415 (Adtech Plastic Systems, Madison Heights, MI, USA).

3.2.3 Hot Embossing

Hot embossing was carried out using a programmable 15-ton hydraulic press with heated platens (Model #3889, Carver Press, Wabash, IN, USA). Two different approaches were used for embossing microfeatures into PS, the choice of which was dependent on the nature of the features. The first approach embossed the pattern into the PS without penetrating the material (i.e., the non-through-hole embossing approach). In this approach, the hydraulic press platens were first heated to an initial temperature of 125°C, ~25°C above the glass transition temperature of PS. The PS sample was then loaded into the press in an arranged stack consisting of (from bottom to top): (1) a mirror-finished stainless steel plate; (2) PS sample; (3) epoxy mold; (4) 1-mm thick silicone rubber (McMaster-Carr, Elmhurst, IL, USA); and (5) ~380-μm thick Teflon film (McMaster-Carr, Elmhurst, IL, USA) **(Fig. 3.2E)**. After loading, the press was closed with an applied force of 900 kgf (2000 lbs) for 15 min (**Fig. 3.2G**, non-through-hole emboss). An in-house cooling system, consisting of a water chiller (Model #ER301, Elkay, Oak Brook, IL, USA; available from McMaster-Carr) and water pump, was connected via tubing to the platens of the hydraulic

heated press in order to accelerate the cooling step in the recipe. Once cooled to ~70°C, the press was opened, and the PS sample was carefully demolded from the epoxy mold.

The second approach was used to emboss the pattern into the PS with penetration of the material at specific locations (i.e., the through-hole embossing approach). With respect to microsystem designs, through-holes are needed as access ports to the microsystem pattern. In this approach, the platens were first heated to 135°C prior to loading the arranged stack containing the PS sample. The arranged stack was similar to the non-through-hole approach, but consisted of an additional 610-μm thick COP sheet and a cellulose acetate film (Cheap Joe's, Boone, NC, USA) between the stainless steel plate and the PS sample. An automated embossing recipe (**Fig. 3.2G**, through-hole emboss) was applied to the stack using the hydraulic press. Cooling and demolding steps were similar to the non-through-hole approach. Note that although PS is able to reflow at these temperatures, the sample needed to be thinner than the height of the mold feature by 100 μm to achieve complete penetration of the mold.

3.2.4 Thermal Bonding of PS Devices

To form enclosed PS devices, thermal diffusion bonding was applied to top and bottom PS sample pieces. Depending on the design, the bottom PS sample was either a simple flat sheet without features (plain substrate), or a PS layer consisting of embossed features; the top PS part was a PS layer containing microchannels and through-hole access ports. In both cases, the top and bottom PS samples were sonicated in water or isopropyl alcohol (30 min, 60°C), rinsed, blow-dried with compressed air, and arranged in a stack consisting of (from bottom to top): (1) stainless steel plate; (2) bottom PS layer; (3) top PS layer; (4) COP sheet; (5) silicone rubber; and (6) Teflon film. The hydraulic press was pre-heated to 90°C for 10 min after which the stack was loaded and the press closed with the required force and for the required time **(Fig. 3.2F)**. Different applied forces and bonding times were tested to determine optimal bonding parameters (see below). The platens were cooled to ~70°C before the bonded PS device was removed from the press.

3.2.5 Bond Strength Characterization

Bond strength was quantified using a crack propagation method and surface energy calculation.[153] Briefly, a 50-μm thick metal shim was inserted between two bonded PS layers, resulting in delamination of the bonded pieces in the form of a propagating crack line. The inserted shim and the crack region were imaged together on an Olympus SZX16 stereoscope (Olympus, Center Valley, PA, USA), and the crack length was then measured using ImageJ software (NIH) **(Fig. 3.3C)**. Shorter crack lengths corresponded to higher surface bond energies, referred to as bond strength [J/m^2] hereafter. We tested a minimum of three independently bonded devices ($n \geq 3$) for nine different sets of bonding parameters (900-kgf, 1350-kgf, and 1800-kgf applied force, each at 15, 30, and 60 min).

3.2.6 Cross-section Analysis

Cross-section analysis was performed on three representative sets of bonding parameters to illustrate how bonding parameters affected cross-sectional shape of microchannels. Bonded devices were cut near the desired cross-sectional plane on a VC-50 precision diamond saw (Leco, St. Joseph, MI, USA). The cut samples were wet-sanded to a glossy finish using 800- and 1200-grit sandpaper, respectively. After achieving the desired finish, the sectioned sample was sonicated in deionized water (10 min, 60°C) and dried. Imaging was performed on an Olympus SZX16 stereoscope.

3.2.7 Evaluation of Device Functionality

Bond quality and microchannel cross-sectional deformation were further evaluated by testing whether fluid flow was blocked in microchannels after thermal bonding. We designed a microsystem containing channels of three different (width-to-height) aspect ratios (AR = 10, 20 and 50), all with the same height of 10 μm. Twelve microsystems were placed in a 3 x 4 array on a single 50 x 75 mm device and fabricated using the through-hole embossing method. The device was then bonded using five of the nine sets of bonding parameters tested for bond strength: (1) 900-kgf, 15 min; (2) 900-kgf, 60 min; (3) 1350-kgf, 30 min; (4) 1800-kgf, 15 min, and (5) 1800-kgf, 60 min. Tests were conducted by flowing colored dye into each microchannel on the device, and counting the number of blocked microchannels.

3.2.8 Cell-based Applications

For our first application, arrays of straight microchannels (150 μm high, 1.5 mm wide, 22 mm long) were fabricated by bonding a through-hole embossed port layer with a non-through-hole embossed microchannel layer, resulting in straight channels containing three access ports. Human umbilical vein endothelial cells (HUVECs) were cultured in EBM-2 media containing SingleQuots (Lonza, Allendale, NJ, USA), and seeded into the microchannels at 3,000 cells/μL. HUVECs were then cultured to confluence over 48 hours, and treated with 10 ng/mL IL-1β for 4 h to induce E-selectin upregulation.[154] After 4 h, HUVECs were fixed, permeabilized and immunostained with monoclonal anti-human E-selectin antibody (R&D Systems Inc., Minneapolis, MN, USA) and Hoechst 33342 nuclear dye (H1399, Invitrogen, Carlsbad, CA, USA). Images of the culture were acquired on a Nikon Eclipse Ti inverted fluorescence microscope (Nikon Instruments, Melville, NY, USA).

For our second application, a microfluidic chemotaxis system (described in detail elsewhere[155]) was fabricated in PS from a 700-μm through-hole embossed layer and a 125-μm sheet for the bottom. The top layer was treated in oxygen plasma for 50 seconds at 100W prior to bonding, and the bottom layer was left untreated. 5 μL of fibronectin at 50 μg/mL was used to fill the microsystem by capillary action. After 1 h the device was rinsed with 5 μL of EBM-2 media with SingleQuots (see above). Human primary neutrophils were extracted from whole blood using common protocols. The cell suspension was diluted to 500 cells/μL. 3 μL of the neutrophil suspension was loaded into one side of the device, and 2 μL of chemoattractant (fMLP) was added to the other side. Time-lapse phase contrast optical microscopy was performed at 10X magnification by taking one frame every 30 seconds using an Olympus IX81 microscope. Tracking of neutrophil migration was performed using software developed in-house.

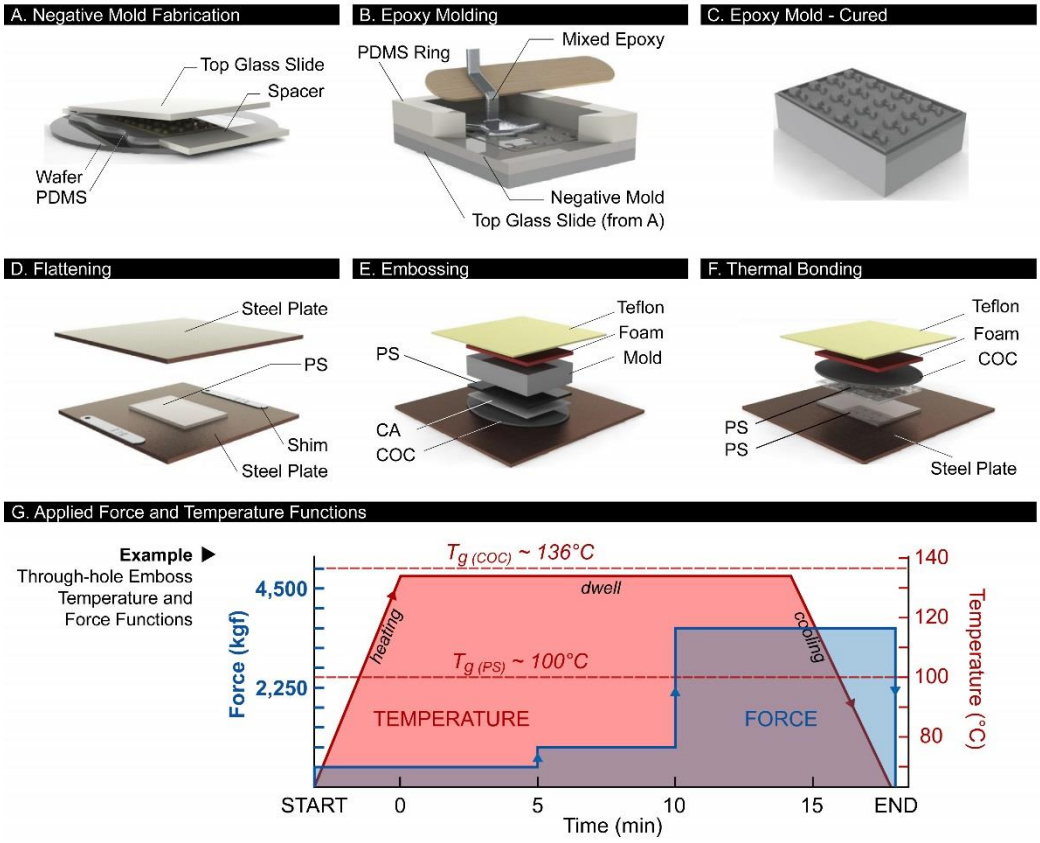

Process	Step	Force (lbf)	Force (kgf)	Pressure (MPa)	Temperature (°C)	Time (min)
Flattening - PS	1	1,000	450	1.15	135	2
	2	5,000	2,250	5.75		2
	3	15,000	6,800	17.25		3
Flattening - COC pellets	1	1,000	450	1.15	155	5
	2	10,000	4,500	11.5		10
Reflattening - COC sheets	1	1,000	450	1.15	155	2
	2	5,000	2,250	5.75		2
	3	15,000	6,800	17.25		3
Emboss - non-through-hole	1	2,000	900	2.3	125	15
Emboss - through-hole	1	1,000	450	1.15	135	3
	2	2,000	900	2.3		3
	3	8,000	3,600	9.2		8
Bonding	1	3,000	1,350	3.45	90	30

Fig. 3.2 Polystyrene microfabrication process. (A) Fabrication of a PDMS slab of uniform thickness to replicate the SU-8 master. (B) Casting of the epoxy in a PDMS cavity comprised of the replicate of the SU-8 mold and a PDMS ring. (C) Cured epoxy mold. (D) Flattening of PS sample to a desired thickness using metal shims. (E) Hot embossing of the PS sheet for through-hole fabrication (remove CA and COC for non-through hole approach). (F) Thermal bonding of two PS sample pieces. (G) Fabrication recipes for different hydraulic press procedures. Pressure is nominal value calculated based on mold surface area of 50 x 75 mm. Force-temperature functions used for through-hole embossing shown as example. Temperature curve consists of heating, dwell, and cooling phases. In the dwell phase, force may be successively ramped over time. During cooling, the final applied force during dwell was maintained to prevent sink marks in the embossed part.

3.3 Results and Discussion

Cell-based applications have specific challenges that can prevent current microfabrication processes from becoming widely adopted in a research context. Because cells are regulated by a complex set of soluble signals, mechanical stimuli, and other microenvironmental cues,[17] a large number of variables need to be investigated and controlled to properly explore such large parameter spaces.[156] The ability to fabricate arrays of microsystems is therefore an important step in enabling high-throughput microfluidic cell-based studies. We were able to achieve this through the development of a streamlined method for fabricating robust and inexpensive epoxy molds from existing SU-8 masters, which enabled a through-hole embossing technique for PS that obviated the need for manual drilling or punching of ports. The protocols were also tailored to be simple and functional for use with affordable benchtop heated presses. Thus, with this relatively accessible and cost-effective method, rapid prototyping of arrayed microsystems in PS - and potentially other thermoplastics – can be achieved with cost and time expenditures approaching that of PDMS-based fabrication **(Fig. 3.1)**.

The fabrication methods developed here are compatible with a wide range of microfluidic designs, functionalities and pumping schemes. The ability to emboss through-hole ports directly makes the presented methods particularly well suited for operation by passive pumping.[157] This pumping scheme can be performed using common micropipettes and has been shown to be well suited for creating accessible cell-based assays. Certain design considerations, however, are central for successful fabrication of functional and reliable devices. We discuss below important aspects of the fabrication process, from creating epoxy molds for hot embossing to bonding devices and preparing microfluidic systems for culturing cells, in order to facilitate better translation to other applications.

3.3.1 Mold Design

A well-designed mold is critical to a successful embossing procedure because it can impact mold longevity, fidelity in replication of the features, and quality of the bond in the final device. The designer should consider several geometric mold parameters, including its overall size, draft angle of the features,

and feature aspect ratios. First, larger mold sizes tend to reduce the uniformity of embossing and bonding of the PS parts, resulting in a less reliable fabrication process. This non-uniformity, caused by minor misalignment of the press platens, can be partially compensated by the use of a layer of firm silicone foam rubber to equilibrate pressures across the sample. The protocols described here used a 50 x 75 mm epoxy mold; we have also achieved devices using molds up to 100 x 100 mm on the same hydraulic press by adjusting the applied force accordingly **(Fig. 3.4)**.

Second, demolding of the embossed part must be done carefully to preserve a high-quality part, and this can be assisted by proper inclusion of draft angles on all mold features. We found that features less than 50 μm tall generally do not require a draft angle, whereas a draft angle is critical for taller features such as through-hole access ports. A draft angle of 15 degrees typically produced good results for parts embossed with CNC (Computer Numerical Control) machined aluminium molds. To achieve a draft angle on our epoxy molds, we used an angled UV exposure technique to create angled side walls on SU-8 masters **(Fig. 3.3A)**. Note that the design of the features in the microsystem must account for the draft angle, which will increase the base-width of features.

3.3.2 Epoxy Mold

Hot embossing of PS requires molds that can withstand temperatures of 135°C (or higher for other thermoplastics) while under high pressures. Traditionally, these molds are fabricated by CNC machining of aluminum or steel, which involves fabrication and polishing steps that are both time consuming and costly. Silicon-SU-8 molds cannot be used directly for embossing since layered features are prone to delamination during the demolding step. To overcome this limitation, Mehta and co-workers developed a method to fabricate bulk epoxy molds (which were not susceptible to delamination) from regular silicon SU-8 molds.[24] While the concept was an important step in improving the process, we found that the choice of epoxy type was critical to mold strength and longevity because the operating pressures and temperatures we used in our processes were at the working limit of most epoxy materials. We tested three different epoxies, including Conapoxy, RenCast and EC-415, to observe their deformation after the

embossing process. RenCast and EC-415, both aluminum-filled composite materials, showed little deformation, whereas Conapoxy (used by Mehta and co-workers), deformed significantly and produced molds whose features became distorted after one embossing cycle. EC-415 ultimately proved to be the most stable over multiple embossing cycles and allowed the fabrication of 15 to 20 parts with through-holes (more parts are possible without through-holes) before displaying significant deformation. Our process permits easy fabrication of additional epoxy molds from the same PDMS master mold. Importantly, the material strength of EC-415 enabled embossing of through-holes in the PS parts, which was particularly demanding for molds because of the need for higher embossing pressures. To assess mold longevity, the deformation of a mold used for through-hole embossing was monitored over a series of hot embossing cycles **(Fig. 3.3B)**. Results showed that the first emboss led to the largest change in port height; subsequent embosses resulted in relatively smaller changes at a constant rate. For the mold used in the experiment, in which the tallest features measured 700 μm, a deformation of ~10% resulted after 15 cycles. In addition, since the epoxy precisely replicated the original SU-8 master, the microfluidic channels displayed excellent optical transparency, and bonding surfaces were smooth. In comparison, aluminum CNC machined molds required an expensive and labor-intensive polishing step before they could be used for fabrication of microchannels with sufficient optical transparency to produce quality microscope images from cell-based studies.

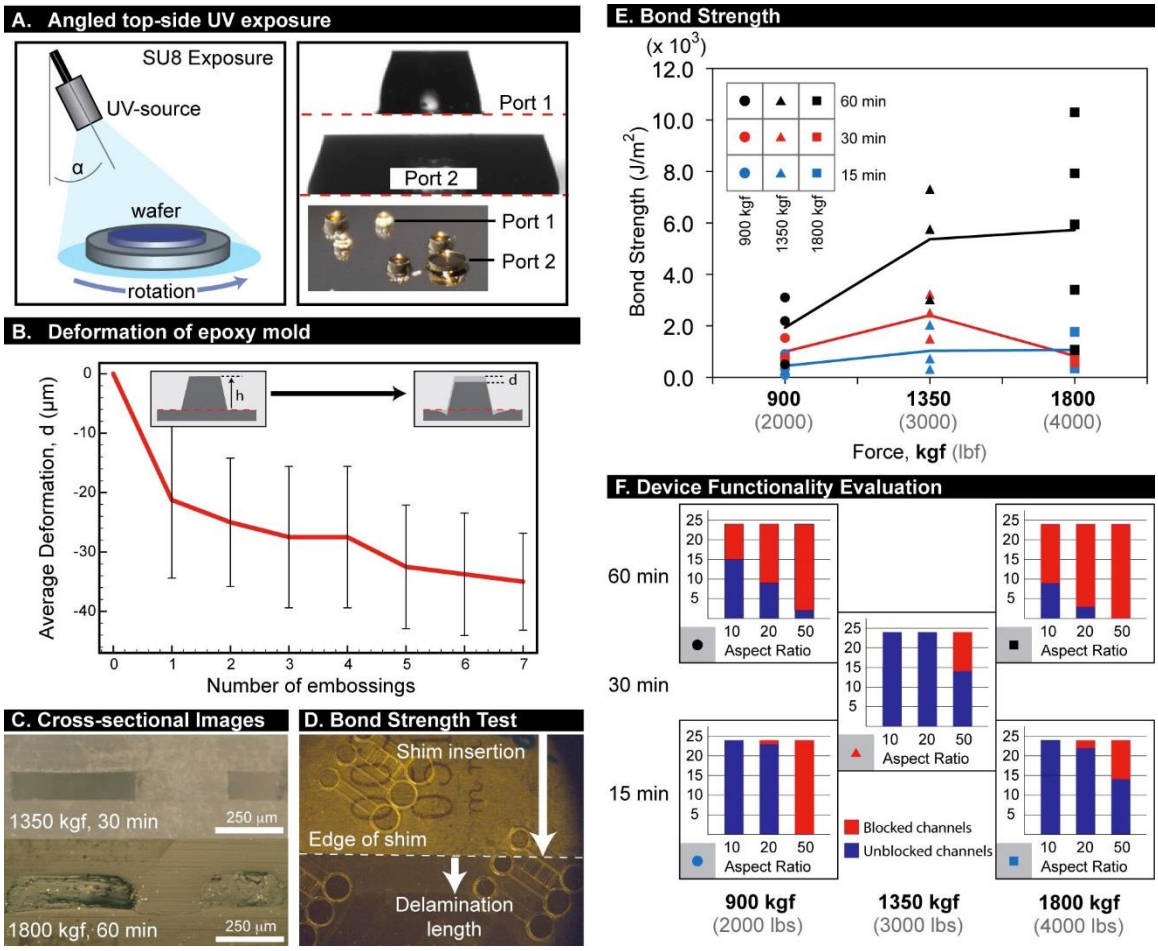

Fig. 3.3 Characterization of hotp embossing molds and methods. (A) UV exposure for SU-8 features with draft angles. Collimated UV light is directed at an angle toward a SU-8-coated silicon wafer under rotation. After development, features display a profile with draft angles. (B) Deformation of the epoxy mold after repeated through-hole embossing. Largest deformation occurred after the first emboss. (C) Cross-sectional images for optimal bonding condition (1350 kgf, 30 min) and suboptimal condition (1800 kgf, 60 min) that led to significant channel deformation. (D) Image of bond strength test. (E) Bond strength results determined by crack propagation method. Total of nine conditions tested, all at least in triplicate (all data points shown to indicate data spread). (F) Evaluation of device functionality by counting number of blocked channels after bonding with given set of parameters. All 24 microchannels for each aspect ratio were measured (heights of bars), and categorized as blocked (red) or unblocked (blue).

3.3.3 Hot Embossing

Hot embossing relies on the viscoelastic properties of thermoplastic materials that are above its critical glass transition temperature (T_g), which is approximately 95 to 100°C for PS.[158] Embossing temperatures of 125°C and 135°C were chosen for non-through hole and through hole embossing, respectively, as it provided a good compromise between preservation of the epoxy mold and melt flow of the polymer.[159, 160] In addition, to prevent the formation of sink marks in the embossed PS layer,[161] it was

necessary to maintain constant applied force at the end of the last dwell step, until cooling of the press to a temperature of 75°C or less. For the more straightforward case of non-through-hole embossing, 125°C for 15 min was generally sufficient to produce good replication of features up to 1.2 mm in height.

In the more complex process of through-hole embossing, a higher temperature was preferable to prevent the formation of thin residual layers (i.e., membranes) in the regions where full mold penetration was desired. To facilitate the complete penetration of the mold through the PS layer, a sacrificial polymer backing layer was added. This material needed to be stiffer than PS at the dwell temperature, but soft enough to compress so that the epoxy mold was preserved. For convenience, COP with a T_g of 136°C was chosen because its T_g was higher than the range of temperatures compatible with PS embossing. Furthermore, the thickness of the PS sheet used for the embossing needed to be ~100 μm thinner than the height of the tallest port features of the mold. To prevent stiction between COP and PS, a thin CA film was placed between them. This multilayer molding approach has been used previously for molding poly(oxymethylene) (POM), with cellulose acetate (CA) as the backing polymer layer, and worked well because of the extremely low T_g of POM (T_g ~ negative 30°C).[161] The use of multilayer molding for through-hole embossing of PS has not been previously reported. This was an important technical achievement in our process because it provided a reliable and repeatable method for direct embossing of access ports in arrays of microsystems, which in some cases can contain hundreds of ports. Thus, this technique removed a bottleneck in the fabrication process by obviating the need for conventional drilling or punching operations for creating access ports.

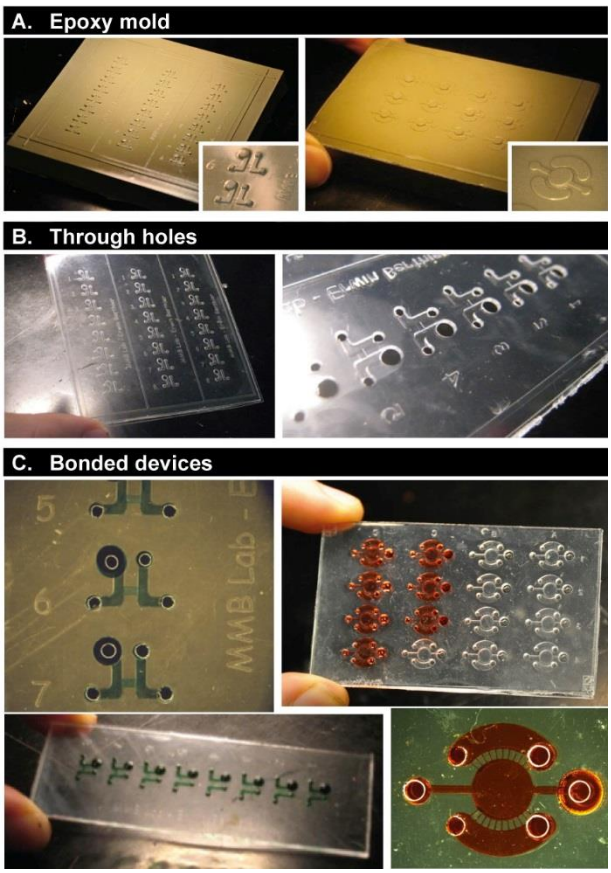

Fig. 3.4 Polystyrene device fabrication via hot embossing and thermal bonding. Images of (A) epoxy molds, (B) through-hole embossed PS parts, and (C) bonded devices. The designs shown are for cell-based applications in neutrophil chemotaxis[155] and non-adherent multiple myeloma cell immunostaining.

3.3.4 Thermal Diffusion Bonding of PS

For applications in cell biology, solvent bonding methods were discounted because of the potentially harmful effects of bonding solvents (e.g. acetonitrile, toluene) on live cells in culture. Thus, we opted for thermal bonding as a chemical-free method for our cell-based devices. While others have previously demonstrated thermal bonding of PS microchannels for cell-based applications,[162] it was necessary for us to extend this work to achieve high bond quality over large arrays of microsystems. Since it has been suggested that thermal bonding below T_g can minimize channel deformation,[163] we focused on a low temperature bonding process to reduce variations in channel dimensions that may subsequently affect surface area-to-volume ratios that are critical in cell biology studies,[164] and ultimately bias biological readouts. To find an optimal bonding recipe, we explored different bonding times and

pressures, and then measured bond strength and evaluated bond quality by examining channel deformations.

For bonding temperature, 90ºC was chosen because it was high enough to permit thermal diffusion bonding but below the T_g of PS. We found that this temperature provided good bonding of the entire device surface over a range of dwell times and pressures, allowing the bonding process to be readily adjustable. Lower forces and times (1350 kgf for 30 min) displayed little deformation when we examined channel cross-sections, while higher forces and longer times (1800 kgf for 60 min) showed significant deformation **(Fig. 3.3C)**. We quantified bond strength for different values of the applied force (900, 1350, and 1800 kgf) and the dwell time (15, 30, and 60 min) using a crack propagation method that determined bond surface energy **(Fig. 3.3D)**.[153] Results for 900 and 1350 kgf showed expected trends where increasing the time led to increased bond strength. Also, for all bonding times, increasing the applied force led to higher bond strength, although results for 1800 kgf were inconclusive due to high variability in the results **(Fig. 3.3E)**.

We designed an indirect method to quantify, over a whole array, the level of deformation of the channel ceiling as a function of channel aspect ratio. An array of 24 microsystems was fabricated, each containing a set of microchannels of (width-to-height) aspect ratios equal to 10, 20, and 50. Five different bonding recipes were tested for channel ceiling collapse by determining whether colored dye was able to flow into the microchannel **(Fig. 3.3F)**. Results showed that bonding for longer times (60 min) led to more collapse of the channels and therefore less reliability in the effective channel heights. Of all the recipes tested, 1350 kgf (3000 lbf) for 30 min appeared to provide the best bond strength with highest aspect ratio achievable without failure (AR = 20), and therefore, was the optimal bonding protocol for our devices (the recommended bonding recipe in **Fig. 3.2G**). Furthermore, this set of results suggested that maximum variability in channel height over the whole array is 5% (1/20 of the channel width). This was an important assessment of device reliability for cell-based assays because of the importance of consistency in channel dimensions for high-throughput applications.

Additional considerations for bonding can significantly improve bond quality and device functionality. A major difficulty when performing thermal diffusion bonding at low temperatures is ensuring good contact between the two surfaces. This difficulty is more apparent for larger device dimensions because sample unevenness is generally magnified for increased sizes. The use of a stiff and deformable polymer (COP) in combination with a foam layer improves local contact between the PS sheets without increasing deformation. Furthermore, bonding tests that used thinner PS sheets (250-μm or 125-μm film on the bottom instead of 330 μm) provided further reductions in deformation for the same recipe. Using thinner bottom PS layers is also advantageous from a practical perspective because it allows high-resolution imaging (with 40x objectives or higher magnification) for live studies of intracellular dynamics and other applications.

3.3.5 Applications in Cell Biology

To demonstrate the flexibility of our process and its amenability to cell biology, we used our protocols to make various devices for different applications **(Fig. 3.5)**. First, an array of straight channels was fabricated using a two-sided embossing process. These microchannels were used in validation experiments involving the upregulation of E-selectin in HUVEC monolayers activated by IL-1β. Results were as expected, i.e., IL-1β resulted in E-selectin expression above baseline levels (for no IL-1β treatment) **(Fig. 3.5A)**. The 48-h culture to reach HUVEC confluence (with feeding after 24 h) demonstrated that long-term cell culture was compatible with our fabrication methods and materials used. Second, a neutrophil chemotaxis device, previously developed in PDMS,[155] was fabricated in a single-sided embossing process using 125-μm PS film as a bottom bonding layer. After the addition of neutrophils and fMLP, the neutrophils migrated toward the source reservoir in a manner similar to that observed in PDMS-based devices **(Fig. 3.5B)**. This device, which included a 50-μm tall gradient channel, was more complex in geometry than the straight microchannel, and thus served as a good test for validating the fabrication process for small microchannels. Furthermore, because the devices were made

using a 100 x 100 mm mold, it demonstrated that the process was extensible to larger molds and that the function of the channels could be preserved.

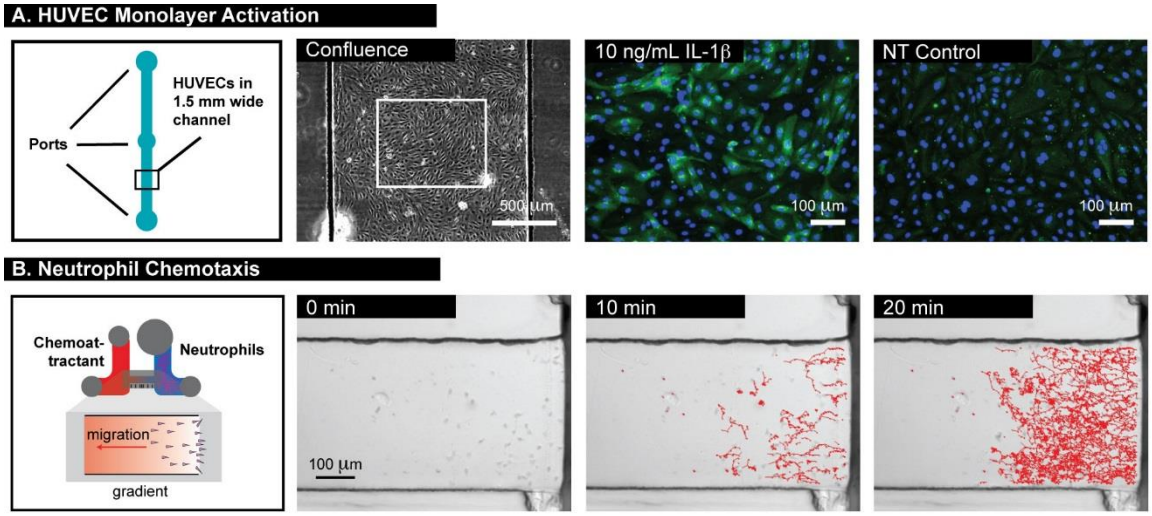

Fig. 3.5 Cell-based assays in hot embossed microfluidic device. (A) HUVEC monolayer culture and activation with IL-1β in a straight PS microchannel. E-selectin expression (green fluorescence) was upregulated after 10 ng/mL IL-1b treatment for 4 h. Nuclei were stained with Hoechst dye (blue). (B) Timelapse imaging and tracking of neutrophils migrating in a PS gradient device.

3.4 Conclusion

Protocols were developed to provide a streamlined methodology for the fabrication of PS devices of arrayed microsystems useful for a wide range of cell-based applications. While PDMS-based devices are appropriate for certain applications, the protocols provided here provide alternative solutions that exhibit comparable cost effectiveness and design-to-device turnaround times in relation to the soft lithography process. Additionally, we believe that several steps in our protocol solved a number of bottlenecks in the typical thermoplastic microfabrication process, rendering PS fabrication of large arrays of microsystems amenable to increased adoption by biologists. Results demonstrate that large arrays of microsystems in PS can be easily fabricated for use in long-term cell studies. Nevertheless, while the methods developed here provide improvements at several key steps in the fabrication process, some limitations remain, notably in the thermal bonding step where the potential for channel collapse increases when width-to-height aspect ratios are too high.

Chapter 4 A combined fabrication and instrumentation platform for sample preparation[3]

4.1 Introduction

Automated instruments have significantly improved diagnostics in the developed world by increasing patient throughput and decreasing diagnostic variability caused by human interaction [165, 166]. Often times these automated instruments are complex "black-box" systems where the operational mechanisms are hidden, making the instrument appear simple. However, such systems typically require expensive service contracts, specially trained operators, and instrument specific disposables [167, 168]. In many developed countries, the benefits of repeatable data and the increased throughput of the black box instruments justify the costs. Unfortunately, in low-resource settings the cost and accessibility to suppliers often limit acquisition, operation, and support of these instruments [169]. Furthermore, such instruments are typically inflexible, prohibiting users from modifying or adding operational protocols as new diagnostic needs arise.

In this work we address these needs through the development of a new molecular diagnostic instrument. This instrument, which is based upon a commercial automated liquid handler (Gilson Pipetmax; **Fig. 4.1A**), leverages on-board wax device manufacturing, and a simplified sample preparation technique, pioneered by our lab, to minimize costs and maximize utility. In this initial demonstration, we integrate microfluidic device fabrication, viral RNA isolation, and RT-qPCR setup onto one instrument **(Fig. 4.1B)**. It should be noted that this functionality is similar in scope to other automated sample preparation systems currently used in molecular diagnostics, such as the Roche Ampliprep or Abbott m2000sp. Our system maintains the traditional automation advantages of operational simplicity and repeatability, while doing so in an "open source" environment. This open

3 This chapter has been adapted from the following publication: "A Combined Fabrication and Instrumentation Platform for Sample Preparation" David J. Guckenberger, Peter C. Thomas, Jacob Rothbauer, Alex J. LaVanway, Meghan Anderson, Dan Gilson, Kevin Fawcett, Tristan Berto, Kevin Barrett, David J. Beebe, and Scott M. Berry. Journal of Laboratory Automation, 2014.

system enables users to expand the functionality of the instrument and develop new assays as new diagnostic demands arise. Additionally, the open system allows users to visually verify that the machine is operating as expected and that all components may be operated manually in the event of a mechanical or power failure (albeit with some reduction in throughput and precision).

We utilize a relatively new sample preparation technique, Immiscible Filtration Assisted by Surface Tension (IFAST) to dramatically simplify the process workflow, thus reducing the complexity of automation infrastructure required **(Fig. 4.1C)**. IFAST is a method of purification that relies on surface tension and immiscibility to separate aqueous phases using an oil barrier [170]. The IFAST device is a microchannel consisting of three interconnected wells containing sample, oil, and elution buffer. Each well is connected via a small constriction designed to stabilize these immiscible phases side-by-side. Initially, the sample is mixed with paramagnetic particles (PMPs) that bind to the analyte of interest, viral RNA in this case. By sliding the device over a magnet, the PMPs are collected and drawn through the oil and into the elution buffer. This intermediate oil well serves as an immiscible barrier, preventing unbound sample from carrying over into the elution buffer. IFAST has been previously used in an automated setting to extract protein from samples in a seroconversion assay [165]. Additionally, various configurations of IFAST have been manually fabricated in wax (data not shown), demonstrating that viral RNA can be extracted from multiple samples in parallel in a simple, efficient, and repeatable manner.

Because viral nucleic acid extraction is critical for many molecular diagnostic assays, we chose to focus on HIV viral load quantification, through RNA extraction, as an initial proof-of-concept application. Frequent monitoring of viral load is necessary to successfully manage anti-retroviral therapy (ART) as mutations in the HIV virus can lead to ART drug resistance [171]. With proper management, ART can be quite successful as clinicians can adjust ART regiments as specific drug resistances develop [172]. Unfortunately, viral load quantification is often prohibitively expensive in the developing world [29] (cost ranges from $50 to >$100) and is frequently not performed. Sample preparation (the extraction of viral RNA from patient plasma) contribute significantly to the operational complexity (and associated cost) of

traditional sample preparation protocols [173]. Automated sample preparation systems must be capable of performing complex, multi-step solid phase extraction (SPE) processes [174, 175]. Thus, a reduction in sample preparation complexity could significantly reduce the total viral load quantification cost, greatly improving access to this critical molecular diagnostic test.

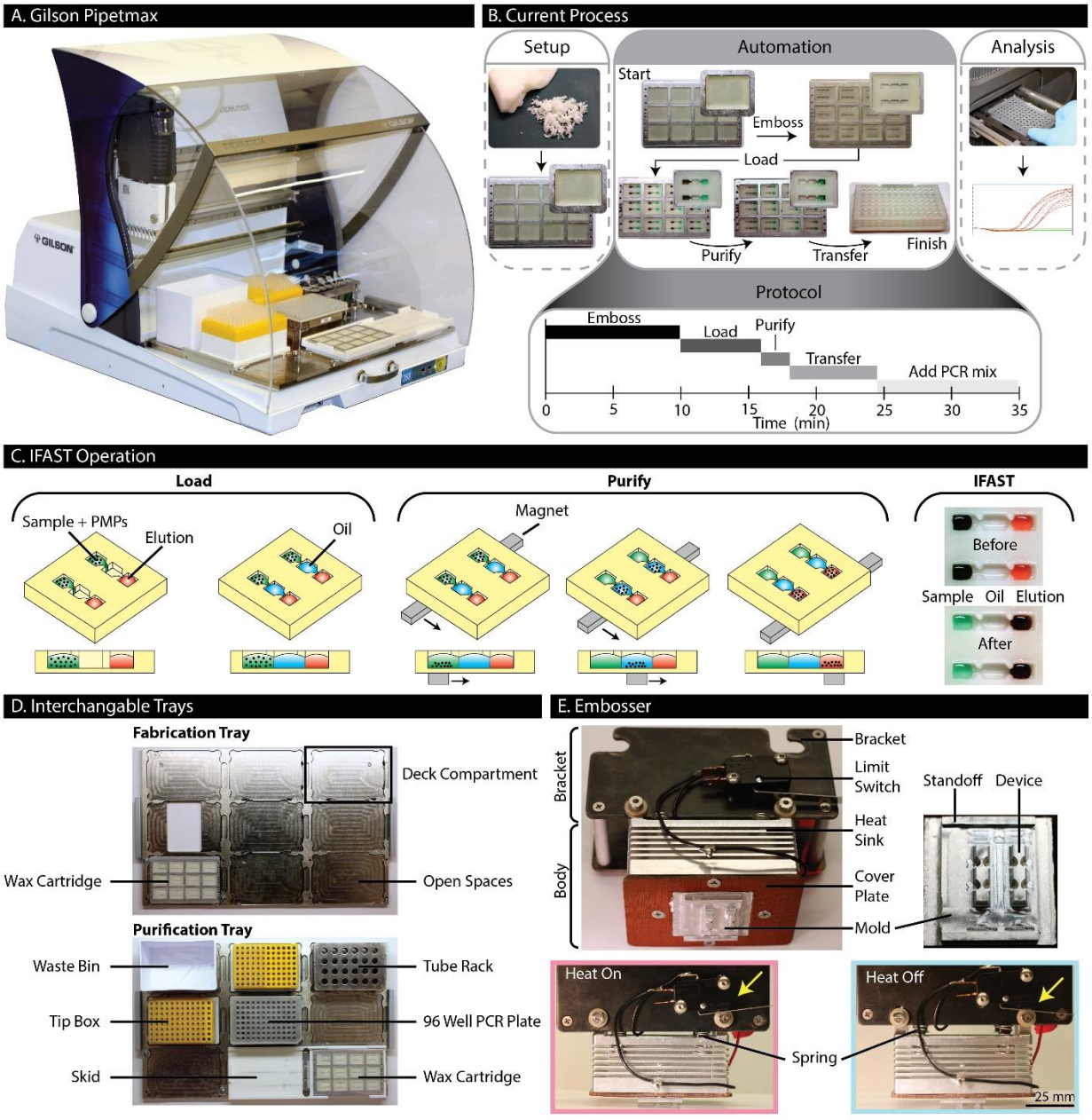

Fig. 4.1 Platform overview. (A) The automated liquid handler setup for purification. (B) Layout of the entire process, including both manually-operated (dashed lines) and automated steps (solid lines). The times for each step in the automated process are shown (bottom), where the total instrument time is less than 35 minutes of instrument time. (C) Schematic of the IFAST device and operation. Sample and elution wells are loaded first, followed by the oil well. The

PMPs are captured and purified from the sample well to the elution well by sliding a magnet underneath the device. (D) The system is utilizes modular trays. In our configuration, one tray was devoted to fabricating wax devices while the other was dedicated to purification. (E) The embosser used to make devices consists of two main components, a bracket and a body. The body consists of a heat sink, a mold, a heater (not shown), and a cover plate. The heater is powered through a limit switch triggered by the mounting screw (shown in the bottom images).

4.2 Materials and Methods

4.2.1 Instrument Overview

The automated liquid handler is designed to accommodate interchangeable trays, each consisting of a 3 x 3 array of standard SBS well plate compartments **(Fig. 4.1D)**. We have developed two custom trays for this application: (1) a fabrication tray that houses cartridges for embossing devices, and (2) a purification tray, which houses all necessary components and reagents for isolating RNA from samples and setting up a well plate for reverse transcription and quantitative polymerase chain reaction (RT-qPCR). While using the fabrication tray, a custom embossing unit (termed the "embosser") is attached to the pipetting head of the robot. While using the purification tray, the embosser was removed and standard eight-channel p20 and p200 pipette heads are used. The robot is programmed using icon-based software (Gilson Protocol Builder). After RNA isolation and RT-qPCR setup are complete, the loaded PCR plate is manually transferred to a real-time thermal cycler to complete the viral load assay.

4.2.2 Wax Setup

Wax IFAST devices **(Fig. 4.1C)** are embossed in cartridges filled with Sasolwax #B7347 (Sasol Wax, Hayward, CA), a wax that is both ductile and stable at room temperature, for extended periods of time. Wax was used because of its low cost, easy manipulability, and relatively low melting point (as compared to many plastics). To assure the wax did not pull out of the cartridge during embossing, the walls of each compartment had an overhang, such that the wax blanks were unable to be lifted vertically from the cartridge. Each cartridge is made from 3.2 mm thick aluminum and matches the footprint of a standard SBS well plate (85.5 x 127.8 mm). At each end of the cartridge is a row of eight holes that are spaced to accommodate tips on an eight-channel pipette head (9 mm spacing), such that the pipette head can be directly used to draw the cartridge across magnets to actuate the IFAST devices. Within each cartridge is a 3 x 4 array of compartments, each measuring 25 mm long, 19 mm wide, and 3 mm deep.

The compartments are filled with wax by heating the cartridge to 115° C and melting wax directly in the compartments. The cartridges are passively cooled at ambient temperature, and then secured to the fabrication tray **(Fig. 4.1D)** using screws at opposing corners.

4.2.3 Embossing Setup

To prepare the robot for fabrication, the embosser is attached to the pipetting head and a wax filled cartridge is placed into the liquid handler. The embosser **(Fig. 4.1E)** is a two-part unit consisting of a bracket and a body. The bracket enables attachment to the liquid handler head using the existing hardware. The body is loosely mounted to the bracket through vertically slotted holes, but mechanically separated from the bracket with springs. The body consists of an aluminum heat sink, a Peltier heater (not shown) (#TEC1-12708, HB Corporation, Shanghai, China), an interchangeable aluminum mold, and a cover plate. The cover plate attaches the mold and the heater onto the heat sink. The heater is powered with 3 A and 18 V from a DC Power supply (#YH-305D, Yihua), controlled through a limit switch affixed to the embosser. The limit switch is mounted to the embosser bracket such that heating is induced when the springs between the body and bracket are compressed. The mold contains two IFAST devices, each device consisting of three wells (sample, oil, and elution well). The wells are 3.3 mm wide, 4.5 mm long, and 2.5 mm tall. Between each well is a constriction that is 1.2 mm wide, 1.5 mm long, and the same height as the wells. All of the features, except the constrictions have a 7° draft to facilitate mold removal. The mold depth during embossing is controlled by standoffs on the side of the mold. The standoffs bottom out on the cartridge, beside each compartment, to leave a 0.4 mm wax barrier between the mold and the cartridge (which serves as the bottom of the device). It is critical to control the thickness of the bottom of the IFAST device (total thickness including aluminum < 1 mm) to ensure consistent spacing between the device bottom and the magnet, located under the cartridge. This spacing influences the magnetic force required to successfully actuate the IFAST device (i.e., if the device bottom is too thick, the magnet will be too far from the PMPs to successfully draw them through the oil barrier and RNA recovery will be adversely affected).

4.2.4 Embossing Protocol and Characterization

To successfully emboss devices with well-defined features, the thermal profile of the embossing process was optimized. This protocol is shown schematically in **Fig. 4.2A**, where the smaller dashed line represents a reference point on the bracket, and the bold dashed line represents a point on the tip (bottom) of the mold. Importantly, the springs allow the body to move independent of the bracket, and the dashed lines of **Fig. 4.2A** demonstrate the relative motion between each component. To start, the embosser is lowered until the mold contacts the wax and continues to lower an additional 2 mm to compress the springs, thereby compressing the springs. This compression triggers the limit switch, activating the heater. The heat softens the wax while the springs press the mold into the wax. After 10 seconds, the mold has depressed partially into the wax and the bracket is lowered by an additional 1 mm to recompress the springs and assure that the limit switch remain triggered. Supplying heat for an additional 20 seconds (total embossing time of 30 seconds) allowed the standoffs to bottom out against the cartridge, thus completing the emboss. At this point, the embosser is lifted by 0.5 mm to de-trigger the limit switch, while simultaneously maintaining compression in the springs to prevent de-molding. For the next 15 seconds (total embossing time of 45 seconds), the mold is passively cooled, allowing the wax to solidify. The bracket is then lowered by 0.5 mm to re-trigger the limit switch. The mold is warmed for 5 seconds (total embossing time of 50 seconds) then completely removed from the wax. This re-warming step prevents the mold from sticking to the wax and fracturing devices during final de-molding. To confirm that this molding protocol was optimal, the embossed wax devices were characterized based on surface roughness of the device. To measure surface roughness, wax devices were removed from the cartridge, sputtered with gold for 50 seconds at 45 mA, and then imaged in a white light interferometer (New View 7300, Zygo, Middlefield, CT). The roughness was reported as the root mean square (RMS) going lengthwise across the channel.

4.2.5 Purification Protocol and Characterization

In preparation for purification, the fabrication deck is swapped for the purification deck **(Fig. 4.1D)**. The purification deck houses all necessary components for the assay, including waste bin, tip boxes, reagent tube rack, and a skid for integrating the previously embossed wax cartridges. The skid provides a smooth surface that spans two of the tray compartments. Embedded in the center of the skid is a row of magnets (#BX041-N52, K&J Magnetics) that actuate the IFAST devices as the cartridge is drawn over. During this process, the PMPs are magnetically captured and traversed from the sample well, through the oil well, and into the elution well **(Fig. 4.1C)**.

Device performance was benchmarked based on recovery yield and purity. To determine recovery yield of PMPs alone, we attached Alexa Fluor 488 conjugated secondary antibodies (Life Technologies, Grand Island, NY) to Protein G coated PMPs (Protein G Dynabeads, Life Technologies, Carlsbad, CA) by incubating them together for 15 minutes at room temperature in PBS with 0.01% Tween-20 (#P1379, Sigma Aldrich, St. Louis, MO). After removing the supernatant, PMPs were re-suspended in 20 µL of RIPA lysis buffer (#20188, Millipore, Billerica, MA) and loaded in the sample well of the device. Wells were filled sequentially, using only one tip on the pipetting head. Next, 20 µL of Buffer MFE (#955235, Qiagen, Valencia, CA) was loaded into the elution well and 15 µL of FC-40 oil (#F9755, Sigma Aldrich, St. Louis, MO) was loaded into the middle well, in that order. After purifying the PMPs by drawing the cartridge across the skid magnet, the contents of the sample well were removed and re-suspended in clear microfuge tubes with 180 µL of PBS. The tubes were measured for fluorescence using a Qubit Fluorometer with an excitation wavelength of 430-495 nm (#Q32866, Life Technologies). The results were compared to a standard curve relating PMP concentration to fluorescent intensity. To determine purity, the sample well was filled with Buffer MFL (Qiagen) supplemented with 2 µL of PMPs (#MD1471, MagneSil KF, Promega, Madison, WI) and Acridine Orange at concentration of 10 µg/mL to serve as a non-specific "background". The elution well was filled with MFE elution buffer. After purification, the contents of the elution well were removed, re-suspended, and quantified in the same

fashion as the PMP loss experiment to determine the concentration of Acridine Orange that had been non-specifically carried over during IFAST operation.

4.2.6 HIV Viral-like Particle Purification

Using the same devices, volumes, and filling protocol as previously described, we isolated viral RNA to measure viral load. To simulate viral load at various quantities, HIV viral-like particles (gift of Dr. Nathan Scherer) were spiked into Fetal Bovine Serum (FBS) at concentrations of 700, 7000, and 70000 copies per 10 μL to create mock patient samples. Note, these sample concentrations were necessary due to volume limitations of the sample well. However, similar work has demonstrated that enlarging the sample well lower the limit of detection to 50 copies per mL [76, 171]. These samples were loaded, into the tube rack, and the liquid handler mixed the samples 1:1 with a mixture of MFL lysis buffer and PMP stock solution (which contained 2 μL PMPs / 8 μL MFL). The samples were incubated for 5 min at room temperature and then the contents were automatically transferred to the sample wells of the wax IFAST devices. As previously described, the PMPs were purified via IFAST into an elution well containing MFE elution buffer. After purification, 10 μL of the eluent was transferred to a 96-well PCR plate, which was then mixed 1:1 with a solution containing RT-qPCR one-step Master Mix (Taqman Fast Virus 1-Step Master Mix, Life Technologies) and ANRS probe (#4332079, Custom TaqMan Gene Expression Assay, Life Technologies) [176]. At this point, the PCR plate was removed from the liquid handler, and placed in a real-time thermal cycler (Roche LightCycler 480, Roche, Indianapolis, IN) for amplification. The amplification protocol was 50°C for 8 min, 95°C for 30 seconds, then 50 cycles of 95°C for 1 second and 60°C for 20 seconds (the ramp rate was 4.4°C/second). Each concentration was repeated six times (n=6), and we obtained copy numbers by comparing Threshold Cycle (C_T) values from these samples with those obtained from standards with known copy numbers. Results were compared against a similar protocol in which IFAST devices were manually fabricated, loaded, and operated.

4.3 Results and Discussion

4.3.1 Wax Device Embossing Characterization

Each step in the embossing protocol plays a significant role in the device quality and overall fabrication time. This process was optimized for our particular system, but some steps may be streamlined or omitted after additional development. For instance, in our configuration, the springs were recompressed 10 seconds into the emboss to assure the limit switch remained triggered. The recompression was necessary because the thickness of the wax was 2.5 mm while the distance where the limit switch was triggered (without colliding with the bracket) was 1.5 mm. Changing components to give the limit switch a larger triggering distance or removing it all together would simplify the embossing step. Furthermore, the temperature of the mold at the start of each embossing cycle plays a significant role in the final quality of the device. Specifically, as more devices are embossed, the embossing step can be shortened. Approximately 30 seconds are required to ensure complete embossing of the wax when the heat sink starts at room temperature. However, as more devices are embossed, the temperature of the mold and the heat sink increase due to heat retention. After a few embosses, the heat sink reaches a steady state operating temperature (shown by the dotted line in **Fig. 4.2A**). At steady state, the temperature cycles from 70 – 90° C, and embossing can be completed in 20 seconds. Even though the embossing was completed in 20 seconds, there were no adverse effects caused by leaving the embosser on for an extra 10 seconds. However, shortening the total emboss cycle time will improve overall assay throughput.

The cooling and re-warming steps directly impact removal of the mold and were essential for fabricating a repeatable device. Additionally, we found that the cooling and re-warming steps are inter-dependent. For example, a cooling time of 15 seconds required a re-warming time of 5 seconds to remove the mold without breaking features. However, a cooling time of 90 seconds required a re-warming time of 45 seconds allowed the mold to be more easily removed, without needing to secure the cartridge to the tray. We hypothesize that there is an optimum temperature to remove the mold, where the wax is soft but well-formed, as opposed to completely solid or melted. Deviating from this optimal temperature was shown to have adverse effects on the outcome of the device. When the mold was too cold, it would stick

to the wax, causing unwanted adhesion to either the cartridge or tray, ultimately breaking device features. On the other hand, if the warming step was disproportionally too long compared to the cooling step, the wax around the mold would over soften and result in high surface roughness.

We characterized the effects of minute temperature variations on the surface roughness of the wax IFAST device surface **(Fig. 4.2B)**. When a channel was embossed as described in the optimized protocol, the RMS surface roughness was 1.6 μm, which was an artifact of the machining marks on the mold. However, when the duration of the final warming step was increased by 5-10 seconds, without altering the cooling step, the surface roughness increased to 10.5 μm. Conversely, when the duration was decreased, features would break off, or a wax would peel from the bottom of the channel. High surface roughness was also encountered when completely releasing the compression in the springs during the cooling step. We speculate that removing the compression forms voids underneath the mold, which do not warm up enough to re-flatten during the warming step. While we anticipate that many mechanisms contribute to higher surface roughness, we have experimentally determined that this high surface roughness is detrimental to the operation of the device. Though we only quantitatively characterized visually smooth devices, the rough surfaces caused PMPs (often a majority) to become trapped during actuation.

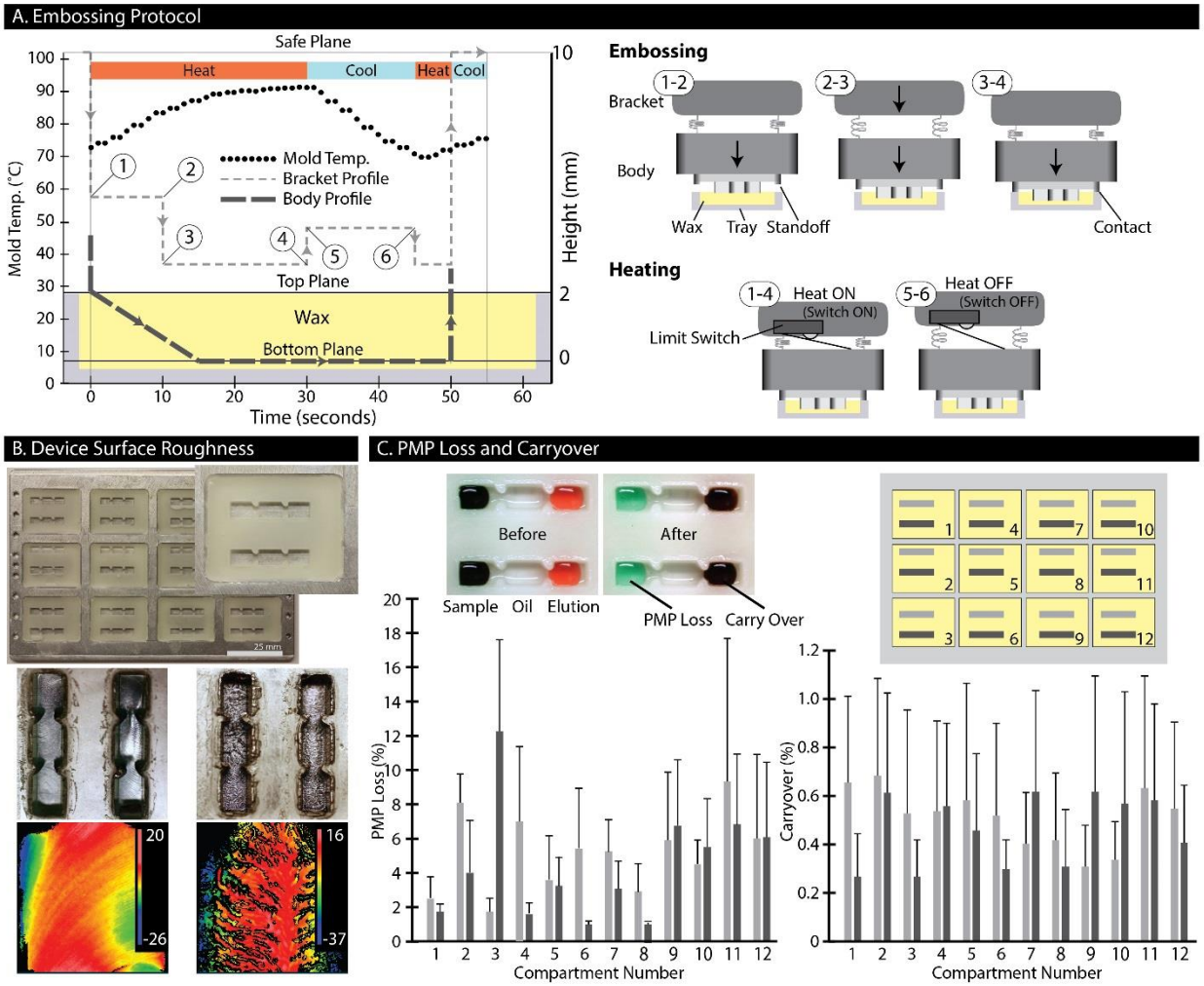

Fig. 4.2 Platform characterization. (A) A plot of the embossing protocol demonstrates vertical motion profiles of the bracket and the body relative to each other. To the right of this plot are schematics that represent the change in position between two time points in the protocol (represented by the numbers in the bubbles). The heater status is also depicted on the top of the plot by bars labeled with Heat (heater active) and Cool (heater inactive). The temperature profile of the embosser (at steady state) is shown by the dotted line. (B) Image of an embossed cartridge (top) followed by individual channels with low surface roughness (left) and high surface roughness (right), and the corresponding profilometer data measuring surface roughness of the channels. (C) PMP loss and non-specific carryover were measured for all cartridge positions (compartment numbers correspond to the schematic (top right), and the light and dark bars correspond to the top and bottom channels, respectively). Images show the device before and after purification (top left).

4.3.2 Purification Characterization

We characterized PMP recovery yield and non-specific carryover for an embossed IFAST device **(Fig. 4.2C)**. PMP loss is characterized as the amount of fluorescent antibody-tagged PMPs remaining in the sample well after purification. Three cartridges of stamped devices (24 devices per cartridge) produced an average PMP loss of 4.8% with a standard deviation of 2.8%, where the highest observed

loss was 18% (n=72). The increased PMP loss was likely due to surface roughness resulting from the non-steady state embossing of devices. Non-specific carryover was quantified by measuring the amount of acridine orange in the elution well after purification. We observed that our devices had an average carryover of 0.48% (by volume) with a standard deviation of 0.51%, where the highest observed carryover was 1.58% (n=72). These numbers are consistent with past performance involving RNA isolation and IFAST [170]. Importantly, we found that this level of purity was sufficient for efficient RT-qPCR amplification and detection.

We demonstrate a diagnostic application by measuring HIV viral load from mock patient samples. The liquid handler was prepared by removing the embosser and exchanging the fabrication tray with the purification tray. The liquid handler automatically mixed samples (by pipetting), dispensed them into the IFAST devices, purified the PMP-bound viral RNA, and setup the RT-qPCR reaction. No speed control was available within the software during the time of experimentation, so the devices were drawn across the magnet on the skid at full speed in increments of 2 mm with a 3 second pause between each motion. The pause allowed the PMPs to aggregate and stay within the magnetic field, thus minimizing loss of the PMP-bound RNA. After purification, the eluted sample was transferred to a 96-well PCR plate and mixed with RT-qPCR master mix. At this point, the plate was manually transferred from the liquid handler to a real-time thermal cycler for RT-qPCR **(Fig. 4.3A, B)**. For comparison, a second purification was performed manually using wax IFAST devices. Comparing the threshold cycle (C_T) values from both methods of purification revealed that the automated purification was, on average, 1-2 cycles lower than the manual purification, suggesting a higher level of RNA recovery (although not statistically significant). Moreover, the standard deviation observed from the automated purification was approximately 10-fold lower than the corresponding manual method, demonstrating the high level of precision of the automated platform.

Many automated systems for diagnostic applications are black-box instruments, limited to few applications/assays and designed to discourage user modification. Conversely, our system is an open

system that is adaptable to a wide range of user definable assays (previously IFAST has been used to isolate cellular, protein, DNA, and RNA analytes). The user can visually verify that the instrument is functioning as expected and manually operate any component that has failed. The modularity of this system and the use of interchangeable trays enable the user to utilize custom protocols and components. If desired, developed protocols can be "locked", preventing inadvertent modifications by less experienced users. We demonstrated the utility of the system by fabricating IFAST devices and performing HIV viral load quantitation with a high degree of operational precision. Our current cost of goods per test is 78 cents, where the device cost is less than one cent and the reagent cost (including lysis buffer, PMPs, oil, and elution buffer) is approximately 78 cents (based on retail price). In regards to labor, fabrication of a tray of devices takes ~5 minutes of manual labor (setup, heating, cooling, etc.) and 10 minutes of automated time for embossing (with no further input from the operator) **(Fig. 4.1B)**. Purification of the RNA requires ~5 minutes of setup time and 25 minutes of instrument time. The instrument time can be further broken down into: 6 minutes to load the cartridge, 2 minutes to purify, 6.5 minutes to transfer the samples to a PCR plate, and 10.5 minutes to add PCR mix to each well. However, the instrument is not limited to this specific application. The embossing capabilities presented here are amenable, without variation, to a variety of molds, enabling design and manufacture of custom devices. In addition, the tray design makes it conceivable to employ a heating element and a fluorescent detector to enable RT-qPCR (or similar analytical reactions) directly on the tray, potentially making this instrument a complete tool for fabricating, preparing, and analyzing a sample.

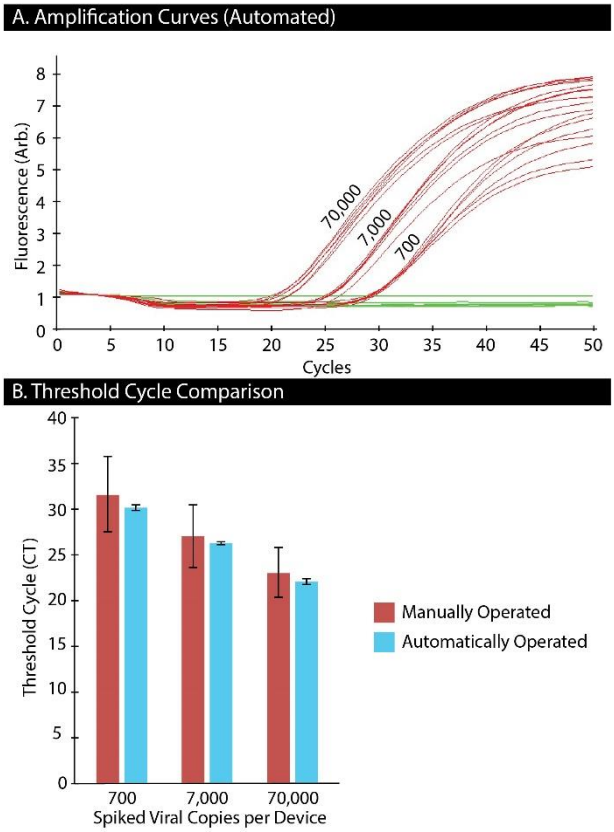

Fig. 4.3 Nucleic acid extraction using wax devices. (A) RT-qPCR amplification curves of RNA purified from samples containing 70000, 7000, and 700 viral particles as well as negative control samples. (B) Comparison of CT values between samples that were purified automatically and purified manually.

4.4 Conclusion

We have demonstrated the ability of a single instrument to both fabricate the assay devices and to perform high-precision sample preparation and RT-qPCR setup. As an example, we developed an assay for HIV viral load quantification, leveraging a new isolation technology (IFAST) to reduce the overall complexity of the assay. This reduction in complexity enables the use of a simple automated liquid handler rather than a more expensive and less adaptable "custom" piece of equipment with greater complexity. Device fabrication was optimized, such that high-quality wax IFAST devices were produced rapidly and repeatedly. RT-qPCR data (performed on a standard thermal cycler) demonstrated that RNA was extracted with high recovery yield and purity relative to a similar manual process. We anticipate the development of additional diagnostic assays on this platform, including complete sample-to-answer assays where the detection / quantitation process is integrated directly on the platform itself. In the future,

we hope that the low cost and “open source” flexibility of the platform will help to improve access to molecular diagnostic techniques, particularly in the developing world where the cost of diagnostic instrumentation often limits access.

Chapter 5 Rapid technique for UV-curable adhesive bonding of glass coverslips to polystyrene microdevices [4]

5.1 Introduction

With several microfabrication techniques now available, including: 3D-printing,[1] micromilling,[2] and hot embossing,[3] in-house fabrication of thermoplastic microdevices has become cheaper, faster, and easier. However, for many applications – such as cell culture and microscopy – these devices must be bonded to optically-transparent substrates such as glass. While bonding similar materials, such as Polystyrene (PS) to PS, is relatively simple, bonding dissimilar materials, such as PS to glass, presents a particular challenge. Current methods to circumvent these challenges include spin coating adhesives, such as polydimethylsiloxane (PDMS), onto sacrificial substrates[4] and injecting adhesive directly into the bond interface.[5] However, equipment requirements, associate long cure times, heterogeneity in glue uniformity, and complexity limit acceptance of these techniques.

Here we present simple technique for applying uniform layers of adhesive to enable rapid – less than a minute – bonding of PS to glass. Using UV-curable adhesives, readily accessible materials, and a simple techniques, we demonstrate how to apply thin uniform layers of adhesive to a microchannel. We provide design suggestions that will improve bonding repeatability, and additional information that may help apply this technique to materials beyond PS and glass.

5.2 What do I need?

- Polystyrene (1.2 mm, #ST313120, Goodfellow)
- Glass coverslip (#260450, Ted Pella, Inc.)
- UV curable adhesive (Ultra Light-Weld 3025, Dymax)
- Silicone foam (Textured) (#31943970, MSC Industrial Supply Co.)
- Isopropyl alcohol (#190764, Sigma-Aldrich)
- Low particulate wipers (#TX609, Texwipe)
- Wooden flat stick (#704, Brightwood)
- UV lamp (OmniCure S1000, Exfo)

4 This chapter has been adapted from the following publication: "Rapid technique for UV-curable adhesive bonding of glass coverslips to polystyrene microdevices" David J. Guckenberger, Jake Kanack, Loren Stallcop, and David J. Beebe. This was submitted as a Chips and Tips article to Lab on a Chip, 2015.

5.3 What do I do?

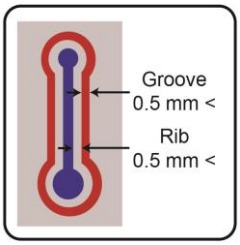

Fig. 5.1 Channel design for adhesive bonding. Schematic view of the channel (blue) demonstrating the groove (red) milled around the channel to for a rib (gray) around the perimeter of the channel.

Step 1: Fabricate the microdevice. To improve bonding repeatability and adhesive distribution we recommend fabricating a groove (thickness > 0.5mm) around the channel - leaving a rib (0.5 mm < thickness < 1.5 mm) around the perimeter of the channel.

> ***Tip****: Rib thickness may need to be tuned for individual adhesives*
>
> ***Tip****: Extra caution while applying the adhesive may be necessary for channels shallower than 0.1 mm*

Step 2: Thoroughly clean the surface of the microdevice, silicone foam sheet, and coverslip using isopropyl alcohol and low-particulate wipers. Remaining particulates can be blown off with compressed air. Ensure PS and glass surfaces remain clean throughout the bonding process.

Step 3: Apply a dollop of UV curable adhesive to the foam sheet.

Step 4: Use a tongue depressor to spread the adhesive into a uniformly thin layer across the foam. The area of the adhesive should be larger than the microdevice – add more adhesive if necessary.

Step 5: Position the device onto the adhesive bonding surface down. Press down gently; avoid sliding the microdevice to prevent build-up of adhesive within the channels. Pick up the device and repeat this step two or three times to ensure the bonding surface is completely covered with adhesive.

***Tip**: Take care to ensure no adhesive is transferred from gloves to surfaces of the device not intended to be bonded.*

***Tip**: Minimize the delay between step 4 and step 5 to help ensure a uniform thickness of adhesive*

Step 6: Position the microdevice above the coverslip, and gently lower it until it makes contact. Once contact is made, release the device, taking extra caution to avoid sliding the microdevice.

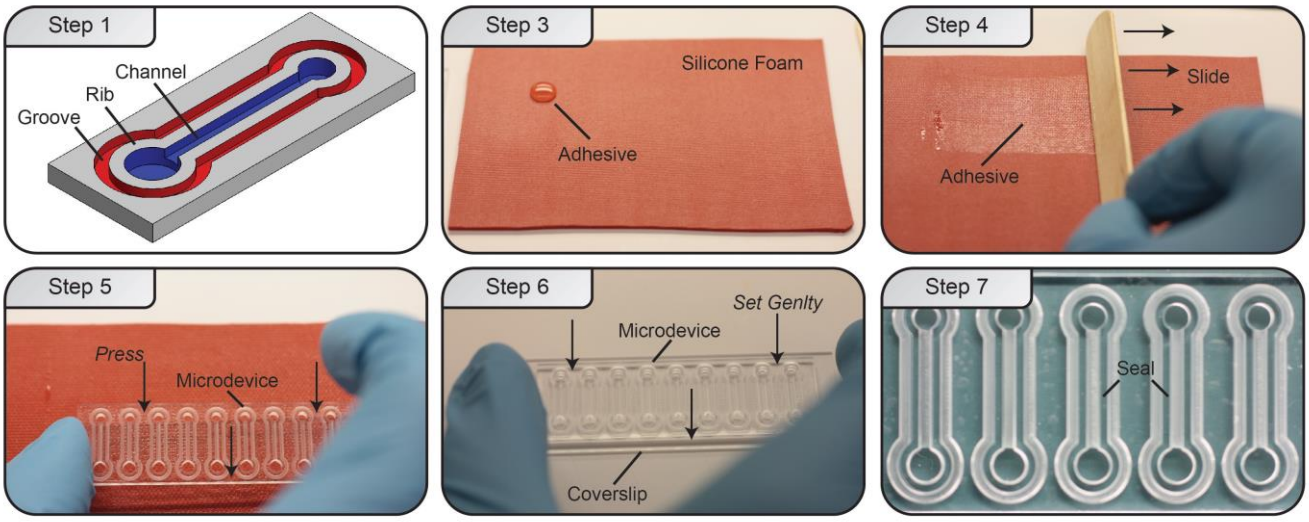

Fig. 5.2 Stepwise workflow of the bonding process.

Step 7: Allow a few seconds for the adhesive to wick along the ribs, then cure device for 20 seconds with ~350 nm UV light

Tip: The adhesive may have a yellow color after bonding. If necessary, allow 24 hours for adhesive to clear

5.4 What else should I know?

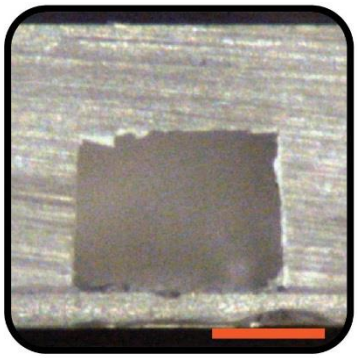

Fig. 5.3 Assessment of the adhesive bonding technique. Cross sectional image of a PS microchannel bonded to a glass coverslip. Scale bar represents 0.5 mm.

- Adhesives are often material-specific. Consult the manufacturer to determine the best adhesive for your application.

Tip: Some adhesives may require post-treatment / aging to reach a full cure.

- We have tested this protocol with Ultra Light-Weld 3025 (Dymax) and Norland Optical Adhesive 68 (Thor Labs, Inc.). These adhesives had similar performance, however the protocol may need to be tailored for other adhesives.
- If the adhesive is too viscous or does not adequately wick around the rib, heat may be applied to achieve thinner adhesive layers, or to improve the wicking of the adhesive.
- This protocol is amenable to wide variety of materials, including: cyclic olefin copolymer (COC), glass, metal, PS, and various rapid-prototyping materials.
- Creating the rib and allowing the adhesive to wick eliminates excess adhesive and prevents adhesive from squeezing into the microchannel.

Chapter 6 Induced hydrophobic recovery of oxygen plasma-treated surfaces [5]

6.1 Introduction

An important aspect in the fabrication of microscale systems is the ability to control wetting and surface tension of fluids by defining regions of hydrophilicity. Hydrophilic surface functionalization is important to myriad applications including capillary filling of microfluidic channels, [177, 178] bonding during fabrication of microdevices,[179] as well as the generation of micropatterned arrays of adhesive patches for cultured cell colonies.[180, 181] Plasma treatment is widely used for creating hydrophilic surfaces and patterns, and for chemically functionalizing the surface. It involves exposing surfaces to reactive ionized atoms that are then incorporated into the surfaces as various chemical species.[182] Because of its simplicity, flexibility, effectiveness, and relatively low cost, plasma treatment has become a popular method in academic labs as well as in industry. However, its attractiveness as a practical and accessible technique is somewhat tempered by the caveat that any exposed surfaces not protected from treatment are rendered hydrophilic. Moreover, no documented methods are available for actively reversing the treatment when needed. Thus, regions designed to be hydrophobic must be shielded by a mask or stencil [181, 183] requiring proper mask alignment and sufficient mask-to-surface contact. Masking is necessary, for example, in open microfluidic systems, i.e., open-channel [183, 184] and passive pumping-based microfluidic devices, [14, 38, 157] that need hydrophilic microchannel walls and hydrophobic top surfaces.[185] Corona discharge probes are an alternative that can locally modify surface hydrophilicity and treat internal channel walls without affecting external surfaces,[186] but this approach is time consuming and tedious at large scales. Materials like polydimethylsiloxane (PDMS) can recover its hydrophobicity passively over time,[142] but this is inefficient, not well controlled, and does not allow selective regions to retain desired hydrophilicity.

---

5 This chapter has been adapted from the following publication: “Title” First M Last, First M Last. Journal Date Chapter has been modified from a manuscript prepared for publication titles,

Here we describe a simple, practical, and efficient technique to actively induce hydrophobic recovery of plasma-treated surfaces. This method relies on a secondary physical contact treatment (PCT) on the plasma-treated surfaces using ubiquitous laboratory materials such as common wipers and adhesive tapes **(Fig. 6.1)**. The method can be used on various thermoplastic and elastomeric materials, and can be tuned to achieve contact angles ranging from less than 10 degrees to the original contact angle of the material. PCT is useful for quickly reversing specific regions to a hydrophobic state while leaving other non-contacted regions hydrophilic. We characterize the PCT-induced hydrophobic recovery process by testing a variety of wipers and tapes (termed "applicators" hereafter) on different materials commonly used in microfabrication, and demonstrate PCT-based patterning applications that can be achieved with this method.

6.2 Materials and Methods

6.2.1 Sample Preparation

Three materials commonly used for microfluidic fabrication were tested: polystyrene (PS) (Goodfellow, Cambridge, MA), cyclo-olefin polymer (COP) (Ajedium, Solvay Solexis Inc., Newark DE), and PDMS (Dow Corning, Midland, MI). PDMS was mixed in a 10:1 ratio, and cured at 90 °C for 1 h. Samples were cut into 51 mm x 51 mm pieces and exposed to oxygen plasma (Diener Electronic, Ebhausen, Germany) at 30 sccm, 50 W, and 40 s to attain hydrophilic surfaces with contact angles between 15 to 25°.

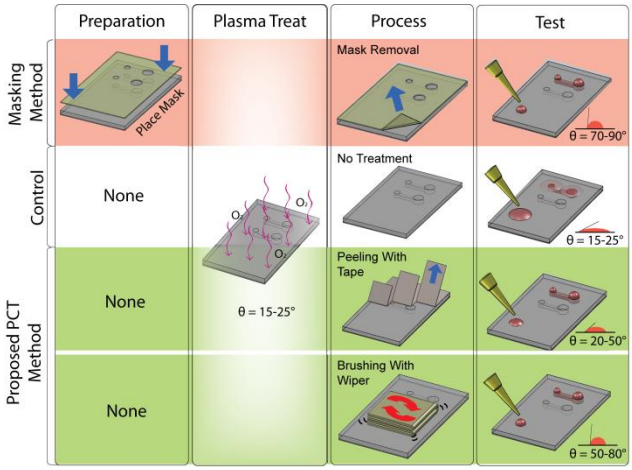

Fig. 6.1 Method comparison for hydrophobic patterning. Comparison between traditional masking method for achieving hydrophilic surface patterning (red) and physical contact treatment (PCT) methods to induce hydrophobic recovery (green). The two PCT methods include (1) peeling with tapes, and (2) brushing with wipers.

6.2.2 Physical contact treatment (PCT)

To induce hydrophobic recovery after plasma treatment, a physical contact treatment (PCT) was applied using common laboratory materials including tapes, wipers, and compressed air. For tapes, Scotch® tape (3M, St. Paul, MN), labeling tape (Fisher Scientific, Pittsburgh, PA), polyethylene surface protection tape (McMaster-Carr, Elmhurst, IL), and Post-It® adhesive notes (Staples, Farmingham, MA), were tested by rolling the tape onto the samples at 85 kPa, and then peeling the tape from the surface. For wipers, Kimwipes® (Kimberly-Clark Professional, Roswell, GA), and TechniCloth® wipers (Texwipe, Kernersville, PA) were tested by brushing the wipers across the sample in a unidirectional manner while pressing it to the surface at ~3 kPa. For both tapes and wipers, constant pressure was achieved by using a foam pad under a weight to uniformly distribute the pressure, and brushing or peeling of the applicators was applied at a slow rate (~0.5 m/s). Compressed air was applied by blowing air at ~410 kPa (60 psi) in a serpentine pattern on the surface at a distance of ~13 mm. Each PCT was performed within minutes after plasma treatment for a desired number of PCT applications.

6.2.3 Contact angle measurements

Surface hydrophilicity was characterized by measuring contact angles of deionized (DI) water droplets using a goniometer (Ramé-hart, Netcong, NJ). Three independent measurements were performed

per condition, where each measurement was the average of three randomly placed drops on a sample surface.

6.2.4 SEM and XPS Imaging

Scanning electron microscopy (SEM; LEO GEMINI 1530) and X-ray photoelectron spectroscopy (XPS; Perkin Elmer 5400) were used to characterize the topography and chemistry of the sample surfaces.

6.2.5 Demonstrations of PCT

Two applications of PCT were demonstrated. 2D surface patterning was performed by applying patterned tapes, either cut by hand or with a laser cutter (JSM3060U, Artsign Science & Technology, Ltd., Jinan City, China), on plasma-treated PS of samples. Application of food colorant was used for visualization of hydrophobic-hydrophilic patterns. For dot arrays, a solution containing 1-µm fluorescent beads (F8816, 1:500 dilution in DI water, Molecular Probes, Invitrogen, Grand Island NY) was applied to the PCT surface, drained, and the remaining drops evaporated, allowing visualization of the hydrophilic areas using an inverted fluorescent microscope (Nikon Eclipse TI, Nikon Instruments). 3D surface patterning was performed in a PS sample piece designed for hanging drop cultures. The device was fabricated with a CNC milling machine (Tormach, Waunakee, WI), and consisted of a port layer suspended by supporting walls **(Fig. 6.4C)**. The ports consisted of an 800-µm diameter top opening and a 1.2-mm diameter bottom opening. After plasma treatment, PCT was performed with a Kimwipe. Droplets of red food colorant in DI water were dispensed into the port, and allowed to form hanging drops on the underside of the device.

6.3 Results and Discussion

We tested the ability of various applicators commonly found in research laboratories to induce hydrophobic recovery on different sample materials used in microfluidic fabrication, including PS, COP, and PDMS. Results from PCT on PS showed that various applicators induced a different level of hydrophobic recovery **(Fig. 6.2B)**. After one application of PCT, labeling tape, Kimwipes and cleanroom wipers resulted in relatively high contact angles of 51°, 55°, and 55°, respectively, while adhesive notes,

protective tape, and Scotch tape resulted in moderate contact angles of 34°, 37°, and 37°, respectively. Subsequent rounds of PCT induced hydrophobic recovery at a decreased rate such that the contact angle approached a plateau that was dependent on the applicator. The largest hydrophobic recovery after successive PCT was caused by labeling tape, which reached ~70° after 5 PCTs, while both types of wipers plateaued at ~60° after 3 to 4 PCTs. Scotch tape and protective tape produced lower final contact angles of ~35° and ~38°, respectively, while adhesive notes reached ~49° in a linear, incremental manner. Compressed air, however, produced an insignificant change in contact angle. The low variance in contact angle measurements provided evidence that PCT is a repeatable process.

These results revealed three distinct groups of applicators with different levels of effectiveness in their ability to induce hydrophobic recovery. The highly effective group of applicators included labeling tape, Kimwipes and cleanroom wipers, which led to the highest hydrophobic recovery both after one PCT and multiple PCTs. Adhesive notes, protective tape, and scotch tape were considered as moderately effective, inducing hydrophobic recovery to a lesser extent. Compressed air was deemed ineffective with little or no change to contact angle. In all cases, final contact angles did not increase above the initial contact angle of the native sample material. These results suggest that induced hydrophobic recovery is a tunable process that can achieve contact angles ranging from a lower limit of < 10° (highly hydrophilic) to an upper limit bounded by the native contact angle of the sample material. Contact angles (to within several degrees) can be obtained by choosing an appropriate applicator and a suitable number of PCTs. Additionally, it is likely that surface hydrophilicity may be further tuned by controlling pressure or directionality of the application of PCTs.

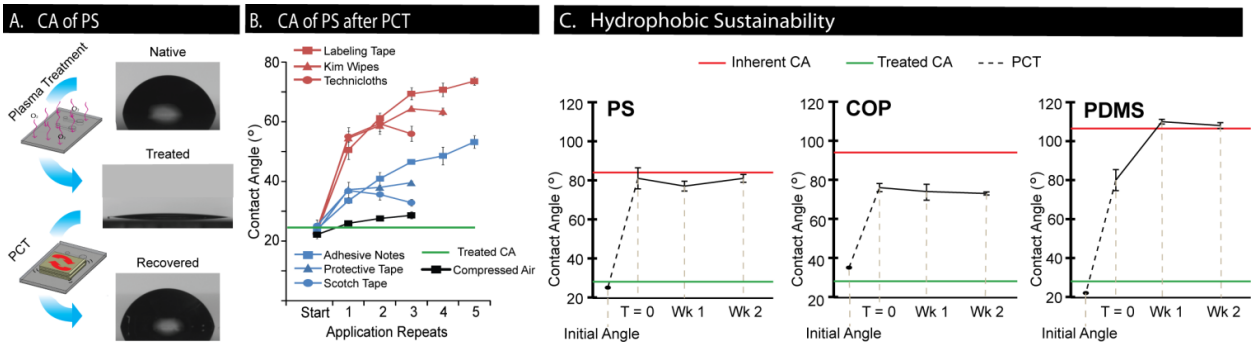

Fig. 6.2 Contact angle measurements from induced hydrophobic recovery. (A) Images of water droplet profiles on native PS, plasma-treated PS, and physical contact treated (PC-treated) PS. PCT was performed with Kimwipe. (B) Contact angle change versus number of PCT applications for various applicators on PS. Red line = average of all contact angles prior to any PCT. Error bars = SE, n = 3 independent experiments. (C) Hydrophobic sustainability for PS, COP, and PDMS after single PCT with Kimwipe brushing followed by two weeks of storage. Green line = average contact angle of samples prior to PCT. Red line = average native contact angle prior to plasma treatment. Error bars = SE, n = 3 independent experiments.

To ensure that induced hydrophobic recovery was stable over time, we performed PCT on different polymeric materials and subsequently monitored their contact angles over two weeks. Contact angles on PS and COP did not change significantly over the two-week period. In contrast, PDMS underwent further hydrophobic recovery as expected, from 80° to 110°, due to the diffusion of low molecular weight species within the PDMS bulk that does not occur in thermoplastics **(Fig. 6.2C)**.[14] These results showed that induced hydrophobic recovery was not a transient effect, and suggested that PCT resulted in physical surface modifications as opposed to, for example, electrostatic charges transferred to the surface from the applicators during PCT.

To further understand the nature of the surface modifications caused by PCT, SEM and XPS were used to visually inspect surface topography and atomic species on PS **(Fig. 6.3)**. XPS of PS revealed surface composition consisting of predominantly carbon and oxygen. Considering only the carbon and oxygen species, non-treated PS was composed of 13% O and 87% C, with a smooth surface **(Fig. 6.3A)**. This smooth surface was maintained on plasma treated samples, except for trace amounts of surface scaling **(Fig. 6.3B)**. Surface composition shifted to 40% O and 60% C, which was expected given the incorporation of oxygen on the surface.[6] XPS of the tapes alone revealed that the surface composition of scotch tape consisted of mainly C (86%) and O (14%), while labeling tape consisted of O (69%), C

(13%), and appreciable amounts of Si (3%) (**Fig. 6.3D**, red). PCT via the wiper and the labelling tape reverted the plasma-treated surface to a composition near the original levels of O and C (**Fig. 6.3C, D**, respectively). While Si was found on the PS surface treated with labelling tape, this trace amount was lower than that of the surface of the tape, and approximately the same magnitude as the original level from the control samples. Thus, XPS data suggested that transfer of material from the tape to the sample likely did not play a significant role in the mechanism of PCT as compared to the reversal of O and C levels. SEM revealed that the tape left a smooth surface with no residue, providing further evidence that no material transfer occurred after PCT with the tape. In contrast, the wiper abraded the surface, leaving striations in the path of the wipe. Thus, the XPS data suggested that PCT reverted a surface to its native hydrophobic state by removing oxygenated groups from the surface.

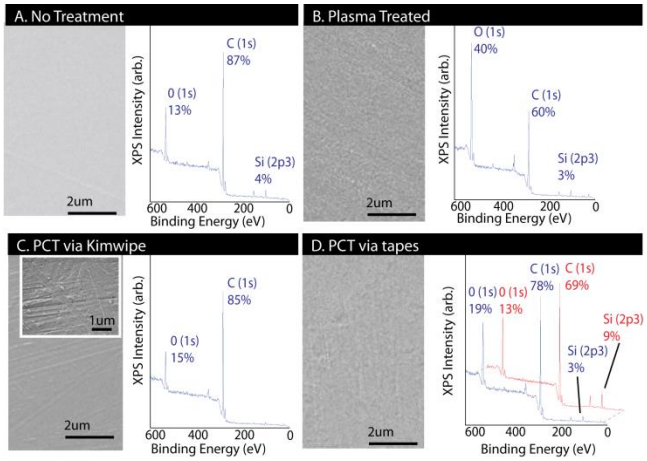

Fig. 6.3 SEM and XPS of hydrophobic recovered surfaces. (A) Non-treated PS (B) Plasma-treated PS(C) PCT of PS via wiper (D) PCT of PS via labelling tape (blue). XPS of labelling tape (red)

The simplicity and flexibility of PCT as a method for inducing hydrophobic recovery enables various applications related to microdevice fabrication. To demonstrate its practicality, PCT was combined with established 2D masking methods to yield mixed hydrophilic-hydrophobic 2D surfaces. PCT-based patterning can be achieved with either a "positive" or "negative" masking strategy **(Fig. 6.4A)**. In positive PCT patterning, a plasma-treated surface was masked in the region where hydrophilicity needs to be retained. This permits application of PCT via brushing with wipers to induce hydrophobic recovery on unprotected regions, thus leaving a hydrophilic pattern on the surface where the

mask was placed (**Fig. 6.4A**, blue). In contrast, negative PCT patterning relied on performing a tape-based PCT where induced hydro-phobic recovery was desired (**Fig. 6.4A**, purple). In both cases, hydrophobic recovery can be induced with specific patterns. As an example, we patterned an array of 1-mm diameter hydrophilic spots with 1-mm spacing on a PS surface via negative-relief masking with labelling tape. After, applying and draining a solution of 1-µm fluorescent beads on the surface, we observed that droplets of solution remained only on non-PCT areas, leaving a pattern of fluorescent-bead spots **(Fig. 6.4B)**. A particularly enabling application is performing 3D surface patterning with wiper-based PCT. We showed that brushing specific 3D features with a Kimwipe induced sufficient hydro-phobic recovery of a plasma-treated device to allow a hanging drop to form on the underside of a suspended port device while retaining hydrophilic inner port surfaces to facilitate filling **(Fig. 6.4C)**. This type of hydrophilic-hydrophobic patterning in 3D would be challenging and impractical with traditional masking techniques.

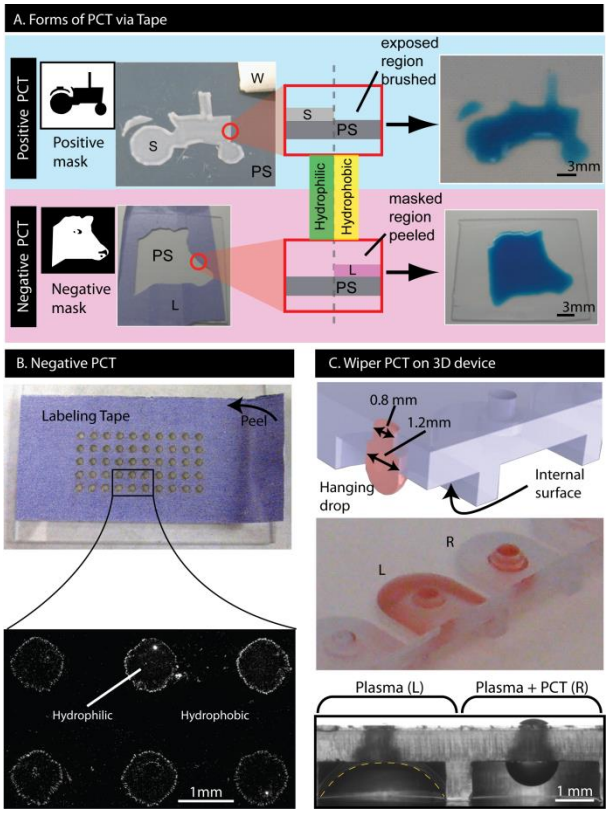

Fig. 6.4 Applications of PCT-based patterning. (A) Positive 2D surface patterning (blue) using scotch tape (S) as a mask and a wiper (W) to induce hydrophobic recovery, leaving a hydrophilic pattern on the PS (tractor). Negative 2D surface patterning (purple) where a labeling tape mask (L) is used to induce hydrophobic recovery, leaving a hydrophilic pattern on the PS (cow head). (B) Negative 2D patterning with arrays of 1-mm dots. (C) 3D surface

patterning of plasma-treated hanging drop device where PCT was applied to internal surfaces of the right-hand cavity (R) but not the left hand cavity (L).

Overall, our characterization of PCT on polymeric surfaces demonstrates that it is a simple and reliable method to actively control surface wettability after plasma treatment. The method is useful in academic laboratories where it can provide a flexible, low-cost approach to reversing the hydrophilicity of plasma-treated surfaces on large batches of devices at once. The method is particularly effective for open microfluidic systems where a hydrophobic top surface is necessary to prevent spreading, overflow, and cross-contamination of fluids introduced into the fluidic network. Importantly, the level of hydrophobic recovery, and hence, surface wettability, can be tuned using different applicators and different number of PCTs. This control over surface wettability can be further coupled with positive or negative PCT-based patterning strategies that can yield mixed hydrophilic-hydrophobic patterns with substantial complexity. As a technique, PCT is easily scalable, and has potential to be used as part of a mass manufacturing high production volume process (e.g., coupled with lab-on-a-foil fabrication[187]) because of its ability to be implemented in continuous mode on microfabricated devices. A rather interesting application of PCT that we have successfully demonstrated is inducing hydrophobic recovery using conformable applicators on non-planar surfaces, or surfaces that contain protruding features, which are not easily amenable to stencil or masking approaches. Finally, PCT can be used to protect plasma treatments and improve shelf life and storage of microfabricated devices. Protective tape, for example, can protect the hydrophilic treatment of a surface, causing minimal or no hydrophobic recovery while protecting the surface from unwanted physical contact.

6.4 Conclusions

We have developed and characterized an accessible technique to induce hydrophobic recovery by applying repeatable PCTs with common laboratory applicators. Brushing with wipers or peeling with tapes can reliably and controllably recover the hydrophobic state of a surface. PCT was shown to be robust for three different sample materials, inducing hydrophobic recovery in both PS and COP, and accelerating hydrophobic recovery in PDMS before natural hydrophobic recovery occurred. PCT is

simple and inexpensive, and does not require any additional alignment or preparation steps, making it a practical method for achieving mixed hydrophilic-hydrophobic surfaces. Combined with positive and negative PCT-based patterning strategies and efficient continuous modes, PCT can potentially be useful in both academic and industrial settings.

Chapter 7 Fluorescence-based Assessment of Plasma-induced Hydrophilicity (FAPH) in Microfluidic Devices via Nile Red Adsorption and Depletion [6]

7.1 Introduction

Hydrophilicity, or wettability, is an important physical property of microfluidic systems, especially regarding its internal surfaces. Many microfluidic systems rely on surface hydrophilicity to achieve various functions such as: (i) facilitating capillary fluid flow into microchannels (*i.e.*, priming)[188]; (ii) preventing non-specific hydrophobic adsorption of sample molecules[189, 190]; and (iii) promoting attachment of mammalian cells in tissue culture for cell-based applications,[126, 191]. For microfluidic systems fabricated in glass, the internal surfaces are naturally hydrophilic, and thus do not require additional treatment to achieve the above functions. However, for microfluidic systems fabricated in other commonly used materials such as poly(dimethylsiloxane) (PDMS)[152], polystyrene (PS)[38], and cyclo-olefin copolymers (COC)[192, 193], the internal surfaces are naturally hydrophobic, and require surface modification to render them hydrophilic. Because these materials are becoming increasingly popular for the development of microfluidic systems [10, 33], the ability to not only render these materials hydrophilic, but to also *retain and characterize* their hydrophilicity are crucial to advancing microfluidics technology, and expanding its applications.

A common method of achieving hydrophilicity is to expose surfaces to oxygen plasma. Plasma treatments are used in many applications including the removal of organic contaminants[182, 194], the control of surface wettability[195], and the traditional application of making plastic substrates hydrophilic to facilitate cell adhesion and growth in laboratory plasticware (e.g., polystyrene Petri dishes and well plates) [196]. In addition, oxygen plasma treatments activate surfaces to enable bonding between two interfaces[179], and have been widely employed in the microfluidics community to bond PDMS to glass (or

6 This chapter has been adapted from the following publication: "Fluorescence-based Assessment of Plasma-induced Hydrophilicity (FAPH) in Microfluidic Devices via Nile Red Adsorption and Depletion" David J. Guckenberger, Erwin Berthier, Edmond W. K. Young, and David J. Beebe. Analytical Chemistry, 2015.

other materials) to create enclosed microchannels[132]. The convenience and accessibility of plasma treatments allow it to be incorporated into laboratory procedures without the need for dry or wet chemical processes.

Although achieving hydrophilicity is straightforward, the ability to retain hydrophilicity is dependent on the material. PS retains its hydrophilicity, allowing commercial plasticware to have long shelf lives (i.e., years). PDMS, conversely, is known to undergo hydrophobic recovery in a matter of hours[142]. This often imposes a time constraint on experimental procedures, adds variability to test conditions, and constitutes one of several important factors that has hindered widespread adoption and commercialization of PDMS-based microfluidic systems. Because of the steady convergence of microfluidics and cell biology applications, and the ongoing pursuit of commercial, user-friendly microfluidic technologies, (including tools for point-of-care diagnostics[30] and platforms for microfluidic cell culture[38]) there is a clear need to develop microfluidic systems made of common manufacturable materials like PS and COC that have potential for high volume industrial production, and can maintain stable surface characteristics such as hydrophilicity.[33] Thus, researchers have been studying and developing methods to facilitate the testing and characterization of robust, surface-treated plastic microfluidic devices in the lab, in hopes of eventually translating these techniques to industry.[33, 38, 71, 189, 197-200]

Two current challenges in fabricating robust plastic microfluidic devices are: (i) the ability to apply uniform plasma treatments within the entire device, and (ii) the ability to characterize the surface hydrophilicity after treatment to assess its uniformity. In the case of PDMS-PDMS and hybrid PDMS-glass microfluidic devices, plasma treatments are typically applied prior to device assembly because it simultaneously activates the surfaces for bonding and uniformly hydrophilizes all internal surfaces. However, in the case of thermoplastic microfluidic devices, oxygen plasma treatment prior to thermal diffusive bonding tends to reduce bond strength[38], making plasma treatment before device bonding undesirable. Applying plasma treatment after bonding is plausible[197], particularly for microfluidic devices

that employ open access ports[74], but because the plasma is entering only through the access ports, the treatment may not be uniform within the device, and penetration into microchannels may be limited **(Fig. 7.1A)**.[201] Further research is therefore necessary to advance our ability to generate and retain uniform hydrophilic surfaces via plasma treatment in plastic microfluidic devices. In addition, improved methods that characterize the uniformity of plasma treatment and correlate it to surface hydrophilicity are needed. While measuring contact angles of droplets is the most common method for assessing wettability, it relies on the use of relatively large (microliter) droplets that are not suitable for assessing *local* wettability at high spatial resolution.

Here, we describe a novel approach called Fluorescence-based Assessment of Plasma-induced Hydrophilicity (FAPH) that is suitable for characterizing local surface wettability at high spatial resolution **(Fig. 7.1)**. The approach relies on adsorption of a hydrophobic, fluorogenic molecule – Nile Red (NR) – on the substrate surface, subsequent plasma treatment to deplete NR molecules, and fluorescence image analysis to quantify the level of NR depletion and determine the *in situ* surface hydrophilicity. The purpose of FAPH is to provide microfluidic designers with insight on microscale geometries and physical dimensions that account for how plasma treatment modifies surface hydrophilicity. By applying this approach, we explored the effects of geometry on plasma treatment penetration, and as a demonstration of its importance in future cell-based applications, studied the downstream effects of the applied plasma treatment on the adhesion of mammalian cells in microscale cell culture.

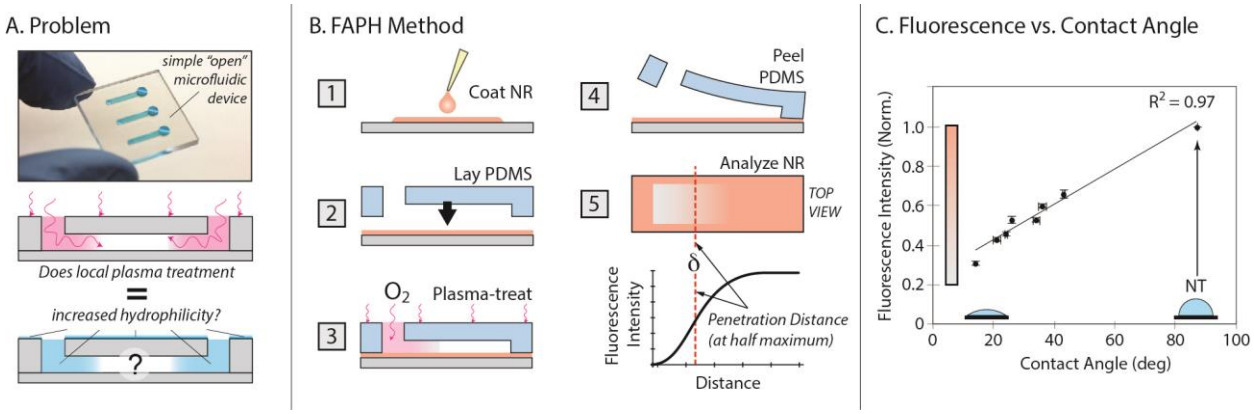

Fig. 7.1 FAPH Overview. (A) Plasma treatment before device assembly can adversely affect bond quality. While it is advantageous to plasma-treat after bonding, the effectiveness of the treatment within the channel is unknown. (B) The FAPH method: 1) Apply the NR coating, 2) assemble microchannels, 3) plasma treat, 4) remove microchannels, and analyze fluorescence. Penetration distance, δ, is determined by finding the half-maximum of fluorescence intensity. (C) Relationship between contact angle and fluorescence intensity, normalized to maximum intensity (untreated PS).

7.2 Methods and Materials

7.2.1 Microchannel Fabrication

Microchannels were fabricated in PDMS using established soft lithography techniques [132, 152]. A master mold was fabricated by spincoating photoresist (SU-8 100, Microchem, Newton, MA) onto a silicon wafer (WRS Materials, San Jose, CA), and patterning the channel features using UV light (Omnicure Series-1000, EXFO, Mississauga, Canada). Unexposed photoresist was removed with SU-8 developer (PG-MEA #484431, Sigma Aldrich, St. Louis, MO). Features were molded by soft lithography using PDMS (Sylgard 184, Dow Corning, Midland, MI) mixed in a 10:1 ratio of elastomer base and curing agent, and baked on a hotplate at 80˚C for 4 h. Channels varied in height from 100 to 350 μm, and in width from 0.10 to 1.0 mm. PDMS microchannels were then passively bonded to PS substrates for subsequent tests.

7.2.2 PS Sample Preparation

Samples were fabricated in 1.2 mm thick PS sheets (#ST313120, Goodfellow, Huntingdon, England). Large (60 x 90 mm) and small (25 x 25 mm) samples pieces were cut using a Personal CNC Mill (PCNC 770, Tormach, Waunakee, WI). Samples were cleaned by rinsing with deionized (DI) water, sonicating for 15 min in 50˚C isopropyl alcohol (IPA), and rinsing again by submerging in a DI water

bath for 1 min. Cleaned samples were pulled out of the DI water bath slowly to ensure that the surface was free from any satellite water droplets. Nile Red (NR) (#N3013, Sigma Aldrich) was diluted to 5 μg/ml in DMSO (#D2650, Sigma Aldrich) to obtain a stock solution, and then further diluted 1:200 (v/v) in IPA to yield the working solution. The working NR solution was applied on one side of the PS sample at ~0.35 μL/mm^2 using a micropipette, and left on the surface for 30 s. The sample was then promptly placed in DI water, and rinsed as previously described. During rinsing, it was important to remove all satellite water droplets because they tended to leave dried spots on the surface that affected image analysis. After rinsing, NR-coated samples were protected from light and dust until ready for use.

7.2.3 Plasma Treatment

NR-coated PS samples were either assembled to create enclosed microchannels, or left un-bonded to expose the entire sample. Samples were then treated with oxygen plasma using a plasma cleaning system (Femto, Diener Electronic, Ebhausen, Germany). Plasma treatments varied in exposure time (5 to 50 s), oxygen gas flow rate (20 to 40 mL/min), and power (25 to 50 W), which were chosen based on previously published work.[7,23,25] Unbonded PS samples were used to obtain a correlation between NR fluorescence intensity and contact angle measurements made via standard goniometry of sessile drops (see *Contact Angle Measurements*). Assembled PS samples, with the passively bonded microchannels, were used for characterizing plasma treatment penetration into microchannels by fluorescence quantification. In these experiments, PDMS microchannels were passively bonded to the NR-coated samples, plasma treatment was applied into the channels, and the PDMS microchannels were then removed after plasma treatment, exposing the entire sample surface to image analysis. Plasma treatments in these experiments were applied consistently for 50 s, at 50 W, and with an oxygen gas flow rate of 20 mL/min.

7.2.4 Contact Angle Measurements

Surface hydrophilicity of PS samples was characterized by measuring and averaging contact angles of three 6 μL DI water droplets on the sample surface using a goniometer (Model 200, Ramé-Hart,

Succasunna, NJ). For all PS samples that were NR-coated and imaged for fluorescence, fluorescence imaging was always performed prior to contact angle measurements, to prevent potential disruption of the homogeneous NR coating via the 6-µL DI water droplets.

7.2.5 Fluorescence Imaging and Analysis

All NR-coated samples were imaged on an inverted fluorescence microscope (Eclipse Ti, Nikon) using appropriate filters. Images of NR-coated samples were acquired both before and after plasma treatment to enable assessment of the depletion of NR fluorescence caused by plasma treatment. To obtain a correlation between NR fluorescence intensity and contact angle, each NR-coated PS sample was imaged at nine locations, which were averaged to represent the fluorescence intensity for that PS sample (three samples per treatment condition). To spatially "map" fluorescence within microchannels, images were flatfield-corrected using Image J, and stitched using Adobe Photoshop. To quantify penetration distance of plasma treatment fluorescence intensity along channel length was averaged across channel width. The resulting intensity profile was analyzed to determine the location where the intensity reached half of its maximum, and this location was then defined as the penetration distance, δ **(Fig. 7.2)**.

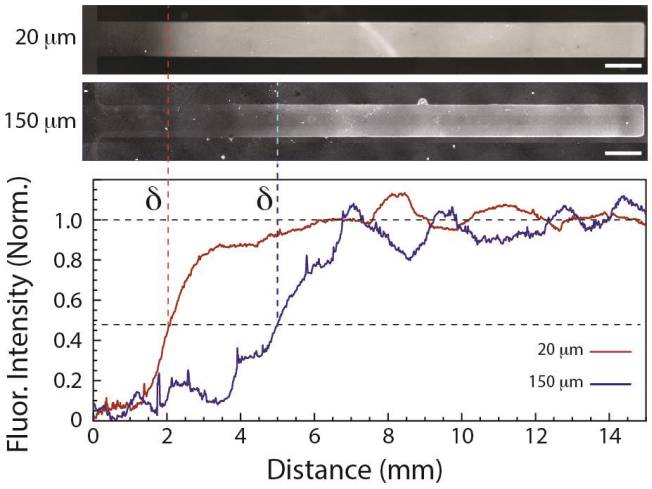

Fig. 7.2 Characterizing plasma penetration with FAPH. Penetration distance, δ, is determined by finding the half-maximum of fluorescent intensity along the channel length. The representative stitched fluorescence maps of 800-µm microchannels are shown for 20-µm (top image) and 150-µm (bottom image) tall microchannels. The fluorescence intensity profiles (averaged across channel width) are normalized to the maximum intensity of each channel, determined by averaging the intensity of the last 4 mm of the channel length. (Scale bars represent 1 mm).

7.2.6 Cell Culture

Two different cell types were used in this study: (1) human umbilical vein endothelial cells (HUVECs) were used in both the main study and the supplemental studies (appendix), and were cultured in EBM-2 media (#CC-3156 and #CC-4176, Lonza, Basel, Switzerland) with 10% FBS and 1% penicillin/streptomycin (P/S); (2) NIH-3T3 mouse fibroblasts were tested for results in the supplemental studies only, and were cultured in MEM-α (#12561-056, Life Technologies, Carlsbad, CA) with 10% FBS and 1% P/S. Cells were seeded at a surface density of ~800 cells/mm^2, and cultured for 24 h before being fixed with 4% paraformeldahyde (PFA) (#43368, Alfa Aesar, Ward Hill, MA). Cells were subsequently permeabilized with 0.1% Triton X-100, and stained with Hoechst nuclear dye (#33342, Invitrogen, Carlsbad, CA) and Alexa Fluor 488 phalloidin (#A12379, Invitrogen) for 15 min each. Stained cells were analyzed for morphology and adherent fraction.

To obtain a baseline for cell morphology and adhesion in microchannels, native (non-NR-adsorbed) PS substrates were passively bonded to cured PDMS layers with microchannels. Prior to bonding, PS substrates were exposed to three different levels of oxygen plasma treatment: (i) highly hydrophilic (<15˚), (ii) moderately hydrophilic (30-60˚), and (iii) hydrophobic (~85˚, untreated PS). Cured PDMS layers containing microchannels were then passively bonded to the PS substrates to create enclosed channels for cell culture. As a positive control for HUVECs, a fourth surface treatment involved coating the PS with fibronectin (FN) at 0.1 mg/mL to promote cell adhesion via attachment to adsorbed matrix proteins that are typically found in endothelial basement membranes[202].

To characterize the effect of plasma treatment patterns on cell adhesion and growth in microchannels, native (non-NR-adsorbed) PS substrates were passively bonded to cured PDMS layers with microchannels to create enclosed conduits. Plasma treatment was applied to each sample at 2 mbar, 50% power, and for 50 seconds. The PDMS was then removed, and cells were seeded over the entire exposed PS surface.

7.2.7 Cell Imaging and Analysis

Images of cell stains of phalloidin (green) and nuclear Hoechst dye (blue) were acquired with a 10x objective, and overlaid using ImageJ. All cell analysis and quantification was performed using ImageJ, where images were converted to binary images using the threshold function. Binary images were used to quantify overall area coverage and number of cells in each microchannel condition. To quantify penetration distance with cell, fluorescence intensity along channel length was averaged across channel width, and the resulting intensity profile was analyzed to determine the location where the intensity reached half of its maximum.

7.3 Results

We developed a method called Fluorescence-based Assessment of Plasma-induced Hydrophilicity (FAPH) that allows characterization of local surface hydrophilicity of internal surfaces within microchannels **(Fig. 7.1B)**, and informs how microfluidic geometries and dimensions can impact the effectiveness of plasma treatment. The methodology relies on the following steps: (1) Uniform coating of sample with NR, a hydrophobic fluorescent dye that adsorbs to hydrophobic surfaces because of hydrophobic interactions; (2) Passive (reversible) assembly of PDMS microchannels onto the NR-coated sample; (3) Treatment with plasma under desired parameters; (4) Removal of PDMS microchannels to expose the plasma-treated substrate; and (5) Fluorescence quantification of NR over the entire microchannel pattern, and correlation to surface hydrophilicity via contact angle calibration.

FAPH relies on the observation that upon plasma treatment, adsorbed NR on a surface undergoes a decrease in fluorescence intensity, or *a fluorescence depletion*, correlated to the level of plasma applied. An important aspect of the method is the need to establish a uniform NR coating. We accomplished this by dissolving NR in IPA, which leveraged IPA's low surface tension and its inherent property of enhancing NR fluorescence.[203] We found the optimal adsorption time for NR to range between 15 and 30 s, which allowed the dye to quench[204], yielding a dimmer but more homogeneous and repeatable NR coating with adequate fluorescence **(Fig. B.1)**. We thus chose a 30 s adsorption time for all experiments.

When protected from light, external contaminants, and extraneous contact, NR-adsorbed PS samples were found to be stable for several weeks, and could be safely stored for weeks before experimentation.

7.3.1 NR Fluorescence Intensity vs. Contact Angle Correlation

To use NR fluorescence as a quantitative indicator of hydrophilicity, we correlated NR fluorescence to contact angle measurements, the standard for characterizing surface wettability. Contact angles were measured, both before and after plasma treatment, via goniometry with water droplets placed on NR-adsorbed PS samples. Adsorbed NR itself did not significantly affect the contact angle measurement, as evidenced by negligible differences between NR-adsorbed and non-NR-adsorbed samples **(Fig. B.2)**. Plasma treatment was controlled by tuning the power, flow rate, and exposure time. We found a linear relationship between NR fluorescence intensity and contact angle **(Fig. 7.1C)** for angles between 15˚ and 50˚. We were unable to obtain contact angles between ~50˚ and 85˚ (note: 85˚was the contact angle of untreated PS), because the most gentle plasma treatment applied (i.e., lowest power setting, highest pressure setting, and shortest duration) resulted in a decrease in contact angle to ~50˚. We were also unable to obtain measurements of contact angles < 15˚ because all angles less than 15˚ could not be distinguished from 0˚ by goniometry, and were thus considered highly hydrophilic. Nevertheless, our results yielded two important observations: (1) fluorescence intensity is linearly correlated to contact angle, and (2) fluorescence intensity can be used to inform us of the contact angle, and thus the surface hydrophilicity. Importantly this information is independent of the plasma treatment parameters used to achieve the contact angle. If two different sets of treatment parameters achieved the same contact angle (e.g., high power over short exposure time *versus* low power over long exposure time) *then the resultant fluorescence intensity would be the same*. This result confirmed that NR fluorescence intensity can be used as an indirect metric for contact angle, and by extension, the hydrophilicity of internal microchannel surfaces.

7.3.2 NR Microchannel Characterization

The linear correlation between NR fluorescence intensity and contact angle allowed us to employ the FAPH method to assess surface hydrophilicity after plasma treatment within microchannel geometries. To assess the effect of geometry and entrance effects on the penetration of plasma treatment into microchannels, we fabricated microchannels with different heights (20, 150, and 350 μm) and widths (0.1 to 1 mm, **Fig. 7.3A** and **Fig. B.3**) The microchannels were open on only one end (left, entrance indicated by dotted red line) to allow unidirectional plasma penetration, and were all treated under the same parameters (see *Materials and Methods*). We observed a visible decrease in NR fluorescence intensity beginning at the channel entrance, and extending into the channel for a specific distance (solid red line path), followed by transition back to the original level of NR fluorescence intensity. Based on our observations that NR fluorescence intensity is linearly correlated with contact angle **(Fig. 7.1C)**, and specific contact angles are correlated to applied plasma treatment, the observed intensity decrease was attributed to local oxygen plasma exposure that depleted the adsorbed NR.

We defined the plasma treatment penetration distance, δ, as the distance from the entrance to the location where the NR fluorescence intensity returns to 50% of the original NR level. Based on this definition and the curve fit between fluorescence intensity and contact angle **(Fig. 7.1C)**, δ represented a contact angle of ~28 degrees, considered moderately hydrophilic. δ was then compared across different microchannel cross-sectional dimensions **(Fig. 7.2 and Fig. 7.3A)**. First, we found that δ was influenced most by microchannel height. For 20-μm tall channels, δ ranged from ~1 to ~1.4 mm, while for 150-μm tall channels, δ reached 5.5 mm. Second, we found that channel width had little impact for 20-μm tall channels, but had significantly more impact for 150-μm tall channels. For 20-μm tall channels, δ consistently reached ~1 mm for widths ranging from 0.1 to 1.0 mm. In contrast, for 150-μm tall channels, δ reached 3 mm into a 0.1-mm wide channel, and 5.5 mm into a 1-mm wide channel. We note that microchannels as tall as 350 μm were tested **(Fig. B.3)**, but these results displayed high variability, suggesting that plasma treatment became less uniform for taller channels. Overall, the results showed

importantly that δ depended on microchannel cross-sectional dimensions. Furthermore, the results demonstrated the utility of FAPH to enable visualization of plasma treatment levels, and led to local "spatial mapping" of surface hydrophilicity. The acquired spatial maps indicated a hydrophilicity gradient from the entrance inward.

7.3.3 Microchannel Cell Characterization

After visualizing spatial maps of surface hydrophilicity, and measuring δ in microchannels, we investigated the impact of the observed hydrophilicity gradient on cell culture **(Fig. 7.3B)**. We hypothesized that cell adhesion and spread in the microchannels would vary depending on a gradient of surface hydrophilicity, and that this gradient would lead to a similar gradient in cell adhesion, i.e., more adherent cells would be near the more hydrophilic entrance region, and fewer adherent cells would be seen further into the microchannel. We used the same microchannel design and plasma treatment parameters as for the NR microchannel characterization above, but used non-NR-adsorbed PS samples to avoid unnecessary interaction with cells. After plasma treatment, channels were removed and the sample was submerged in a suspension of HUVECs for 24 h to allow homogeneous and geometry-independent cell seeding **(Fig. 7.3B)**. HUVECs were chosen because they are known to demonstrate a noticeable difference in adhesion and spread when cultured on hydrophobic versus hydrophilic surfaces **(Fig. B.4)**. We measured the distance from the channel entrance to the point at which cell adhesion was half as high as in the treated area **(Fig. 7.3B)**, and compared this to δ obtained by NR depletion. As hypothesized, we observed cells adhering more to the hydrophilic regions compared to hydrophobic regions. Adhesion correlated with plasma treatment δ, and similar trends were observed for both 150 μm and 20 μm tall channels, with results matching more closely for the taller channels ($R^2 = 0.95$) than for the shorter channels ($R^2 = 0.77$) **(Fig. 7.3C, and B.5)**.

7.3.4 FAPH in Microchannel Networks

Finally, we applied FAPH to a multi-channel network consisting of multiple 500-μm wide horizontal microchannels extending from a main 1-mm wide vertical microchannel **(Fig. 7.3D)**. Such a

configuration mimics the design for a cell culture microchannel connected to perpendicular conduits, which may then be attached to adjacent cell culture compartments. We were interested in visualizing the effect of oxygen plasma treatment into an open port (P) and through this configuration. When we analyzed δ in the vertical main channel, we found δ_{PQR} = 2.24 mm, which did not reach the entrance of the second horizontal arm. When we subsequently analyzed δ in all the horizontal arms, only the channel closest to the inlet port showed detectable NR depletion, with δ_{PQS} = 2.38 mm. This total straight-line path measured from the inlet port P to location S **(Fig. 7.3D)** was ~6% longer than the straight-line path from P to R, indicating a consistency in the penetration distance due to plasma treatment, independent of the tortuosity of the path. Collectively, these results show the importance of homogeneity of plasma treatment in microchannels, and the potential of FAPH for characterizing plasma treatment in simple and complex channel designs.

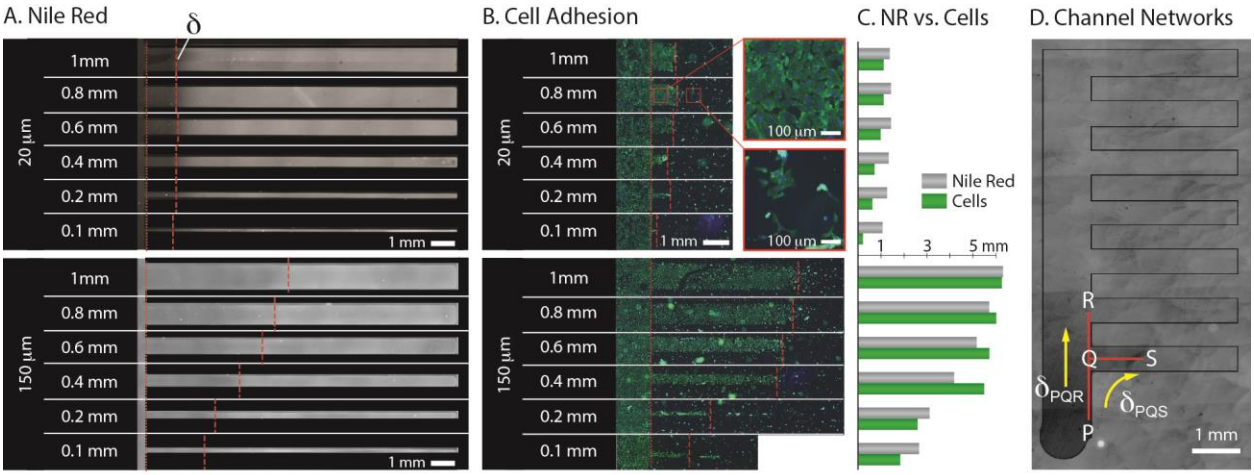

Fig. 7.3 Impacts of channel design on plasma penetration and cell culture. (A) Stitched fluorescence maps of plasma-treated NR coatings in 20 and 150 µm tall channels. (B) HUVECs cultured on plasma-treated surface after microchannel removal. Insets show HUVEC morphology in hydrophilic and hydrophobic regions of channel (green = f-actin stained via phalloidin; blue = nuclei stained via Hoechst dye). In A and B, dotted red line = entrance; dashed red line = δ. (C) Graph comparing measured δ in A and B. (D) Stitched fluorescence map of a microchannel network. Red lines indicate δ measured as straight line path from inlet port P. δPQR = 2.24 mm, and δ PQS = 2.38 mm.

7.4 Discussion

To our knowledge, FAPH is the first fluorescence-based approach for characterizing the internal surface hydrophilicity of microchannels. The main advantage of FAPH is its ability to provide quantitation of the *local* surface hydrophilicity in a manner that cannot be obtained by conventional

methods such as goniometry. Goniometry is effective and efficient for large planar substrates where droplets can be placed on a flat surface and imaged to determine contact angles. Enclosed microchannels, however, are not accessible to contact angle measurements via goniometry because they are not open to sessile drop formation. Furthermore, contact angle measurements only provide a measure of the surface hydrophilicity over areas that cover the footprint of the droplet or larger, so spatial resolution is limited. FAPH is applicable for simple and complex channel designs and configurations **(Fig. 7.3D)**, and is useful for assessing plasma treatments in enclosed microchannels quantitatively in terms of penetration distance δ. δ was found to correlate closely in cell culture systems with the channel location delineating regions of high and low cell adhesion **(Fig. 7.3B)**, and was found to be dependent on channel dimensions **(Fig. 7.3C)**. Specifically, δ appeared to decrease with decreasing channel width for deep (150-μm tall) channels, but was found to be so short for shallow (20-mm tall) channels that decreasing channel width had no additional effect on δ. It was also discovered that δ was similar in length for different tortuous paths in a complex microchannel network after plasma treatment through a single inlet port **(Fig. 7.3D)**. These geometric effects on plasma treatment are important in cases where microdevices are treated after assembly, which is commonly done for microdevices fabricated in PS because plasma treatment before assembly can adversely affect bonding procedures.[38] FAPH enables characterization of the quality of local plasma treatment in the microchannel network with unparalleled spatial resolution. The technique offers a convenient visual readout via fluorescence that spatially "maps" the surface hydrophilicity, which is impossible with goniometry. This visual information can then be used to inform the user about heterogeneities in wettability and guide optimization. Depending on the biological or fluidic requirements of a microchannel, the designer could choose to use the appropriate microchannel height to ensure homogenous surface treatment in the channel. For example, if a total channel length of 10 mm is desired, a microchannel that is 1-mm wide and 150-μm tall will ensure plasma penetration of at least 5 mm from one port. Adding a second port at the other end of the microchannel will therefore ensure complete plasma treatment into the center due to penetration from both ends. δ was found to be independent of the quantity of access ports, and simply dependent on channel geometry (see Appendix).

FAPH currently works best when NR is pre-coated on the substrate prior to device assembly because it ensures uniform NR adsorption on the surface. The method also yields more consistent fluorescence quantification when the device is disassembled after plasma treatment and before image analysis. We currently achieve this by using a passively bonded PDMS channel layer that can be removed after plasma treatment. This was sufficient to model the effects of channel dimensions on plasma treatment effectiveness, since it was found during preliminary testing that the use of PDMS instead of PS did not change the resultant measurements of δ. Future work will investigate how to extend the FAPH method to work directly in enclosed, fully assembled microchannels without the need for precoating of substrates or the need for device disassembly.

In terms of the choice to use NR, we tried other fluorophores (e.g., Texas Red), and found NR to offer the most sensitive detection and yield the most repeatable results. NR sensitivity was further improved by dissolving NR in IPA, which offered increased fluorescence intensity while also improving surface coverage during the dye adsorption step because of the low surface tension of IPA. NR emission wavelengths can be adjusted by changing the solvent[203], so further optimization can be achieved for other applications if necessary.

The underlying physics of plasma treatment continues to be an active area of research.[205] FAPH has potential to uncover answers to previous questions related to the mechanisms of plasma treatment, particularly in its penetration and effectiveness in complex geometries and configurations. In addition, there may be potential applications where non-uniform plasma treatment is an advantage. In such cases, FAPH will provide a quantitative method for optimizing designs to provide the desired surface treatment, and to assist with the visual "mapping" of surface hydrophilicity.

7.5 Conclusion

FAPH is a method for characterizing and mapping the local plasma treatment within microchannels. Our data suggests that NR fluorescence can be directly correlated to contact angle, and by extension plasma treatment penetration. Microchannel cross-sectional shape appears to have a

significant effect on plasma treatment penetration distance. Channel design therefore plays a critical role in plasma treatment quality. Using this method, channels can be characterized prior to cell culture, thereby aiding device design, and reducing the time needed to develop and optimize a functional cell-based assay.

Chapter 8 The VerIFAST: An integrated method for cell isolation and extracellular/intracellular staining[7]

8.1 Introduction

The collection and characterization of rare cell populations is critical for many tumor biology and blood-based studies including tumor cell heterogeneity[206, 207] , stem cells [208-210], circulating tumor cells (CTCs)[211-213], T-cells[214-216], and neutrophils[155, 217]. Macroscale methods to isolate and analyze these cells require long, expensive, and laborious procedures that typically result in significant sample loss [211]. Thus, effective devices for cell isolation and downstream analysis will involve integrating these methods to save time, reagents, and ultimately reduce sample loss [218-220]. Microfluidic systems have offered unique solutions to these systems by providing the ability to perform complete analyses on a single device[221-224]. The ability to integrate high purity, high efficiency, and flexible cell isolation with downstream techniques for extra- and intracellular staining will enable high-content studies of rare or precious samples.

Microfluidic platforms for cellular isolation have been demonstrated that can achieve sensitivity and specificity unattainable using current macroscale systems[213]. These platforms include functionalized micropost arrays, patterned surfaces, and systems that leverage density, size, or other physical characteristics to isolate cells of interest from non-target cells[221, 224]. While successful isolations have been demonstrated with these platforms, limitations with on-chip imaging, cell removal, cell viability, and retention of the original sample for further processing may ultimately limit widespread adoption[211, 212, 224].

Immiscible phase filtration (IPF) has shown promise for isolation of nucleic acids[170, 225, 226], proteins[227, 228], and cells/lysates [229], from a particulate background. Immiscible Filtration Assisted by Surface Tension (IFAST) leverages the dominance of surface tension over gravity at the microscale to

7 This chapter has been adapted from the following publication: "The VerIFAST: An integrated method for cell isolation and extracellular staining" Benjamin P. Casavant*, David J. Guckenberger*, Scott M. Berry, Jacob T. Tokar, Joshua M Lang, and David J. Beebe. Lab on a Chip 2012

* Authors contributed equally

establish "virtual walls"[230] between the immiscible (e.g. oil) and aqueous phases to create a micro scale IPF device. The virtual walls are used to filter contaminants in a single step, thereby eliminating centrifugation, multiple washing steps and multiple PMP capture steps while maintaining cell viability. [231]

This system exhibits multiple advantages over existing methods in its simplicity, efficiency, and ability to isolate a variety of analytes[232]. However, geometric configuration of the IFAST (termed the "Horizontal IFAST" in this manuscript) has revealed specific limitations. First, the Horizontal IFAST has lower efficiency of recovery and overall purity for samples containing large particulates that settle out of solution (e.g. debris, precipitates, or other cells). Second, the paramagnetic particles (PMPs) used for the isolation are difficult to remove from the cells, impairing downstream applications such as fluorescent imaging. Finally, while cellular staining is possible in the Horizontal IFAST, it can be prohibitive due to the number of wells necessary for a staining process (i.e. two wells necessary for each step, see Appendix C).

Here we present the VerIFAST **(Fig. 8.1)**, a significant improvement upon the Horizontal IFAST for the capture and molecular analysis of rare cell populations. The VerIFAST is an improvement upon previous IFAST technology with three important additional features: 1) large particle contaminants settle out of the operational path of the IFAST, resulting in increased purity, 2) excess PMPs can be easily removed for improved visualization and imaging, and 3) complex cellular staining protocols (e.g. fixation, permeabilization, staining, washing) can be performed directly in a single well within the device. The VerIFAST combines features of the previously described IFAST[170] and density-mediated immiscible phase filtration [228], resulting in increased performance, operational robustness, and reduced reagent volumes. In the VerIFAST, the PMPs are pulled along the sidewall instead of across the bottom surface, allowing non-target cells to settle out of the operational path of the analyte-bound PMPs. We demonstrate that the VerIFAST enables isolation of rare cells from a heterogeneous background of peripheral blood mononuclear cells (PBMCs) in an elegant integrated front-end processing step. Further, by leveraging the vertical orientation and the ability fabricate a microporous membrane within the device, the VerIFAST

allows for the creation of a chamber (termed the Sieve Chamber) in which cells and reagents are contained in two adjacent wells separated by a membrane. The Sieve Chamber is designed to have a microporous membrane large enough to allow PMPs to sieve through the membrane, yet small enough to prevent cells of interest from passing through the filter. Furthermore, addition and removal of fluid can be performed within the Sieve Chamber without perturbing the sample, yet when necessary the sample can, at any point, be removed from the device. The VerIFAST is able to take cell capture beyond enumeration endpoints, as cells are able to be isolated from a background in a method that maintains viability, and has an integrated method appended to perform fixation and permeabilization for more intricate intracellular analyses.

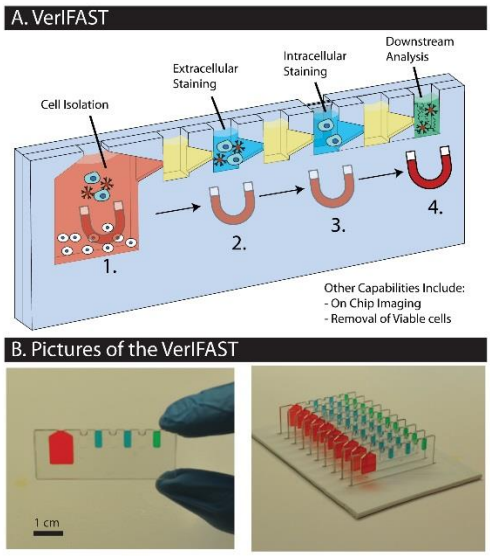

Fig. 8.1 VerIFAST overview. (A) The VerIFAST utilizes novel methods to enable cell isolation, extracellular staining, intracellular staining, and downstream analysis in a single and simple device. (B) Images of the VerIFAST devices.

8.2 Methods & Materials

8.2.1 Device Preparation

The VerIFAST device was fabricated in 2mm thick polystyrene (PS, Goodfellow, UK) via micromachining (PCNC770, Tormach, USA). The well height and widths can be varied, but were constrained such that the input well had a 200 µL capacity and each successive well had a 30 µL capacity. Each well is connected by a funnel that is a constant 200 µm deep and has a height that tapers from 2 mm

to 0.8 mm between the inlet and outlet, respectively. The alternative device for intra-cellular staining employs an 8 µm microporous membrane (Part PET8025100, Sterlitech, USA) and a second layer of PS. The second PS layer, containing one 30µL well, was solvent bonded (Weak solvent based chip lamination, Zhou, 2010) to the original PS piece, with the membrane sandwiched between. For both the single layered device and the membrane device, an adhesive backing was applied to both sides of the device to contain the fluids (MicroAmp, Applied Biosystems, USA).

8.2.2 Paramagnetic Particle Preparation

The paramagnetic particles (PMPs) used for these experiments were Dynabeads® M-280 coupled with Streptavidin (Life Technologies, USA). To remove the stock buffer solution from the PMPs, the PMPs were washed and re-suspended with 0.01% Tween-20 in phosphate buffered solution (PBS). 5 µM of biotinylated antibody (R&D Systems, USA) for the epithelial cell adhesion molecule (EpCAM) was added to the PMP solution. The PMPs and antibodies were mixed on a shaker for 30 minutes at 800 rpm to allow binding, then was washed three times and re-suspended with 0.1% BSA in PBS.

8.2.3 Cell Culture

Target cells used in these experiments were human lymph node carcinoma of the prostate (LNCaP) immortalized cell lines. Cells were maintained at 37ºC and 5% CO2 in MEM-alpha culture medium supplemented with 10% fetal bovine serum (Gibco, USA), 100 U/mL penicillin (Gibco, USA), and 100 µg/mL streptomycin (Gibco, USA). Before running quantification experiments, cells were incubated for ten minutes with calcein AM (Life Technologies, USA) at a concentration of 2 µM in serum-free MEM-alpha culture media. The cells were centrifuged and washed three times with 0.1% BSA in PBS, then counted with a hemocytometer and re-suspended in 0.1% BSA in PBS.

Peripheral Blood Mononuclear Cells (PBMCs) were collected from healthy volunteers under a University of Wisconsin IRB-approved protocol. PBMCs were isolated by density centrifugation, counted in a hemocytometer, and used as non-target cells for cell purification experiments. PBMCs were treated with CellTracker Red CMTPX (Life Technologies, USA) at a concentration of 2.5 µg of CellTracker in 1

mL of serum-free MEM-alpha cell culture medium for 30 minutes. Following incubation, the PBMCs were washed three times then resuspended with 0.1% BSA in PBS.

8.2.4 Experimental Setup

250 µg of PMPs and assay-dependent numbers of LNCaPs and PMBCs were added into a mixture of 5 mM EDTA, 0.001% Tween-20, and supplemented with 0.1% BSA in PBS. This mix was tumbled for 30 minutes in a 4ºC cold room to bind PMPs to cells. The mixture was added to the input well of the device for each experiment, with alternating wells of olive oil (Unilever) and PBS (Life Technologies, USA) through the device. Olive oil was chosen due to its robust interfacial energy with aqueous solutions [21], see Appendix C.

To count the number of cells that were either pulled through or left behind, the device was imaged using an inverted fluorescent microscope (Olympus IX-70). The device was placed on its side, and imaged for calcein AM (492 nm excitation) and the CellTracker (572 nm excitation).

8.2.5 Staining Protocols

Antibodies used for in-line staining endpoints in the VerIFAST was a PE-bound EpCAM antibody (Abcam, USA). Staining was achieved in the wells of the IFAST device by adding the antibody at a 1:50 dilution into a solution of 0.1% BSA in PBS. Cells were pulled into the staining well and refrigerated at 4ºC for 30 minutes prior to being pulled into a final well for imaging containing 0.1% BSA in PBS. Primary antibodies used for intracellular staining were a pan-cytokeratin with tagged FITC antibody (Abcam, USA) at a 1:50 dilution and a Ki-67 antibody (Abcam, USA) at a 1:50 dilution, both in 0.1% BSA in PBS. The secondary antibody used in conjunction with the Ki-67 was an APC-bound goat anti-rabbit antibody (1:100). Nuclear staining was achieved using 0.02 mg/mL Hoescht stain. Staining was achieved in the membrane well in an eight step process including wash steps. Appendix C Table 1 illustrates the steps involved in the intracellular staining protocol.

8.3 Results and Discussion

8.3.1 Settling Chamber

While the VerIFAST operates according to similar principles as the Horizontal IFAST, the VerIFAST enables isolation of rare or low quantity cells more effectively. Due to the orientation and design of the Horizontal IFAST, PMPs are pulled along the bottom surface of the device **(Fig. 8.2A)**. Since the cells settle to the bottom of the device, the PMPs push unwanted cells through the oil phases, thereby decreasing the efficiency of the isolation **(Fig. 8.2B)**. The VerIFAST mitigates this issue by utilizing an alternative orientation and design of the input well, allowing cells to settle out of the path of the PMPs. **(Fig. 8.2A,B)** The input well where the sample is loaded is deep and is followed by a series of alternating immiscible phases (e.g. oil) and aqueous phases (e.g. stains, elution buffers, washes). By utilizing a well that is both deep and narrow, two goals are accomplished. First, the aspect ratio of the opening holds fluids in the device such that the device can be inverted and turned without losing fluid. Second, PMPs are pulled along the side of the device, instead of the bottom, which allows non-target cells to settle out of the way of the PMPs. Therefore, the PMPs do not pull non-target cells through the oil. This is particularly important since non-target cells pulled through the oil would necessitate additional traverses to achieve high levels of purity. The purity levels and corresponding number of traverses were characterized by isolating LNCaPs from a background of PBMCs **(Fig. 8.2C)**. In the Horizontal IFAST device, three oil traverses were necessary to achieve 77% purity, which was due to the effects previously described. The VerIFAST is capable of achieving the same level of purity in one traverse. Furthermore, because target cells are lost with every traverse, the VerIFAST has a higher efficiency of isolation by achieving higher levels of purity in fewer traverses. The robustness of the VerIFAST method was demonstrated with the isolation and visualization of a single cell placed into a background to 20 million PBMCs **(Fig. 8.2D)**. This technique can also remove target cells from high numbers of background cells without impacting the recovery rate of the device, enabling this method to be used following a batch process for cellular enrichment, as is the case with a Ficoll-Paque density centrifugation. Specifically,

target LNCaPs were removed from various amounts of background PBMCs (5-100 million cells in 200µl), and the isolation efficiency remained high (>80%) for each level of background cells **(Fig. 8.2E).**

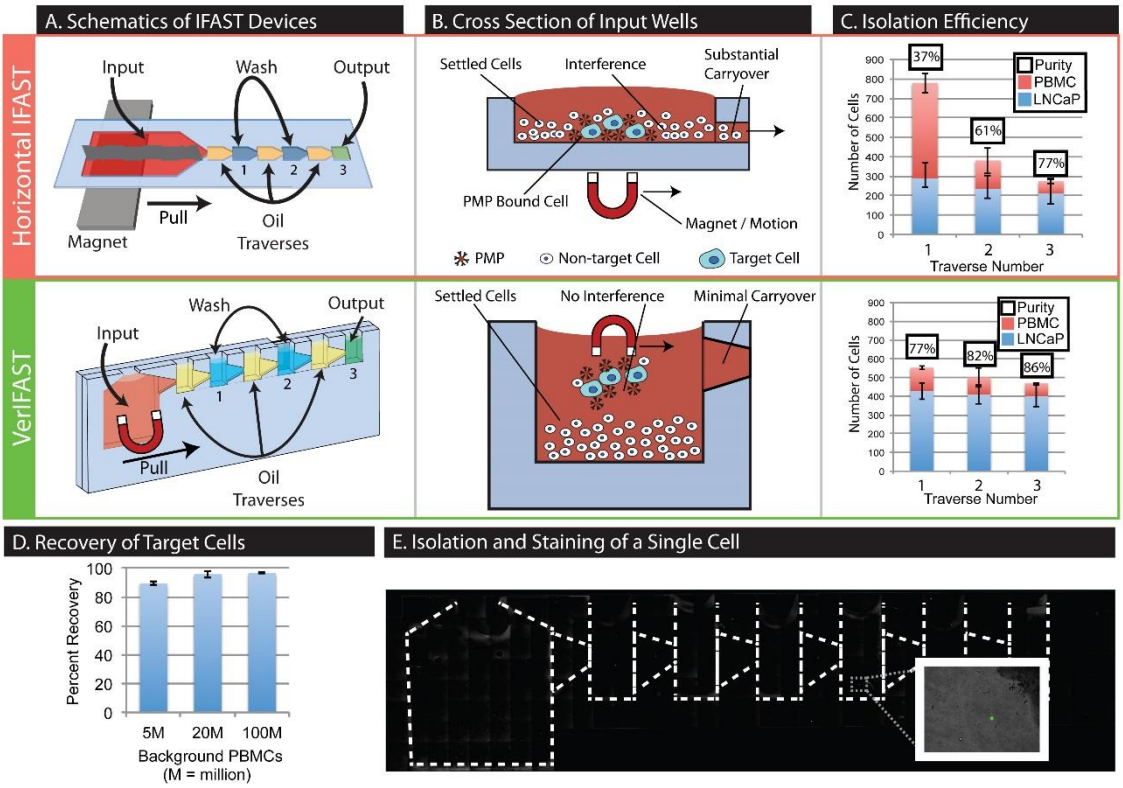

Fig. 8.2 Method comparison and cell isolation. (A) Schematics of the Horizontal IFAST and the VerIFAST. (B) Cross sectional view of the IFAST devices. In the Horizontal IFAST cells settle to the bottom and interfere with the beads, causing high levels of non-target cell carryover. In the VerIFAST, cells settle out of the path of the PMPs, significantly reducing the amount of carryover. (C) Purity level of target cells (LNCaPs) after isolation from a background of non-target cells (PBMCs) (D) Percent recovery of target cells isolated from varying levels of non-target cells. (E) Stitched image of the VerIFAST after isolating one LNCaP tumor cell from a background of 20 million PBMCs. Isolation was through to the 5th well, keeping the 7th well open for further analytical techniques (e.g. RNA, DNA, proteins).

8.3.2 In-Line Staining

Extracellular surface stains are important to many cellular analyses, as these stains can be performed without the need for cell fixation and enable visualization of many surface proteins (i.e. EpCAM, CD4, etc.). We demonstrate the ability of the VerIFAST device to perform simple in-line extracellular staining for the surface protein EpCAM. This process is completed by simply pulling cells into a well containing antibody tagged with a fluorophore **(Fig. 8.2D)**. The immiscible barriers on each

side of the well contain the antibody and cells in an aqueous solution for the duration of the incubation (30 minutes at 4ºC). After the incubation, the magnet is used to pull the PMP-bound cells through the oil phase, leaving behind unbound antibody in a single wash step. Oil well traverses have been previously demonstrated to maintain cell viability[30].

8.3.3 Sieve Chamber

Isolating, staining, and imaging cells within a single device can be advantageous for low or rare populations of cells as it eliminates the need for wasteful transfer or centrifugation steps. The VerIFAST mitigates cell loss by enabling cell isolation via PMPs and immiscible phases with a simplified workflow. However, the PMPs involved in the isolation can cause issues with downstream analyses or experimentation. We have overcome this obstacle by integrating a sieve chamber into the VerIFAST to facilitate removal of background PMPs from a cell suspension.

The sieve chamber **(Fig. 8.3A)** utilizes a polycarbonate microporous membrane (8 μm pores) that is bonded between two wells. The front well is coplanar with the other wells in the VerIFAST and is the recipient of the isolated cells. The rear well is adjacent and of identical size to the front well and the same size, but separated by the microporous membrane. After the PMP bound cells are pulled into the first well, the magnet is removed and reapplied to the backside of the device, against the rear well. This magnetic force pulls the PMPs (3 μm diameter) through the membrane pores (8 μm diameter) while the target cells are held in the first well as the target cells (average 15 μm diameter [232]) are physically too large to get through the membrane. The pore size of the membrane is particularly important, as the pores must be larger in diameter than the PMPs yet smaller than the diameter of the target cells. This process removes excess unbound PMPs from the solution.

Unbound PMP removal is necessary for imaging purposes. The optical benefits of PMP removal are illustrated by comparing a well containing PMPs to a well without PMPs **(Fig. 8.3B)**. Visually, the PMPs cause the well to become nearly opaque, making bright field imaging of the target cells difficult. To expand this analysis, the solutions were analyzed by spectrophotometry both before and after PMP

removal within the sieve chamber. Spectrophotometry revealed that removal of the PMPs decreases fluorescent interference by seven-fold, seen in both red (572 nm) and green (492 nm) channels **(Fig. 8.3C)**.

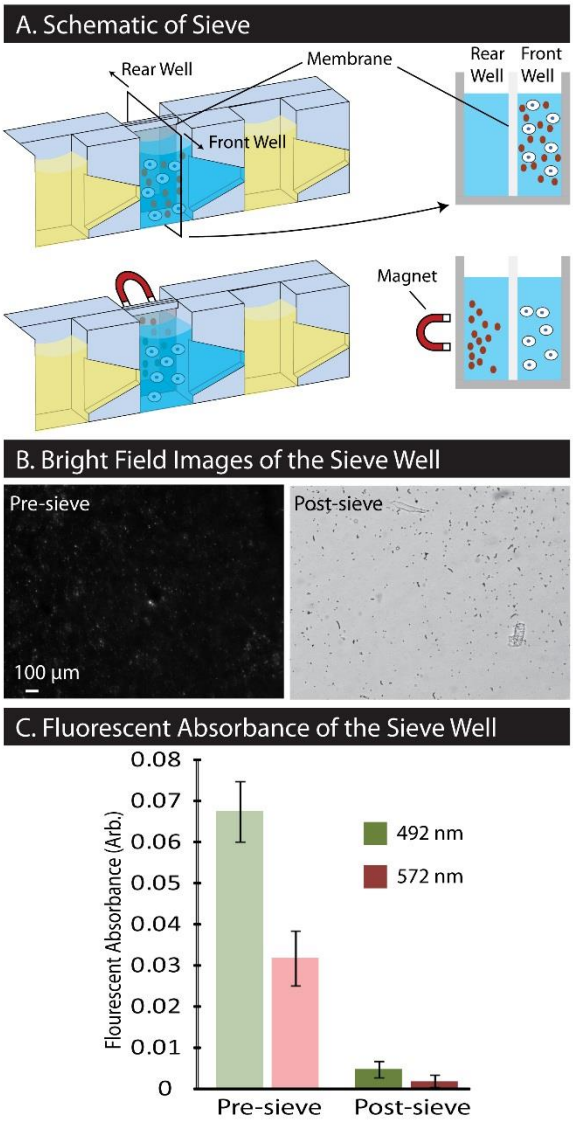

Fig. 8.3 PMP removal via the Sieve Well. (A) When a magnet is placed on the backside of the device, PMPs pull through a microporous membrane, separating the PMPs from the cells. (B) Bright field images of the sieve well before and after PMPs are removed via the sieve method. (C) Fluorescent absorbance of the fluid contents of the sieve well before and after the PMPs were removed. Absorbance was measured at two different wavelengths (492nm and 572nm) and the presence of beads in solution contributed to an approximate 7-fold decrease in absorbance upon beads being sieved from the device.

8.3.4 Sieve Chamber Staining

To expand the capabilities of the VerIFAST we integrated intracellular staining into the process. Cells isolated with the VerIFAST were assayed for intracellular proteins on-device without any transfer steps. Elimination of the transfer step is key to conserving cells, as cells are inherently lost during the transfer. Similar to the PMP removal process, the same microporous membrane was used to add and replace fluid without perturbing the cellular sample on the front side of the membrane **(Fig. 8.4A)**. This is performed in a two-step fluid handling process **(Fig. 8.4B)** and is operated entirely by pipette for all fluid transfer steps, a simple and flexible alternative to syringe pumps. The first step is to aspirate the liquid from the rear well (left). The difference of hydrostatic pressures forces the liquid through the membrane, from the front well to the rear well, thereby enabling complete removal of the liquid. Once the liquid is removed, new liquid is added into the rear well. Again, the difference in hydrostatic pressure will force the liquid through the membrane, but this time to fill the front well. As this form of washing is not reliant upon diffusion, fluid transfers can be performed rapidly within the device. Using a single well is beneficial for multi-step methods, but can include problems of carryover and incomplete fluid removal, which can be ameliorated through the use of extra wash steps without sample loss. The sieve chamber can be used for a variety of processes (e.g. fixation, permeabilization, washing, fluorescent staining) without requiring removal of the cell sample from the device.

The use of a membrane for fluid replacements simplifies complex, multi-step and multi-fluid processes into a single well. Further, it enables both rapid fluid replacements and efficient use of space. For example, a thirteen step intracellular staining process for LNCaPs, including stains for intracellular proteins (pan cytokeratins and the proliferation marker Ki-67), can be completed in a single well of the VerIFAST device **(Fig. 8.4C, Process detailed in Appendix C)**. Importantly, all of the cells are contained within the well and are never directly contacted, thereby minimizing cell loss. To characterize the effectiveness of the membrane in terms of reducing cell loss, cells were counted after each wash for five washes **(n = 3, Fig. 8.4E).** The data shows that cell loss due to the membrane is statistically

negligible through five wash steps, making the membrane and the VerIFAST a simplified platform to enable isolation and staining of precious samples.

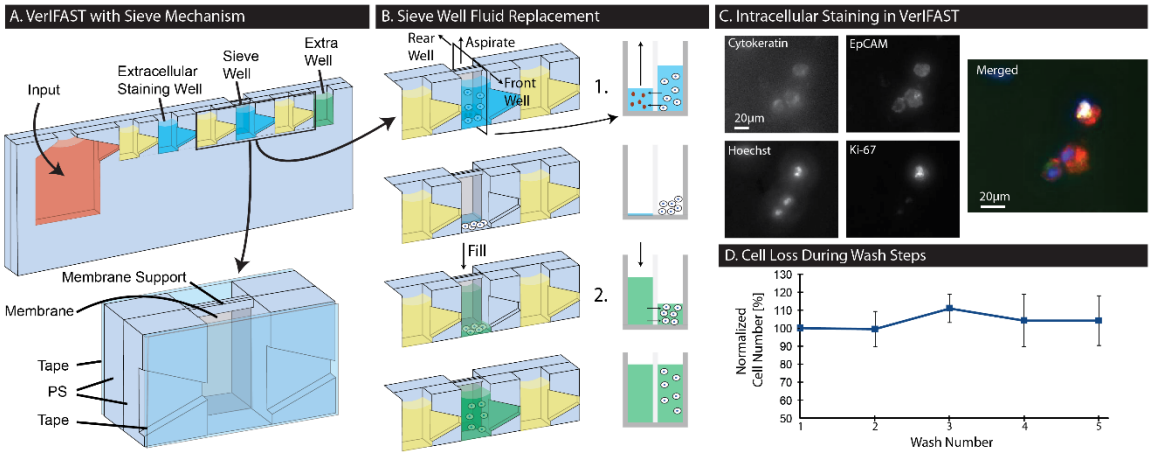

Fig. 8.4 Intracellular staining via the sieve well. (A) Schematic and enlarged view of the VerIFAST with the sieve mechanism. The extra well is for optional downstream extractions/isolations. (B) Fluid replacement is completed in two simple steps, namely aspirating unwanted fluid and dispensing new fluid into the device. (C) Images of cells that have been stained in the VerIFAST for both extra-cellular (EpCAM) and intracellular (Cytokeratin, Ki-67, Hoechst) markers. D) Repeatability of the quantity of cells remaining in the sieve well after a specified number of washes (n=3).

8.4 Conclusions

We present a device that integrates cellular isolation with downstream analytical methods for extracellular and intracellular staining in an integrated, flexible platform well suited for rare or precious samples. By incorporating a front-end settling chamber, we add a passive pre-processing step resulting in a six-fold reduction in background through a single traverse with high efficiency regardless of background cell number. An in-line staining chamber is used to perform extracellular staining quickly and without wash steps, resulting in a viable population of labeled cells for downstream assays. Finally, a membrane-separated well is used to perform more sensitive analytical methods on an unperturbed sample, enabling the observation of cytoplasmic or nuclear proteins within an isolated cell population without significant cell loss. Cellular isolation is a powerful tool that is used for a litany of diagnostic and research techniques. An integrated method that can expand the abilities of isolation methods to include ubiquitous downstream techniques of immunohistochemistry and flow cytometry will enable and enhance the analysis of circulating tumor cells, in which rare samples need to be interrogated without sample loss.

Chapter 9 Rapid and efficient sample preparation from complex biological samples using a Sliding Lid for Immobilized Droplet Extractions (SLIDE)[8]

9.1 Introduction

Methods for isolating DNA, RNA, and protein from biological samples are central to molecular biology. However, these methods are often overlooked as new assays are developed for the biological sample processing workflow[233, 234]. As such, sample preparation methods have become a limiting factor to the advancement of downstream analytical techniques[173]. Many of the traditional methods used for sample preparation are time consuming due to the multitude of steps needed. These steps can include substrate binding and several washes, liquid transfers, or dilutions. The time-intensive nature of these steps can result in sample loss and degradation[233].

The utility of exploiting functionalized paramagnetic particles (PMPs) for analyte isolation has proven useful on a wide range of platforms[235]. One advantage of using PMPs is the ability to simply and thoroughly interrogate a fluid for analyte capture. In contrast with immobile functionalized surfaces, the PMPs can be suspended in a solution, allowing the functional surfaces of the PMPs to interact with a large portion of the fluid, without the need for complex mixing or flow focusing techniques. Another advantage is that the particles can be used in many different embodiments, as only a magnet is required for actuation and analyte isolation[76, 77, 170, 232, 235-238].

The ways to isolate an analyte of interest from a given sample using PMPs can be further divided into three basic methods **(Fig. 9.1)**. In the first method, most commonly used in commercially available kits, background sample and any contaminants are removed by washing fluid (i.e. buffers) over the substrate and immobilized PMPs[235]. Limitations of this widely used method include 1) the loss or dilution

8 This chapter has been adapted from the following publication: "Efficient Sample Preparation from Complex Biological Samples Using a Sliding Lid for Immobilized Droplet Extractions" Benjamin P. Casavant*, David J. Guckenberger*, David J. Beebe, and Scott M. Berry. Analytical Chemistry 2014.

* Authors contributed equally

of the original input sample, which limits the ability to re-interrogate the sample, and 2) a time and fluid-intensive assay protocol due to the repeated liquid transfers required to wash the PMP-captured analyte[234]. In the second method, PMPs are selectively removed from a sample of interest. In these methods, analyte-bound PMPs are physically dragged out of the original sample along the surface of a device, through an immiscible phase (e.g. oil), and into a second aqueous phase[170, 173, 225, 228, 229]. This method for PMP sample preparation has been highly effective at isolating analytes with high specificity and selectivity while simplifying workflows - isolation can be performed in a matter of seconds[76, 170]. Though effective, limitations for this method exist due to potential sample loss associated with the friction created by dragging the PMPs along a surface. Further, the need to incorporate oil, air[225], or surface[238]/geometric[232] pinning complicates these devices. In the third method of isolating PMPs, and the focus of this manuscript, analyte-bound PMPs are pinned to a surface, the surface is removed entirely from the background present in the original sample, and then the surface and PMPs are brought into contact with a second solution to elute the analyte. This method builds upon the benefits of simple workflows found with the second method, but does not involve any dragging of the PMPs, significantly reducing loss due to friction and simplifying the device operation.

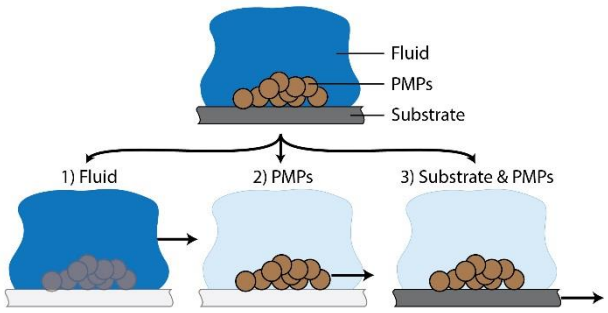

Fig. 9.1 Different methods to isolate paramagnetic particles (PMPs) from a fluid. A) Move the fluid - by keeping the PMPs and substrate stationary, fluid can be washed over the PMPs, isolating and purifying the analyte. B) Move the PMPs - by moving the PMPs and bound analyte, the analyte can be effectively removed from an original sample into an elution buffer. C) Move the substrate with the PMPs- by keeping the PMPs stationary with respect to the substrate, the substrate can be removed from the original sample and placed into an elution buffer.

In this paper, we present a method that enhances the benefits of previous exclusion-based sample preparation methods and leverage a new technology called Sliding Lid for Immobilized Droplet Extractions (SLIDE). The SLIDE was developed to achieve gentle and reliable extraction of analyte-

bound PMPs for sample preparation by leveraging surface tension of fluids and hydrophilic / hydrophobic patterning of surfaces. The operational principle of the SLIDE involves pulling analyte-bound PMPs to a hydrophobic surface (the 'lid'), and pulling the entire surface from an input sample to an output drop. By creating simple hydrophilic pinning regions on the bottom plate, the surface tension of the fluid will maintain the drops in place, while the PMPs can be moved from one drop to the other without any loss due to PMPs dragging along the surface. Here, we demonstrate the ability of SLIDE to leverage simple fluid characteristics to create a robust and easy-to-use device for sample preparation for a range of analytes.

9.2 Materials and Methods

9.2.1 SLIDE lid and base fabrication.

The SLIDE method uses two components, a base and a lid **(Fig. 9.2)** that were rapid prototyped via stereolithography with Accura 60 (3D Systems, Rock Hill, SC). The base component serves as a holder for disposable cartridges, houses magnets located underneath the patterned fluid drops, and acts as a guide for the handle. The lid contains two arms that guide the lid along the base and control the spacing between the bottom of the handle and the drops. Built inside of the handle are vertical slots spaced 12mm apart, and designed to guide magnets during operation. Each of the magnets contained a stack of five 3/16" cube magnets (#B333-N52, K&J Magnetics, Jamison, PA), which are interconnected on the top by a steel thin steel bar (MSC) to reduce the effect of the neighboring magnets by sharing a magnetic field.

9.2.2 SLIDE operation.

The SLIDE technology utilizes surface tension and fluid drop pinning dynamics for simple and low cost analyte isolation. A key advantage of the SLIDE is the usability of the device with an easily recognizable and intuitive platform that operates similar to that of a traditional credit card imprinter. As previously mentioned, the SLIDE operates by placing magnets on a top hydrophobic surface (the lid) and immobilizing PMPs relative to that surface. To re-disperse the PMPs in the output fluid, the magnets must be removed from the lid, allowing beads to drop into the output fluid **(Fig. 9.2, Fig. D.1a)**. Initially, this

was accomplished using a system of cams that mechanically lifted the upper magnets as the lid passed over the output drops of the SLIDE device **(Fig. D.1c)**. However, we found that this cam system added unnecessary complexity to the system. In the final version of the SLIDE device, this mechanical actuation of the upper magnets was replaced with a magnetic field-driven mechanism. The upper magnets are allowed to freely move within vertical slots in the lid, while lower magnets of opposing polarity, are held stationary in the base, below the cartridge. As the lid passes over the lower magnets, the upper magnets are deflected into the top of the lid. Because PMPs do not have permanent magnetism, they will naturally re-polarize and move toward the more powerful magnetic field. Thus, when the upper magnets are deflected into the top of the lid, the PMPs will travel toward the lower magnet and dissociate from the lid surface **(Fig. B.1)**. During SLIDE operation, PMPs will travel to the lid surface when no magnet is present in the base (as in input drops) and to the bottom surface when a magnet is placed in the base (as in output drops).

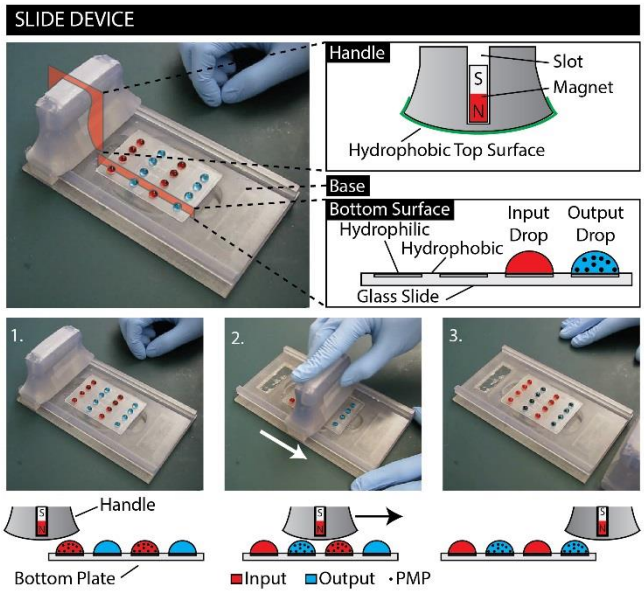

Fig. 9.2 Image of the magnetic version of the SLIDE device. The device consists of a handle that houses the magnets and a hydrophobic layer, a base that houses the cartridge, and an insert that contains hydrophilic/hydrophobic patterns to position liquid drops (top right). SLIDE is simply operated by sliding the handle over the cartridge (bottom).

9.2.3 SLIDE disposables.

The SLIDE integrates two main disposables, which are necessary for biological safety and cross-contamination minimization. The first is a cartridge patterned with wax to create a hydrophobic geometry to constrain the drops. The substrate used for the cartridge is a 2” x 3” glass-slide, and the wax is a paraffin-based wax (Sasol Wax, Hayward, CA). To pattern the wax on the slide, a stencil was made from silicone rubber (#31938707, MSC Industrial Supply Co., Melville, NY). The stencil consists of a 4 x 4 array of 6 mm diameter holes separated by 19 mm and 12 mm in the length and width directions, respectively. This stencil is preheated on a hot plate at 105°C and melted wax is spread over the stencil with a transfer pipette. Next, a clean glass-slide is placed on the stencil and allowed to sit until the wax covered the entire interface between the stencil and the glass-slide. The stencil and glass-slide are removed from the hot plate and allowed to cool at room temperature, at which point the silicone stencil is removed from the glass-slide, exposing a hydrophobic region surrounding hydrophilic regions designed to hold 40 µL. The second disposable is a strip of parafilm (#P7793, Sigma Aldrich, St. Louis, MO) which serves as a hydrophobic barrier separating the droplet from the lid. The parafilm was held in place with Scotch tape (504662, Staples Inc., Framingham, MA) and changed between every operation. A step-by-step description of the process is illustrated in the Appendix **(Fig D.2).**

9.2.4 Carryover study.

To assess the amount of fluid carryover in the SLIDE device, an acridine orange solution was made at a concentration of 0.5 mg/mL in stock solutions of 0%, 0.1%, and 1% Triton X-100 in DI water. For each experiment, 2 µL of Magnesil PMPs (#MD1471, Promega, Madison, WI) were added to each input solution of 40µL. Droplets of de-ionized water were used as the output drop. To evaluate the amount of carryover, an acridine orange dilution curve was created, and a linear fit was used to calculate the percent carryover based on the arbitrary intensity units measured using a Qubit Fluorometer with an excitation wavelength of 430-495 nm (#Q32866, Life Technologies, Grand Island, NY).

9.2.5 Protein readouts.

To evaluate the utility of the SLIDE for protein purification, green fluorescent protein (GFP) was purified from a mixture of *E.* coli expressing both GFP and red fluorescent protein (RFP). Specifically, a solution containing 12.5 mg/ml of Protein G-conjugated PMPs (Dynabeads Protein G, Invitrogen) and 0.031 mg/ml anti-GFP antibody in PBS supplemented with 0.01% Tween 20, was prepared and incubated for 30 minutes at room temperature to allow antibody attachment to the PMPs. Following washing with PBS supplemented with 0.01% Tween 20, the antibody-labeled PMPs were re-suspended in PBS (15 mg/ml PMP concentration) and 2% (by volume) E. coli bacterial lysate was added. At this dilution, the concentrations of the GFP and RFP were approximately 12 mg/ml and 240 mg/ml, respectively. After incubating the GFP and RFP lysate with antibody-PMPs on a shaker for 10-minutes at room temperature, 50 µL of this solution was purified using SLIDE as previously described. The green and red fluorescence of the output drops (and the input drops) were measured with a fluorescent scanner (Typhoon Trio, GE Healthcare) to determine recovery and specificity, respectively. Samples were also run on an SDS-PAGE gel (NuPAGE 4-12% Bis-Tris Gel, Invitrogen) and silver stained (SilverQuest Silver Staining Kit, Invitrogen) to determine if GFP was effectively separated from the bulk of the non-fluorescent bacterial proteins.

9.2.6 DNA readouts.

Samples to measure DNA extraction were prepared by lysing LNCaP cells in Buffer RLT (Qiagen) for 5 minutes at room temperature with 2 µL of MagneSil PMPs (Promega). Lysates were prepared at concentrations of 1,000 and 10,000 cells per 50 µL device input volume. Lysates were loaded onto SLIDE and processed as previously described in the manuscript. DNA was eluted from the PMPs in nuclease free water. As a comparison, other aliquots of this sample were purified using a conventional technique, where PMPs are captured against the side of a 1.5 mL microcentrifuge tube, the supernatant is removed, and the PMPs are re-suspended in buffer (Promega Wizard Kit Wash Buffer). In the comparison samples, this wash process was repeated four times. Extracted DNA was amplified and

quantified using qPCR on a LightCycler 480 (Roche) thermal cycler. Isolated DNA was mixed with 2X Taqman Gene Expression Master Mix (Life Technologies) and a commercially available assay for GAPDH genomic DNA (Life Technologies, Cat. # 4331182). The thermal cycler ran 40 cycles of 60° C for 1 minute and 95° C for 15 seconds and threshold cycles (C_T) were calculated by the LightCycler software using the 2nd derivative algorithm.

9.2.7 RNA readouts.

Samples to measure viral RNA extraction were prepared by spiking HIV viral-like (VLPs; viral envelope removed to render particles non-infectious; generous gift of Dr. Nathan Scherer) into fetal bovine serum (Gibco). Samples were lysed for 5 minutes at room temperature in Buffer MFL (Qiagen) in the presence of 2 µL of MagAttract PMP solution (Qiagen). Samples were prepared at VLP concentrations of 100 and 10,000 copies per SLIDE input volume. Samples were purified using SLIDE as previously described and viral RNA was eluted into Buffer MFE (Qiagen). Reverse transcription was performed in a Techne TC-412 thermal cycler at 37° C for one hour followed by 85° C for five minutes. The resulting cDNA was mixed with qPCR master mix (Taqman Gene Expression Master Mix, Life Technologies) and primers and probe specific to the LTR region of HIV (forward primer: 5'-GCCTCAATAAAGCTTGCC-3'; reverse primer: 5'-GGCGCCACTGCTAGAGATTTT-3'; probe: 5'-AAGTAGTGTGTGCCC-3'; taken from Veronique *et al*. and synthesized by Life Technologies[176]). qPCR thermal cycling and analysis was performed as previously described for the DNA samples.

9.3 Results and Discussion

9.3.1 Drops rolling on the surface of the SLIDE.

When a drop of fluid moves along an inclined hydrophobic surface, it rolls on that surface, leaving behind little to no residue[239-242]. The flow profiles within the drop reflect a fluid recirculation in drops that are rolling down an inclined hydrophobic surface[243] The interaction of the pinned fluid drop within the SLIDE on the top hydrophobic surface is similar to these cases of a drop rolling on inclined surfaces. The recirculation effect of a rolling drop was experimentally validated in the case of the SLIDE **(Fig. 9.3A)**,

demonstrating similarities in the two fluid systems. Because the fluid is rolling and not sliding down the surface, an important implication is the active detachment of the fluid from the receding edge of the fluid drop that is caused by the surface tension of the fluid pulling away from the surface. This detachment ensures that there is a low amount of residual fluid left on the surface to contaminate the subsequent elution drop. However, as a surface is separated from being in contact with a drop there will be residual fluid left on the surface, or "carryover" from the fluid drop. This concept of "carryover" is very important for the operation of sample preparation devices, as there can be many contaminants in an input sample that could interfere with downstream molecular analyses, and thus represents a critical area of study with the SLIDE device. Because of the similarities of fluid motion in the SLIDE to a drop on an inclined surface, existing literature can be leveraged to better understand characteristics of the top surface that will result in lower carryover.

9.3.2 Surface properties and the effect on carryover.

Surfaces can play a large role in the amount of carryover. Hydrophilic upper surfaces will cause most biologically relevant fluids to 'streak' along the top surface, resulting in high amounts of carryover. Hydrophobic surfaces minimize the interaction of the sample fluids to the surface, and as such were exclusively explored for use with the SLIDE as the lid material. There are three classifications of hydrophobic surfaces that relate the "stickiness" of that surface to a fluid: Cassie, Wenzel, and smooth surfaces[241] **(Fig. 9.3B)**. In the example of a Cassie surface (a super hydrophobic surface), micro and nano features are used to create a thin layer of air below the sample drop. While the hydrophobicity would be beneficial and potentially provide lower carryover, PMPs drawn by the magnetic force would be pulled into these spaces and get stuck, making deposition into the subsequent drop challenging. Similar to a Cassie surface, the Wenzel surface relies on micro- and nano features to improve surface hydrophobicity, but unlike the Cassie surface, there is no layer of air, and the fluid contacts the surface directly. Though Wenzel surfaces can have a higher contact angle than smooth hydrophobic surfaces, the 'stickiness' of Wenzel surfaces results in more fluid and contaminants left behind, as this roughened surface will carry

more input fluid into the output fluid. This was experimentally validated by observing the carryover resulting from a hydrophilic top surface (cellulose acetate), a hydrophobic top surface (paraffin) and a Wenzel hydrophobic top surface (roughened paraffin). The smoother hydrophobic top surface was demonstrated to have the lowest carryover **(Fig. 9.3C)**.

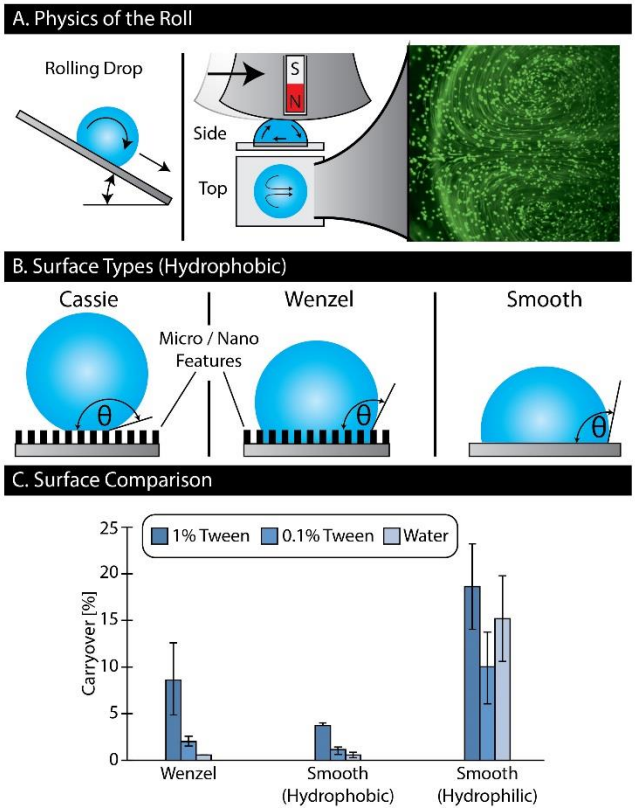

Fig. 9.3 Churning effect of the fluid droplet. A) Drop rolling on an inclined surface is similar to that found in the SLIDE (right). SLIDE image taken by suspending 1µm FITC microspheres into the fluid drop and opening exposure on the microscope for one second to show fluid motion. B). Three types of hydrophobic surfaces shown. The Cassie surface has features in close enough proximity to prohibit wetting between the features, whereas the Wenzel surface has features far enough apart to permit wetting between. The smooth surface does not have these features. C) The Wenzel and smooth surfaces were characterized using water and solutions of tween in PBS. Both hydrophilic and hydrophobic smooth surface were tested for comparison.

9.3.3 Fluid properties and the effect on carryover.

While the composition of lid surface has significant impact on sample carryover, the physical shape of the lid was demonstrated to be important. In order to create a device with simple user operation (similar to a credit card imprinter), the SLIDE was designed with a lid that the user could move across the sample in a single motion to perform all purification steps and have immediate access to the purified analyte. This operation requires the lid to contact a fluid drop, and then be removed from that fluid drop.

However, when the edge of a lid passes over a fluid drop, contact is severed between the fluid and the lid. This breakup event often results in the deposition of a residual "satellite" droplet on the surface of the lid **(Fig. 9.4A)**. During SLIDE operation, this satellite droplet is composed of original sample material, and can result in excess carryover. The influence of fluid properties was tested to evaluate the impact on the amount of material carried within this satellite droplet. Fluid viscosity did not seem to impact the amount of carryover to a viscosity of approximately 10 cP. Fluid viscosity of less than 10 cP did not seem to impact the size of the satellite droplet. However, fluid viscosities in excess of 10 cP yielded a high Stokes' drag, preventing the PMPs from moving towards the magnet **(Fig. D.3)**. In these cases the drop acted as a ferrofluid and followed the magnet out of the hydrophilic pinning region. Surface tension was found to affect the size of the satellite drop, as increasing the amounts of Triton-X 100 in the solution resulted in increased contaminant carryover **(Fig. 9.4A).**

9.3.4 SLIDE design to mitigate carryover.

In order to mitigate the effect of satellite droplets, a curved lid was designed to promote controlled and reproducible drop, while maintaining operational simplicity. When using a flat lid, the drop dissociates at the edge quickly, yielding a large and variable satellite droplet. The curved lid reduces the size of the satellite droplet by gradually removing the top surface from the fluid drop, while maintaining the one-direction swipe operation of the device. However, due to the nature of fluid separation from a surface, a small droplet (~0.1 μL) is still left behind, the size of which will differ with various fluids and operating parameters. In most conditions tested, the amount of carryover from the input drop to the output drop using a Parafilm surface was below 2%. When there is a concentration step (e.g., the output drop is smaller than the input droplet), however, this percentage could be higher. There are many solutions that might be implemented to mitigate this carryover. Three methods for decreasing carryover were evaluated for their efficacy and operational simplicity: 1) wash drops were placed between the input and output drop **(Fig. 9.4B)**, 2) the center of the input drop could be offset from the magnet and output drop **(Fig. 9.4C)**,

and 3) a two-way operation of the lid where the PMPs are taken to the output drop, then the lid is pulled backwards before the satellite droplet can contact the output drop **(Fig. 9.4D)**.

Wash drops: Drops of fluid placed between the input and output drops that come in contact with the SLIDE lid surface allow contaminants to reconstitute into the intermediate buffers instead of into the output drop. Assuming that the main source of contamination in the SLIDE is due to the carryover instead of interstitial space of the collected PMPs[6], the PMPs do not need to be mixed into each of the wash steps to effectively remove the source of contamination. To test this method of purification, three sets of devices were tested: 1) no wash drop, 2) one wash drop, and 3) two wash drops. Each wash was seen to produce a 2-fold removal of background contaminant, with the contamination in the two-wash device in all cases to be below 0.6% **(Fig. 9.4B)**.

Offset drops: As the lid is removed from the drop, the highest point of the drop is naturally above the geometric center of the pinning region. This represents the point at which the drop will detach and form a satellite drop on the upper surface. Because the drops used were semispherical in shape and the magnet is above the center of the drop, the satellite droplet and PMP pellet are both aligned with the apex of the drop. However, by offsetting the input drop relative to the magnet or by changing the geometry of the input drop, the apex can be guided away from the PMP pellet as the lid is moved out of the input drop. By separating the apex from the PMP pellet, the satellite droplet is no longer collinear with the output drop and the PMP pellet. As a result of this simple geometrical change, the satellite drop avoids the output drop, preventing contact and thus carryover of input fluid via this satellite droplet **(Fig. 9.4C)**. When this hypothesis was tested, it resulted in carryover below 0.6% **(Fig. 9.4C)**.

Two-way operation: The SLIDE is designed to work akin to a credit card imprinter, in that one swipe produces purified, isolated samples. However, to avoid introducing the carryover drop to the elution drop, a two-way operation was introduced to only allow the PMPs to drop into the elution, and pull the lid back towards the input drop prior to introducing the satellite droplet to the output. The observed carryover with this method was below 0.6% **(Fig. 9.4D)**.

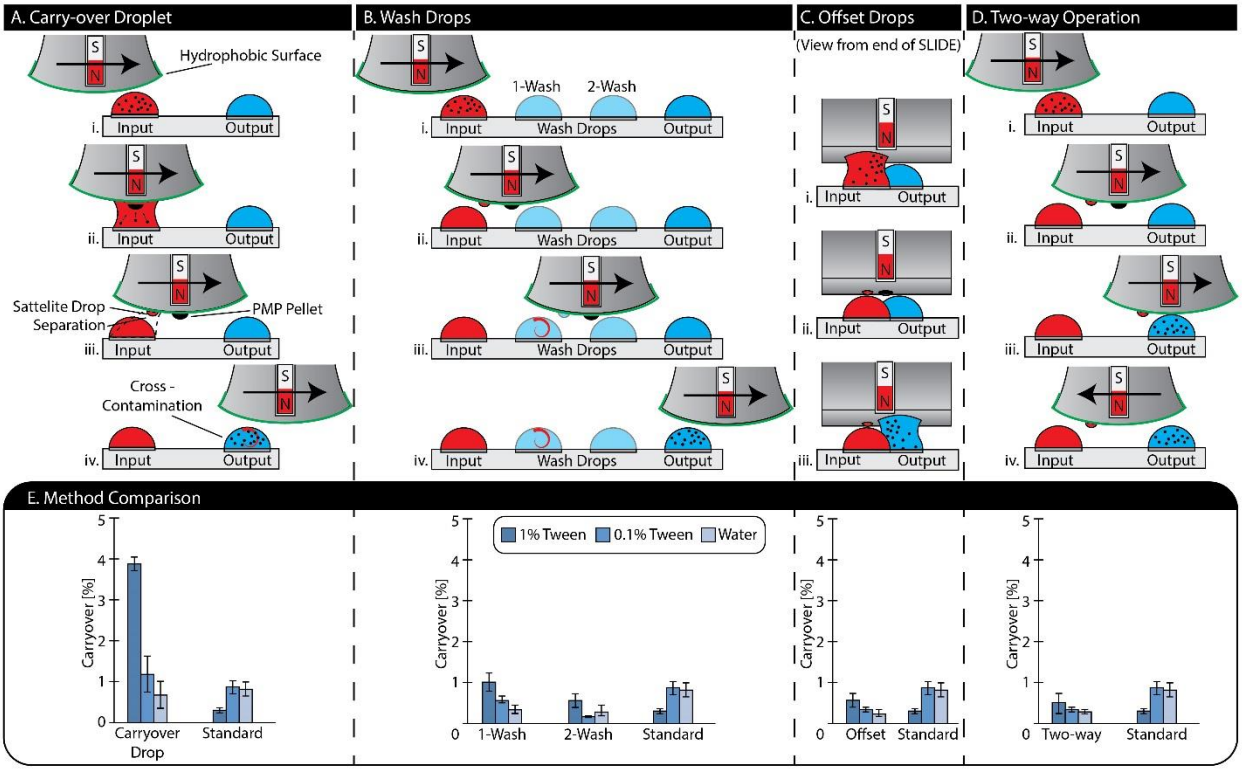

Fig. 9.4 The generation and mitigation of carryover. A) A schematic demonstrates how a carryover droplet is created as the handle is removed from a drop. B) Using wash drops can reduce the effect of carryover by rinsing and diluting. The wash method reduces the amount of carryover proportionally to the number of wash steps. D) Two-way operation can be used to prevent carryover from ever contacting the output drop by moving the top surface backwards before the carryover drop makes contact. C) Offset drops are able to create a PMP pellet that is not in line with the carryover drop, thus allowing PMPs to be transferred without the carryover drop. E) Each method was characterized and compared to a standard macro-scale technique. The data for each method is demonstrated below its respective method. In each case, error bars represent standard deviation of the mean (n=4).

9.3.5 Applications of the SLIDE isolation technique.

To demonstrate the utility of the SLIDE to isolate a variety of analytes, cell, protein, and DNA capture were performed in the SLIDE device. A specific cell type was isolated with high specificity **(>90%, Fig. 9.5A)** from a heterogeneous mixture of multiple cells (similar to the buffy-coat layer after a Ficoll-Paque density centrifugation of blood samples). Leveraging the in-drop mixing that occurs during the operation of the SLIDE, a simplified staining protocol was performed. Cells remained on the lid during staining, and were transferred into a PBS containing output drop for imaging. In 40 minutes and within a single linear operational path, cells were bound to PMPs, isolated from background cells, stained, and placed into a drop for imaging **(Fig. 9.5B)**. To demonstrate the purity and specificity of analyte isolation from complex samples using the SLIDE, we evaluated the ability to isolate GFP from a complex

cell lysate containing GFP, RFP, and cellular proteins. Without performing any purification steps, we demonstrated highly specific capture of GFP, illustrating the low background carryover with a silver stained gel **(Fig. 9.5D)**. This specificity was demonstrated to be greater than 99% of the amount of RFP based on band intensity analysis of the silver stain gel **(Fig. 9.5D)**. Based on the results of the carryover quantification, we decided to modify our nucleic acid protocols to include a wash volume between the sample and elution buffers. Specifically, Wizard Wash Buffer (Promega) was used for the DNA samples and Buffer MFW2 (Qiagen) was used for the viral RNA samples. qPCR of the DNA indicated that there is no significant difference in C_T values between sample purified with SLIDE and those purified with conventional washing methods **(Fig. 9.5C)**. Furthermore, the isolation of viral RNA using SLIDE demonstrated the high precision of this method, including SLIDE's ability to handle samples with low numbers of analyte copies **(~100, Fig. 9.5E)**. Taken together, these data demonstrate that SLIDE is a viable alternative as a sample preparation process for isolating nucleic acids.

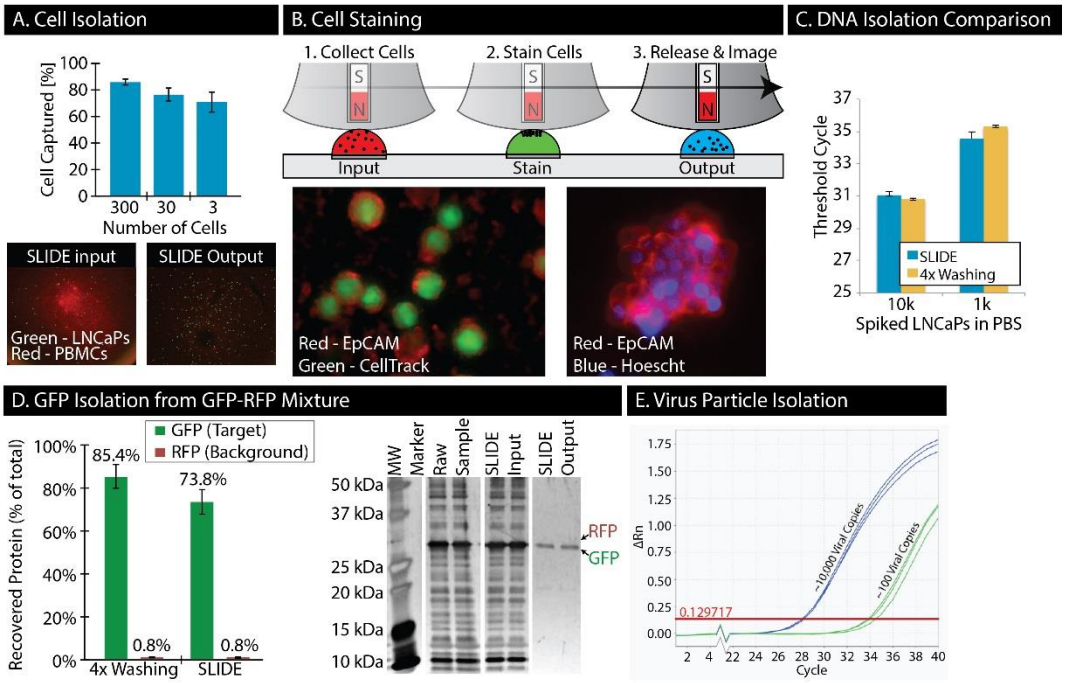

Fig. 9.5 Applications of the SLIDE. A) The SLIDE can be used for cell capture from a background of 5 million fixed peripheral blood mononuclear cells with an efficiency of >70% for each of three cellular densities (300, 30, and 3 cells, n=3 per experiment). B) Cell staining using SLIDE involves loading the samples, moving the lid from being positioned over the input drop to collect sample, to over a staining drop to perform cell staining methods, to a final release well to image the cells. C) DNA isolation using SLIDE shows comparable DNA extraction from lysed LNCaPs to standard washing methods. D) Low carryover of the SLIDE demonstrated with GFP isolation from complex GFP-

RFP expressing E. Coli bacterial lysates, with an efficiency of >70% and a specificity of GFP capture of >99% compared to RFP non-specific carryover (n=3, left). Silver stained gels demonstrate the purity of the sample from background proteins (right). E) HIV Virus-like particle isolation demonstrated in the SLIDE from lysed human plasma spiked samples.

9.4 Conclusions

We have presented a sample preparation method that leverages moving the substrate instead of the fluid containing sample. Importantly, this eliminates the need for dilutive and/or washing steps during which analyte can be lost, the need for immiscible fluids, or complicated manifolds for collecting and purifying analyte from a complex sample. The SLIDE is enabling for the simplicity and inherent usability of the device - operation of the SLIDE is similar to a credit card imprinter, and needs few parts to operate. During initial characterization experiments, a mode of device failure was found when using low surface tension samples, resulting in non-specific carryover of sample into the elution buffer. It was demonstrated that this carryover was a result of droplets created from the fluid detaching from the SLIDE lid. Three strategies to mitigate the effect of this satellite droplet were evaluated, including 1) adding non-dilutive wash drops between the input and output drops, 2) changing operation to a two-step motion, and 3) offsetting the input drop from the output drop. Without contamination mitigation strategies, approximately 2% of the sample was carried over into the output drop. While this may be adequate for certain downstream analysis techniques, a carryover of approximately 0.6% was achieved when using any of the three strategies, putting SLIDE performance on par or better than existing commercial purification protocols. Further, the simple workflow can be translated to cell capture and staining protocols to streamline these processes, saving time and reagents. The SLIDE is an enabling method, as the fundamental operational principles will translate to simple embodiments that can be employed for the isolation of any analyte with high purity.

Chapter 10 Automated Exclusion-based Sample Preparation Platform for Rare Cell Isolation[9]

10.1 Introduction

Emerging discoveries have begun to highlight the biological significance of rare, discrete cell populations masked within large, diverse bodies of cells. The bloodstream provides one such highly populous, complex backdrop from which to capture events. In the bloodstream, rare cells (e.g., minority 'stem' populations, circulating fetal cells, and circulating tumor cells) circulate amongst billions of background cells.[244, 245] If interrogated, each of these rare cells has the potential to provide invaluable biomarkers and clinical information to enhance patient care.[246-248] However, to access their information, rare populations must first be isolated – requiring the identification of differentiating characteristics to discern between rare target cells and the vast background populations in which they reside.

Dominating the growing field of cell isolation, antibody-based approaches utilize one of two methodologies, positive or negative selection. Positive selection, or antigen-dependent capture, yields a captured population based on a specific cellular marker (antigen, glycoprotein, etc); while precise, positive selection requires the marker to be specific to the target population and known *a priori*. As such, positive selection becomes limiting if distinguishing markers are unknown or non-differential (i.e., shared by neighboring cell populations), even at differing expression levels. Alternatively in antibody-based approaches, negative selection leverages known non-target markers to deplete background populations. In this approach, the target cells remain uncaptured, enabling a true "discovery" approach to isolation. Despite these advantages, negative selection typically results in incomplete background removal, yielding

9 This chapter has been adapted from the following manuscript in preparation: "Automated Exclusion-based Sample Preparation Platform for Rare Cell Isolation" Hannah M. Pezzi*, David J. Guckenberger*, Jennifer Scherer, Scott M. Berry, Jacob Rothbauer, Sacha Horn, Jamie Sperger, Josh Lang, and David J. Beebe

* Authors contributed equally

relatively low purity.[249] Largely, platforms have been forced into a trade-off between "richness" of data (e.g., number of endpoints), specificity (higher with positive selection), and sensitivity (higher with negative selection).

Limitations in existing positive and negative selection technologies have recently come to light: a result of the more stringent requirements needed for rare cell isolation, such as those required for isolating circulating tumor cells (CTC). CTCs are cancer cells, which separate from the primary tumor or metastatic site and enter the bloodstream. The cancerous origin of CTCs from an initial tumor paired with their easy, minimally invasive accessibility through a blood draw make CTCs uniquely poised to monitor cancer progression. However, the rarity of CTCs (1 in 1-10 million PBMCs) paired with their circulation amongst the diverse populations of the bloodstream make CTCs a challenging target to both capture and purely isolate - requirements, which must be met to enable the next generation of CTC studies. Both between and within cancers, heterogeneity including: antigen expression levels, different antigen profiles (e.g., EpCAM-positive CTCs[250, 251], CTCs undergoing EMT [252-255], cancer stem cells) , unknown markers, and varied background populations[256, 257] has presented new problems that prevent adoption of methods capable of only positive or negative selection. The presence of heterogeneity requires technologies to be adaptable - not limited to a single, specific marker – and maintain the capability of discovery-based negative selection for CTCs for which traditional capture markers, such as EpCAM have remained ineffective [253, 258]. Recently, the CTC-iChip introduced the capability to switch between positive selection and negative depletion allowing users to benefit from both techniques independently; yet, the iChip was unable to provide users with the ability to integrate both technologies into a single sample. Existing technologies in the CTC field require users to decide between positive or negative selection, unable to integrate both approaches on the same sample, thereby limiting their potential.

Multiple cell isolation technologies used in initial prostate cancer and breast cancer CTC studies demonstrated the prognostic value of CTC enumeration (based on EpCAM-captured CTCs) in predicting treatment response. While enumeration has proven powerful, further interrogation beyond enumeration

will be required to elucidate the full potential of CTCs. However, in moving beyond enumeration, captured populations will need to meet a new level of purity in order to facilitate integration with downstream molecular analyses (RT-PCR, Whole genome amplification (WGA), sequencing, etc.) to ensure the target signal is not lost in the background populations. As is, existing positive and negative selection platforms alone will not be adequate to meet the next generation of CTC purity benchmarks.

Building on a suite of exclusion-based sample preparation (ESP) technologies [259-262], we have developed an automated cell isolation platform termed the multiplexed platform for automated extraction (mTAE) to enable users to perform both positive and negative selection on a single sample in any order. PMP-bound cells are removed from the high- background sample population using the Sliding Lid for Immobilized Droplet Extraction (SLIDE) technology – a low shear method for achieving high purity extraction of PMP-bound analytes. PMPs and bound cells are pulled to the top of sample wells and collected on a hydrophobic surface for removal. Due to the limited interaction of the surface and sample, SLIDE leaves the sample readily available for re-interrogation. By limiting sample disturbance, the platform enables users to easily chain together positive and negative selection to achieve both high purity and specificity. Once extracted, PMP-bound cells can then be deposited into wash wells to improve purity, staining wells for cell identification, or wells for ESP-based nucleic acid extractions. Integrated staining and nucleic acid extraction capabilities will facilitate downstream analytical pipelines (cell identification/enumeration, qRT-PCR, sequencing, WGA). By allowing the user to freely perform selections and depletions in series, populations can be fully interrogated, no longer limited to a one-selection methodology.

10.2 Materials and Methods

10.2.1 Automated ESP Platform Overview

Cells and nucleic acids were isolated on a PIPETMAX automated liquid handler (Gilson Inc.) by integrating exclusion-based sample preparation (ESP) technologies: SLIDE[259] and the magnet box [263]. SLIDE - the sliding lid for immobilized droplet extraction - is a technique for isolating and purifying

magnetic bead-bound analytes. SLIDE leverages convex droplets in wells and a head containing magnets which is used to transfer samples between wells. The SLIDE technology has been integrated into Gilson's EXTRACTMAN technology, thus we used EXTRACTMAN extraction plates (#22100008, Gison) and bead capture strips (#22100007, Gilson) to achieve these isolations. The magnetic box is a magnetic technology that operates in unison with the magnetic head and leverages magnet proximity to manipulate the magnetic beads; the box allows beads to move up to the head (capture) or into the well (release) depending on relative distances between the magnets. Magnetic-bead-bound analytes are captured from a sample well and carried to, released in, mixed, and recaptured in a series of sample wells, then released in an output well for image analysis. All cell fixation, permeabilization, and staining (both intra- and extracellular) is performed in the wash wells. For protocols including RNA or DNA extraction, the bead-bound analytes are then carried to a separate plate, lysed, washed, and eluted.

10.2.2 Cell Culture

All cell lines used for characterization of the automated platform (LNCaPs, HCC2218, PC3-MM2) were cultured in RPMI media (#11875-093, Thermo Fisher Scientific) supplemented with 10% Fetal Bovine Serum (FBS) and 1% Penicillin Streptomycin. Cells were maintained under sterile conditions at 37° C in the presence of 5% CO_2. For characterization experiment, cells were counted via hemocytometer. For easy identification and characterization, cells were stained prior to use as described in the following sections.

10.2.3 Blood Processing and PBMC Isolation

Venipuncture collected whole blood was processed via Ficoll Paque PLUS (GE Healthcare) density centrifugation. For characterization of the platform, pints of whole blood treated with K2 EDTA were purchased from Biological Specialty Corporation. The blood was drawn from healthy donors, received within 24 hours of the blood draw, and processed the same day it was received. Cancer patient samples were collected from patients who had a signed informed consent document under a University of Wisconsin-Madison IRB approved protocol. The blood was collected in EDTA tubes, and processed

within 5 hours of collection. Briefly, whole blood was mixed 1:1 with 1x PBS, supplemented with 2 mM EDTA. 35 mL of diluted whole blood was overlaid on 15 mL of Ficoll. The tubes were centrifuged according to the manufacturer's instructions and the buffy coat diluted in 35 mL of wash buffer (1x PBS, supplemented with 2mM EDTA PBS, 0.1% BSA, 2.5% FBS). The cells were pelleted at 200 x g for 10 minutes and the supernatant decanted. The wash was repeated, after which the cells were resuspended in 400 ⌈L of wash buffer and counted by hemocytometer.

10.2.4 PMP Conjugation and Binding

For positive selection via EpCAM (used in platform characterization and patient samples), the M270 bead coupling kit (#14311D, Thermo Fisher Scientific) was used to conjugate anti-EpCAM antibody (clone VU-1D9, #ab98003, Abcam) to PMPs at a concentration of 2 ⌈g Ab/mg PMP. The final stock concentration of the beads was 10 μg PMP / μL and 25 μL of PMPs were used in each sample. Prior to use, however, the desired volume of PMPs was placed in a tube and washed by collecting the beads to the side of the tube, removing the supernatant, and resuspending in double the volume of PBS supplemented with 0.1% Tween 20 (PBST). After recollecting the beads again and removing the PBST, the beads were either resuspended in wash buffer or blocked with FBS for 30 minutes on ice (blocking reduces non-specific binding of cells to the beads). Ultimately, the beads were resuspended in wash buffer until ready for use. For experiments involving negative selection or depletion of PBMCs, M270 PMPs were coupled with antibodies against CD45 (clone HI30, #304002, Biolegend), CD14 (clone M5E2, #301802, Biolegend), CD34 (clone 581, #343502, Biolegend), and CD11b (clone M1/70, #101202, Biolegend). The antibodies were coupled using manufacturer protocols at a concentration of 10 μgAb/ mg PMP. For both positive and negative selection, the sample (~450 μL) was placed in the input well and 25 μL of beads was spiked into the sample (total of ~475 μL/sample). The samples/beads were bound on ice for 30 minutes, with mixing of the well at minute 5, 15, and 25 minutes.

10.2.5 Characterization of the Automated Platform

In order to validate the platform and select ideal operating conditions for positive selection from liquid biopsies we assess the impact that mixing rate, cell populations, and cell phenotypes have on cell loss, cell purity, and capture efficiency. Because CTCs are known to have variable EpCAM expression, the platform was characterized with three cell lines with different expression levels of EpCAM: LNCaPs, HCC-2218, and a MM2 clone of the PC3 cell line. These target cells were placed into a background of PBMCs, creating a pseudo-sample. To differentiate between target and non-target cells the two were prestained with Cell Tracker Red and Calcein AM (Life Technologies) (for 30 min and 20 min, respectively). After staining, the cells were washed according to the manufacturer's protocol before being resuspended at the desired density in complete media. Cell counts are are based on counts from a hemocytometer and serial dilutions, thus cell counts presented in this paper are approximate. Nevertheless, all technical replicates were taken from a larger master sample, thus cell counts in the technical replicates should be consistent. The pseudo-samples were mixed with PMPs – preconjugated with anti-EpCAM antibody, allowed to bind for 30 min on ice, and then transferred to the mTAE,

To evaluate the cell loss as a result pipette mixing, pseudo-samples consisted of XXX target-cells in a background of 1 million non-target PBMCs (from a healthy individual). The beads were first collected from a sample well and transferred to a small wash well, leaving behind unbound target and non-target cells. Without mixing, the beads were recollected and transferred to a second wash well, ridding any non-bound cells that were non-specifically carried with the beads (i.e. interstitial space). In the second wash well, the beads were mixed for four (aspirate/dispense) cycles at flow rates ranging 1 – 20 mL/min, with a no mixing best case scenario (0 mL/min). After mixing, the PMPs were transferred from the second wash well to the output well, leaving behind cells that detached from the beads as a result of the mixing. Loss of target cells was quantified by collecting the contents of each well and counting the number cells. Similarly, the loss of non-target cells, as a result of shear, was quantified by counting the

number of PMBCs present in each well. A mixing flow rate of 5 mL/min was utilized for all subsequent experiments.

To assess how the quantity of target cells impacts purity and capture efficiency, pseudo-samples consisted of roughly 10, 100, 1000 target cells in a constant background of 10 million PBMCs. Beads were collected from the sample well, washed in three wash wells, the released in the output well. Conversely, to assess how the quantity of non-target/background cells effect purity and capture efficiency, the amount of non-target cells was varied from 0 to 20 million cells while the number of target cells was held constant at 1000 cells. In both cases, percent capture represents the number of target cells in the output well divided by the total cells spiked into the sample. The purity is the number of target cells captured divided by the number of non-target cells in the output well.

10.2.6 Patient Sample Cell Staining

For positive selection via EpCAM-based capture, a staining panel was performed to identify captured cells. For patient samples, staining was performed in a sieve device as described by Zasadil et al. and Casavant et al [262, 264]. First, the cells were fixed at room temperature in 4% PFA (diluted in PBS) for 15 minutes. The cells were then washed once in wash buffer and resuspended in 100 µL of extracellular staining buffer and stained on ice for 30 minutes. The extracellular staining buffer consists of wash buffer containing: anti-EpCAM-PE (#ab112068, Abcam) and anti-CD45 (#304002, Biolegend), anti-CD14 (#301802, Biolegend), anti-CD11b (#101202, Biolegend), and/or anti-CD34 (#343502, Biolegend), all diluted at 1:100. Antibodies against CD45 (PBMC marker), CD14 (monocyte marker), CD11b (NK, monocyte, neutrophil marker), and CD34 (endothelial marker) were conjugated to Alexa Fluor 647 (#A-20186, Thermo Fisher Scientific) and comprise what is herein referred to as the dump channel. After the extracellular staining, the cells were washed in 200 µL of wash buffer and then permeabilized for 30 minutes at room temperature using PBS supplemented with 1% Tween20 and 0.05% Saponin. The permeabilization buffer was removed and 100 µL of an intracellular staining buffer was added, containing: the nuclear stain Hoechst (diluted 1:250) and a

pan-cytokeratin antibody (FITC) (clone C-11, #ab78478, Abcam) (diluted 1:100) for two hours. The cells were washed 3x and then transferred to a well for imaging.

10.2.7 Imaging and Image Analysis

All imaging was done on a Nikon TI Eclipse inverted microscope. For characterization of the automated platform, the cells were transferred to a 96-well plate, allowed 30 minutes to settle to the bottom of the well, then imaged with a 10x apo objective. All patient sample depletions were imaged in a 96-well plate at 10x, but the captured portion of the sample (either positively or negatively selected) was imaged in the sieve device using either a 20x or 40x apo objective. Enumeration of the cells for platform characterization was accomplished using the "Find Maxima" function in ImageJ. For patient samples, however, an ImageJ macro was developed that first identified the location of cells based on positive nuclear staining then measured the mean fluorescence intensity of each marker (dump channel, nuclear, cytokeratin, and EpCAM). Each identified cell was plotted based on dump channel intensity and cytokeratin intensity, then, using the entire population, thresholods were created to differentiate between negative and positive fluorescence intensity. CTC events were defined as cells that had a nucleus, and were for positive cytokeratin stain but absent of any contaminant population markers (CD45, CD14, CD34, CD11b). Due to patient-to-patient variability, thresholds were determined on a patient-to-patient basis using the entire population of cells. Each CTC event were then visually re-inspected to ensure that: (a) the event was indeed a cell (verified by bright field images) and (b) the event did not have any nearby staining artifacts that could artificially enhance the cytokeratin intensity. To test the specificity and sensitivity of both the platform and image analysis program, multiple healthy patients were analyzed, all of which did not identify any CTC events**.**

10.2.8 Nucleic Acid Extraction and Quantification

Both RNA and DNA extractions were integrated into mTAE and validated. To validate the DNA protocol samples of 10, 100, and 1000 LNCaPs were lysed on mTAE in RLT PLUS (Qiagen) along with Magnesil KF PMPs (Promega). The bound DNA was then subjected to three washes with mixing and

eluted in nuclease-free water. For comparison, DNA was extracted from identical samples using the same reagents in a manual tube-based approach as well as the commercial QIAamp DNA Mini spin columns (#51304, Qiagen). For elution, 15 µL was used across all platforms. Extracted DNA was quantified based on a housekeeping gene, GAPDH (#402869, Thermo Fisher Scientific) on a real-time thermal cycler (LightCycler 480 II, Roche). In brief, 2 µL of eluted DNA was mixed with 5 µL of Roche LightCycler480 Master Mix, 0.5 µL of mRNA specific primers to GAPDH (Taqman, FAM), and 2.5 µL of nuclease-free water. The mix was amplified for 45 cycles (95 °C for 15 seconds, 60 °C for 30 seconds). Cycle threshold values for each result were then calculated based on 2nd derivative function.

10.3 Results

10.3.1 Automated cell isolation platform design and optimization

mTAE was designed as a multiplexed, versatile rare-cell isolation platform enabling: positive and negative selection (both independently and combined), on-chip cell fixation and staining, and extraction of RNA or DNA from a single sample. mTAE builds upon a PIPETMAX automated liquid handler, leveraging the SLIDE technology described by Casavant et al.,[259] the magnetic system described by Guckenberger et al.,[263] and EXTRACTMAN (Gilson) consumables (i.e., strips and plates)(**Fig. 10.1**). Cells are isolated from a sample, in this case a buffy coat loaded into the input well, via: (i) a *positive selection* mode, whereby CTCs are identified and selected based on extracellular expression of EpCAM or Muc-1, and (ii) a *negative selection* mode, whereby cells (i.e., PBMCs) are selected for removal based on expression of CD45, CD14, CD11b, and CD34. The selection modes were performed both independently and in sequence. Magnetically bound cells are carried through a series of washes, wherein beads can be gently mixed via magnetic mixing or vigorously mixed via pipette mixing. We assessed the impacts of pipette mixing on the platform in terms of loss of both target cells **(Fig. 10.2A)** and non-target cells. After mixing bead-bound cells (HCC, PC3, and LNCaP) at various flow rates and assessing loss, a mixing rate of 5 mL/min was selected for all subsequent experiments **(Fig. 10.2A)**. Wash wells contained generic washing buffers, stains, permeabilization buffers, and fixation buffers as described in the methods section. For enumeration, cells could be imaged directly in the plate, via a glass-bottom well, or

transferred, via pipette, to a secondary imaging platform. Non-fixed cells, intended for NA extraction, were magnetically recaptured after imaging and brought to a subsequent well for lysis. mTAE was tested and characterized with commercially available beads and antibodies, enabling straightforward adaptation to new targets. The sample remains available for re-interrogation, despite repeated PMP additions and cell capture steps. As such, specific cellular populations can be serially isolated using any desired combination of positive and negative selection, which is later shown to improve isolation efficacy.

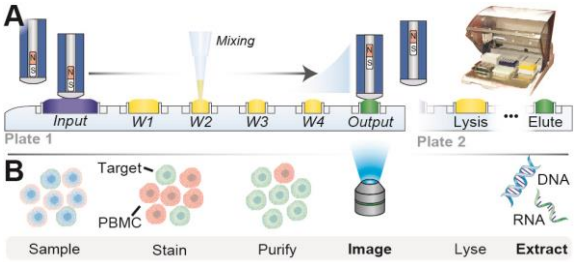

Fig. 10.1 mTAE system overview. (A) The cell extractions are performed on a Gilson PIPETMAX. The extraction plate contains six wells per sample with four samples per plate. The input is filled with sample and anti-target PMPs (buffy coat), the remaining wash wells (W1-W4) contain either wash buffer or stains. A second plate is added to the system if the user requires additional processing steps (i.e., fixation, permeabilization), RNA extraction, or DNA extraction. A magnetic head moves the bead-bound analyte between wells and adjacent plates. (B) Schematic overview of the process. Cells are stained and purified in the wash wells, then either transferred to an output well for imaging or transferred to a second plate for NA extraction.

10.3.2 Cell Capture Characterization and Validation with Contrived Samples

Contrived samples – EpCAM-positive cells lines spiked into a background of PBMCs isolated from a healthy donor – were used to evaluate capture efficacy and purity. Three EpCAM-positive cells lines were used as model target cells: two prostate cancer cell lines LNCaPs (high EpCAM expressing human prostate adenocarcinoma cell line) and PC3-MM2 (highly metastatic PC3 derivative) as well as HCC2218, a cell line isolated from a woman with a stage III primary ductal carcinoma. We first assessed capture efficacy (i.e., captured target cells/total number of target cells inputted) for the three separate EpCAM positive cell lines (LNCaPs, HCC2218, PC3-MM2) from a background of 10 million PBMCs **(Fig. 10.2B)**. Each cell line demonstrated repeatable capture efficacy, ranging from ~40% (HCCs) to >95% (LNCaPs). We also investigated inherent temporal variability in capture efficacy across experiments performed on different days **(Fig. 10.2C)**. To evaluate, cells were collected at three to five

time points over the course of 40 days and isolated to determine the capture efficacy recorded. In all cases capture efficacy temporally fluctuated but was generally within a 20% range, except HCCs which had a 40% range; although 80% of the samples fell with the 20% range seen with the LNCaPs and PC3s. Next, we varied the quantities of target cells in the contrived sample to assess how order of magnitude differences in target cells impact capture efficacy and purity **(Fig. 10.2D-E)**. The capture efficacy remained nearly constant (LNCaPs: <3% variation, HCCs: <5% variation), but the purity increased proportionally to the number of target cells. This increase in purity is an artifact of the higher numbers of target cells being captured, and suggests that the quantity of captured non-target cells is not proportional to the initial quantity of target cells. Next, to assess how background populations impact capture efficacy and purity we isolated target cells from contrived samples comprised of 1000 target cells and a range from 0 to 20 million non-target cells (PBMCs) **(Fig. 10.2F-G)**. The capture efficacy remained relatively unchanged across the conditions (no significant difference) for both LNCaPs and HCCs . The purity (i.e., the number of target cells captured/total number of cells captured), however, decreased as the background populations increased, suggesting that pre-isolation depletions may prove advantageous for applications requiring higher purity. Lastly, to validate that the cells remain intact and viable post-isolation, we cultured the cells (with beads) for 10 days or until confluency, whichever came first **(Fig. 10.2H-I and Fig. E.1a)**. The cells remained proliferative and viable over the 2 week culture. Together, these results validate this platform as a gentle, effective method of isolating rare cells from diverse background populations and begin to characterize the impact of captured contaminant populations.

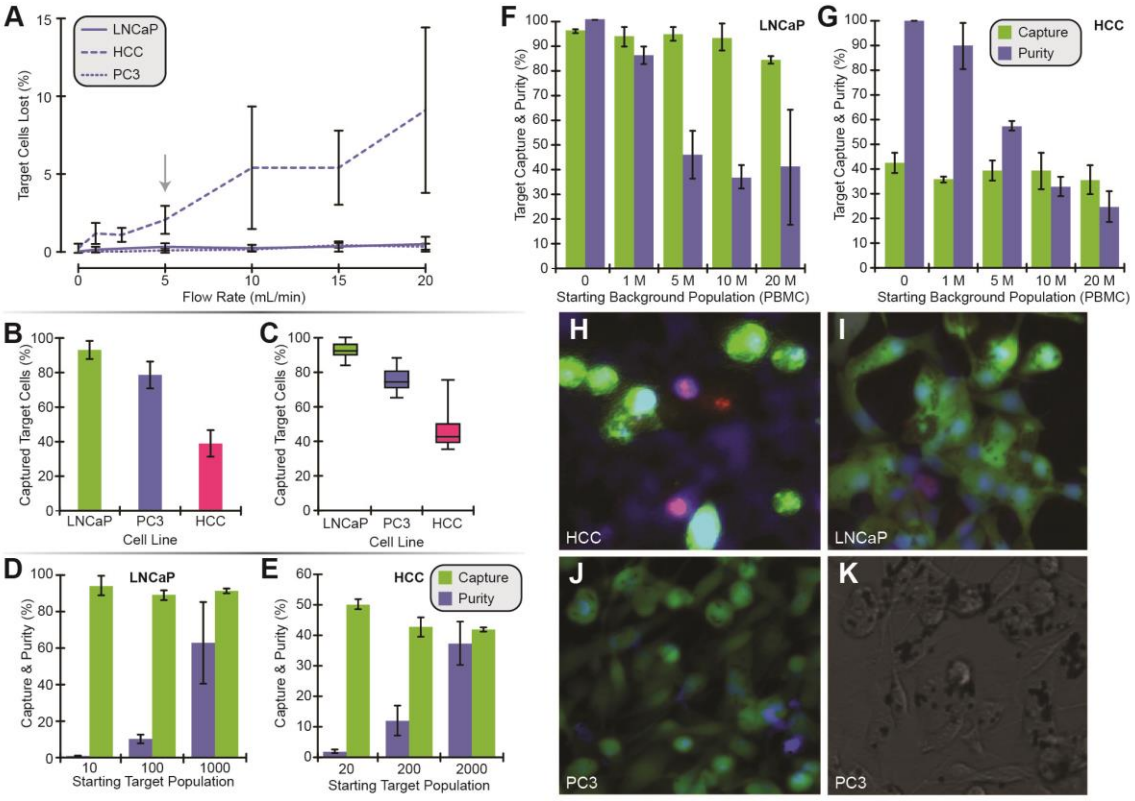

Fig. 10.2 Platform characterization and cell line validation. (A) Loss of target-cells as a result of pipette mixing with flow rates ranging from 0 and 20 mL min-1. A flow rate of 5 mL min-1 was used for all subsequent experiments as noted with the arrow. (B) Capture efficacy of 500 target cells spiked into a background of 10 million PBMCs. (C) Inherent variability in capture efficacy resulting from temporal differences between cell passages. Each bar represents capture efficacy taken at 3-5 time points over the course of 40 days with a no less than three replicates per time point. (D, E) Impact of target-cell quantity on purity and capture efficacy, for both LNCaPs (D) and HCCs (E). In both cell lines, specific quantities of target-cells were spiked into a constant background population of 10 million PBMCs. (F, G) Impact of background population on purity and capture efficacy, for both LNCaPs (F) and HCCs (G). For both cell lines, 500 target cells were spiked into specific background populations, ranging from 0 to 20 million PBMCs. Cell counts represented in figures D-G are estimates based off of hemocytometer counts. (H-J) Live dead assay of HCCs, LNCaPs, and PC3s following isolation from a background of 10 million PBMCs and a 2 week culture, with the beads (live: green, dead: red, nucleus: blue). (K) BF images of PC3s after a 2 week culture show the PMPs still attached to the cultured population.

10.3.3 Positive Selection: CTC purification from patient samples via EpCAM

Positive selection enables target cell isolation via known markers. In the field of CTCs, the extracellular marker EpCAM has been extensively utilized as a positive selection CTC target for both prostate and breast cancer [251]. In a subset of cancers, EpCAM has provided predictive insight into prognosis and overall survival [265, 266]. To evaluate positive selection on mTAE, we assessed EpCAM-based PMP isolation of CTCs from samples (i.e., buffy coats spun from 5-10 mL of whole blood) obtained from prostate cancer patients (n=16), breast cancer patients (n=8), and healthy patients (n=4).

Once captured from the sample, the cell-bound PMPs were washed in a series of one large and three small wells, containing: i) a nuclear stain and extracellular stains for EpCAM, CD45, CD34, and CD11b, ii) a fixative, iii) a permeabilization buffer, and iv) an anti-pan cytokeratin (pCK) intracellular stain. CTCs were identified as cells staining positive for pCK and a nucleus, but negative for all exclusionary markers (i.e., CD45, CD34, and CD11b). Exemplary images of CTCs and PBMCs from both breast and prostate cancer patients are shown in **Fig. 10.3A,B**. While most CTCs were found as individual cells, clumps of CTCS **(Fig. 10.3C)** were identified in a subset of patients, a phenomenon previously observed[42, 267]. Capture efficacy was reported by quantifying the captured, positively identified CTC events and dividing by volume of blood from which sample was isolated **(Fig. 10.3D)**. Variable CTC counts per milliliter of whole blood for both prostate and breast cancer patients were identifying ranging from 0 to ~13 CTCs per milliliter of whole blood. Patient-to-patient variability in CTC count is expected, as counts will vary based on a patient's treatment, disease progression, and treatment response. Importantly, no CTCs were identified in healthy patients (n = 4 patients), helping to validate the specificity of our CTC identification parameters and exclusionary markers. Upon collection of CTC counts, purity was also evaluated in addition to the relationship between purity and CTCs in each sample **(Fig. 10.3E,F)**. We observed variable purity ranging from <1 % to ~37%. Two prostate cancer samples had purity greater than 20%; this was largely the result of an atypically small contaminant population and a moderate number of CTCs. Across the entire sample set, purity generally increased as the density of CTCs increased, suggesting that the impact of CTC count has a greater impact on purity than the number of contaminant cells captured.

CTC counts can provide clinically relevant information, but purity (target cells : non-target cells) is often paramount for downstream analysis. In addition to capture of target events, purity requires the removal or reduction of contaminants. With positive selection, we observed ~4-5 $\log_{10}$ fold reduction in non-target/background cells, which was consistent across healthy, prostate cancer, and breast cancer patients **(Fig. 10.3G)**. Yet, samples demonstrated a wide range of carryover, contaminant -non-CTC

populations, ranging ~11 to >800 contaminant cells per milliliter of whole blood (average of ~110 contaminant cells per milliliter of whole blood, standard deviation of 164 across all samples). Notably, this carryover was not related to the number of CTCs; rather the variable number of contaminant cells captured seemed to vary patient-to-patient. The non-CTC captured population often stained positive for exclusion markers (CD45, CD11b, CD34). To evaluate if this non-target capture population was specific to the anti-EpCAM antibody, healthy samples were spiked with both capture (anti-EpCAM M-270) and blank (unconjugated M-270) PMPs; both yielded similar numbers of contaminant cells. Thus, we hypothesize a subset of the PBMC fraction nonspecifically adheres to the PMP surface rather than through the capture antibody and, due to its interaction with the PMP surface, is not removed during the wash steps nor removed with additional washes. The exact mechanism by-which the contaminant cells non-specifically adhere to the anti-EpCAM PMPs and unconjugated PMPs is currently unknown, yet the existence of this non-specifically captured population will impact the overall purity of the extracted population. Though powerful, positive selection is incapable of capturing analytes for which a specific, known marker is not present, such as CTCs with very-low or no expression of EpCAM.[268] Thus negative selection is necessary to enable discovery-based approaches and separation of cells with unknown markers.

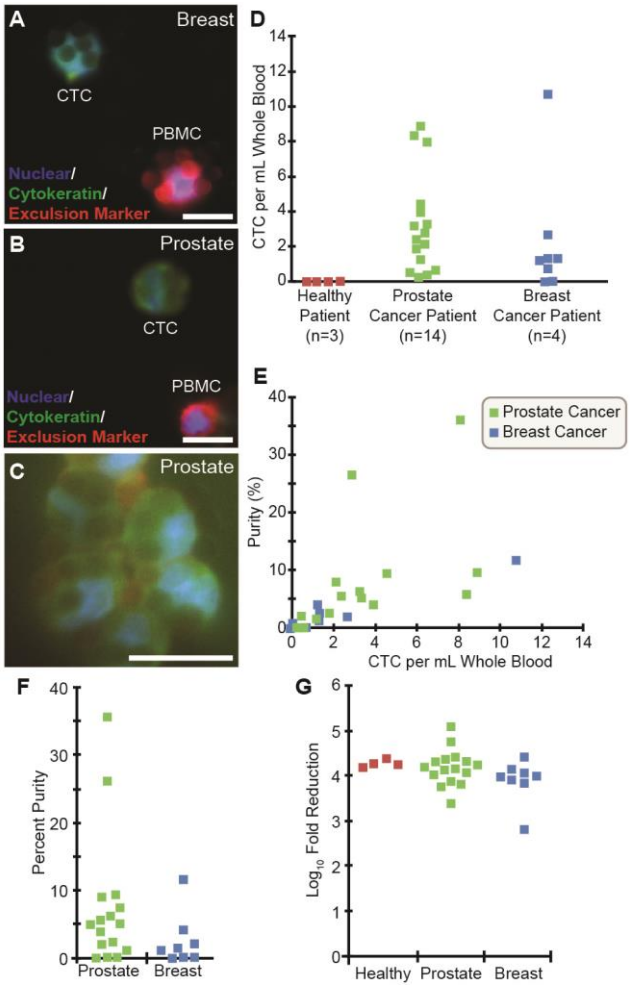

Fig. 10.3 Positive Selection. (A,B) Image of a CTC and PBMC captured from (A) a breast cancer sample and (B) a prostate cancer sample. (C) Image of a CTC clump captured from a prostate cancer sample. (D) Quantity of CTCs captured per milliliter of whole blood from prostate cancer. (E) The correlation between purity and CTCs captured per mL of whole blood, using the same patient from the previous plot. (F) Percent purity observed in prostate and breast cancer patients. (G) Fold reduction of PBMCs. (A-C) Scale bars represent 10 μm. (D-G) Each dot represents a single patient and the same patients are represented in each plot.

10.3.4 Negative Selection: CTC purification from patient samples via CD45, CD14, CD34, and CD11b depletion

Negative selection enables discovery-based approaches for rare cell isolation. To isolate the target population, negative selection removes contaminant cells via known markers, making the approach especially useful when target markers are unknown or shared with non-target populations. Because the M-270 PMPs used in this platform can be conjugated to a variety of antibodies, the platform easily transitioned from positive to negative selection. To perform negative selection, non-target largely

PBMC populations are removed from the sample using M-270 PMPs pre-conjugated with antibodies against CD45, CD14, CD34, and CD11b. When used in combination on a selection of breast cancer patient samples, this series of exclusion markers yielded an average ~2 fold $\log_{10}$ reduction in PBMCs **(Fig. 10.4)**. When a duplicate sample underwent positive selection in parallel, an average reduction of ~4.2 fold $\log_{10}$ reduction in PBMCs occurred. Due to the number of cells that must be successfully targeted in negative selection compared to positive selection, negative selection mode yields an overall less pure population. In addition to the reduction in background, we assessed potential improvements of negative selection over positive selection in isolating CTCs. While negative selection suffered from reduced background depletion, negative selection resulted in a greater number of CTCs identified. This increase could be due to a number of factors. With positive selection, an additional selection criteria of a capture marker (i.e., EpCAM) is placed on CTCs; thus the additional CTCs identified with negative selection may not express the capture marker or at a very low level preventing their capture by positive selection. Due to the suspected heterogeneity of CTCs both within a patient and patient-to-patient, the potential for EpCAM low or negative CTCs is high and could explain the increase in CTCs identified with negative selection. Additionally, the depleted population is more likely to house populations with low expression of contaminant markers as the remaining population is composed of cells missed during depletion. Thus, some of these cells may stain very low or not at all for contaminant markers; if the cells also stain positive for cytokeratin, they would be incorrectly included in the CTC population. Although negative depletion is less effective at removing contaminants (i.e., lower purity than positive selection), negative selection minimizes the risk of missed, un-captured CTCs.

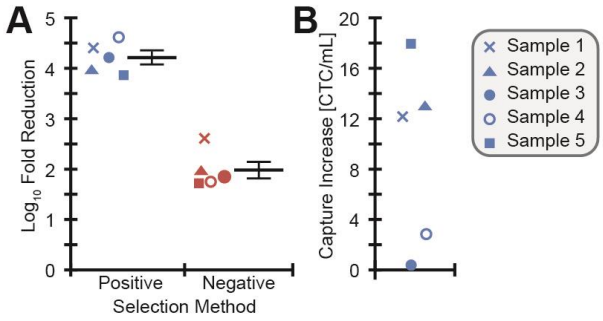

Fig. 10.4 Negative Selection. (A) A comparison between positive and negative selection demonstrating the efficacy in reducing the background PBMC population. Positive and negative selection are representative of cells remaining in the output and input wells, respectively. Each point represents a (breast cancer) patient sample. The large line represents the average and error bars represent standard error. (B) A comparison between positive and negative selection demonstrating the increase in capture efficacy for negative selection.

10.3.5 Combinatorial Selection: Negative and Positive Selection

While positive selection enables the extraction of targeted, specific populations and negative selection allows for the discovery of cells with unknown identifiers, combining negative and positive selection allows 1) increased removal of contaminant populations to achieve higher purity and 2) the removal of contaminant cells which may also express a desired positive selection marker. To evaluate the impact of implementing a negative depletion step prior to EpCAM-based PMP capture, PMPs specific to CD45, CD14, and CD11b were conjugated for depletion. Patient samples were then split and either underwent solely positive EpCAM selection or underwent a combination of negative depletion on the platform followed by EpCAM capture. In general, depletion of CD45 events followed by EpCAM capture resulted in a significant increase of captured CTCs as well as an increase in purity, likely due to the increase in captured CTCs.

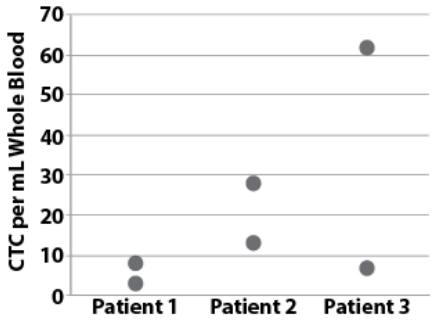

Fig. 10.5 Combinatorial isolation. This plot demonstrates the improved capture efficacy resultant from sequential negative and positive selection, respectively.

10.3.6 Automated Nucleic Acid Extraction Protocols: Development and Validation

Cell isolation is only the first step in obtaining cellular information where isolation is followed by molecular extraction and analysis (e.g., RNA, DNA). Molecular analytes often require high yields (i.e., low loss) and purity. Pipette-based transfer of samples between systems is inherently lossy (residual volume in the pipette tips, loss volume in wells resulting from transfer), reducing available material with each transfer. Thus to minimize sample loss and fully utilize the platform's capabilities, processes for RNA and DNA extraction were developed, tested, and integrated into mTAE.

To validate NA extraction we first benchmarked mTAE against commercial, non-PMP based NA isolation products (e.g., spin columns) and a manual tube alternative, using samples of ~10 to ~1,000 LNCaPs **(Fig. 10.6)**. Extracted RNA and DNA was quantified by qRT-PCR or qPCR respectively. Upon comparison, RNA yields via mTAE extraction with were within one cycle of alternative methods. Each method of DNA extraction resulted in statistically identical yields (p-value > 0.05).

Next, we tested if the presence of M-270 beads - used for isolating the cells - impacted NA acid yields. NA was extracted from cells (LNCaPs) that were first bound to and captured by M-270 PMPs; the yields were then compared to NA extraction of the cells alone (i.e., without M-270s). The presence of M-270 PMPs enhanced RNA yield by on average ~1 fold **(Fig. E.3)**; however, the presence of M270 PMPs had an adverse impact on DNA, severely inhibiting DNA capture and detection **(Fig. E.4)**. We speculate the loss in DNA was due to DNA irreversibly binding to the M270 PMPs, preventing detection and

quantification. We circumvent this issue by first lysing the M270-bound cells in the RNA lysis buffer and magnetically removing the M270 beads. DNA lysis buffer and DNA specific PMPs are then added to and isolated from the sample. This method of pre-lysis depletion was enabled by a specifically design well and resulted in equivalent yields to DNA extraction cells alone.

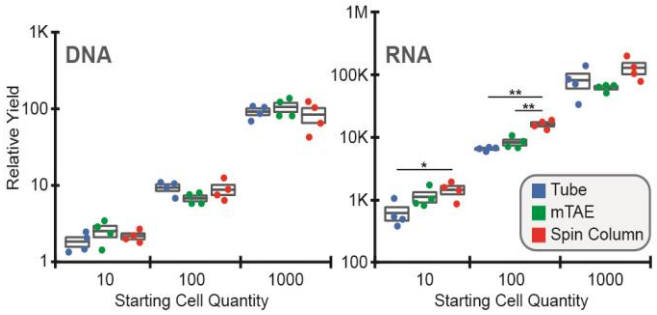

Fig. 10.6 NA acid extraction from contrived samples. (A) DNA Extraction from 10, 100, and 1,000 cells compared across three methods: manual tube-based method, mTAE, and Qiagen QiAmp DNA Mini spin columns, (n=4). (B) RNA extracted from 10, 100, 1000 cells compared across three methods: manual tube-based method, mTAE, and Qiagen RNeasy Plus Micro (n=4). Each point represents a sample (n = 4 per condition). Boxes demonstrate average and standard error, Statistical significance based on T-Test is represented by * $P < 0.05$ and ** $P < 0.005$ (C) Detection of prostate-related transcripts from approximately 10 or 100 LNCaPs and 22rv1s.

10.4 Discussion

Knowledge and understanding of rare cells is continually evolving as potential applications for the interrogation of rare cell populations (prognostic, diagnostic, etc.) continues to expand. However, simple and versatile platforms will be needed to meet demands in this dynamically changing field. CTCs provide a relevant example of a rare-cell population masked within a complex and diverse background; a field where isolation demands and parameters are constantly changing. Objectives of CTC technologies have spanned enumeration-based cell capture (i.e., where background is less impactful) to high purity population isolation, compatible with downstream nucleic acid interrogation (i.e., contaminant populations can mask or skew information contained within CTCs). The variable demands and constraints governing CTC technologies make CTCs an ideal population with which to test and evaluate a cell isolation platform.

Patient-to-patient heterogeneity, cancer heterogeneity and variations in the CTCs themselves all culminate to make CTCs a difficult population to isolate, purely. The background bloodstream

populations from which target cells are captured, can change with disease and treatment, impacting the dynamics between PMPs and contaminant cells. Furthermore, the target cells themselves vary, evident by the lack of a 'one size fits all' capture antigen for CTCs. Rather, CTC capture markers vary in expression level and utility across cancers. This heterogeneity in nearly all aspects of CTC isolation emphasizes the need for flexibility in isolation platforms to accommodate the aforementioned challenges. PMP-based technologies provide users with a degree of flexibility, allowing the targeting of any surface marker by conjugating a desired antibody to the PMP surface.

Within the existing PMP-based technologies, platforms often perfect either positive or negative selection, purifying cells via known markers (positive selection) or removing cells, via a marker specific to non-target cells, to leave behind a target population. Deciding between positive and negative selection dictates resultant populations and purity. Positive selection captures a population specific to the applied selection marker. However, in choosing a selection marker for positive selection, it is important to note all selection markers do not yield the same purity-one must consider its specificity. Specificity of the marker will be impacted by the background population in which the target cells reside. If non-target cells express the chosen marker, one must evaluate the suspected size of the target population and determine an appropriate level of purity. Additionally, it is important to consider other nonspecific interactions the antigen might have (e.g., cross reactivity) that may lead to non-specific capture of non-target cells. If a selection marker is appropriately chosen, positive selection can yield a specific, pure population due to robust separation from the background. Negative depletion results in a much larger endpoint population, resulting from incomplete removal of contaminant populations (e.g., weak expressors). Despite the generally low purity, negative selection often yields higher quantities of target cells; the key reason for this is that negative selection does not make any assumptions about differential markers expressed by the target population. Reliance on such differential capture markers may result in incomplete capture of the intended target population (i.e., not capture low expressors) or may not encompass the entire population (i.e., EpCAM may not capture CTCs undergoing EMT). Thus with negative selection, a population of

interest can be isolated regardless of its expression (high, low, or even none) of a particular surface marker. However, the one caveat is that the markers being used to negatively select out the background population cannot be expressed by the population of interest; else, the population of interest will be depleted. Nevertheless, negative selection is unhindered by target cell diversity. Both positive and negative selection are powerful tools, yet many technologies are limited to only one methodology. In order to maximize flexibility of the platform and enable a wide range of analytes, integration of both positive and negative selection will be key.

mTAE is an automated sample preparation platform allows user to combine both positive and negative selection (in nearly any order imagined) to isolate cells; users can then follow cell isolation with either RNA or DNA isolation in a single, one-platform workflow. Using mTAE, we demonstrate the platform's utility in isolating rare cells from complex biological samples, using CTCs as a surrogate for rare cells. We highlight mTAE's versatility by demonstrating positive and negative selection can be performed independently or in any combination, followed by on-chip intra- and extracellular staining (enabling CTC enumeration and quantification) and/or extraction of either RNA or DNA. Though the current embodiment is only capable of processing four samples simultaneously, the platform has been designed such that scaling to eight samples or adding on additional workflow steps can be achieved without added complexity. Using this technology, we have isolated CTC from patients with various cancer phenotypes, including: prostate cancer and breast cancer while demonstrating specificity through the evaluation of healthy blood and demonstrate the platform's capacity with integrated RNA or DNA extraction.

mTAE is designed around PMPs in combination with exclusion-based sample preparation (ESP), a purification method where PMPs are drawn through an interface to isolate the PMP-bound material and leave the contaminant background behind. As a PMP technology, certain considerations and limitations exist. In applying PMPs to cell selection, it is important to consider the PMP itself, as PMP choice and different PMP utilizations can impact results. PMPs provide several mechanisms through which non-

target cells can be captured, including: binding to the PMP surface, phagocytosis of the beads, or entrapment in interstitial space. A variety of PMP types, surface coatings and blocking agents were evaluated, and we found M270s to yeild the best results. A spectrum of nonspecific binding was observed across a variety of PMP types coated with the identical anti-EpCAM Ab as well as blank beads. The responsible phenomena leading to the variation in contaminant cell capture observed is likely due to a multitude of factions both within and across patients. Non-target cells may respond to PMPs introduced to the sample through a type of immune response; a response, which may vary based on the PMP composition, surface structure or topography, presentation of the attached antibody, and charge. Thus non-specific binding may inherently limit purity in positive selection approaches to rare cell isolation as a fraction of the non-target cells may always be captured due to such responses. While we tried to minimize binding across a number of different PBMC donor sample, a PMP with lower non-specific binding could exist and would easily integrate into mTAE with minimal modifications. While phagocytosis of PMPs was not directly assayed due to the size of PMPs used (~2.8 um), in switching PMPs, phagocytosis could result in unintended capture and thereby hinder positive selection purity. Additionally, entrapment of PMPs in the interstitial space could impact unintentional capture. Through the inclusion of shear mixing and multiple washes in mTAE with limited contaminant cell removal by the last wash, the level of PMP dispersion limited the risk of entrapment in the existing platform.

mTAE's use of exclusion-based sample preparation allows the user to perform positive and negative selection, both independently or in combination. In positive selection of CTCs from patient samples, CTCs were successfully capture via EpCAM from both prostate and breast cancer patients as identified by positive cytokeratin staining, a nucleus, and the absence of any contaminant markers (CD45, CD11b, CD34). Positive selection resulted in improved depletion of contaminant cells and improved purity when compared to negative depletion on mTAE. Negative depletion, while poor purity, resulted in an increase CTC yield. Unlike positive selection, negative narrow selection of CTCs to a single capture marker; rather our negative selection mode only assumed that the CTC population does not express

CD45, CD14, CD34, and CD11b by targeting those populations for removal. Thus, across a direct comparison of positive and negative selection, negative selection yielded the most CTCs while amongst a much larger background of contaminant cells. In addition, mTAE allows users to easily combine positive and negative selection on a single sample. When applied to CTCs, implementing negative depletion steps prior to positive selection resulted in both higher CTC yields than positive selection of CTCs alone and higher purity than either of the positive or negative selection independently. This suggests that by removing contaminant cells, CTCs were more efficiently captured. Interestingly, however, in characterization with cell lines, this phenomena was not observed as decreasing (or increasing) background had no discernable impact on target cell capture. Thus spiking cell lines into a PBMC background may not fully mimic the complexity of patient samples, lacking potential interactions between PBMCs, blood factors and CTCs and making cell lines much easier to capture. While it is difficult to precisely discern the mechanism behind the increased CTC yields obtained following negative selection of background, it seems likely due to the interactions occurring between the CTCs, blood cells, and PMPs. Interactions within the sample - between CTCs and surrounding cells - may block or impair contact between the PMPs and CTCs. Thus, a depletion step may help to reduce these potential interactions and broaden access to CTCs. Some have hypothesized that CTCs may be cloaked by different factors (e.g., platelets, others?) which hide them from the immune system; this cloaking of CTCs may in turn mask the CTCs from anti-EpCAM PMPs, reducing capture. PBMC removal by negative depletion prior to positive selection may reduce the interactions of PBMCs and CTCs directly or alternatively agitate the sample leaving CTC markers more open to antibody capture. Additionally, low EpCAM expressing CTCs may benefit since the reduction in background increases the PMP to cell ratio, a greater likelihood of CTC capture.

Endpoints are arguably as essential as cell capture, especially in the case of rare cells where repeated transfers between platforms can result in significant sample loss. mTAE allows users to dynamically and flexibly integrate staining, fixation, and permeabilization into the platform washes. This

allows users to readily transition the platform to fit their needs. If an extracellular stain is required, the PMPs and bound cells can just be left in the wash well containing the stain for the desired duration then the PMPs and bound cells collected and moved to the next wash. In a similar manner fixation and permeabilization can be performed. ESP allows users to add on modules easily within the automated platform so following isolation, an additional fixation and staining plate can be added on. Similarly, the user can manipulate the PMPs and bound cells from the final wash, staining, or imaging wells to nucleic acid extraction all on platform. Characterization against manual and commercial methods, mTAE demonstrated nearly identical nucleic acid yields for both RNA and DNA. Additionally, RNA was successfully isolated and evaluated for AR splice variants which were appropriately identified in cell lines and also identified in patient samples. The easy integration of these valuable and arguably mandatory processes in a cell isolation platform with such flexibility will ensure mTAE's utility to the maximal number of researchers.

While mTAE has great potential to enable versatile cell isolations, considerations must be made by the user prior to operation. mTAE's reliance on PMPs to isolate populations allow users to easily exchange PMPs and thus readily adapt to new capture populations. However, the user is limited to available PMP types, which as mentioned, can vary in terms of non-specific cell capture impacting purity and captured populations. While PMPs can impact background binding, available PMP types are only likely to grow as PMP-based techniques are continually expanding. Furthermore, while PMPs allow users to readily manipulate cells in and out of wells for staining, a high density of PMPs may impair visualization of the cells and imaging. While a problem, alternative strategies can overcome this limitation such as dilution of the captured PMPs to a lower density or manual size exclusion of the PMPs and cells (i.e., the PMPs are significantly smaller than the cells at 2.8 uM allowing them to be removed through a sieve while the cells remain). To image, the sample plate must be removed from the platform during which the droplets are prone to evaporation and must be replenished on return to mTAE if continuing with nucleic acid extraction. Additionally, many potential users may prefer alternative robotic

systems outside of the PipetMAX utilized here. Fortunately, due to our system's unique use of a magnetic pipette head and a magnetic box[263] , adapting this to a different automated platform should be straightforward as no physical actuation besides the raising and lowering of magnets within the pipette head are required. While versatile, mTAE does face restrictions as to the order samples can be processed; while 4 samples can be processed in parallel, there is currently no way to perform different operation on the different samples, each sample must be processed identically. Despite, the presented limitations, mTAE remains an enabling tool for researchers to fold to their dynamically changing needs in an automated platform.

Chapter 11 In vivo tumor sampling via a needle-implantable microdevice[10]

11.1 Introduction

The goal of precision oncology and personalized therapy is to identify unique factors in each cancer to develop an effective therapy. Precision Oncology promises to reduce unnecessary cost, side effects, and delay in effective treatment.[9] Additionally, precise selection of oncologic drugs permits improved cure rates by increasing effectiveness of adjuvant therapy. Thus, there is a critical need for technologies which account for the unique factors associated with each tumor and predict treatment efficacy.[269, 270] A dominant approach in precision oncology currently is to identify unique genetic signatures of the cancer to uncover tumor specific directed therapies.[271-273] However, it is increasingly understood that the stroma as well as the genetic alterations in a tumor impacts tumor behavior. Although robust models of tumor-stroma interactions have been developed in animals[24, 274] or ex vivo using human tissues,[275] it is difficult to directly assess biology of the microenvironment natively within a human tumor. Thus, it would be of strong scientific value to be able to sample the tumor microenvironment in humans at the time of treatment with novel systemic treatment agents.

Another benefit from tumor sampling would be early detection of response to treatment. Response to existing therapies is notoriously heterogenous between patients. Currently efficacy of cancer medications are assessed by measuring changes in tumor burden (i.e., total amount of tumor) in response to systemic therapy. However, several weeks of treatment and observation is required to assess response to therapy; in the interim, the patient may be receiving toxic treatment without beneficial effect. For instance, breast cancer systemically treated with paclitaxel typically requires 8-12 weeks of treatment to generate a detectable effect. A major advance would be to identify response to therapy within days of the single dose. This would greatly reduce the harm of therapies that happen to be ineffective in individual

10 This chapter has been adapted from a manuscript in preparation for publication: "In vivo breast tumor sampling via a needle-implantable microdevice" David J. Guckenberger, Jay W. Warrick, Alka Choudhary, Amanda Schulman, Jennifer Mirrielees, Lee Wilke, Mark E. Burkard, and David J. Beebe.

patients. Thus, there is a need for faster clinical approaches that can be flexible to predict the outcome from multiple drugs and at multiple different disease stages.

Here we present a fully implantable technology that enables intra tumor sampling in vivo for downstream cytokine profiling. The technology is simple to manufacture and tune, enabling both long and short term sampling periods to accommodate a wide range of therapies. The sampling technique relies on diffusion to specifically capture soluble factors from a localized region within a tumor. The sample can be easily extracted from the technology for downstream analysis, such as a MAGPIX assay which can be used to assess up to 500 analytes simultaneously. In this manuscript, we present numerically simulated results, in vitro characterization, and in vivo (murine) characterization to fully demonstrate the utility and potential of this implantable technology. Using this implantable device coupled with a MAGPIX assay we demonstrate the ability to capture and detect a cytokine profile to predict tumor response in vivo.

11.2 Materials and Methods

11.2.1 Capsule Design (fab / assembly)

The 10 mm long tubes are cut from polymethyl methacrylate (PMMA) capillary tubing (0.667 mm I.D.; 1 mm O.D.) (#MORCAP25, Paradigm Optics) by circumferentially scoring with a razor blade and bending the piece to break cleanly along the scored line. Anchors were prepared by cutting 1” lengths of .004” (102 μm) diameter stainless steel wire (#GWX-0040, Component Supply Co.), and bending them in half. Capsules were assembled by: (1) inserting the creased end of the anchor into the tube until it was flush with the back end; (2) a 1 mm long plug of UV curable glue (#1128A-M-T, Dymax) was capillary filled into the back end of the tube and cured with UV light, thus securing the anchor and sealing the back end to define the reservoir. The anchors were trimmed to a length of ~2 mm from the front reservoir and bent to a ~45 ° angle. Once assembled, capsules were sterilized through 15 min treatment of UV light.

11.2.2 Capsule filling and emptying

Multiple capsules were simultaneously filled and emptied by centrifugation. To fill the capsules, enough reagent (e.g., PBS, agar) to fully submerge the capsules was placed into a 1.5 mL tube. Multiple

capsules (1 - 10) were placed in the microtube with orifice facing upward. The tube was spun for 15 seconds in a microfuge at 2000 rcf, which was sufficient to fill capsules with 100% success rate. Once filled, the edges of the capsules were dried on a sterile wiper, then stored in PBS, on ice to prevent evaporation. Capsules were filled within 1 hour of implantation. Capsules were filled with 2% agar solution. Agar was loaded in its liquid state, then solidified in the capsule by cooling in the PBS. To remove fluid, capsules were placed with the orifice (front) facing downward in an empty 1.5 mL tube and centrifuged for 15 seconds. Multiple capsules could be emptied simultaneously in a single tube; however, to keep contents separate we emptied them individually.

11.2.3 Design and Fabrication of the Implantation Device

The mechanism for implanting the capsules was comprised of 3 components: a 10 mL syringe (#309604, Becton Dickinson), a push-rod, and an injection needle **(Fig. F.1)**. The injection needle - a 0.75" long 16 G hypodermic needle (#SC-360857, Santa Cruz Biotechnology) - was mounted to the end of the syringe. The push-rod - a 1.5" long 19 G blunt end needle (#NE-193PL, Component Supply Co) - was placed within the cavity of the syringe; its tip was placed into the base of the injection needle. The capsule was placed inside of the injection needle, such that the anchors were completely contained. After the needle is inserted into the desired location, the capsule is ejected by pushing on the syringe plunger, whereby the push-rod would go into the injection needle and push the capsule out. Importantly, to prevent compressed air from ejecting the capsule and prevent air from being inserted into the mouse, an air escape hole was drilled into the front of the syringe reservoir.

11.2.4 Cell Culture

The MDA-MB-231-luc-D3H2LN human breast epithelial carcinoma cells (Caliper Life Sciences) were cultured in a humidified atmosphere at 37 °C with 5% CO2. These cells were cultured in DMEM-HG media supplemented with 10% FBS, 1% Penicillin streptomycin, passaged every 5 Days at a 1:5 dilution, and used prior to passage 6. The cell line was generously donated by Dr. Jamey Weichert.

11.2.5 Mouse anesthesia

Under an approved UW IACUC (Insitutional Animal Car and Use Committee) and UW RARC (Research Animal Resources Center) animal protocol (protocol #M02624), mice were anesthetized by first inducing at 4% isoflurane in a chamber over a period of approximately 1 minute until the loss of righting reflex has been observed. The animal was then removed from the chamber and a nose cone was used to deliver isoflurane at 1-2% for the duration of the procedures. Anesthesia was used during xenografting and capsule implantation.

11.2.6 Xenograft Tumors

Mice (5-7 weeks old homozygous nu/nu female nude mice (Jackson Laboratories; Maine)) were xenografted by injecting 100 μL of DMEM-HG medium + 10% FBS of 2.5×10^6 MDA-MB-231 -luc-DH3L2N cells into the rear flank of the mouse. Tumors were allowed to grow for 4-6 weeks, and were measured weekly to monitor the growth of the tumor.

11.2.7 Capsule Implantation and Removal

Using the previously described implantation device, capsules were implanted when the average tumor size along the tumor major axis was ~10 mm (typically at ~3wks post injection). At the time of implantation, tumor sizes ranged from 6-15 mm. Capsules were implanted from the posterior side of the mouse, generally parallel to the cranial-caudal axis. Intratumoral capsules were implanted at a depth of ~4-6 mm, leaving roughly half of the reservoir sticking out of the tumor; extratumoral capsules were implanted subcutaneously ~2-4 mm from the tumor. The wound (from the implantation device) was sealed with Vetbond (3M tissue adhesive 1469, Fisher Scientific). Mice were euthanized via carbon dioxide gas, the tumors were immediately excised, and the capsules removed. Capsules were stored in 0.6 mL tubes to limit evaporation and processed within two hours after removal.

11.2.8 Micro MAGPIX Assay

Capsules were implanted both intra- and extra-tumorally. Based upon previous work quantifying cytokine secretion from MDA-MB-231 cells, a MAGPIX assay was used to quantify analyte

concentrations collected via the implantable capsule.[276] The wash buffer, calibrator diluent, standards, and microparticle cocktail were prepared following manufacturer protocol. However, prior to use, the microparticles were concentrated by collecting the particles via a magnet, removing the supernatant, and resuspending in bead diluent provided with the kit to a 3 μL total volume per sample. This allowed mixing of the small 3 μL samples at 1:1 [vol:vol] with the microparticle cocktail as suggested in the manufacturer's protocol. To do so, the outside walls of the capsules were dried with lint free wipes (to prevent contamination) and the contents of each capsule (~3 μL) were spun into independent 0.6 mL tubes. 3 μL of microparticle cocktail was immediately added to each sample. The tubes were placed on an orbital shaker for 3 hours at 300 rpm. After incubation, 100 μL of wash buffer was added to the tubes and samples were transferred to the microplate provided with the kit. All subsequent steps were performed following manufacturer protocols. Each MAGPIX assay was run with the provided standard, a background control (i.e., PBS spun from the capsule), standard which was spun into and out of a capsule, and standard premixed with agar spun into and out of a capsule. Data from the MAGPIX assay were calculated using mean fluorescence intensities.

11.2.9 Venous and Tumoral plasma collection

As a comparison to the sample collected by the capsule, plasma was collected from whole blood and the tumor directly. Blood, acquired from the tail vein, was centrifuged at 2000 RCF for 30 s to sediment the red blood cells. 3 μL (the same volume as the capsules) of plasma were collected by pipette, put in a tube, and processed in parallel with the samples collected via the capsules. We attempted to collect plasma from the tumor directly using a 26 g needle and a 10 mL syringe. This method did not yield enough plasma to perform any MAGPIX analysis.

11.2.10 Systemic Treatment

Mice were systemically treated with DOX by intraperitoneal (IP) injection. Dox was injected only once and mice were sacrificed three days after the injection.

11.2.11 Computational Modeling

COMSOL Multiphysics software (COMSOL Inc.) was used to model capsule function in a simplified model of the tumor environment. The tumor model consisted of published, physiologically relevant cell densities, diffusion characteristics, and proliferation rates **(Fig. F.2)**. Capsule features, including reservoir length, diameter, and volume, were probed to assess design impacts on capsule function. Analyte capture was assessed by quantifying average reservoir concentrations of analyte over time. The capsule function was modeled over a 14 day period and reported at 0.1 day intervals. A full description of the model setup, including parameters and constitutive equations, can be found in the appendix..

11.2.12 Statistical Analysis

Specific statistical tests and sample sizes are described along with results. Throughout, the term ‘technical replicates’ is used here to refer to replicate measurements performed on the same sample while ‘biological replicates’ refer to measurements taken from different mice/tumors or from separate experiments.

MAGPIX data was preprocessed as follows. The data was first transformed to log-scale for subsequent calculations. Standard curves were analyzed to assess a limit of detection for each analyte. The median absolute deviation was used to robustly estimate the standard deviation of measurements for each analyte. The limit of detection was then calculated as mean plus 3 standard deviations. Undetectable values were set to 0. Any analyte that was 0 for all samples in the sample group was removed from subsequent analysis. Data was then standardized for each group by subtracting the mean and dividing by the standard deviation.

RandomForest (RF) and Naive-Bayes (NB) machine learning was performed using the ‘randomForest’ and ‘e1071’ packages for R, respectively. ROC curves were built from confusion matrices of each fold of cross-validation. Leave-one-out cross-validation was used. Backward feature selection was embedded in the training process. For NB, features were eliminated one at a time based

upon ROC AUC. For RF, features were eliminated one at a time based upon Mean Decrease Accuracy (MDA). Overall importance of each analyte was assessed by separately running RF without feature selection on all detectable analytes.

11.3 RESULTS

11.3.1 Capsule concept and design

The capsules were designed to be robust, simplistic, versatile, manufacturable, and comprised of materials approved for in vivo applications. The capsule is comprised of two key components: a reservoir and anchors **(Fig. 11.1A)**. The reservoir is made of 1 mm O.D. / 0.667 mm I.D. poly(methyl methacrylate) (PMMA) tubing which provides sufficient rigidity to withstand implantation, yet small enough to fit into a standard size biopsy needle (16 G). Anchors are made from stainless steel wire. We found the .003" - .004" thick wire to be ideal as thicker wires were overly stiff (making them difficult to get into the implantation needle) and thinner wires were overly flimsy (they did not provide sufficient support to immobilize the capsule). The anchors were bent to a 40° ± 10° degree angle from the axis of the capsule. Angles greater than 50° would straighten while loading the capsule into the implantation needle and angles under 30° were less effective at immobilizing the capsule in vivo. The anchors and needle are fixed to the reservoir with biocompatible UV curable glue. When glue is applied to the end of the reservoir capillarity acts to pull the glue into the reservoir and around a portion of the anchors. The length of the glue plug is controlled by the volume of glue administered. Volumetric variability of the reservoir, as a result of error in the length of the glue plugs, was ~ ± 0.1 μL (95% confidence interval, n = 68 capsules) **(Fig. 11.1B)**.

For simplicity we devised a method of filling and removing fluids from the capsules, using a standard benchtop microcentrifuge **(Fig. 11.1C)**. We filled capsules by first submerging the capsules (orifice facing upward) in fluid within a microtube, then centrifuging the microtube to replace the trapped air within the capsule with fluid. We validated the centrifugal filling technique with a variety of water based solutions including 2% agarose (prior to gelation). Generally, capsules fill within 10-15 s; however,

as viscosity of the solution increases or the size of the orifice decreases, longer durations (~30 s) were required. Capsule filling was visually verified by checking for bubbles through the transparent tubing from which the reservoir was made. Importantly, the centrifugal method was highly effective at filling the capsules: no failures in over 100 attempts and no bubbles formed post filling. Capsules were emptied by placing the capsule in an empty microtube (orifice facing downward) and centrifuging. Similar to filling, the time required to completely empty a capsule is typically <15 s but depends on fluid viscosity and orifice size.

11.3.2 In-situ micro sampling:

We characterized the ability to locally sample cytokines via diffusion into the capsule. Computational models and physical results demonstrate how various design considerations affect capsule operation. We evaluated the use of a MAGPIX assay to characterize several proteins extracted from the tumor. Finally, we demonstrate results from in vivo testing in mice.

To optimize the diffusion system, we computationally modeled how design considerations affected the sampling of soluble factors in the tissue microenvironment. Design elements considered included the orifice diameter and reservoir length, using the analyte lactase dehydrogenase (LDH)—an intracellular metabolic enzyme released during cell death. We modeled diffusion of LDH into the capsule and assessed the internal analyte concentration over a course of 14 days, adjusting reservoir length **(Fig. 11.2A)** and diameter **(Fig. 11.2B)** to maintain a constant volume and length, respectively. For this study we selected tubes with an O.D. of 0.6, 1.0, 1.1, 1.2, 1.3, and 1.4 mm, corresponding to I.D. 0.40, 0.66, 0.73, 0.80, 0.87, and 0.93 mm (aspect ratio of 2:3), respectively. The time for the capsule to reach equilibrium (t_{eq}) reduces significantly as the reservoir diameter is increased and reservoir volume is constant. For example, if we set 90% of maximum as a threshold limit for capture, t_{eq} for a 0.8 mm I.D. reservoir (4 mm in length) is ~ 6 days; meanwhile t_{eq} for a 0.6 mm I.D. reservoir (8 mm in length) is ~14 days. This shortened t_{eq} is directly correlated to the shortened length of the reservoir. To demonstrate this, we varied the diameter of the reservoir while maintaining a constant length **(Fig. 11.2B)**. The average concentration

of analyte increases similarly for each reservoir diameter, as expected because diffusion rate is unaffected by the reservoir diameter. However, since the volume of the reservoir increases as diameter increases, the sample volume

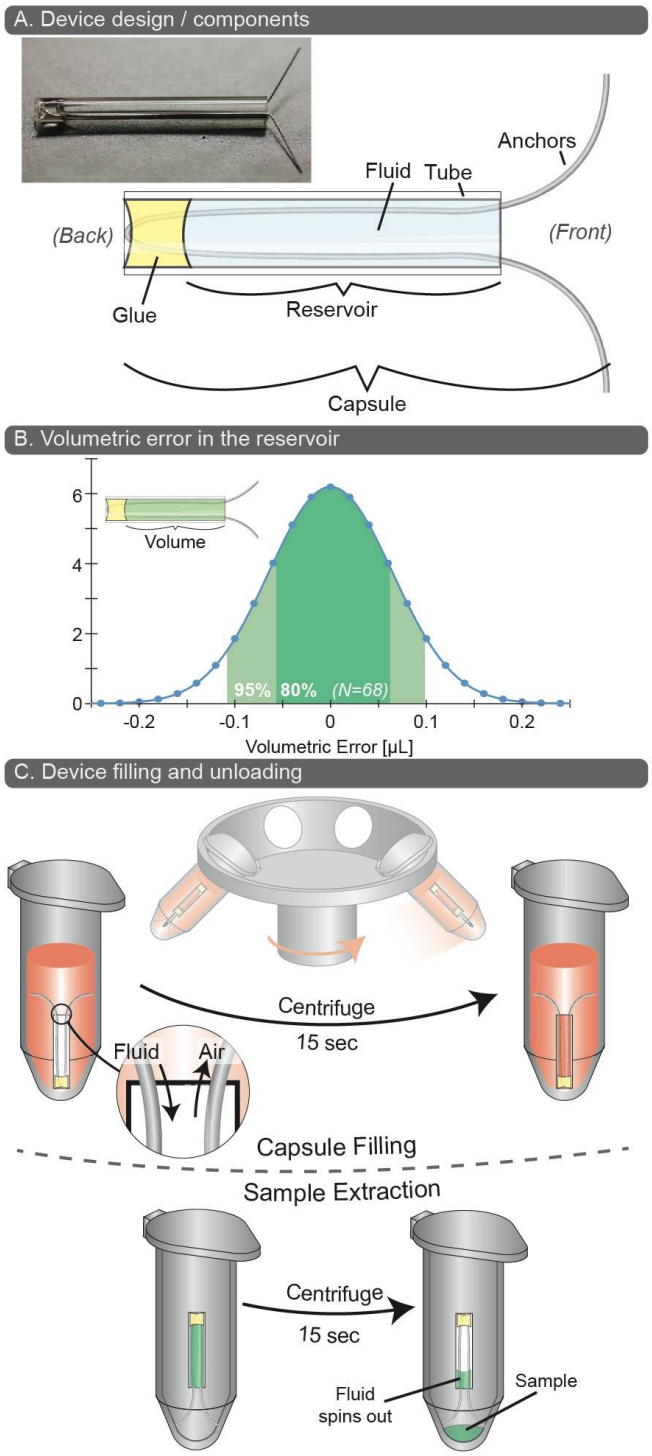

Fig. 11.1 Design, assembly, and fabrication overview. (A) Schematic of the capsule design and layout. The tube length is 10 mm. (B) Volumetric error for reservoirs as a result of variation in glue length. Average volume is 3.1 ± .06 µL. 95% and 80% confidence intervals are shown (n = 68 capsules). (C) Capsules are filled by submerging in fluid and centrifuging. Capsules are emptied by centrifuging upside down in an empty tube.

and thus the amount if analyte captured by the capsule increases with diameter **(Fig. 11.2C)**. Of note, these diffusion times shown are specific to LDH, and should be scaled appropriately for diffusion coefficients of other analytes. Thus, these results demonstrate tunability to meet a range of capture necessities.

To facilitate quantitative multiplex analyte readouts, we adapted a MAGPIX pix assay to work with the small sample volume of the capsule. We first validated that the ~3 µL from our capsule was quantifiable via the MAGPIX assay **(Fig. F.3)**. Using the provided standards from the MAGPIX kit for IL-6, IL-8, MMP-9, VEGF, and VEGF-R3, we compared 3 µL sample volume to the 50 µL recommended by the kit. To do so, a separate concentrated bead mixture was prepared for quantifying the 3 µL volume of standard to maintain a 1:1 bead mixture volume to sample volume ratio. Thus, the number of beads incubated with a 3 µL sample was the same as the number of beads incubated with a 50 µL sample in order to avoid low bead counts during downstream analysis using the MAGPIX instrument. We noticed similar trends, but a potential slight reduction in sensitivity. We suspect that the increased bead-to-analyte ratio potentially results in slight depletion of concentration during binding, attenuating signal slightly. For this reason, all future experiments were compared to standard curves created using 3 µL volumes of standard to match our 3 µL experimental volumes and prevent bias.

To minimize potential for convective mixing and cell infiltration, we loaded agar gel into the device. Thus, it was important to assess the effect of agar on measured analyte concentrations **(Fig. 11.2D)**. To do this, capsules—filled with either PBS or a 1% solution of agar—were placed in an analyte-spiked fluid for two weeks, allowing diffusion. For positive controls, solutions with analyte spiked into gel or PBS were spun into new capsules just prior to the assay. Comparing positive controls, there is little effect of agar on measurements, as expected given agar accounts for 1% of the total volume. Importantly, this shows that the gel does not impede analyte extraction from the capsule or measurement. To determine whether agar affected analyte collection, we compared capsules with and without gel. There was no statistically significant differences in capture rates ($p = .26$, student's t-test), although the data is

consistent with modestly lower analyte capture in agar, as expected. Despite this minor concern, our results are consistent with the known property of 1% agar gels,that minimally impact diffusion coefficients relative to those in water (< 25% reduction) for even large proteins. Given this, all sampling capsules in future studies were filled with an agarose gel at a concentration of 1%.

After validating a MAGPIX readout and testing the impacts of the agar, we tested the capsules in vivo. To validate the capsule in vivo, mice were xenografted with MDA-MB-231 human triple-negative breast cancer cells to generate tumors on both flanks. Once the tumors reached 4 mm diameter, capsules were implanted by needle insertion. After 1, 3, or 10 days, mice were sacrificed and the capsules were removed within 10 minutes of to prevent any appreciable collection of death-related factors. After excision, capsules were sealed in tubes to prevent evaporation and the MAGPIX assay was performed within 2 hours to minimize analyte degradation. We first assessed the potential of cytokine spikes, resulting from the implantation, by implanting intra- and extratumoral capsules for durations of 1, 3, and 10 days (n = 3 mice per duration) and screening for IL-8, MCP1, and VEGF - three cytokines with known differential expression in response to chemotherapy **(Fig. 11.2E)**.[276] No significant differences ($p > .05$) in cytokine expression were observed between the 1-, 3-, or 10-day time points. We next implanted intra- and extratumoral capsules for durations of 5 days to assess differences in cytokine expression and validate the utility of the capsules for measuring cytokine expression **(Fig. 11.2F)**. As expected, there were significant differences in cytokine expression between intra- and extratumoral capsules for both IL-8 and MCP1 (VEGF was mistakenly excluded from the assay during reagent preparation). Notably, the MAGPIX panel consisted of antibodies for human analytes yet cross-reactivity likely exists. Thus, signal from the extratumoral capsules likely results from a combination of cross-reactively, diffused local analyates from the tumor, and circulating analytes from the tumor (the last two dependent on tumoral expression). However, given the low levels and low variability in the extratumoral measurements, we suspect that the measurement is likely resultant of cross-reactivity. These data suggest that the capsule samples soluble factors specific to its local environment and may be suitable for in vivo sampling.

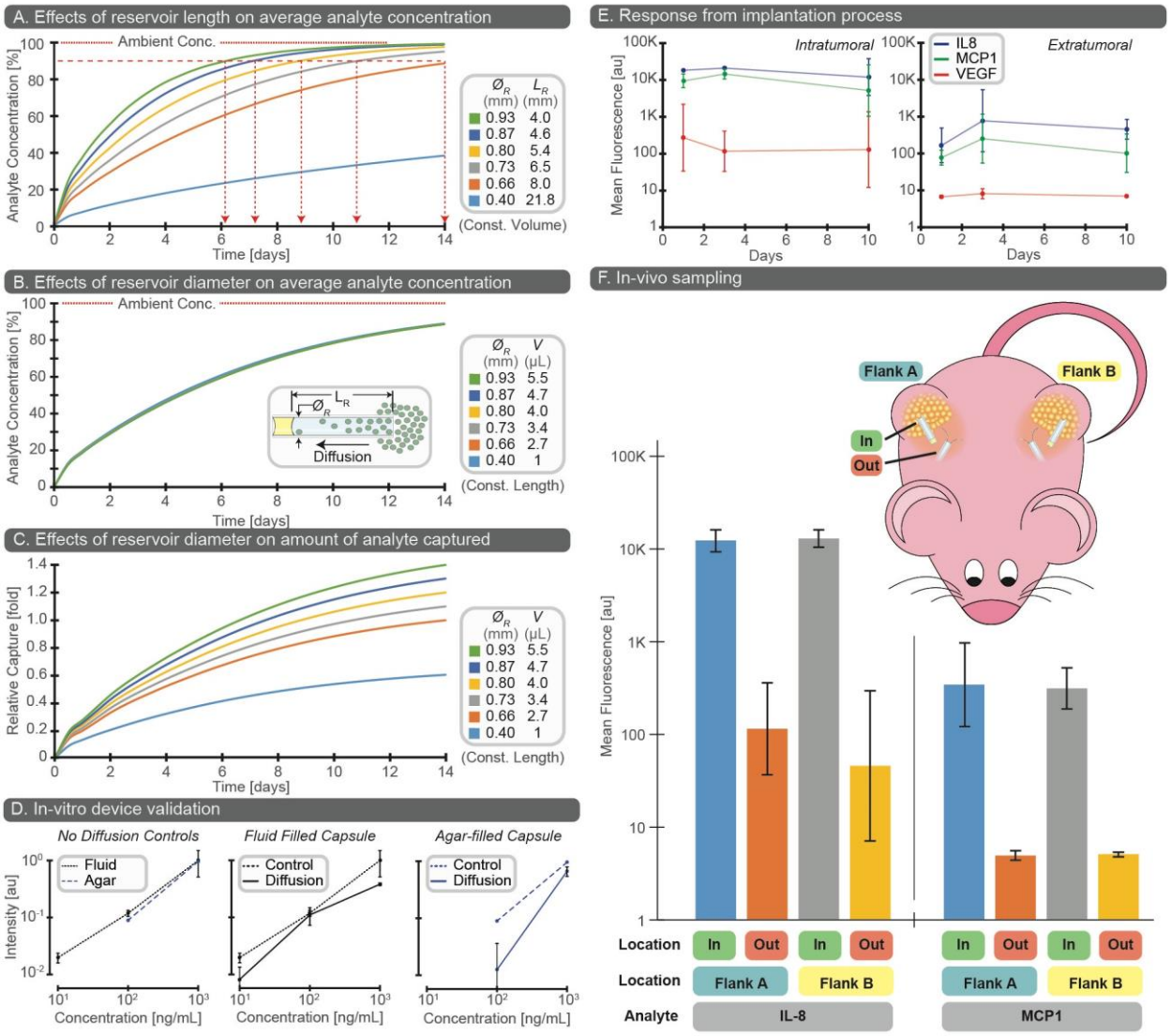

Fig. 11.2 Localized sampling characterization. A, B, and C are computational models; D, E, and F are experimental results. (A) A model showing how changes in reservoir diameter affect analyte capture via average concentration in the capsule with respect to time. In this model, a constant volume is maintained through each condition by changing the length of the reservoir. The (red) horizontal dashed line represents the threshold at which the reservoir concentration is 90% that of the ambient concentration. Vertical arrows depending from the horizontal line indicate the time to equilibrium (t_{eq}) (B) Similar to plot A but, in this model, a constant length is maintained through each condition and reservoir volume changes as a result of the changing diameter. (C) A model demonstrating how the total amount of analyte captured is affected by changing the reservoir diameter. In this model, a constant length is maintained through each condition and reservoir volume is impacted by the changing diameter. (D) Plots demonstrating the impacts filling the reservoir with agar of fluid. (left) comparison between two capsules: one filled with agar and the other with fluid. (middle) reservoir filled with fluid where analyte was spun directly into the control then analyzed but analyte was allowed to diffuse into the diffusion reservoir. (right) same as the previous but reservoir was filled with agar instead of fluid. Error bars represent SD of the means, n = 3 mice. (E) Capsules were implanted intra- and extratumorally for 1, 3, and 10 day periods to detect the presence of cytokine spikes as a result of the implantation. Error bars represent SD of the means, n = 3 mice. (F) Capsules were implanted intra- and extratumorally and screened for both IL-8 and MCP1 to assess differences in cytokine expression levels. Logarithmic error bars represent SD of the means, n = 7 mice.

11.3.3 In-vivo sampling with systemic treatment:

Given the positive results from the first two in vivo sampling experiments, we tested if the capsule would be sensitive enough to detect a tumoral response to systemic treatment, in vivo. Fourteen mice were xenografted with human breast cancer cells to generate tumors on both flanks. Capsules were implanted both intra- and extra-tumorally, and mice were returned to their cage for 5 days to mitigate cytokine spikes that might influence the read-out. After five days, a systemic chemotherapy treatment (Dox) was administered by IP injection to 6 mice; meanwhile 7 mice were IP injected with vehicle (PBS). Three days later mice were sacrificed, devices removed, and the captured samples quantified via micro MAGPIX assay, as previously described. This assay quantified 39 analytes, which were selected based on relevance to breast cancer and known changes as a result of Dox chemotherapy.

To assess the sensitivity and specificity of the cytokine profiles, we applied machine learning approaches (see Statistical Analysis). Data was analyzed for two different groups of samples, blood samples (BL) and samples from intratumoral capsules (Cap). Data preprocessing included estimating limits of detection for each analyte, removing analytes that were uniformly below detection limits, and standardizing the data for the BL and Cap groups separately by subtracting the group mean and dividing by the group standard deviation. Out of 39 total analytes, blood samples had 13 detectable analytes while Cap samples had 29 **(Fig. 11.3A)**. We built Random Forest (RF) and Naive Bayes (NB) models to predict whether a sample was from a treated or untreated mouse. Generating these models allows us to identify analyte signatures that might exist in either the tumor or blood that could be indicative of drug response and whether or not the signatures may be similar or different between the blood and the tumor. ROC curves were generated from leave-one-out cross-validation results to assess performance for each modeling approach and sample group **(Fig. 11.3B, C)**. RF and NB models detected systemic Dox treatment based on Cap sample signatures with overall accuracies of ~ 75 % and ~ 68 % and areas-under-the-curve (AUCs) of 0.78 and 0.81, respectively. The RF and NB models detected treatment effect in BL samples with overall accuracies of ~ 93% and ~ 93 % and AUCs of 1 and 0.94, respectively.

We plotted the mean decrease in accuracy (MDA) of the RF model to estimate which set of analytes contributed most strongly to detecting dox treatment **(Fig. 11.3D, E)**. Notably, the set of analytes most important for detecting dox treatment in BL and Cap samples were significantly different. The 5 most predictive analytes in BL either demonstrated negative MDA values in Cap (IFN-beta, IL-6, IL-8, TNF-alpha) or were not detectable (IL-19), suggesting that these analytes are neither significant nor predictive in the tumor microenvironment, **(Fig. 11.3A)**. Similarly, the 7 key predictive analytes in Cap either had low predictability (G-CSF), were not detectable (M-CSF, IL-23, MIP-1 alpha), or were not predictive (MMP-9, VEGF-D, IL-11) in the peripheral blood. Further, though we found a detectable signature for treated mice in BL, the concentrations of analytes was generally just above baseline measurements, 2-3 orders of magnitude lower than most analytes from Cap. Thus, it is possible that the BL results are not actually indicative of tumoral response, but rather an innate systemic response to the Dox. Further, it should be noted that the relative size of the xenografted tumor compared the mouse is quite large compared to a similar tumor in a human. Thus, the potential for the tumor to significantly impact blood levels of cytokines is likely enhanced in the mouse xenograft model compared to humans. Again, we point out that the MAGPIX assay was designed for human analytes with uncharacterized cross-reactivity with mouse analytes, limiting the ability to make interpretations regarding the underlying biology of the model. In sum, though a response was detectable in BL samples, the vast difference in the drug-specific analyte signatures between BL and Cap coupled with significantly different quantities of captured analyte (2-3 orders of magnitude) suggest that the devices are capable of locally detecting a tumor specific response. Thus, results demonstrate the potential of our sampling methodology to be used as a means to assess drug efficacy and tumoral response based on microvolume cytokine profiles diffusively captured directly from the tumor.

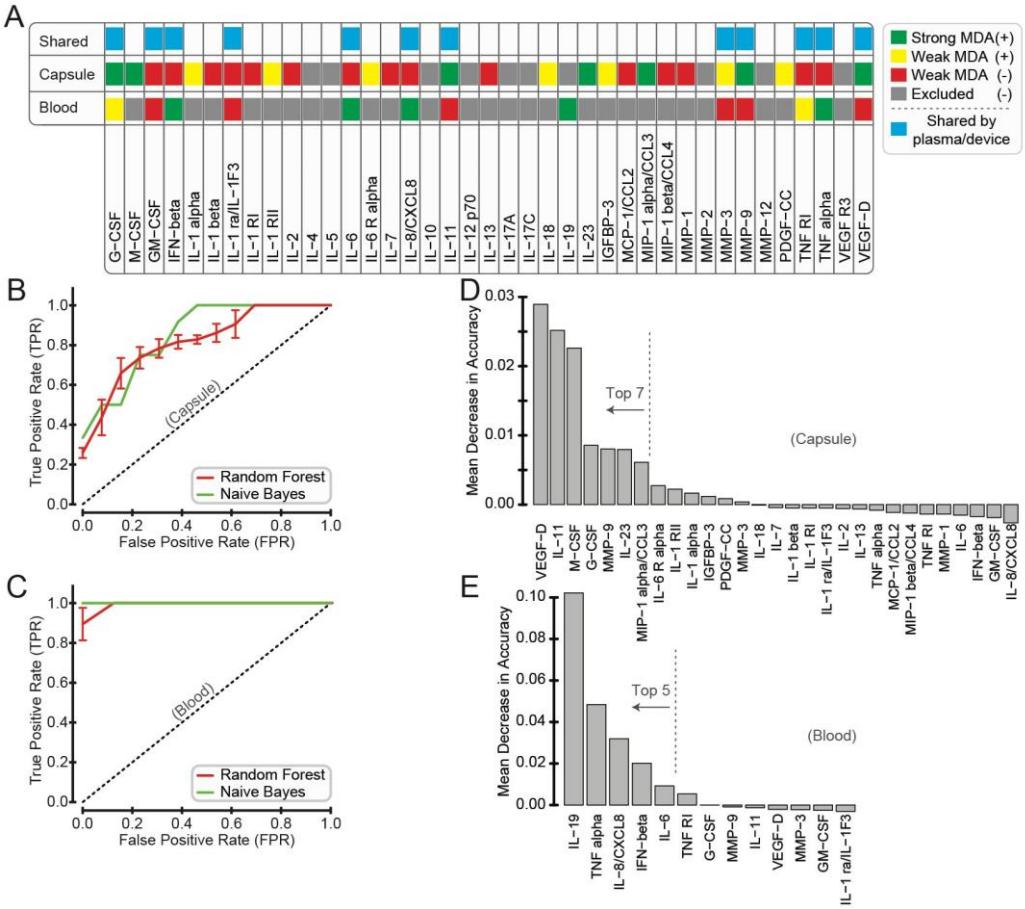

Fig. 11.3 Using cytokine profile signatures to predict a response to systemic treatment. (A) A list of all 39 sampled analytes, highlighting the detectable analytes for both blood (BL) and capsul (Cap) samples. The heatmap demonstrates the relative impact on predicting tumoral response, as well as the analytes that were excluded from the analysis because they were undetectable. (B,C) Machine learning techniques are used to assess the sensitivity and specificity of the analyte signature for detecting tumoral response to Dox. ROC curves are shown for both capsule (B) and blood (C) samples. (D,E) Mean decrease in accuracy (MDA) of an RF model is plotted and used to determine which analytes have the largest impact in the cytokine signature. Dashed lines are drawn to visually highlight analytes that appear to be most important for discriminating treated and untreated tumors/mice. MDA plots are shown for both capsule (D) and blood (E) samples.

11.4 DISCUSSION

Researchers and clinicians rely on semi-quantitative and qualitative techniques, such as histology or radiologic observations, to assess the impact of cancer targeted therapies. Histology, though valuable, is limited in that it focuses on fixed cells and depends on microscopy which limits the range of obtainable readouts. Radiologic readouts of tumor response are highly useful, but do not detect drug effects until weeks into the course of therapy. Here, we present an implantable, versatile technology that samples the tumor directly and facilitates multiplexed quantifiable readouts from localized regions in vivo. We characterize the technology extensively through computational simulations as well as in vitro and in vivo

experimentation. Further considerations and modifications will help advance this technology and move it closer to clinical implementation. In this section, we describe various benefits of the technology, propose potential modifications, explain important considerations, and discuss possible future applications.

A major advantage of our design is the simplicity, modularity, versatility, and manufacturability. The capsule is assembled with commercially available components that are glued together. The use of tubes and wires and facilitates easy modifications to the reservoir volume and sampling rates. The caveat is that the length of the glue plugs is subject to error—affecting reservoir volume. Thus, more controlled methods of delivering glue or sealing capsules will be necessary to assure repeatability. The materials used in this study are biocompatible, and the transparency of the PMMA tube enables quick quality control to ensure that the reservoir has filled properly. However, for clinical use, alternative materials (e.g., stainless steel, titanium) may be necessary to visualize devices during implantation (e.g., ultrasound). Though quality control to assure filling will be difficult with opaque capsules, alternative techniques, such as weighing the device, may be utilized; nevertheless, our studies have demonstrated reproducible success rates for filling. One challenge with filling is capsule buoyancy—capsules occasionally float in the fluid preventing submersion of the orifice. The anchors (sticking above the fluid surface) provided enough mass to push the orifice below the fluid surface, but capsules with large reservoirs may require additional mass to overcome buoyancy. Additionally, the anchors are also crucial to emptying the capsule as they hold the orifice above the fluid, enabling air to enter through the orifice **(Fig. 11.1C)**. Though a microcentrifuge was sufficient to fill and empty our capsule, faster centrifuges may be necessary if the orifice is substantially smaller (i.e., higher resistance) or if the fluid viscosity is substantially higher. The dimensionless Bond number can be used to estimate the g-force necessary to fill the capsule.

Modifications to the capsule design and the implantation device have the potential to further simplify implantation and improve repeatability. Capsules are implanted through an implantation needle, where a push-rod urges the capsule from the needle. The expanding anchors resist forward motion of the

device, requiring simultaneous removal of the implantation device. An improved device would, instead of a push-rod, have a stationary inner rod with a retracting outer implantation needle, allowing the capsule to remain immobilized as the implantation needle is retracted. The size of the implantation needle—dictated by the diameter of the capsule—creates a practical lower limit on tumor size, which, with a 16 gauge (G) implantation needle (1.65 mm O.D. and a 6.16 mm bevel length), was ~4 mm. This lower limit was partially due to the long bevel having to go entirely through the tumor and partially because a 4-mm tumor was physically difficult to align with the large needle. However, many clinically observed human breast cancer tumors exceed this size.[277] Another concern during implantation is evaporation from the capsule, which can cause a bubble to form near the orifice of the capsule that will prevent sampling. There is a practical working time of about 2-5 min before excessive evaporation may cause capsule failure. Thus, the capsule was kept hydrated (e.g., by storing in fluid prior to implantation), the working time is not longer and issue. A final concern is biocompatibility. While implanted, the mice did not present signs of infection nor exhibit significant immune response around the device. This lack of inflammation may be due to the partial immunodeficiency of the athymic mice. Further testing in an immunocompetent background is necessary. However, methods to passivate the device surface such as poly(p-xylylene) (i.e. Parylene) coating might be employed to further ensure tolerance and prevent an immune response that could affect interpretation of results.

It is important to note that our capsule samples over a course of several days, meaning the device contents represent an average over the entire implantation period with a bias towards recent events. The time span and effect of the bias is dictated by the size of the capsules. Smaller capsules will portray a flatter average over the entire implantation period while larger capsules will be much more affected by recent changes in concentration. The effect of the bias is dictated by the size of the capsule, where large capsules are more representative of recent events and smaller capsules represent more of an average over the entire implantation period, making the capsules less sensitive to temporally localized spikes in concentration. Further, because the capsules are filled with gel, the capsules capture analytes via

diffusion, increasing specificity toward soluble factors and reducing capture of other factors such as cell debris. The caveat to long implantation periods is the potential degradation of captured analytes. For instance, many interferons (e.g., IFNα, IFNβ IFNγ) have half-lives on the order of 3-4 days,[278] while some cytokines, such as plasma IL-8, has have half-lives on the order several hours.[279] Thus, the implantation period and device design may need to be tuned to maintain sensitivity to analytes with short half lives.

We have demonstrated one key readout—the MAGPIX assay—but the capsule has a versatile design amenable to a range of readouts, assays, and capabilities. We validated the assay with MAGPIX, as it provided a multiplexed platform amenable to 100s of analytes that can be analyzed in any combination. However, the sample can be processed for RNA, DNA, proteins, or nearly any soluble factor. In validation studies, we have tested this with streptavidin coated M280-dynabeads, looking for only specific proteins. If the analyte of interest is low in abundance, the size of the reservoir can be increased, though it may be challenging to tune a greatly enlarged reservoir for desired sampling rates. An alternative strategy would be to fill the capsule with analyte-specific beads to create a large sink. The challenge here is that additional filling techniques might be needed as centrifugal filling may be incompatible with large beads. A similar approach would be to coat the inside of the reservoir with an antibody specific to the target analyte using standard techniques.[280] This would enable ELISAs to be performed inside the reservoir simply by spinning antibodies, washes, and stains/substrates into and out of the reservoir and imaging directly through the transparent reservoir material. Thus, this could enable in-capsule analysis, but carries with it similar limitations to traditional histology (i.e., readouts are limited in terms of number of analytes that can be measured), unless multiple capsules were implanted which would enable multiple endpoints (e.g., MAGPIX and DNA). Additionally, multiple capsules could permit sampling of distinct regions of heterogenous tumors. Finally, multiple device would, in principle, permit sampling for different time periods as devices could be inserted or removed asynchronously. We have not evaluated simultaneous implantation of multiple devices and thus further testing would be necessary.

One potential application of the device is initially as a companion diagnostic for assessing neoadjuvant therapies in breast cancer. In this setting, patients typically have a needle biopsy followed by a period of systemic treatment and subsequent tumor assessment and removal. We envision implanting the device at the time of the needle biopsy and assessing device contents upon tumor removal, thus integrating into current clinical practice with minimal alteration. The major steps towards realizing this goal are straightforward and well-defined. Although we see an immediate utility in assessment of cancer therapies, this technology is not limited to implantation in tumors. Given the small size of the capsule and diffusion-based operation, the capsule could be implanted into a variety of tissues in the body (i.e., normal or abnormal), further increasing the potential impact of this method. We envision advancing our approach to enable removal of the device without resection of the tumor to enable earlier timepoints of assessment. We also plan to explore the potential to simultaneously deliver drug locally and assess the effects of that drug using a single device. Such a method would avoid drawbacks of systemic therapy (side-effects, cost, and time) and allow our assessment approach move beyond the neoadjuvant setting.

11.5 Conclusion

This paper describes the first known design and implementation of a simple and flexible microscale implantable device capable of rapid (days) or long-term (weeks) sampling of tumors to accommodate diverse types of treatment responses and disease kinetics. Results demonstrate the ability to quantify and distinguishing soluble factor signatures of tumor treatment response via diffusion based-localized sampling of soluble factors within tumors. Moreover, the device enables measurement of significantly different treatment-specific analyte signatures inside the tumors compared to immediately adjacent to the tumors and in the peripheral blood. Taken together, the approach offers a new ability to locally assess drug response with a minimally-invasive, highly-multiplexed, and rich functional endpoint. We envision initial application of this approach is best-suited for neoadjuvant settings as a companion diagnostic to demonstrate its utility as a more rapid approach to assessing therapeutic efficacy.

Chapter 12 Integrated drug delivery and tumor sampling via a needle-implantable microdevice[11]

12.1 Introduction

Cancer is inherently difficult to predict and manage due to the genetic heterogeneity and instability of the disease.[269] This challenge is exacerbated by patient-to-patient heterogeneity resulting in unique combinations of evolving disease in unique genetic and epigenetic backgrounds. As a result, today, it is not possible to predict which therapies will be effective in any given patient. The goal of precision medicine is to better predict which therapy will work for a given patient to reduce unnecessary cost, side effects, and delay in effective treatment.[9] Additionally, precise selection would allow selection of drugs to optimize cure rates when given as adjuvant therapy. Thus, there is a critical need for technologies to predict treatment efficacy accounting for the unique factors in individual patients.[9, 269, 270]

Many approaches have been developed to predict therapeutic efficacy. One major approach is to predict therapeutic sensitivity based upon genetic signatures of both the individual and the disease.[271-273] Advantages of the approach include flexibility for application across nearly all tumor types and a relatively straightforward path towards a simple and robust molecular assays. However, challenges of genetic heterogeneity, instability, and evolution as well as the limited rate at which data can be gathered limit the application of genetic signatures alone.[271, 273, 281] Additionally, it is challenging to develop therapeutic strategies directly targeted at specific genetic features of cancer such as tumor suppressors or oncogenes such as KRAS with exceptionally high ligand affinity.[282, 283] A more empirical approach would test efficacy in each tumor separately: for example, ex vivo drug sensitivity assays to test multiple cancer therapies at a time on tumor cells ex vivo for a given individual and cancer at any stage of disease, a process known as chemotherapy sensitivity and resistance assays (CSRAs).[284-286] However, standard

11 This chapter has been adapted from a manuscript in preparation for publication: "Integrated drug delivery and tumor sampling via a needle-implantable microdevice" David J. Guckenberger, Jay W. Warrick, Alka Choudhary, Amanda Schulman, Jennifer Mirrielees, Ross Vitek, Brian Johnson, Lee Wilke, Mark E. Burkard, and David J. Beebe

CSRAs perform poorly in predicting therapeutic efficacy.[284-286] This failure in predictive value may arise from inability to recapitulate the influence of the tumor microenvironment and pharmacology of a drug ex vivo.[287, 288] Still, the potential advantages of empirical tests has spurred new generations of CSRAs. These next generation CSRAs largely differ with respect to the extent to which the in vivo environment is recapitulated, ranging from multi-cell type 2D, 3D, and organotypic cultures to patient derived xenografts (PDXs) implanted in immunodeficient mice. Although these are promising, they are nevertheless limited as model systems which cannot fully recapitulate the natural environment that exists within a human tumor. We conclude that the best and most direct way to test drug sensitivity in a tumor would be to deliver drug locally into the intact tumor and to assess response locally in the intact tumor.

These approaches are also showing promise, yet there exists the possibility to potentially assess drugs directly within the patient, referred to here as minimal risk in vivo assessment (MRIA). Few examples of MRIA exist,[289, 290] but the general concept remains the same. Whereas *systemic* drug delivery or implantable therapeutic devices[291-294] deliver high doses of drug with risk of significant toxicity, MRIA technologies deliver drugs in small doses directly into the tumor, intended to assess drug efficacy rather than treat the tumor. This localized delivery of small doses imposes minimal risk, but is sufficient to assess therapeutic efficacy. However, a fundamental challenge associated with MRIA is that it is challenging to assess drug-specific efficacy amidst the heterogeneous background within the tumor. Prior studies have typically employed histology, which has several issues that impair uniform and valid assessment of response. First, the device itself can impede histologic analysis as it is removed, asymmetrically disrupting the tissue adjacent to the device. Second, histology often requires immunostaining which is limited to ~5 analytes per histology slide. Finally, tumor excision is not always clinically indicated. Analysis is particularly cumbersome because drug responses must be assessed geographically within the adjacent tissue as drug concentration and tumor heterogeneity will vary with distance from device. Another challenge with existing technology is that the duration of delivery is limited to 72 hr,[289, 290] which is not an appropriate time-frame for all therapeutic options. Thus, a method

that could deliver drug for longer durations and simultaneously assess local effects of drug would overcome many of these difficulties and help to standardize MRIA technology for future clinical usage.

Here we present a fully implantable technology that enables simultaneous drug delivery and intra tumor sampling in vivo for downstream cytokine profiling. The technology is simple to manufacture and tune, enabling long term delivery (weeks as opposed to days) to accommodate a wider range of therapies. Because this technology relies on diffusion, it simultaneously samples as it delivers. Thus, a downstream MAGPIX assay can be used to assess up to 500 analytes simultaneously, captured from a localized region. We evaluate numerous design configurations and demonstrate how the various configurations impact delivery, sampling, and simultaneous delivery in sampling. We present numerically simulated results, ex vivo characterization, and in vivo (murine) characterization to fully demonstrate the utility and potential of this implantable technology.

12.2 MATERIALS AND METHODS

12.2.1 Capsule Design (fab / assembly)

The implantable capsule consists of three components: a reservoir, and needle (to regulate diffusion), and anchors **(Fig. 12.1)**. The 10 mm long reservoirs, made from polymethyl methacrylate (PMMA) tubing with a 0.667 mm I.D. and a 1 mm O.D. (#MORCAP25, Paradigm Optics), were cut to size by circumferentially scoring with a razor blade and bending the piece to break cleanly along the scored line. The 30 G stainless steel needles were custom cut to a length of 4 mm (304SS tubing, T.I.G. welded and plug drawn, hard temper, 30RW, bias point; VITA Needle). Anchors were prepared made by cutting 1” lengths of .004” (102 μm) diameter stainless steel wire (#GWX-0040, Component Supply Co.), and bending them in half. Capsules were assembled by: (1) inserting the creased end of the anchor into the tube until it was flush with the back end; (2) a 1 mm long plug of UV curable glue (#1128A-M-T, Dymax) was capillary filled into the back end of the tube and cured with UV light – sealing the back end and securing the anchor; next, the needle was inserted into the front of the tube to a depth of 1 mm; (4) glue was added and allowed to capillary-fill around the inserted portion of the needle (the glue pins [295] at

the end of the needle without covering the open end) then cured with UV light. The reservoir was defined as the region between the two plugs of glue. The anchors, sticking out past the needle, were trimmed to a length of ~2 mm and bent to a ~45 ° angle. Note, steps 3 & 4 are only pertinent to capsules with needles, the collection capsules only used steps 1 & 2. Assembled capsules were sterilized through 15 min treatment of UV light.

12.2.2 Capsule filling and emptying

Multiple capsules were simultaneously filled and emptied by centrifugation. To fill the capsules, enough reagent (e.g., drug, dye, PBS, agar) to fully submerge the capsules was placed into a 1.5 mL tube. Multiple capsules (1 - 10) were placed in the microtube with the needles facing upward. The tube was spun for 30 seconds in a microfuge at 2000 rcf. Open faced capsules would fill completely, however capsules with needles in them would occasionally have a small bubble near the needle – a result of the glue contracting and forming a small pocket. To relocate the bubble to the opposite end of the capsule, the capsules were inverted, placed back into the reagent, and spun for ~2 seconds. Filled capsules were rinsed with PBS—to remove drug from the outside of the capsule—then stored PBS on ice until implantation. Capsules were filled within 1 hour of implantation, and were stored in PBS to avoid evaporation—which could form a bubble in the needle. Capsules used for drug delivery were filled with a 2% agar solution with appropriate concentrations of drug. Capsules used to capture analytes were filled with 2% agar solution. Agar was loaded in its liquid state, then solidified in the capsule by cooling. To remove fluid, capsules were placed with the needle facing downward in an empty 1.5 mL tube and centrifuged for 30 seconds. Though multiple capsules could be emptied simultaneously in a single tube, we emptied them individually.

12.2.3 Design and Fabrication of the Implantation Device

The mechanism for implanting the capsules was comprised of 3 components: a 10 mL syringe (#309604, Becton Dickinson), a push-rod, and an injection needle **(Fig G.1)**. The injection needle - a 0.75” long 16 G hypodermic needle (#SC-360857, Santa Cruz Biotechnology) - was mounted to the end

of the syringe. The push-rod - a 1.5” long 19 G blunt end needle (#NE-193PL, Component Supply Co) - was placed within the cavity of the syringe; its tip was placed into the base of the injection needle. The capsule was placed inside of the injection needle, such that the anchors were completely contained. After the needle is inserted into the desired location, the capsule is ejected by pushing on the syringe plunger, whereby the push-rod would go into the injection needle and push the capsule out. Importantly, to prevent compressed air from ejecting the capsule and prevent air from being inserted into the mouse, an air escape hole was drilled into the front of the syringe reservoir.

12.2.4 Capsule Performance Characterization

Capsules were characterized for leakage, delivery rate, and reservoir volume in vitro. Capsules were filled with fluorescein at a concentration of 5 mg/mL, rinsed in baths of PBS to remove excess dye, then placed into a 0.6 mL tube containing 400 μL of PBS. Over the 30 day time period, the fluorescent intensity of the bulk PBS (i.e., the amount of leaked or delivered dye) was measured on a fluorospectrometer (NanoDrop 3300, Thermo Scientific). Measurements for the leakage test (n = 60 capsules) were made weekly, while measurements for the delivery rate (n = 16 capsules) were made daily. To prevent normal delivery of the dye, the needles of the capsules utilized for the leakage testing were sealed with the glue prior to placing into the 0.6 mL tube . Fluorescent values were normalized to a standard curve to alleviate any issues of photobleaching. After 4 weeks of delivery, each capsule was imaged on a stereoscope. The reservoir length was measured using ImageJ and the volume was calculated. The volume of reagent within the reservoir was calculated by calculating volume of the reservoir and subtracting the volume of bubbles, when present. Each capsule was then rinsed, dried, placed upside down in a microtube tube, then spun to remove the contents of the tube. The contents of each tube were measured on a NanoDrop to assess the remaining fluorescence in the capsule (i.e., to calculate percent delivery).

12.2.5 Cell Culture

The MDA-MB-231-luc-D3H2LN human breast epithelial carcinoma cells (Caliper Life Sciences) were cultured in a humidified atmosphere at 37 °C with 5% CO2. These cells were cultured in DMEM-HG media supplemented with 10% FBS, 1% Penicillin streptomycin, passaged every 5 Days at a 1:5 dilution, and used prior to passage 6. The cell line was generously donated by Dr. Jamey Weichert.

12.2.6 Mouse anesthesia

Mice were anesthetized by first inducing at 4% isoflurane in a chamber over a period of approximately 1 minute until the loss of righting reflex has been observed. The animal was then be removed from the chamber and a nose cone was used to deliver isoflurane at 1-2% for the duration of the procedures. Anesthesia was used during xenografting and capsule implantation.

12.2.7 Xenograft Tumors

Mice (5-7 weeks old homozygous nu/nu female nude mice (Jackson Laboratories; Maine)) were xenografted by injecting 100 μL of DMEM-HG medium + 10% FBS of 2.5×10^6 MDA-MB-231 -luc-DH3L2N cells into the rear flank of the mouse. Tumors were allowed to grow for 4-6 weeks, and were measured weekly to monitor the growth of the tumor.

12.2.8 Capsule Implantation and Removal

Using the previously described implantation device, capsules were implanted when the average tumor size along the tumor major axis was ~10 mm (typically at ~3wks post injection). At the time of implantation, tumor sizes ranged from 6-15 mm. Capsules were implanted from the posterior side of the mouse, generally parallel to the cranial-caudal axis. Intratumoral capsules were implanted at a depth of ~4-6 mm, leaving roughly half of the reservoir sticking out of the tumor; extratumoral capsules were implanted subcutaneously ~2-4 mm from the tumor. The wound (from the implantation device)was sealed with Vetbond (3M tissue adhesive 1469, Fisher Scientific). Mice were euthanized via carbon dioxide gas, the tumors were immediately excised, and the capsules removed. See ‘Histology’ for description of subsequent tumor processing.

12.2.9 Histology

After imaging for doxorubicin, the tumors were fixed for 2 days in a 10% formalin (EMD Millipore, 65346). They were then put into 70% ethanol (Fisher Scientific, 04355223) for up to 1 week. The position of the capsule was marked with pins. The capsule was removed from the tumor. The tumor was then bivalved using the pins as guides. The tumor halves were then paraffin embedded and sectioned. Histology sections were made parallel to the bivalved faces. Serial step sectioning was performed, acquiring 5 consecutive sections of 5 µm thickness followed by a 250 µm step, repeated 3 times for a total of 15 histology slices per tumor half. Sections were mounted on charged slides, incubated for 20 mins at 80°C. Sections were deparaffinized in 3 changes of xylene, 5 mins each. Sections were hydrated through graded ethanols, then rinsed for 5 min in dH_2O. For some sections, we performed heat-induced epitope retrieval (HIER) in citrate buffer (pH 6.0, 10mM citric acid, 0.05% tween-20) for 3 mins in a Biocare decloaker (Biocare Medical), cooled for 30 mins, and rinsed in PBS. Sections were blocked with 10% goat serum for 1 hr @ RT. There were 4 different staining protocols: (A) no DAPI, no antibodies, no antigen retrieval; (B) no DAPI, no antibodies, with antigen retrieval; (C) DAPI, Ki67 (1° @ 1:50 - Vector, VP-K452; 2° @ 1:500 - LI-COR, 926-32210), cleaved caspase 3 (1° @ 1:200 - Cell Signaling, 9579S; 2° @ 1:500 - Invitrogen, A-21244). Primary antibodies were diluted in PBS with 1% goat serum; and (D) standard hematoxylin and eosin staining. Secondaries were diluted in PBS. Sections were then rinsed 3 times with PBS and finally in dH_20 for 5min. Prolong Gold antifade reagent was used for mounting coverslips. When nuclear staining was included, DAPI (Invitrogen, D130) was included with the mounting reagent. The sections were imaged on an automated Eclipse Ti inverted epifluorescence microscope (Nikon) equipped with an ORCA-Flash4.0 V2 Digital CMOS camera (Hamamatsu) and customized SPECTRA X light engine for NIR applications (Lumencor).

12.2.10 Micro MAGPIX Assay

Capsules without needles were implanted both intra- and extra-tumorally. After excision, the capsules were immediately stored in 0.2 mL PCR tubes to limit evaporation and processed within an

hour. Based upon previous work quantifying secretion from MDA-MB-231 cells, a MAGPIX assay was used to detect IL-8 and MCP-1 collected via the implantable capsule.[276] The wash buffer, calibrator diluent, standards, and microparticle cocktail were prepared following manufacturer protocol. However, prior to use, the microparticles were concentrated by collecting the particles via a magnet, removing the supernatant, and resuspending in bead diluent provided with the kit to a 3 μL total volume per sample. This allowed mixing of the small 3 μL samples at 1:1 [vol:vol] with the microparticle cocktail as suggested in the manufacturers protocol. To do so, the outside walls of the capsules were dried with lint free wipes (to prevent contamination) and the contents of each capsule (~3 μL) were spun into independent 0.6 mL tubes. 3 μL of microparticle cocktail was immediately added to each sample. The tubes were placed on an orbital shaker for 3 hours at 300 rpm. After incubation, 100 μL of wash buffer was added to the tubes and samples were transferred to the microplate provided with the kit. All subsequent steps were performed following manufacturer protocols. Each MAGPIX assay was run with the provided standard, a background control (i.e., PBS spun from the capsule), standard which was spun into and out of a capsule, and standard premixed with agar spun into and out of a capsule. Data from the MAGPIX assay were calculated using mean fluorescence intensities.

12.2.11 Comsol Modeling

COMSOL Multiphysics software (COMSOL Inc.) was used to model capsule function in a simplified model of the tumor environment. The tumor model consisted of published, physiologically relevant cell densities, diffusion characteristics, proliferation rates, and drug cytotoxicity. Capsule features, including reservoir length, volume, and diameter, as well as needle length and diameter, were probed to assess design impacts on capsule function. Analyte capture, drug delivery, and simultaneous capture/delivery were assessed by quantifying average reservoir concentrations of analyte/drug over time. The capsule function was modeled over a 14 day period, and reported at 0.1 day intervals. A full description of the comsol model, as well as the parameters and constitutive equations, can be found in the appendix.

12.3 RESULTS AND DISCUSSION

12.3.1 Capsule concept and design

The capsules were designed to be robust, simplistic, versatile, manufacturable, and comprised of materials approved for in vivo applications. We use two types of capsules: diffusion regulated and open orifice. Diffusion regulated capsules are assembled with additional hypodermic needle as the orifice to control the rate of diffusion and are primarily used here for localized drug delivery. Open orifice capsules are fabricated without a needle to maximize diffusion rates into the capsule for studies focused on sampling the tissue microenvironment. The capsule is comprised of three key components: a reservoir, anchors, and a regulation needle **(Fig. 12.1A)**. The reservoir is made of 1 mm O.D. / 0.667 mm I.D. poly(methyl methacrylate) (PMMA) tubing. for sufficient rigidity to withstand implantation, yet small enough to fit into a standard size biopsy needle (16 G). Anchors are made from stainless steel wire. We found the .003" - .004" thick wire to be ideal as thicker wires were overly stiff (making it them difficult to get into the implantation needle) and thinner wires were overly flimsy (theY did not provide sufficient support to immobilize the capsule). The anchors were bent to a 40° ± 10° degree angle (from the axis of the capsule). Angles greater than 50° would straighten while loading the capsule into the implantation needle and while angles under 30° were less effective at immobilizing the capsule in vivo. The needle used in diffusion regulated capsules not only controls drug delivery rate but also provides a point source to localize the treatment (see Localized Drug Delivery section). For our localized drug delivery applications, we selected a 3.5 mm long 30 G needle, given modeling suggested this geometry would provide persistent drug delivery for 2 weeks to ~2 mm diameter region of tissue. Diffusion-based delivery rates into the tumor are easily and predictably varied by altering the diameter or length of the needle (see COMSOL modeling in the SI). The anchors and needle are fixed to the reservoir with biocompatible UV curable glue. When glue is applied to the end of the reservoir capillarity acts to pull the glue into the reservoir and around a portion of the anchors and needle. The length of the glue plug is controlled by the volume of glue administered. Volumetric variability of the reservoir, as a result of error in the length of the glue plugs, was ~ ± 0.3 μL for the capsules with needles (95% confidence interval, n = 67 capsules)

(Fig. 12.1B), but variability was roughly half of that for capsules without the regulation needle. More precise methods of controlling the volume will likely be necessary for future applications. We assessed the stability of the glue seal in PBS, by monitoring leakage of a concentrated fluorescent marker from the capsule for four weeks; no leakage was observed (n = 16 capsules).

For simplicity we devised a method of filling and removing fluids from the capsules, using a standard benchtop microcentrifuge **(Fig. 12.1C)**. We filled capsules by first submerging the capsules (orifice facing upward) in fluid within a tube, then centrifuging the tube to replace the trapped air within the capsule with fluid. We validated the centrifugal filling technique with a variety of water based solutions including 2% agarose (prior to gelation). Generally, capsules fill within 10-15 s; however, as viscosity of the solution increases or the size of the orifice decreases, longer durations (~30 s) are required. Capsule filling was visually verified by checking for bubbles through the transparent tubing from which the reservoir was made. Capsules with a needle would occasionally develop a small bubble (average size of .172 +/- .154 μL) near the base of the needle as a result of short filling of the glue. When present, bubbles were moved away from the base of needle to avoid potential blockage by inverting the capsule in the same fluid and centrifuging briefly (1-5 seconds). Importantly, no bubbles formed post filling, normal handling or inverting did not move bubbles, and no bubbles were present in open-orifice capsules which do not have needles. Capsules were emptied by placing the capsule in an empty microtube (orifice facing downward) and centrifuging. Similar to filling, the time required to completely empty a capsule is typically 15 s and depends on fluid viscosity and orifice size. The centrifugation-based method of filling and emptying was 100% effective.

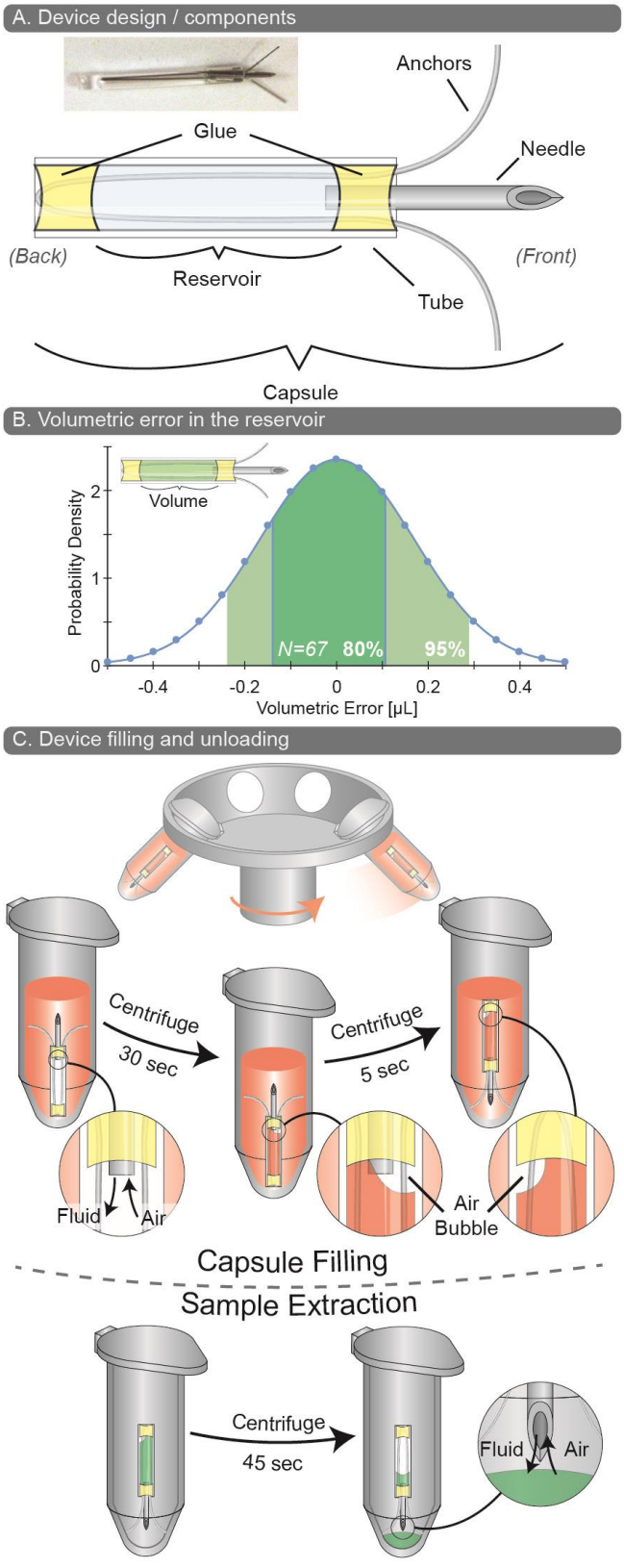
A. Device design / components
Anchors
Glue
Needle
(Back)
Reservoir
(Front)
Tube
Capsule
B. Volumetric error in the reservoir
Volume
Probability Density
2
1
0
N=67
80%
95%
-0.4
-0.2
0
0.2
0.4
Volumetric Error [µL]
C. Device filling and unloading
Centrifuge
30 sec
Centrifuge
5 sec
Fluid
Air
Air
Bubble
Capsule Filling
Sample Extraction
Centrifuge
45 sec
Fluid
Air

Fig. 12.1 Design, assembly, and fabrication overview. (A) Schematic of the capsule design and layout. Some capsules use for sampling were assembled without the needle and front glue. The tube length is 10 mm. (B) Volumetric error for reservoirs on capsules with two glued ends and a needle. 95% and 80% confidence intervals are shown (n = 67 capsules). (C) Capsules are filled by submerging in fluid and centrifuged. Capsules with needles may develop a bubble near the needle; in these cases, the capsule is inverted and centrifuged briefly (1-5 second) to force the bubble to the back of the reservoir. Capsules are emptied by centrifuging upside down in an empty tube.

12.3.2 Localized Drug Delivery

Computational modeling provides a method for exploring the impact of different device geometries on drug delivery and suggesting parameters for in vivo studies. The simulated device is initially filled with a the standard drug concentration given to patients, which is ~1000 fold higher than the estimated IC50 of the cells that make up the tumor in order to create a sufficient gradient for effectively treating a tissue perfused by the blood stream. Given the miniscule size of the capsule (under 3 μL) even a catastrophic failure or capsule leakage would be of minimal risk to the patient. Drug delivery is controlled by resistance from the regulation needle and volume of the reservoir. Thus, we created a model to characterize changes in drug delivery as a result of changing the needle diameter. In the following models we alter inner diameter of the regulation needle, using diameters of: 0.60, 0.41, 0.31, 0.26, 0.18, 0.16, 0.11, and 0.08 mm; by changing the needle G - 20, 22, 24, 26, 28, 30, 32, and 34 G, respectively. In addition, as the needle diameter is changed we either: (*case 1*) change both the length and diameter of the reservoir to maintain constant resistance or (*case 2*) change just the length of the reservoir to maintain a constant volume (i.e., as the needle diameter increases the reservoir length must decrease to maintain volume). In our first study, we investigate reservoir depletion by modeling the average amount of drug in the capsule over a time span of 14 days **(Fig. 12.2A)**. The time-to-depletion (t_{dep}) is highly affected by case 2 (black lines); a capsule with a 20 G needle will fully deplete ~3 days, whereas a capsule with a 34 G needle will only deplete by < 20%. This severe change is indeed due to the fact that diffusive resistance is highly affected by changing the needle diameter. The change in t_{dep} is much less drastic for capsules that maintain a constant resistance (blue lines). In case 1, the increasing t_{dep} as a result of increasing needle diameter is an effect of increased fluid volumes.

For each desired drug, it is important to know the desired concentration to be delivered to elicit the biologic effect. As drug diffuses out of the capsule and into the tumor, a concentration gradient is formed, originating at the orifice and extending into the tumor. In this study, we evaluate the distance between the orifice and the point at which the concentration matches the IC50 of the drug ($IC50_{dist}$) **(Fig. 12.2B,C)**. Using doxorubicin (Dox) as a model drug, a rapid increase in $IC50_{dist}$ is observed in the first ~0.5 days; this spike is a result of the concentration gradient forming. Then, as the reservoir depletes, the $IC50_{dist}$ recedes back towards the orifice. To assess how the $IC50_{dist}$ is affected in case 1, we modeled the $IC50_{dist}$ for 22, 24, and 26 G needles (**Fig. 12.2B**); needles smaller than 26 G would be longer than the tube itself, and needles larger than 22 G would be shorter than the length of the glue plug. As expected, the largest needle diameter had the longest $IC50_{dist}$ and receded more quickly than the 24 or 26 G needles due to reservoir depletion. Next, we picked four representative needle diameters - 20, 24, 30, and 34 G - to assess the how $IC50_{dist}$ is affected in case 2 **(Fig. 12.2C)**. For large needles (e.g., 20, where resistance is low) drug is released quickly and the reservoir is depleted quickly, thus the $IC50_{dist}$ changes by ~ 3 mm over the course of only 2 days. In contrast, diffusion through small needles (e.g., 34 g) is much slower, thus the $IC50_{dist}$ changes by only ~0.3 mm over the course of 14 days - which is key to maintaining steady treatment zones. Importantly, at treatment relevant concentrations, certain drugs, such as Dox, require prolonged treatment before effects are evident. Klinghoffer et al. and Jonas et al. report max treatment periods of 72 hr and 48 hr, respectively.[289, 290] By coupling a reservoir with regulated diffusion we are able to obtain prolonged delivery (order of weeks), which will be necessary to accommodate wider ranges of therapeutic options.

To experimentally validate our numerical models we tracked drug delivery over the 30 day time course in vitro. The capsule was filled with fluorescein (M.W. 332 g/mol, D=414 $\mu m^2/s$) - a dye that comparable in molecular weight to the cancer therapy medication doxorubicin (M.W. 543 g/mol) - which was allowed to diffuse into a 400 µL volume of fluid. We tracked the concentration of fluorescein in the surrounding fluid and plotted the results against a theoretical delivery curve **(Fig. 12.2D)**. Our data fall

within the 95% confidence intervals of our theoretical curve, demonstrating the ability to predict device behavior based upon geometry.

12.3.3 Drug Delivery In-Vivo:

The current design enables robust implantation and immobilization of the capsule throughout the implantation period. The capsules were implanted in tumors with a diameter of ~6 mm ± 2.3 mm (n = 27 tumors) . Capsules were not implanted into tumors less than 4 mm in diameter or those showing signs of necrosis. Resistance from the tumor provided tactile feedback which aided in locating the periphery of the tumor. Devices were successfully implanted with the tip of the device anchored in the peripheral region of the tumor and was qualitatively verified for all tumors upon tumor removal. As the capsule emerges from the implantation device **(Fig. G.1)**, the anchors expand and insert into the tissue to immobilize the capsule. Throughout the two weeks of implantation, the anchors were, in all cases, effective at holding the capsule in the tumor. Capsules that were implanted subcutaneously, adjacent to but not in the tumor, remained generally immobilized – some motion may have been present, but the general location and orientation of the capsules was maintained. Throughout the implantation time course, there was no evidence of irritation or inflammation resulting from the capsules; however, the capsules were tested in immunodeficient mice (Jackson Labs, female homozygous NU/J).

To verify that the capsule was capable of delivering drug in vivo, we implanted capsules filled with a live-cell fluorescent dye (CellTracker Red (CTR)). After excision, tumors were fixed, bivalved (see 'Histology') perpendicular to the capsule axis, near the tip of the capsule, then fluorescently imaged **(Fig. 12.3)**. Noted in **Fig. 12.3A** with dotted lines are the recessed holes left in the fixed tissue from the needle and anchoring wires after removing the device, indicating tumor tissue eventually surrounded the device closely. The diffuse fluorescence surrounding the capsule shown in **Fig. 12.3B** and **Fig. 12.3C** demonstrates that the device did not plug upon implantation. Further, the size of the needle orifice avoids plugging caused by to biofouling during the delivery period, allowing prolonged drug delivery. Tissue eventually surrounded the device closely, as evident by the holes where the needle and anchors were,

suggesting proliferation around the capsule. Noticeably, there is heightened fluorescence around the needle and each anchor; this is likely resultant of a fluidic path surrounding the needle that allows delivered substance to not only diffuse but mix with the interstitial fluid immediately surrounding the circumference of the needle and anchors. Thought this may influence the pattern of delivery, the localized and diffuse pattern of CTR illustrates device operation in vivo.

We tested in vivo delivery of Dox and assessed the feasibility of histology based quantification via Ki-67 and cleaved caspase 3 (Cl-Casp3): markers of proliferation and apoptosis, respectively. We expected an apoptotic Ki-67$^-$/Cl-Casp3$^+$ region around the orifice surrounded by a proliferative Ki-67$^+$/Cl-Casp3$^-$ region **(Fig. 12.3B**; representative image**)**. Noticeably, there is a void of cells immediately surrounding the needle orifice; this may be caused by overexposure of drug or wiggling (motion) of the capsule as a result of mouse motility. In several tumors, such as the one demonstrated in **Fig. 12.3B**, we observed the hypothesized effect, shown by the fan-like Ki-67$^-$/Cl-Casp3$^+$ region extending from the needle orifice. Intratumor heterogeneity, however, makes this treated region difficult to quantify. A comparison with an untreated tumor that was never implanted with a device **(Fig. 12.3C)** highlights significant challenges facing histological endpoints for quantifying localized drug efficacy. The untreated tumor illustrates Cl-Casp3$^+$ prevalence towards the center of the tumor and a Ki-67$^+$ (prolific) periphery; yet, the boundary between these regions and extent of heterogeneity was variable. We also tested the potential of ɣ-H2A.X, a marker of double-stranded DNA breaks[276] using additional sections of these tumors as a more Dox-specific readout of drug effect. Despite success detecting response to Dox in vitro using the same antibody and histology protocol, only basal levels of ɣ-H2A.X were detected in vivo. It is likely that these initial tests were not acquired at the right time-point match the kinetics of the ɣ-H2A.X phosphorylation in response to Dox. These attempts highlight the number of possible parameters and challenges in optimizing histological endpoints for just one drug and a few markers. Further optimization would be significantly time and additional costly mouse experiments. Given this natural intratumoral

heterogeneity, challenges of histology, and limited number of readouts that could be acquired, we explored new avenues of detecting drug-specific effects.

These initial studies made it clear additional mouse experiments to optimize histology with respect to sample preparation, alternative endpoints, and treatment-response kinetics, quickly becomes a costly and daunting task. For these reasons, we began to explore whether the factors that are diffusing into our device while delivering drug might be indicative of tumor response. Such an approach might have multiple advantages. First and foremost is that the device samples from precisely the same region that is treated by the drug. This approach keeps the treated and sampled regions inherently co-registered, contrasting significantly with histology where many careful steps are required ensure the final stained tissue sections and quantified regions are co-registered with the treated region of the tumor. The second major advantage is that hundreds of endpoints can be explored in a single sample. For histology, there is physically not enough tissue in the treated region to enable fair comparison of such a large number of biomarkers. By increasing the number of analytes per sample, informatics methods can be leveraged to identify predictive signatures, avoiding reliance on any one (or few) measure(s). Lastly, measurements of soluble factor concentrations are much easier to make quantitative than histology through the use of validated protein standards, significantly increasing the ability to translate such a readout to a clinical setting across many sites. Certainly histology is an ever changing field and advanced techniques such as mass-spec imaging could potentially be used to address many of these concerns.[296] However, such advanced approaches typically introduce additional parameters to be optimized, further illustrating the value of a straightforward biochemical readout.

For these reasons we explore the use of our device for simultaneous drug delivery and sampling of the tumor microenvironment to enable simple and robust biochemical testing and assessment from a single microscale implantable device. However, prior to testing simultaneous delivery and sampling, we first characterized the performance with respect to sampling alone.

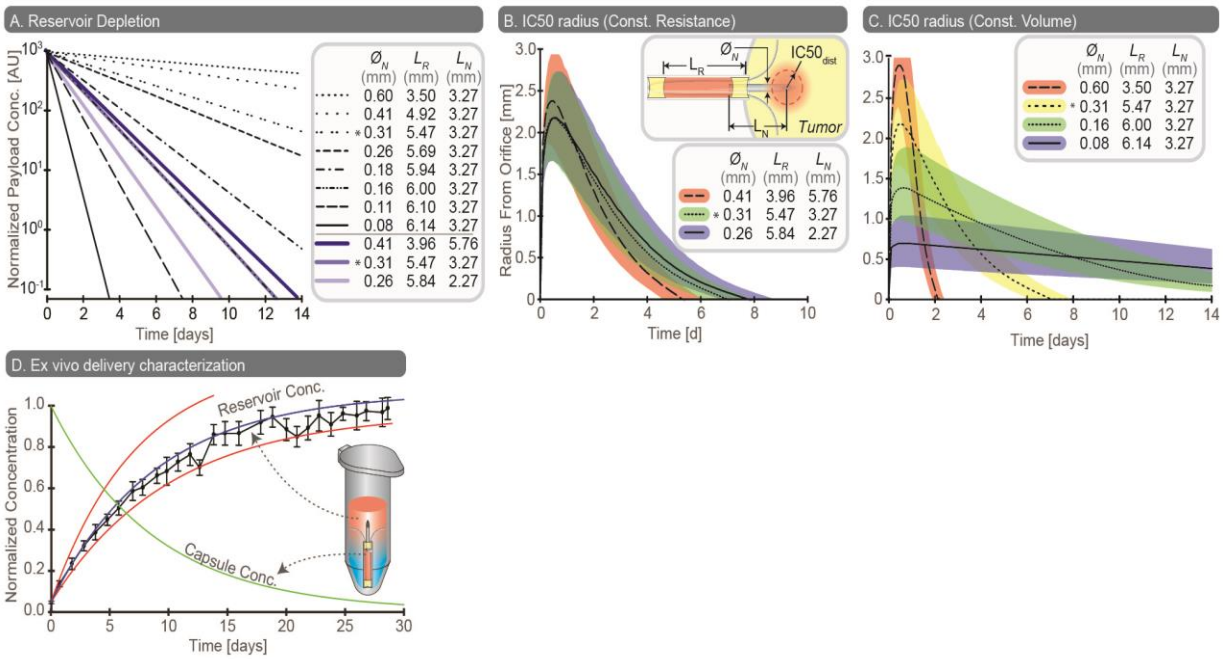

Fig. 12.2 Drug Delivery Characterization. (A) A plot of the simulated average drug concentration in the reservoir over time. Here we plot the effects of varying the reservoir diameter while maintaining a constant diffusive resistance (blue lines) and while maintaining a constant reservoir volume (black lines). Parameters marked with an asterisk are identical across conditions. (B & C) Simulated plots of the radial distance from orifice to the location at which the concentration matches the IC50 value (modeled for Dox). Colored region for each line represents the 2x and 0.5x of the IC50. Here we plot the effects of varying the reservoir diameter while (B) maintaining a constant diffusive resistance and (C) maintaining a constant reservoir volume. (D) A plot of the amount of payload that was delivered over a 30 day time course, in vitro. Black dots represent the experimental data, blue line (center) represents the theoretical delivery curve, and the red lines (upper and lower) represent the 95% confidence interval for this data (Error bars represent SD of the means, n = 27 capsules).

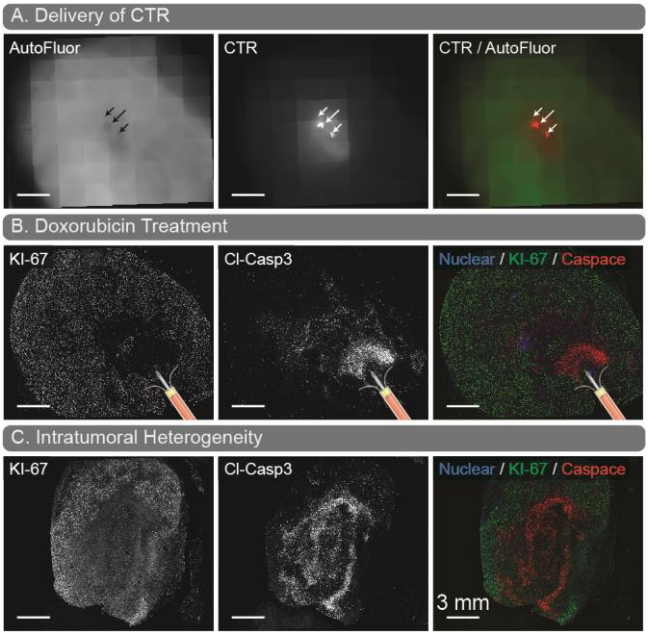

Fig. 12.3 Device validation using murine xenografts. (A) Bivalve image of a tumor after delivery of a CellTracker Red (CTR), demonstrating delivery of a compound from the capsule. Image is taken perpendicular to the capsule axis. AutoFluor represents the background autofluorescence of the tissue. Arrows indicate the location of the delivery needle (middle arrow) and anchors (outer arrows). (B) Cell death (KI-67-/Cl-Casp3+) as a result of treatment with Dox. (C) KI-67 and Cl-Casp3 heterogeneity of an non-treated, non-implanted tumor. Scale bars represent 3 mm.

12.3.4 Simultaneous drug delivery and sampling

Due to inherent challenges associated histology, and other analytic techniques often associated with assessment of chemotherapy, a capsule capable of both drug delivery and simultaneous sampling could prove beneficial. Because our capsule functions on diffusion, which occurs simultaneously in both directions, we are able to not only deliver drug but sample simultaneously. Though certain exceptions exist, in an ideal case we would likely deliver at a controlled rate, but sample as quickly as possible. In practice, this is not trivial. With just a single reservoir, drug will diffuse out at a rate controlled by the needle, but the needle will limit diffusion of analyte into the capsule. Thus, we theorized that, when using a single reservoir, there would be an ideal needle size to maintain stable delivery while capturing enough analyte for downstream analysis. Using the same parameters as our delivery models, we look at average analyte concentration in the capsule to assess how changing needle diameter affects delivery characteristics when the resistance (case 1) or volume (case 2) are held constant **(Fig. 12.4A,B)**. In both cases we observe a rapid (<1 day) spike in analyte concentration; this is an artifact of the rapid cell death

caused by formation of the gradient, causing rapid release of LDH. The concentration of analyte then continually decreases towards the equilibrium value in the tumor. Noticeably, larger orifice capsules deplete faster than the small orifice capsules. This is partially due to the fact that analyte can diffuse out quicker; but, more importantly, large orifice capsules deplete of drug faster, thus analyte production diminishes and the baseline to which the capsule is equilibrating is lower. Given these results, the ideal time to remove the capsule (to achieve the highest concentration of analyte) would be within half a day of the expected response (although longer if the orifice is small enough). However, despite the rather quick loss of analyte from the reservoir, capsules removed several days or even weeks after implantation will still show significant differences between detected analyte and baseline measurements **(Fig. 12.4C)**, and are less affected by slight changes in time (i.e., more stable).

One obvious concern with simultaneous delivery and detection is that cells close to the orifice will be exposed to excessive concentration of drug, and some of the analyte captured will be affected by these over-treated cells. The cells within the region defined by the $IC50_{dist}$ **(Fig. 12.2C)** forms a shell containing the treated cells of interest. This shell surrounds a sphere of overexposed cells. To determine the impact that of overexposed cells on the overall readout, we compare the volume of the shell to the volume of the inner sphere **(Fig. 12.4D)**. This volumetric ratio increases rapidly due to the fact that the $IC50_{dist}$ recedes as time goes on. However, because the smaller needles diffuse slowly (maintaining a more steady treatment that remains closer to the needle) the volumetric ratio is more favorable for smaller needles, as it rises quickly, then remains comparatively stable. Nevertheless, the signal from the overdose cells (inner sphere) should be largely masked by the signal of the appropriately dosed cells (shell), validating the utility our capsules for simultaneous delivery and sampling.

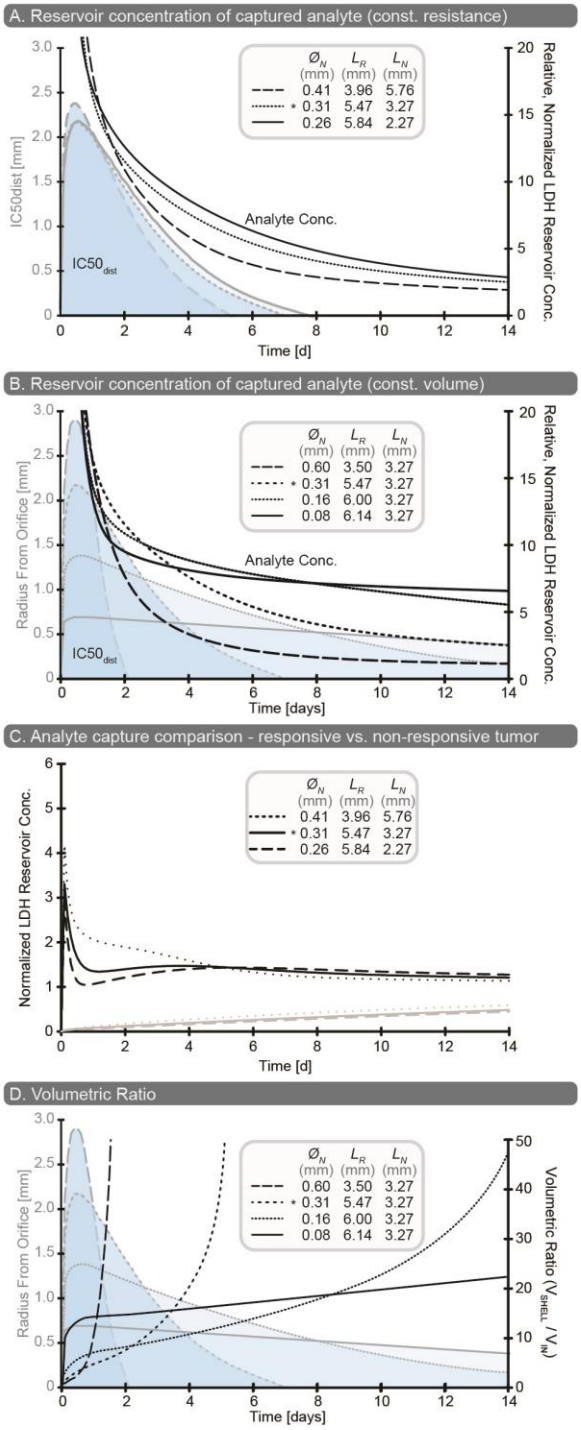

Fig. 12.4 Simultaneous sampling and delivery. (A & B) Plot of the simulated average concentration of captured analyte (using LDH as a model analyte). Here we plot the effects of varying the reservoir diameter while (A) maintaining a constant diffusive resistance and (B) maintaining a constant reservoir volume. (C) Analyte concentration differences between capsules placed in a responding (black) and non-responding (gray) tumor. Capsules placed in a responding tumor show significantly higher amounts of analyte. (D) A plot of the ratios between the volume of cells in the near-IC50 band versus the volume of cells exposed to excess drug doses as a result of close proximity to the needle orifice. Ratios greater than one indicate that the volume of the shell is 'X' times larger than the volume of the overdose cells.

12.4 DISCUSSION

Recent technological advances have facilitated localized drug delivery in vivo, enabling drug assessment prior to systemic treatment. However, researchers and clinicians rely on semi-quantitative and qualitative techniques, such as histology, to assess the impact of these drugs. Histology, though valuable, is dependent on microscopy which limits the range of obtainable readouts. Moreover, often drugs need to be delivered over long-periods of time to see a histopathologic effect in most tumor types. Here, we present an implantable, versatile sampling technology that facilitates multiplexed quantifiable readouts from localized regions in vivo. We demonstrate an added ability to locally deliver drug, and characterize the technology extensively through computational simulations as well as in vitro and in vivo experimentation. Further considerations and modifications will help advance this technology and move it closer to clinical implementation. In this section, we describe various benefits of the technology, propose potential modifications and important considerations, and discuss possible future applications.

A major advantage of our design is the simplicity, modularity, versatility, and manufacturability. The capsule is assembled with commercially available components that are glued together. The use of tubes and needles makes assembly and manufacturing simple and facilitates easy modifications to the reservoir volume and delivery and sampling rates. The caveat is that the length of the glue plugs is subject to error - affecting reservoir volume. Thus, more controlled methods of delivering glue or sealing capsules will be necessary to assure repeatability. The materials used in this study are biocompatible, and the transparency of the PMMA tube enables quick quality control to ensure that the reservoir has filled properly. However, for clinical use, alternative materials (e.g., stainless steel, titanium) may be necessary to visualize devices during implantation (e.g., ultrasound). Thought quality control to assure filling will be difficult with opaque capsules, our studies have demonstrated 100% success rates for filling. The one challenge with filling is capsule buoyancy -- capsules occasionally float in the fluid preventing submersion of the orifice. The anchors (sticking above the fluid surface) provided enough mass to push the orifice below the fluid surface, but capsules with large reservoirs may require additional mass to overcome the buoyancy. Tangentially, the anchors are also crucial to emptying the capsule as they hold

the orifice above the fluid, enabling air enter through the orifice **(Fig. 12.1C)**. Though a microcentrifuge was sufficient to fill and empty our capsule, faster centrifuges may be necessary if the orifice is substantially smaller (i.e., higher resistance) or if the fluid viscosity is substantially higher. The dimensionless Bond number can be used to calculate the g-force necessary to fill the capsule.

Modifications to the device design and the implantation device have the potential to further simplify implantation and improve repeatability. Capsules are implanted through an implantation needle, where a push-rod urges the capsule from the needle. The expanding anchors act as a plow, requiring simultaneous removal of the implantation device. A more ideal device would, instead of a push-rod, have a stationary inner rod with a retracting outer implantation needle, allowing the capsule to remain immobilized as the implantation needle is retracted. The size of the implantation needle - dictated by the diameter of the capsule - creates a practical lower limit on tumor size, which, with a 16 gauge (G) implantation needle (1.65 mm O.D. and a 6.16 mm bevel length), was ~4 mm. This lower limit was partially due to the long bevel having to go entirely through the tumor and partially because a 4 mm tumor was physically difficult to align with the large needle. However, many clinically observed human breast cancer tumors exceed this size.[277] Another concern during implantation is evaporation from the capsule, which can cause a bubble to form near the orifice of the capsule that will prevent both sampling and delivery. There is a practical working time of about 2-5 min, whereafter excessive evaporation will cause capsule failure. However, if the capsule is kept hydrated (e.g., by storing in fluid prior to implantation), the working time increases greatly. A final concern is biocompatibility. While implanted, the mice did not present signs of infection nor exhibit significant immune response around the device. This is most likely due to the immunodeficiency of the mice. Further testing in an immunocompetent background is necessary. However, methods to passivate the device surface such as parylene coating might be employed to further ensure tolerance and prevent an immune response that could affect interpretation of results.

It is important to note that our capsule samples over a course of several days, meaning we are, in essence, getting an average value from the entire implantation period with a bias towards recent events. The time span and effect of the bias is dictated by the size if the capsules. Smaller capsules will portray a flatter average over the entire implantation period while larger capsules will be much more affected by recent changes in concentration. The effect of the bias is dictated by the size of the capsule, where large capsules are more representative of recent events and smaller capsules represent more of an average over the entire implantation period, making the capsules less sensitive to temporally localized spikes in concentration. Further, because the capsules are filled with gel, the capsules capture analytes via diffusion, increasing specificity toward soluble factors and reducing capture of other factors such as cell debris. The caveat to long implantation periods potential degradation of captured analytes.

Simultaneous delivery and detection is conceptually feasible, but will need more characterization to become practically applicable. One major concern is that cells nearest to the needle will experience an extremely high concentration of drug, and as a result the readout will be impacted by these cells. Through the volumetric ratio, we have demonstrated that the signal from the targeted region should dominate the signal from the overdosed region, although the true correlation between this ratio and in vivo events will need further characterization. Nevertheless, a single point source for both delivery and detection may not be ideal. Alternative embodiments, where the sampling region is offset by $IC50_{dist}$, may be less impacted by the overdosed region but will also receive less analyte from the targeted region, thus we believe that, for this application, a single point for both delivery and sampling will work best. In a preliminary study, we attempted to both deliver drug and sample from the delivery region. We did not see a significant difference between the capsule that delivered drug and the capsule didn't deliver drug. However, we speculate that this is a result of poorly selected experimental parameters (i.e., the time period was too long that we missed the effect from the drug), rather than capsule function. Further treatment investigation, such as sampling tumors during systemic treatment, may be a next best step assess drug impacts, then attempt to repeat the dual delivery and capture.

We have demonstrated one key readout - the MAGPIX assay - but the capsule, again attributed to the versatility, is amenable to a range of readouts, assays, and capabilities. We validated the assay with MAGPIX, as it provided a multiplexed platform amenable to 10s of analytes that can be analyzed in any combination. However, the sample can be processed for RNA, DNA, proteins, or nearly any soluble factor. In validation studies, we have tested this with streptavidin coated M280-dynabeads, looking for only specific proteins (data not shown). The caveat, of course, is that there may not be detectable levels of the analyte of interest. The most-simple way to increase the amount of captured analyte would be to increases the size of the reservoir, which comes with the aforementioned difficulties of tuning the needle and reservoir to achieve set sampling rates. An alternative strategy would be to fill the capsule with analyte specific beads to create a large sink. The challenge here, of course, is that large (micron sized) beads will settle out of solution during the filling process, thus centrifugal filling methods may not be compatible with all bead sizes. A similar approach would be to coat the inside of the reservoir with an antibody specific to the target analyte using standard techniques.[280] Such an approach would enable ELISAs to be performed inside the reservoir simply by spinning antibodies, washes, and stains/substrates into and out of the reservoir and imaging directly through the transparent reservoir material. This approach would enable in-capsule analysis, but carries with it similar limitations to traditional histology (i.e., readouts are limited in terms of number of analytes that can be measured). Given this capsule is able to deliver a steady gradient, this type of device , could be used to capture migratory cells, similar to other demonstrations of in vivo cell migration and capture assays.[297, 298] However, agarose blocks cell migration, thus alternative gels (e.g., collagen, matrigel) or no gels may be necessary to facilitate migration. Something of interest to both migrational studies and cancer treatment studies are competitive gradients, and combinatorial effects. Capsules could be placed adjacent to one another for create two gradients or either a drug or a chemoattractant. However, placement of the capsule and control of proximity, and tissue heterogeneity may complicate this, thus further testing would be necessary.

Though we see an immediate utility in assessment of cancer therapies, we don't see any reason why this technology would be limited to tumor implantation. The capsule can be implanted and immobilized in nearly any location. However, at this point, the capsules are removed through recision. Thus, alternative structure will likely be necessary to facilitate capsule removal. Though further work is necessary, these capabilities and examples high the versatility of our technology, and provide methods by which researchers adapt this assay to meet their needs.

In sum this paper describes the first known design of a device capable of simultaneous drug delivery and tumor sampling. The device described here is capable of long-term drug delivery over weeks. Moreover, we have demonstrated the ability to detect reproducible variation in cytokines within tumors compared with outside tumors. Further advances in this device will allow low-toxicity delivery of anticancer drugs into tumors and simultaneous assessment of response to therapy. We anticipate that this method promises to allow multiple drugs to be tested simultaneously and empirically so that the most effective cancer treatments can be selected as precision medicine for cancer patients.

Chapter 13 Kit-On-A-Lid-Assays for accessible self-contained cell assays.[12]

13.1 Introduction

In-vitro cell based assays, have become essential tools for elucidating the mechanisms of human diseases and powerful platforms for drug discovery and testing.[299] A plethora of in-vitro assays have been developed to measure cellular phenotypical features of interest, such as proliferation,[300] migration, [155, 301] adhesion,[21] soluble factor secretion,[302] co-culture,[18] or gene expression.[303, 304] However, cell-based assays are not standardized, require a multitude of different reagents, pieces of equipment, and processing steps, and often require significant re-development. Furthermore, as limitations of immortalized cell lines have become well established, biologists and medical researchers are moving towards more relevant cell models, such as human primary cells, and stem cells. However, the rarity of these cells, and the unique source of these cells (e.g. specific clinic for patient primary cells) impose logistical barriers and limit the accessibility to advanced biomedical research. There is therefore a need for developing platforms that allow a more efficient use of rare cells and reduce logistical barriers to sharing and collaborating between clinicians and biomedical researchers.

Kits containing all the reagents required for a particular assay, such as PCR or nucleofaction, have facilitated the operation certain assays. However, few exist that integrate the whole cell-based assay including pre-packaged reagents, plastic-ware, and cryopreserved cell-suspensions. Similarly, several microfluidic platforms that allow pre-packaging of the reagents have been demonstrated and belong to two main categories. The first is point-of-care diagnostics, and comprises platforms allowing the measure of a particular bio-chemical marker in a human sample.[305, 306] The second are high-density combinatorial platforms, such as the SlipChip,[307] that allow performing a multitude of mixing combinations with a given

12 This chapter has been adapted from the following publication: "Kit-On-A-Lid-Assays for accessible self-contained cell assays." Erwin Berthier*, David J. Guckenberger*, Peter Cavnar, Anna Huttenlocher, Nancy P. Keller, and David J. Beebe. Lab on a Chip, 2012.

* Authors contributed equally

sample, but does not integrate fluid handling and cell cryopreservation. Here, we demonstrate a microfluidic kit-on-a-lid-assay (KOALA) platform that integrates every aspect of cell-based assays, including reagent pre-packaging, cell cryopreservation, cell culture, and fluid handling. The KOALA platform enables the creation of self-contained cell-based assays that reduce the need for laboratory equipment and significantly reduce the time and reagent requirements for cell-based assays **(Fig. 1)**. To our knowledge, this represents the first microfluidic platform that allows the freezing, cryopreservation, and thawing of cell-suspensions.

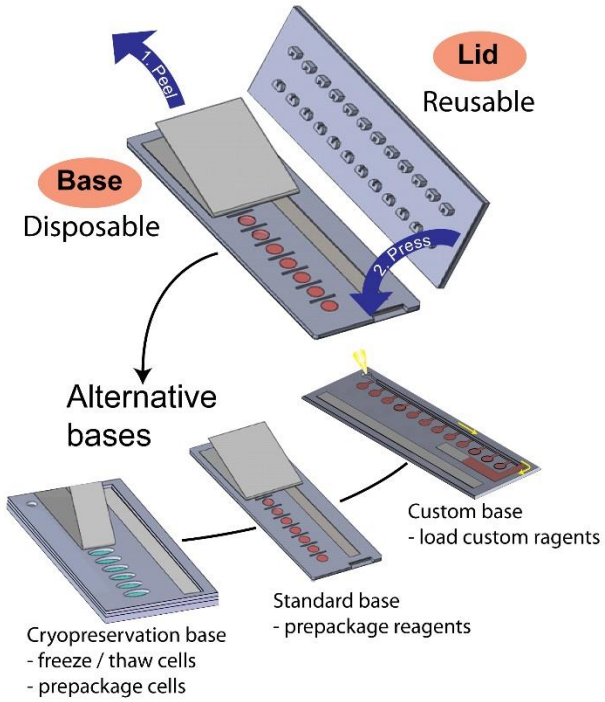

Fig. 13.1 KOALA concept overview. A lid containing microchannels is put in contact with a base containing pre-packaged reagents. Upon contact the fluid in the base flows into the microchannels replacing the fluid it previously contained. The KOALA platform is modular and multiple bases with specific functions can be developed for the cryopreservation of cell suspensions, the shipping and storing of reagents, or the rapid custom loading of reagents for instance.

Microfluidic methods have been shown to improve on many traditional in-vitro assays for the studying of soluble factor interactions in multiculture systems,[18] the interaction between cells and their substrate,[308, 309] and properties of cell migration. [155] Furthermore, microfluidic methods improve various aspects of fluid handling including the control of fluid paths,[310] washing efficiency,[311] and reagent use.[312]

While the highest degree of precision is achievable with syringe-based microfluidics,[313] the equipment and skill required represent a barrier to adoption in biology laboratories. An increasing body of work has identified this issue and developed more accessible open microfluidic platforms. For instance, passive pumping systems,[14, 157] capillary systems,[314] and systems integrated into well plates,[23] are operable with a traditional pipette and have been successfully applied to biological and clinical investigations. These methods, however, still require that all the reagents be prepared in a traditional way (e.g. using eppendorf tubes, pipettes, centrifuges, etc.). Furthermore, every channel is usually filled manually and sequentially, limiting the claims of efficiency and user-friendliness as device and reagent preparation can represent a large part of the experimental process.

The KOALA platform alleviates these issues by enabling the pre-packaging of all the reagents required in a cell-based assay and integrating novel fluid handling ability. The KOALA platform is composed of two parts, one is a lid containing microchannels and the other is a base containing microwells filled with the reagents to flow into the channels **(Fig. 1)**. When the two parts are placed in contact, the fluid in every channel is replaced simultaneously by the fluid contained in the wells. This process can be repeated with a second base, in order to flow a second reagent in the microchannels contained in the lid Furthermore, the microfluidic base containing the reagents can be sealed, frozen, and stored for extended periods of time. This methodology is amenable to a multitude of assays as most fluids (e.g. cell culture media, washing buffers, cell suspensions, fixing/staining solutions, un-polymerized gels, etc.) can be handled.

We demonstrate that the KOALA platform can be used to perform simple and efficient fluid handling with pre-packaged reagents. Secondly, we show that the KOALA platform allows the culture of cells for extended periods of time. Further, we demonstrate functionalized KOALA-bases, which allow the thawing and preparation of cell suspensions for culture without requiring centrifuges or traditional laboratory equipment. Finally, we demonstrate the broad applicability of the KOALA platform by

performing a cell-assay with multiple types of readouts, including live-cell dyes, molecular stains, and immunochemistry.

13.2 Materials and Methods

13.2.1 Fabrication of the KOALA device.

The KOALA platform was fabricated using plastic micromachining methods. In brief, the lids of the KOALA device containing the channels were fabricated out of two 1.2 mm thick polystyrene (PS) sheets (640-597-67, Good fellow, UK) **(Fig. 1A, Lid)**. The pieces were modeled in Solidworks (Dassault Systemes, USA), imported into SprutCam (Sprutcam Technology Inc, Russia), and exported into a TAP file for milling on a CNC milling machine (PCNC 770 mill, Tormach, USA). The top piece consists of a series of posts with a horseshoe-shaped cross-section. The posts on the input side of the channel were 1 mm tall, and those on the output 0.6 mm. The post is a cylinder of 1.5 mm diameter in which was placed a 0.8 mm wide slot extending from the edge to the center of the post. A through hole of 0.8 mm was milled at the center of the post to connect with channels milled in a second lid part. The channels have a width of 0.8 mm and span 8 mm from the centers of the two posts. The depth of the channels varied such that the channel was 250 um deep near the inlet and outlet, and tapered to 1 mm deep in the center. The two pieces were bonded together using a solvent bonding approach consisting of heating one piece up to 65 degrees Celsius, applying Acetonitrile (2710004, Sigma Aldrich, USA) to the other piece, and placing them in contact on a hot plate while applying gentle pressure.[315] After 20 seconds the pressure was released, and the remaining traces of solvent were left to evaporate for 2 hours. Finally, the channel was treated with oxygen plasma (FEMTO, Diener Electronics GmbH, Germany) for 50 seconds at 50W with a 20 sccm oxygen flow. A method developed previously to induce hydrophobic recovery of plastic surfaces was used on the top surface around the posts to revert the contact angle back to that of untreated PS.[197] Similarly, the KOALA standard bases **(Fig 1A, Base)** were fabricated in two pieces of PS; one of 1.2 mm thickness in which the microwells were milled as well as a groove designed to hold a strip of absorbent pad. (CFSP223000, Millipore, USA) The piece was then solvent bonded to a 250 μm thick PS sheet. All

additional and specialized bases **(Fig 1)** were fabricated in a similar fashion to the KOALA-lid and standard base.

13.2.2 Fabrication of the KOALA cryopreservation base.

The KOALA cryopreservation base was fabricated using the same micro-milling technology as described in the previous section. Four parts were fabricated: the bottom part milled in a 1.2 mm sheet, comprising of a large well for holding the dialysis media, and three parts milled in a 250 µm sheet comprising of elliptical holes of small radius 2 mm and large radius 4 mm. A micro-porous polyester membrane with a pore size of 3 µm (T30CP14220, GE Water & Process Technologies, USA) was bonded between upper parts, with two on one side of the membrane and one on the other, using the same weak solvent bonding approach. Finally, the bottom part was bonded to the structure containing the porous membranes.

13.2.3 Cell preparation and culture.

HUVECs, BEAS-2B, HEK-293, and 3T3 cells suspensions were prepared from cell cultures grown to confluency in a T25 flask. After a 4 min trypsinization process, the cell suspension was diluted in culture media (following the recommendation from ATCC for each cell line), centrifuged for 3 min at 600 RCF, and re-suspended to 2 million cells per mL. Cells prepared for freezing were re-suspended in 10% dimethyl sulfoxide (DMSO), 20% fetal bovine serum, and 70% culture media. For immediate loading into the KOALA device, 8 µL of cell suspension were loaded into each well of a KOALA-base. For freezing, 10 µL were added to each of the wells in a KOALA cryopreservation base, and scotch tape was used to seal the device, which was subsequently placed in a -80 degrees Celsius freezer until the time of use.

13.2.4 Cell-based KOALA.

When using the KOALA cryopreservation base, thawing was performed by removing the base from the freezer, and adding 1 mL of warm media in the dialysis chamber. The dialysis process was accelerated by gently rocking the platform by hand. When using a freshly prepared cell suspension, 8 µL of the cell suspension at 2 million cells per mL were added to each well of a standard KOALA-base. In

both cases, the cells were loaded into a KOALA channel by placing the KOALA-lid on top of the base containing the cells, thereby causing the cell suspension to fill the channels. After loading the cells, the KOALA-lid containing the channels and cells was placed on a standard KOALA-base, which was devoid of the absorbent pad and for which the wells were filled with cell culture media to mitigate evaporation during the incubation. The lid and its accompanying base were then placed in an Omnitray (242811, NUNC, USA) containing sacrificial PBS, to further reduce evaporation. The Omnitray was then incubated in a CO_2-regulated incubator. After 24 h of culture, a series of pre-filled KOALA-bases were applied to the KOALA-lid to perform the cell-based assay. A first lid filled with 4% para-formeldhayde was applied and the channels were incubated for 30 min. A second lid filled with 0.1% triton was applied and incubated for 10 min. Then, a lid containing DAPI stain, phalloidin stain, and tubulin antibodies was applied and let incubate for 30 min. Finally a lid filled with PBS was applied to wash the microchannels. The KOALA platform was finally imaged using an Eclipse Ti fluorescent microscope (Nikon, Japan).

13.3 Results and Discussion

We demonstrate a novel class of microfluidic cell-based assays, called Kit-On-A-Lid-Assay (KOALA), allowing the creation of self-contained kits that integrate all the reagents, fluid handling methods, and cell cryopreservation methods required. The approach uses two microfluidic parts: a lid containing microchannels and a series of bases containing pre-packaged reagents, cryopreserved cell-suspensions **(Fig. 1)**. First, we developed a method to reliably transfer fluids from the bases to the lid. As the lid is placed in contact with a base, posts located on the input and output of each microchannel in the lid come in contact with a microwell and an absorbent pad, respectively, in the base. The combination of post design and contact with the fluid and absorbent pad drive fluid from the base into the microchannel. Using a series of bases containing different reagents, a range of fluids can be sequentially flowed into the microchannels allowing the creation of multi-step assays. Further, specific bases can be designed for pre-packaging reagents, cryopreserving cell-suspensions, or preparing user-specific reagents, thereby making the KOALA platform a modular technology for a wide range of biochemical and cell-based assays.

13.3.1 Microfluidic design

The transfer of fluid from the base to the lid leverages capillary forces to provide a reliable and passive flow generation in the microchannels. In brief, when the lid is placed on the base, a post located at the input of the microchannel in the lid contacts a microwell with reagents in the base, and a post located at the output of the microchannel in the lid contacts an absorbent pad in the base **(Fig. 2A)**. The variance in height between the posts accounts for the difference between the depth of the wells and the pads. Furthermore, the system was designed to (1) ensure that good fluidic connection is made between the lid and base parts, and (2) to ensure that the fluidic connection can be severed at the right time to leave a precise amount of fluid in the microchannels at the end of the operation.

In order to create a robust fluidic connection between the microchannels and the wells, we designed a connection system that eliminates the risk of capturing air bubbles upon application of the lid on the base. The posts placed at the input and the output of the microchannels have a horseshoe shaped cross-section such that air bubbles can escape when the post contacts the fluid in the microwells situated in the base. Further, the horseshoe shaped cross-section allows capillary force to pull the fluid into the channel and into contact with the absorbent pad.

Secondly, once the fluidic connection is initiated both on the inlet side (in contact with the microwell) and the outlet side (in contact with the absorbent pad), the capillary phenomenon must cease before the entire contents of the channel gets emptied into the absorbent pad. To accomplish this the horseshoe shaped design enables an air gap to form, severing the fluidic connection between the channel and the absorbent pad **(Fig. 2B)**. An additional design consideration needs to be validated to ensure that the fluid preferentially remains in the microchannel. For this to occur, the capillary pressure, $\Delta P_{channel}$, generated by the fluid in the channel (and providing the driving force to keep the fluid in the channel) must be higher than the capillary pressure, ΔP_{post}, generated in the horseshoe post (and providing the driving force to empty the channel). Both pressures, $\Delta P_{channel}$ and $\Delta P_{post,}$ can be written as a function of θ,

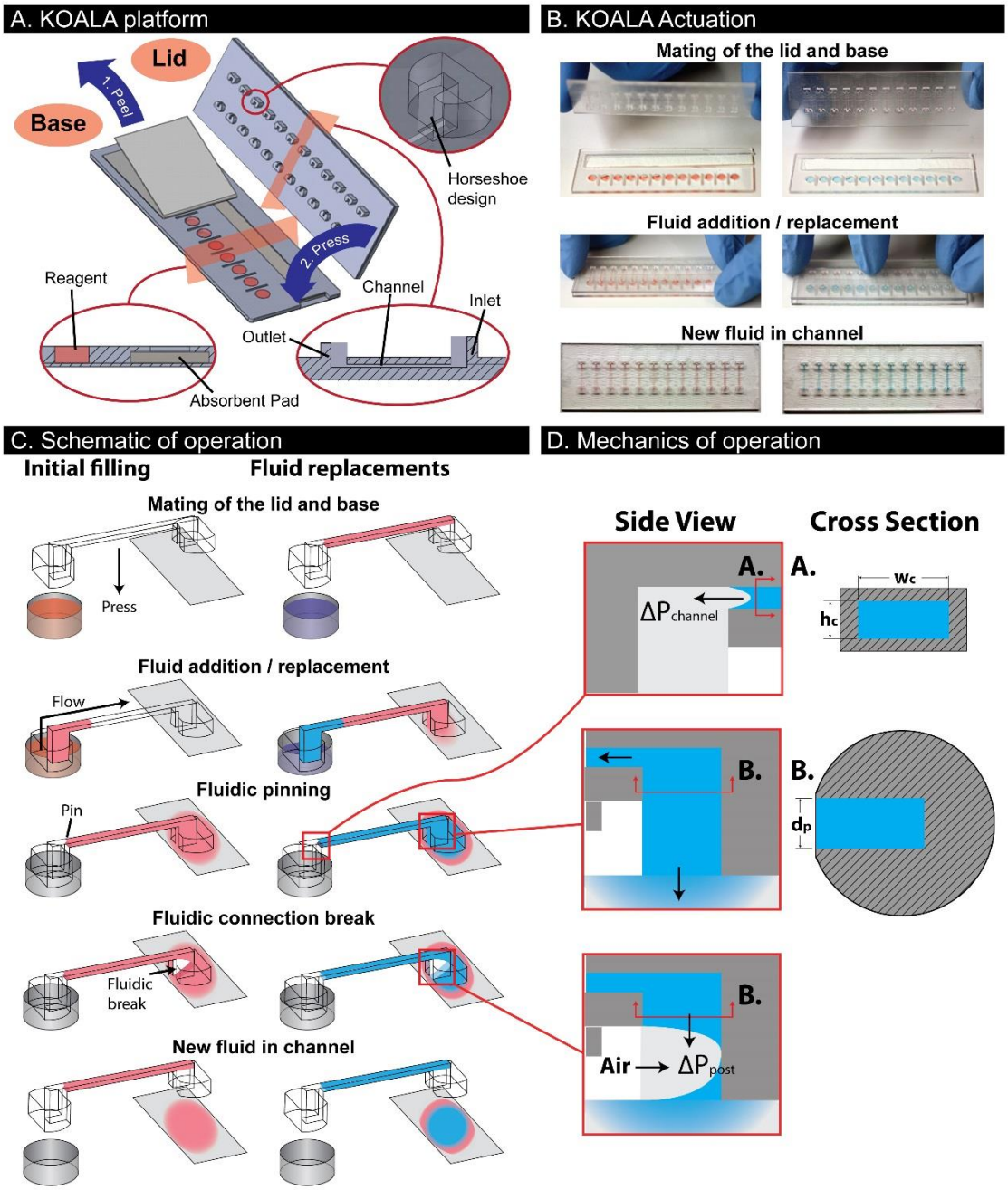

Fig. 13.2 KOALA design and operation. (A) Schematic of the KOALA platform. (B) Illustration of the operation of the KOALA platform using red food colorant for the initial filling, and blue food colorant for the subsequent fluid replacement. (C) Operation of the KOALA platform. After the lid is mated with the base, an absorbent pad drives the flow, causing the replacement of the fluid within the channels. Once the input microwell is empty, the flow stops and the lid can be removed from the base. (D) Design consideration of the KOALA microchannels. The posts on either side of the microchannels are designed to enable capillary flow, and thus create fluidic contact with the absorbent pad. When the microwell is empty, the dimension of the horseshoe relatively to the channel is such that the fluid stays pinned within the channel and an air bubble extends into the post, breaking the fluidic connection, and thus stopping the flow of fluid.

the contact angle of the fluid, γ, the surface tension of the liquid, w_c and h_c, the width and height of the channel respectively, and d_p the depth of the horseshoe **(ESI)**:

$$\Delta P_{channel} = 2\gamma \left(\frac{\cos(\theta)}{w_c} + \frac{\cos(\theta)}{h_c}\right) \quad \text{Eq. 13.1}$$

$$\Delta P_{post} \leq 2\gamma \frac{\cos(\theta)}{d_p} \quad \text{Eq. 13.2}$$

$$\Delta P_{channel} > 2\gamma \frac{\cos(\theta)}{d_p} \geq \Delta P_{post} \quad \text{Eq. 13.3}$$

13.3.2 Microfluidic operation.

During the operation of the KOALA device (placing the lid on a base containing microwells) the fluid in all the microchannels contained in the lid is replaced simultaneously **(Fig. 2C)**. This aspect is advantageous for time-sensitive cell-based experiments, as every microchannel is treated at the exact same time. Thus, phenomena such as evaporation do not affect some channels more than others. Simultaneous fluid transfer also allows straightforward scaling of the number of channels, as the time requirement is constant. Furthermore, we show that cell suspensions can be flowed into the microfluidic device and that cells can be cultured for extended periods of time. As the volume of the microchannels is minute (~2 µL), we have previously found that evaporation may have a strong impact on cell culture.[316] Evaporation was mitigated by placing the lid onto a base containing blank media during the incubation stage. Using this approach, we observed that BEAS-2B cells were viable after 24 hours culture, as shown by a live/dead stain. For cultures lasting more than 24 hours, the culture media can be replaced using a fresh base. In order to create advanced assays integrating multiple fluid handling steps, such as cell fixing or staining, we quantified the reliability and repeatability of the fluidic replacements. The data shows that 24 fluid replacements were performed on 12 channels before a failure was observed, with one channel failing on the 25th replacement. Noticeably, 24 sequential replacement are sufficient for developing most cell-based assays.

13.3.3 Cryopreservation and thawing

We have developed cryopreservation methods that enable the freezing, and thawing of cell-suspensions. A key feature is the removal of the cytotoxic cryopreservation fluid added to the cell suspension prior to freezing.[317, 318] In this embodiment, we developed a KOALA-base containing microwells with a micro-porous membrane on the bottom **(Fig. 3A)**. Cell suspensions are prepared in the desired cryopreservation media, placed in the wells, sealed, and stored in a -80°C freezer or liquid nitrogen until ready for use. Before use, the base is removed from the freezer, and the cryopreservation fluid, typically DMSO, is removed through dialysis, by adding warm culture media to the chamber adjacent to the wells. The dialysis process leverages the rapid diffusion timescales enabled by microfluidics as the height of liquid in the well is in the order of tens to hundreds of micrometres. To further accelerate the process, the base can be placed on a rocker or rotated from one side to another, in order to increase the mixing of the media in the dialysis chamber **(Fig. 3B)**. We have characterized the dynamics and efficiency of the dialysis process by monitoring the extraction of fluorescent dye (Alexa 488) into PBS **(Fig. 3C)**. The results reveal that after 6 minutes of dialysis ~97% of the dye is extracted. As the diffusion coefficient of DMSO is higher than Alexa488, the result suggests that this timeframe allows the removal of a sufficient amount of DMSO for healthy cell culture. For higher extraction efficiency, the dialysis can be performed twice, consecutively. To prove the effectiveness of the device, we froze various cell lines (3T3, BEAS-2B, HEK-293, and HUVEC) for at least 72 hours in a solution containing 10% DMSO, performed the dialysis, and cultured cells for 24 hours in KOALA-microchannels. The data indicates a greater that 70% viability for each cell type, which is on par with the viability obtained when preparing the cells using traditional methods (centrifuge, eppendorf tubes, etc..) and culturing them in the microchannels **(Fig. 3D)**.

The KOALA approach for cell cryopreservation is user-friendly and scalable, as multiple wells are prepared simultaneously and each can contain a different cell line / strain. More importantly, this method allows the freezing and thawing of only the required amount of cells for each microchannel. We

envision this to be a critical aspect for cell-based assays using primary, patient, or stem cells, as a large number of these KOALA-bases can be loaded from the same sample and used at later dates without requiring the thawing of the whole sample. Additionally, this may also allow researchers to go back to the same batch of cells, as tens/hundreds of these KOALA-bases can be prepared from the same original cell sample.

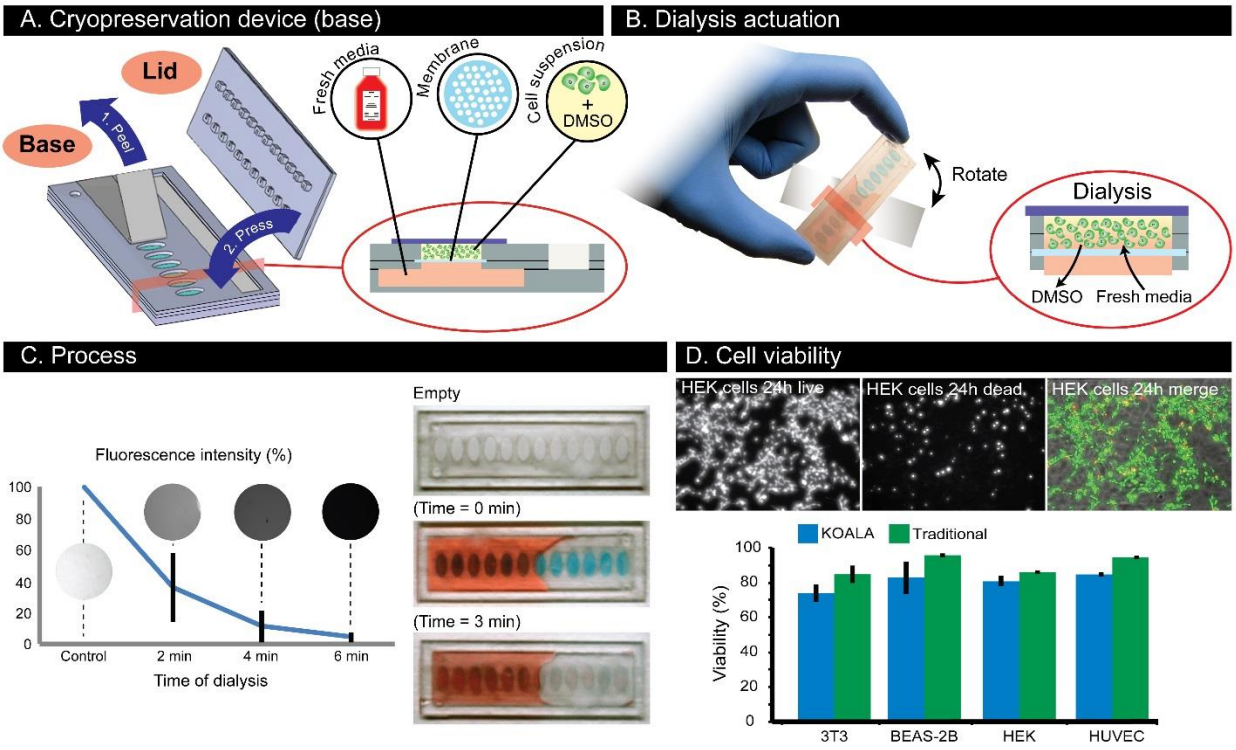

Fig. 13.3 KOALA cryopreservation. (A) Schematic of the cell cryopreservation embodiment where cells are contained in a well enclosed by a tape and a microporous membrane. (B) The device is rocked back and forth to accelerate dialysis for replacing the freezing media with fresh media, after which the tape is removed and the lid is placed on the base for seeding cells. (C) Quantification of the dialysis of Alexa488 dye in PBS (left). After 6 minutes ~97% of the dye was removed from the wells. Demonstration of dialysis using blue food colorant (right) (D) Viability of various cell lines through the KOALA freezing and thawing process compared to that of the traditional freezing and thawing process. Microscopy images of the live/dead stain for the HEK cell line, after KOALA process, are shown.

13.3.4 Integrated cell-based KOALA assays.

Using the KOALA microchannels and the KOALA cryopreservation lid, we demonstrate that the KOALA platform enables the creation of entirely self-contained cell-based assays. A typical immunohistochemistry readout was chosen to illustrate the potential of the KOALA assay. HELA cells

were frozen in a KOALA base, thawed, and cultured in KOALA microchannels. After 24 hours in culture, a series of treatments using KOALA-bases was performed in order to wash, fix, permeabilize, and stain the cells in culture. We show that the KOALA platform allows the use of various reagents critical for cell assays, such as paraformaldehyde, surfactant, live cell stains, small molecule stains, and antibody-based stains **(Fig. 4)**. The KOALA platform thus raises the possibility of developing standardized and optimized in-vitro phenotype screens in which the researcher could screen a mutant cell strain or disease model for a whole series of phenotypes and morphology features all at one time, without having to prepare and optimize each combination of antibodies and assay reagents. The potential impact for this technology is to reduce the time required for identifying and characterizing the functional role of genes of interest, by discarding those with little or no phenotype of interest. Further, the assay described here was performed by a cell-biology researcher that did not have an engineering background. This emphasizes the underlying goal of the KOALA assay, which is to provide a simple user-friendly assay that can be used by an audience that is not versed in microfluidics and medical engineering.

While the KOALA platform is efficient for streamlining assay steps by pre-packaging reagents and cell lines, some users may want to customize one or more steps of the assay. An obvious option is to provide the user with an empty base, in which each well can be loaded with a custom solution.To facilitate such workflows, we demonstrate a KOALA-base that allows the user to load a reagent of interest in one pipetting step **(ESI)**. This approach allows the allocation of user-inputed fluid into set volumes, and the preparation of this liquid for subsequent interfacing with the KOALA workflow. More advanced assays can also be performed by changing the microchannel configuration in the lid. For example we show that a chemotaxis and gradient-generation device can be created by joining adjacent channels **(ESI)**. These examples shows the modularity of the KOALA approach to create a variety of cell-based assay that can be performed in a simple, inexpensive, and rapid way.

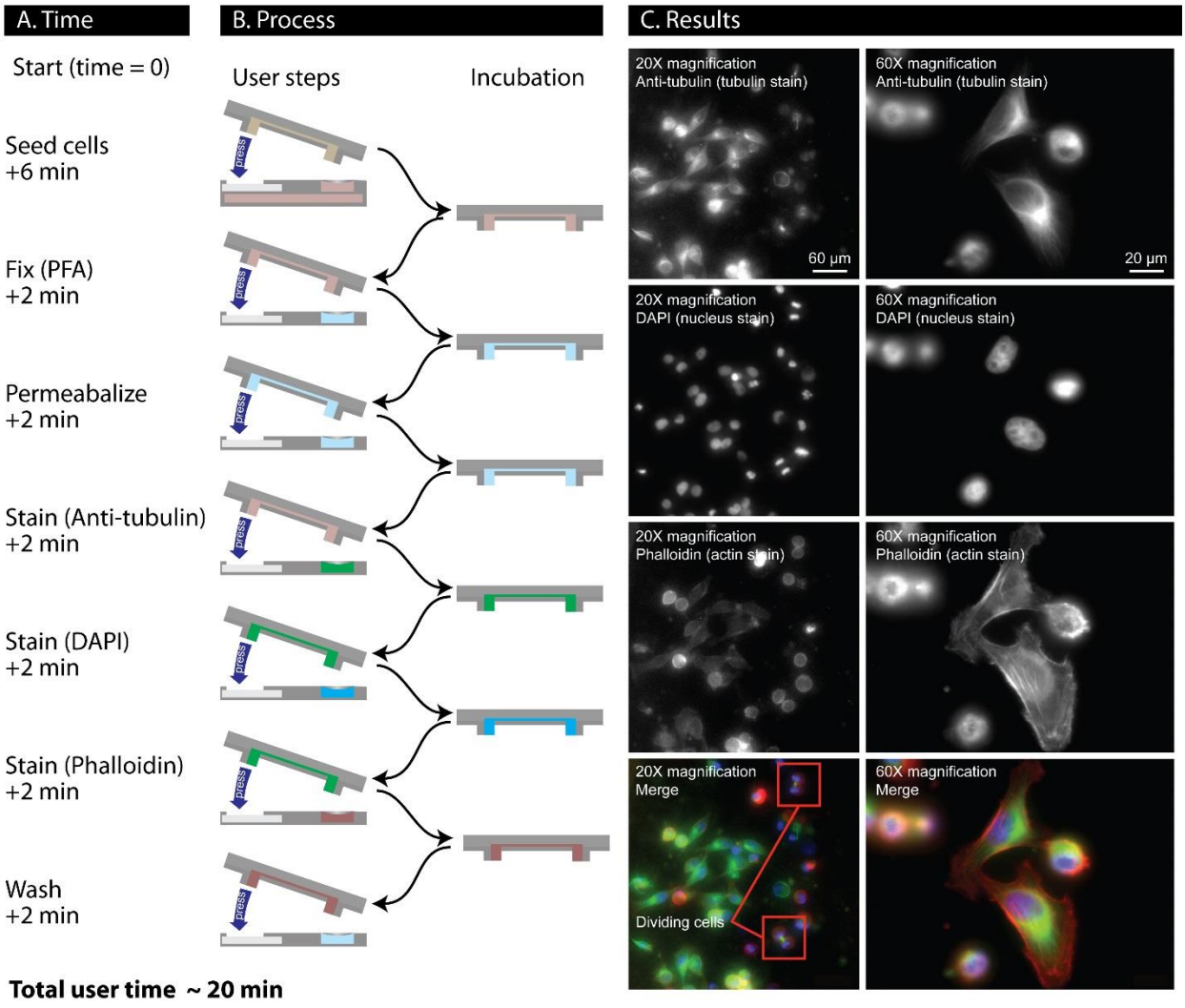

Fig. 13.4 Cell based assays using KOALA. Using a series of lids, as whole cell-based assay can be pre-loaded into the KOALA platform. Here BEAS-2B cells were loaded in a cryopreservation base, and an immunostainning assay was loaded in a series of pre-packaged reagent bases. After cell loading and culture in a KOALA lid, each step of the immunostaining assay was performed by thawing the specific base required, and applying a specific lid onto the microchannel culture. Fluorescent microscopy was used to image the assay performed. All 12 channels of the KOALA lid were treated simultaneously at each application of a new base, removing the need to prepare each reagent individually and treating each channel individually.

13.4 Conclusions

We present a novel microfluidic technology for handling fluids in microfluidic platforms that enable the exchange of fluids between two open microfluidic parts: a base and a lid. This technology, dubbed Kit-On-A-Lid-Assay (KOALA) technology, enables the creation of entirely self-contained assays that can be stored, shipped, and operated without any specialized equipment. Further, we developed

methods to freeze and thaw cell suspensions with nearly zero dead volume. Using these methods, we show the ability of creating cell-based assays in which all reagents are pre-packaged, and that require no equipment other than an incubator. This enables streamlined and standardized in-vitro cell based assays that use very little reagents as only what is needed is thawed. The significant time and material/reagent savings are particularly important for primary patient samples as well as immunocytochemistry applications. For these, the KOALA allows the researcher to prepare a large batch of assays and use only the amount required for each assay. The KOALA technology has the potential to be a broadly applicable platform for creating user-friendly in-vitro cell-based assays.

Chapter 14 High-density self-contained microfluidic KOALA kits for use by everyone [13]

14.1 Introduction

Cell-based assays and in vitro models are essential tools for a wide range of biological and chemical applications such as cell biology, drug discovery, and toxicology.[319] However, traditional assays, including microfluidic assays, suffer from significant limitations preventing more widespread use.[320,321] Amongst these barriers to adoption are the cost of cells and reagents, the limited scalability of the assays due to the reliance on a serial (vs. parallel) operation process, and the requirement of both preparation and equipment – such as pipettes and centrifuges **(Fig. 14.1)**. Perhaps more importantly, traditional assays require trained staff which limits accessibility of these assays to labs that don't have cell culture expertise and/or facilities, such as natural product discovery labs, educational labs, engineering labs, or environmental research labs.[322] The need for simplified assays has been highlighted by assays such as the SlipChip.[307] Yet, there remains a dearth of technologies for cell-based assays that are low cost, simple to operate, and that integrate the ability to perform sequential and complex fluid replacements.

The Kit-On-A-Lid-Assay (KOALA) technology is a novel microscale platform that aims to reduce barriers to adoption of cell-based assays by enabling precise and advanced fluidic handling in a self-contained, user-friendly interface.[74,19] KOALA integrates several features to simplify complex assays. First, pre-packaging eliminates the need to prepare reagents, label tubes, and distribute reagents to each assay, a time-consuming and often under-estimated part of traditional assays. Second, KOALA is a micro-to-micro platform, reducing waste by eliminating the need to dilute/prepare reagents for the assay via macro-scale tubes (as is currently done even for microscale platforms). Finally, the integrated fluid handling system of KOALA eliminates the need for fluid handling equipment, such as pipettes, mixers, and centrifuges. The KOALA fluid handling system utilizes a series of lids that are used in conjunction

13 This chapter has been adapted from the following publication: "High-Density Self-Contained Microfluidic KOALA Kits for Use by Everyon" David J. Guckenberger, Erwin Berthier, and David J. Beebe. Journal of Laboratory Automation, 2014.

with a single base containing a set of microchannels. Different sets of lids are used for different assays. Lids are prepackaged with only the necessary volumes of pre-diluted reagents required for each step of the assay. Each step (i.e., fluid exchange step needed to apply a treatment or reagent on the cell culture) is then performed by removing a lid from the freezer, thawing it, peeling a protective layer covering micro-wells containing reagents, and "clicking" the lid onto the base **(Fig. 14.2)**.

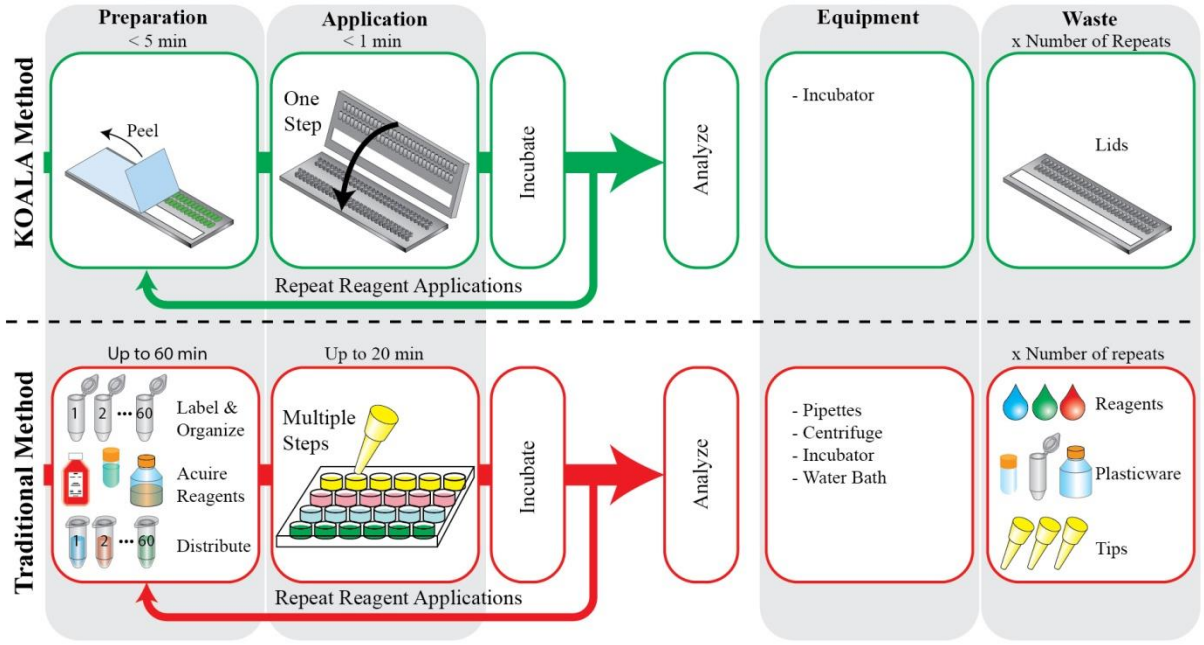

Fig. 14.1 Workflow comparison between KOALA and traditional culture. Schematic represents the workflow differences between a KOALA microfluidic platform (top) and a traditional assay (bottom). KOALA enables prepackaging of reagents into lids, parallel fluid applications, minimal demands for equipment, and minimal waste. Traditional assays often require significant preparation, a serial process for fluid application, several pieces of equipment, and large amounts of waste.

Current KOALA methods have described the basic principles for exchanging fluid between a lid and a base. However, significant limitations remain for using these methods for high-density and robust screening applications[74], including modes of cross-contamination between neighboring wells and channels, fluid replacement efficiency and overall fluid characterization, and validating the technology on for functional cancer cell assays. We address these limitations through multiple design enhancements that enable a high-density KOALA (KOALA-HD) format with throughput on par with 384 well plates in a platform that can be operated by hand without any fluid handling equipment **(Fig. 14.2B)**. The following

describes the geometrical parameters (i.e. feature characteristics, orientation, and dimensions) and fabrication processes that are necessary to enable KOALA-HD while preventing cross contamination. We present and characterize the washing efficiency, operation, and performance of the KOALA-HD platform for repeated and higher-density applications in terms of fluidic function and for facilitating cell-culture applications lasting more than 24 hours. Finally, we demonstrate the utility of KOALA-HD for high-throughput cell-based applications by performing a screening assay with complex immunohistochemistry (IHC) endpoints.

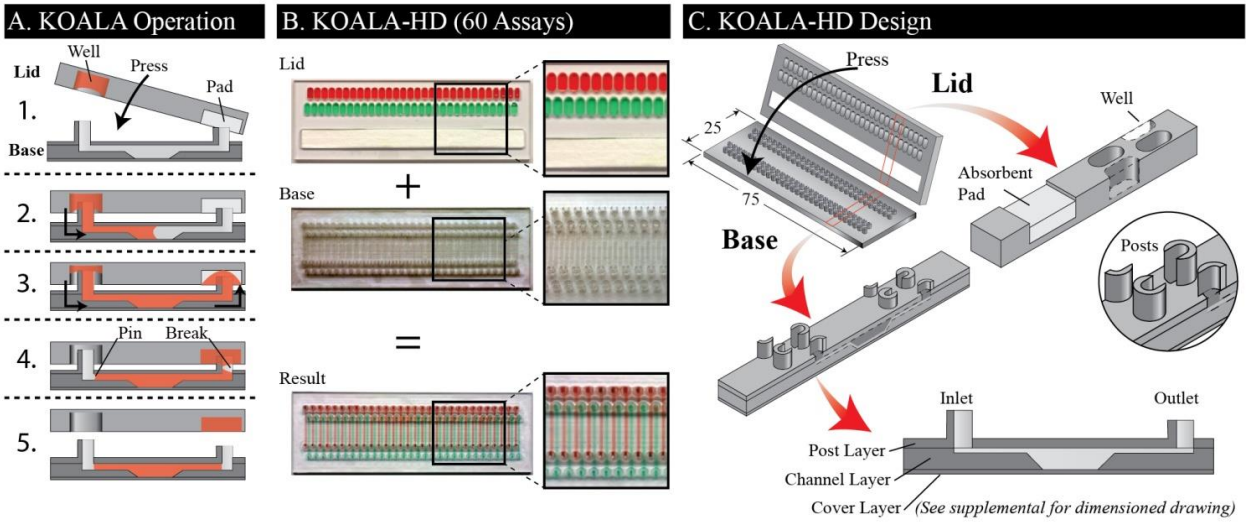

Fig. 14.2 KOALA-HD design and operation. (A) KOALA operation entails pressing a lid, containing micro-wells with reagents and an absorbent pad, onto a base, containing microchannels. When the microfluidic post contacts the fluid, flow is initiated by capillary action. Once the channel is full, an absorbant pad sustains the flow until the well is empty. Once empty, the fluid pins at the entrance of the channel and an air bubble forms in the channel exit. This bubble breaks the fluidic connection between the channel and the absorbent pad – assuring that the channel is not emptied – and completes the fluid transfer. (B) An image of the KOALA-HD pre-filled lid and base, and the resultant base after application of the lid. (C) KOALA-HD compresses 60 assays into the foot print of a traditional glass slide. Lids house micro-wells and absorbent pads, while the bases consist of staggered microchannels. A post is located at both ends of the microchannel. A dimensioned drawing is available in the supplementary information.

14.2 Materials and Methods

14.2.1 Device Fabrication and Preparation

The lids and bases are fabricated by CNC milling (PCNC 770, Tormach, Waunakee, WI) with standard microscope slide dimensions (25 mm x 75 mm). Bases are comprised of three layers: (1) a post layer, (2) a channel layer, and (3) a cover layer **(Fig. 14.2C and Fig. J.1)**. (1) The post layer is milled from 2 mm thick PS (#ST313200, Goodfellow, Coraopolis, PA) and encompasses an inlet and an outlet

post for each channel. Both posts have a horseshoe like cross section with an outside diameter of 1 mm. The inlet post for each channel is 1.5 mm tall with a slot width of 0.8 mm and the outlet post is 1 mm tall with a slot width of 0.5 mm. Lengthwise the spacing of the posts matches that of the channels, however widthwise the posts and channels are staggered by 3 mm to facilitate close packing. (2) The channel layer is milled from 1.2 mm thick polystyrene (PS) (#ST313120, Goodfellow) and encompasses 60 microchannels spaced by 1 mm (from channel centers). Each channel is 0.5 mm wide, 2 mm long, and 0.3 mm deep. In the center of each channel is a micro-well that is 0.5 mm wide, 4 mm long, and 1.2 mm deep, with bevels at both ends to facilitate fluid flow. (3) The cover layer is 25 mm x 75 mm and is cut from 0.190 thick PS (#ST313190, Goodfellow). Prior to assembly, all three layers are treated with oxygen plasma (Femto, Thierry Corp., Royal Oak, MI) for 50s at 50 W. Layers are assembled by acetonitrile bonding.[315] In brief, Acetonitrile (#271004, Sigma Aldrich, St. Louis, MO) is applied drop wise to one layer of the device, which is then promptly mated with a second layer. The excess acetonitrile is aspirated from the channels and the mated pair is gently pressed together on a hot plate preheated to 70° C. After 30 s the process is repeated for the third layer. After bonding, the device is plasma treated again with the same settings, and hydrophobic recovery is induced between the posts using a wiper.[197]

Lids are milled from 2 mm PS. Each lid contains a micro-well for each channel (i.e., 60 micro-wells) and a slot for absorbent pads. Each micro-well has an elliptical shape which is 1.5 mm wide, 4 mm long, and 2 mm deep, and is spaced to match the pattern of the input posts. The slot for the absorbent pad is 10 mm wide, 72 mm long, and 2 mm deep. The lids are assembled by first applying an optical adhesive cover (#04 729 757 001, Roche, Basel, Switzerland) to the back of the lid then placing two layers of absorbent pad (#CFSP223000, Millipore, Billerica, MA) in the designated slot. Both bases and lids are UV sterilized for 30 minutes, prior to cell culture, and lids are loaded with reagents prior to each application.

14.2.2 Fluid handling

Fluid exchanges are characterized by (i) measuring the duration, (ii) washing efficacy, and (iii) cross contamination during fluid replacements. Fluid replacements are initiated by mating the lid with the base, thereby inserting the series of posts into the micro-wells. (i) To assess time required for fluid replacement, the micro-wells are filled with 15 μL of DI water and the lid is clicked on the base. Time is measured from the point of initial fluid contact, between the post and the fluid, to the point at which the micro-well is emptied. (ii) Washing efficacy is assessed by measuring the depletion of a fluorescent dye after individual wash steps. Channels are pre-loaded with a fluorescent dye (Alexa Fluor 488, #D-22910, Life Technologies, Carlsbad, CA), then washed by applying lids containing 15 μL of DI water per micro-well. Channels are imaged after each wash is completed (IX-70, Olympus, Shinjuku, Tokyo, Japan) and fluorescence intensities are measured using ImageJ. The background autofluorescence, inherent to the PS, is measured, averaged (n = 8 locations), and subtracted from the channel fluorescence. After subtraction, all channels are normalized to the average of the starting fluorescence intensity, and averaged (n = 60 channels) (error bars represent one standard deviation). (iii) To assess cross contamination, alternating micro-wells are filled with 15 μL of either Alexa Fluor 488 or Texas Red (#D-3328, Life Technologies). After completing the fluid exchange, each channel is imaged for both dyes and fluorescence intensity is quantified using ImageJ. Autofluorescence noise is subtracted from each channel, for both wavelengths.

14.2.3 Cell Culture for IHC Assay

In this section, all fluid transfers, including cell seeding, are executed by filling each of the 60 micro-wells with 15μL of the respective reagent then mating the lid with the base. NMuMG cancerous epithelial cells are seeded in KOALA-HD channels at a surface density of 400 cells / mm^2, and cultured at 37° C for a total of 72 hr. For the first 24 hours, cells are cultured in DMEM media with 4.5 g/L glucose (#10-017-CV, Corning Cellgro, Manassas, VA) supplemented with 10 μg/mL insulin and 10% fetal bovine serum (FBS). For the next 48 hours, the cells are cultured in the same media supplemented with a 0, 2, 20, or 200 pM concentration of TGF-β1 (#100-21, Pepro Tech, Rocky Hill, NJ). The media is

replaced every 24 hours. Cells are washed with 1x phosphate buffered saline (PBS), fixed with 4% paraformaldehyde (#43368, Alfa Aesar, Ward Hill, MA) for 15 min, and permeabilized with 0.1% Triton X-100 (#807426, MP Biomedicals, Santa Ana, CA) for 30 min. Channels are washed with 1x PBS, then blocked with 1x PBS supplemented with 3% bovine serum albumin (PBS+BSA) for 30 min. Primary antibody solutions are prepared by separately diluting anti-β-catenin (rabbit) to 2 μg/mL, anti-E-Cadherin (mouse) (#610182, BD Biosciences, San Jose, CA) at 1 μg/mL, anti- FAK (rabbit) (#ab40794, Abcam, Cambridge, England, UK) to 2 μg/mL, anti-N-Cadherin (rabbit) (#ab18203, Abcam) to 6 μg/mL, or anti–Vimentin (mouse) at 1:50 into PBS+BSA supplemented with 0.1% Tween 20 (PBST+BSA) (#P1379, Sigma Aldrich). Primary antibody solutions are added to appropriate channels (with n = 3 for each concentration of TGF-B1) for 1.5 hours, then washed twice with PBS+BSA. Secondary antibody solutions are prepared by diluting both Alexa 488 Goat anti-mouse (#A-11029, Life Technologies) and Alexa 568 Goat anti-rabbit (#A-11036, Life Technologies) to 4 μg/mL into a single solution of PBST+BSA, which is applied to all channels for 1 hour. A Hoechst 33342 nuclear stain is applied to all channels for 15 minutes then washed twice with PBS+BSA. Bases are imaged on an inverted fluorescent microscope (Eclipse Ti, Nikon, Tokyo, Japan) in three wavelengths: 345, 488, and 572 nm. Channel images are taken at 4x magnification and stitched automatically (NIS-Elements Ar, Nikon), and high magnification images are taken at 10x magnification and overlaid using ImageJ. ImageJ is also used to measure the fluorescence intensity of the channels. Background fluorescence is taken from surrounding regions, averaged, and subtracted from the fluorescence values of the channels. Within each staining category (i.e., β-catenin, E-cadherin, etc.) the channels are normalized to the maximum intensity of their respective category, and averaged (n = 3). Error bars represent one standard deviation.

14.3 Results and Discussion

KOALA-HD represents a novel class of high-throughput microfluidic platforms that can be operated quickly, reproducibly, and reliably with minimal demands for training or equipment. The KOALA-HD compresses 60 microfluidic assays into the 25 x 75 mm footprint of a traditional glass slide, enabling medium- to high-throughput applications by hand without the need for an automated liquid

handler. The number of assays that can be performed in this footprint, i.e. assay density, is comparable to that of a 384 well plate. However, unlike assays performed in 384 well plates, fluid replacements for KOALA-HD are performed in all 60 assays simultaneously. The high density format of the channels in the base resulted in design challenges that needed to be resolved in order to prevent cross-contamination of reagents and support reliable operation of the device. These design challenges and solutions are discussed here.

14.3.1 Fluid exchanges in KOALA-HD

All fluid handling mechanisms necessary to operate KOALA are integrated into the KOALA lids and bases. Each lid is a one-time-use component comprised of 60 micro-wells, which houses reagents and an absorbent pad to drive fluid flow **(Fig. 14.2C)**. Similarly, each base is comprised of 60 microfluidic channels; however, unlike the lids, the base is used for the duration of the assay. Each fluid replacement – performed by clicking a lid onto the base – is completed for all 60 channels within 15 seconds (See Supplemental Video). By measuring the average time required to empty each well, we find that the average flow rate through the channel is ~7 μL/sec. Standard microfluidic techniques to produce alternative channel designs or absorbent pad compositions can be used to achieve different flow rates for other applications if needed. When the lid is applied to the base fluid flows from the micro-well (of the lid), through the channel (of the base), and into the absorbent pad (of the lid), thus completing a fluid exchange. After which, the lid is disposed of and the base is incubated until the next fluid replacement. The novel design of the base leverages horseshoe shaped posts to enable fluid exchanges through several functionalities.[74] The posts provide a method of connecting the base to the lid to prevent air bubbles from being trapped in the channels, while ensuring proper volumes during fluid exchanges. Posts are located at the channel inlet and outlet, which, when a lid is applied, make contact with the fluid in the micro-well and which the absorbent pad, respectively. Fluid flows through the channel initially driven by capillary forces in the channel and subsequently by wicking in the absorbent pad. When the micro-well is emptied, the fluid pins in the bottom of the inlet post, and the outlet post severs the fluid flow by allowing a bubble

to form within the horseshoe, thus disconnecting the absorbent pad from the channel. This process completes the fluid exchange.

To make KOALA suitable for HD applications, however, several obstacles must be overcome including: (1) determine a configuration suitable for densification, (2) eliminate cross contamination, and (3) achieve complete and defined fluid exchanges in the new HD format.

To determine a setup that best supports the densification we test two designs, a format that uses individual posts as described above and a common rail configuration **(Fig. J.2)**. The lid for the common rail design comprises a single trench surrounded by half elliptical micro-wells while the base comprises a single rail with several protruding fins. When the lid is applied to the base, the fins provide the conduit for wicking fluid from the lid into the channel. We found that a design with individual posts for each channel is superior for two reasons. First, the separation between the inlet posts prevents cross contamination via Concus-Finn filaments. More explicitly, the corners between vertical and horizontal features act as a conduit for fluids, which leads to cross contamination. Second, the small diameter inlet and outlet posts prevent excessive displacement of fluid in the micro-wells, and support improved contact with the absorbent pad.

To eliminate cross contamination, hydrophilicity between the posts and fluid displacement in the micro-wells is decreased. After plasma treatment, we implement a novel approach, described by Guckenberger et al.[197] to recover surface hydrophobicity between the posts, thus mitigating hydrophilicity based cross contamination. Inadequate contact between the outlet posts and the absorbent pad lead to cross contamination via rapid displacement of the fluid in the micro-wells. This issue is circumvented by ensuring proper connection between the outlet posts and the absorbent pad prior to inserting the inlet posts into the micro-wells. In the future, a small reusable device for repeatably aligning and mating the lid and base (i.e., a jig) will be designed to facilitate this connection and prevent the possibility of user-error.

To ensure complete and defined fluid exchanges for each channel, we leverage the designs of the micro-wells, the posts, and the absorbent pads. The volume allotted for each fluid exchange is dictated by

the volume of the micro-well. However, maximizing use of the fluid in the micro-well, and thus minimizing dead volume, depends on the orientation of the inlet post and the size of the absorbent pad. We found that to minimize dead volume, the open side of the horseshoe should be directed towards the end of the micro-well **(Fig. J.3)**. In doing so, the dead volume of each micro-well is reduced to <3 μL. Further, to assure that all the micro-wells are emptied entirely, the absorbent pad has to be sufficiently large to assure that it does not saturate during the fluid exchange. Put together, these solutions make KOALA-HD fluid exchanges repeatable and robust.

14.3.2 Evaluating KOALA-HD Function

In order to make a highly functional platform to be used for toxicology and cell-based studies, we assess the platform for its ability to: (1) ensure proper fluid replacement in the channels, (2) ensure no cross contamination between adjacent channels, a difficultly particularly compounded by higher throughput, and (3) perform several fluid exchanges without failure.

We quantify the depletion of a fluorescent dye after washing steps to assess the efficiency of fluid replacements **(Fig. 14.3A)**. To fulfill this, a lid filled with fluorescent dye is applied to the channels, followed by two washing lids. We quantify the fluorescent depletion after each wash and normalize it to the starting intensity. We found that one washing lid is capable of removing ~60% of the initial fluid, and a second washing lid reduced the dye concentration by over 98% (n = 60), which, based on the volumes of the channels and fluid exchanges used here, is comparable to washing of traditional microfluidic channels.[311]

Cross contamination is assessed by quantifying fluorescence in each microchannel after applying a lid pre-filled with two fluorescent dyes **(Fig. 14.3B)**. The lid is strategically filled such that each micro-well containing green dye is directly adjacent to four micro-wells with red dye (illustrated with food coloring), enabling detection of cross contamination from both horizontally and diagonally adjacent micro-wells. This lid is applied to a base, and each channel in the base is quantified for both red and green fluorescence **(Fig. 14.3B, bottom)**. The results reveal no cross contamination between channels based on

no increase in fluorescence intensity between channels (n = 1), which is confirmed by observing no fluidic connection between the adjacent posts or micro-wells. Notably, these data are collected using high-surface tension fluid (water), but for low surface tension fluids (e.g. oil, high-surfactant reagents) the lid and base may be inverted. This result sets the stage for using the KOALA-HD in toxicological screens or pharmaceutical identification of natural products, including readouts such as protein expression.

Finally, we assesses the ability to operate a fluidic assay without failure by applying a series of lids and verifying complete flow in each channel. A series of 20 lids are pre-filled with dyed water and applied to a single base. For comparison, about 15 fluid replacements are typically required for a traditional immunochemistry staining. Each lid is filled with alternating colors to make channel failure obvious. All 20 fluid exchanges are completed without a single channel failure.

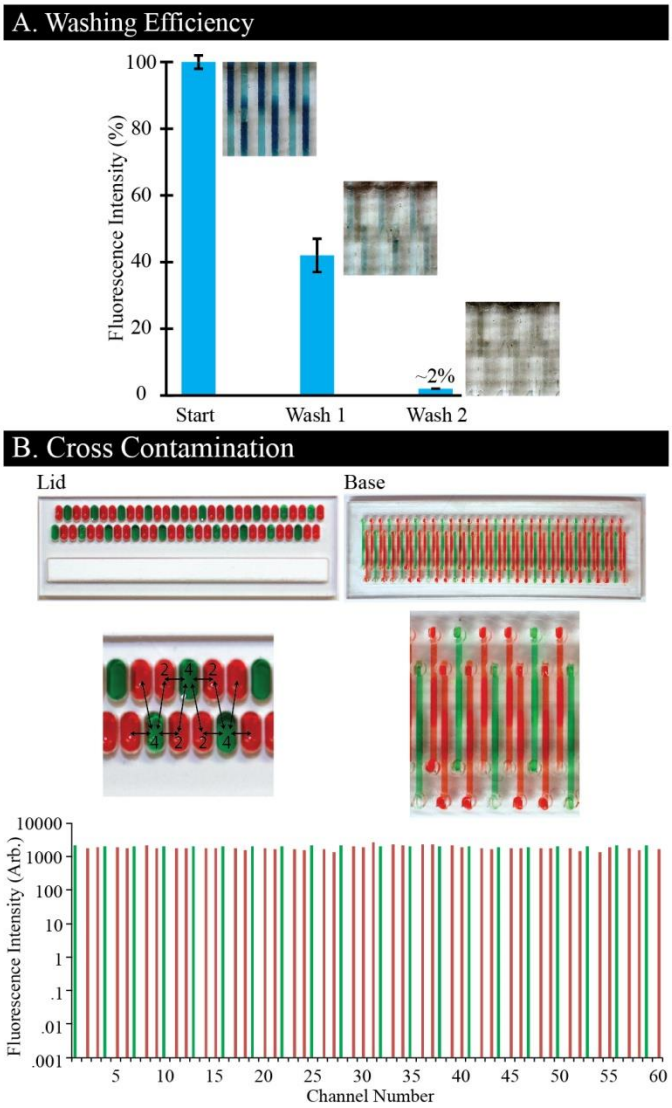

Fig. 14.3 Fluidic characterization of the KOALA-HD. (A) Washing efficiency of lids is quantified by measuring a decrease in fluorescent intensity after each lid (n = 60). (B) Cross contamination is assessed by filling a lid with two different fluorescent dyes (depicted by food coloring), and applying that lid to a base. Fluorescent intensities for both red and green are measured and represented for each channel. No cross contamination is evident.

14.3.3 Channel design for cell culture

To ensure suitability for cell culture, KOALA-HD is designed to: (1) allow precise readouts of cellular functions (proliferation, protein localization, etc.), (2) contain enough media to maintain cell viability throughout the incubation period, and (3) be negligibly impacted by evaporation. The channels are designed with a lowered region in the center that serves three purposes. First, the decreased plastic thickness enables better cellular readouts (e.g., higher magnification microscopy, less autofluorescence from the plastic). Second, the increased channel size reduces the shear stress by slowing fluid velocity. Third, the lowered region increased the volume and thus increases the reservoir of nutrients that are available for the cells. With this channel design, we are able to culture cells for 24 hours without media exchanges.[323,143] However, for more highly-active or sensitive cells more frequent fluid replacements may be necessary. Evaporation is mitigated using previously described and characterized methods.[316,139]

14.3.4 IHC assays

We demonstrate the ability to perform high density IHC assays and complex staining processes reliably and without the need to prepare antibody dilutions or source specific reagents. We chose an IHC assay based on their ubiquity in screening applications and for the multitude of steps necessary to complete the assay (i.e., cell-culture, fixation, permeabalization, staining, washes, etc.). We use a relevant cancer specific assay where NMuMG epithelial cells are treated with various dosages of TGF-β1, inducing an epithelial-to-mesenchymal transition (EMT).[324] Markers of this transition include: down regulation and localization of β-catenin and E-cadherin to cell-cell contact areas[325], and increased expression of FAK[326], N-cadherin[327], and Vimentin.[328] Such complex readouts require cell culture, treatment with a drug, and IHC staining. We demonstrate cell culture in KOALA-HD by culturing NMuMG cells in 60 channels for 72 hours. The process requires 15 sequential fluidic steps, all performed using the KOALA platform (i.e. cell seeding, media replacements, TGF- β1 dose treatments, fixing solution, washing buffer, primary antibody staining, and secondary antibody staining). The platform is able to perform each fluidic step in all channels simultaneously without failure or cross contamination.

Each fluidic exchange requires about 15 seconds with a simple mating of the required lid with the base containing cells.

Cells are treated in four groups of 15 channels with varying concentrations of TGF-β1. After which, cells are fixed, permeabalized, stained with a nuclear stain, and stained in triplicate for β-catenin, E-cadherin, FAK, N-cadherin, and Vimentin **(Fig. 14.4A)**. We found that β-catenin decreases and N-cadherin increases with increasing levels of TGF-β1, as expected. We did not observe any decrease of E-cadherin for increasing levels of TGF-β1, but we did observe localization to the cell-cell contact areas. FAK decreases with increasing levels of TGF-β1, which is inverted from typical results but has been observed in NMuMG cells expressing D119A-β_3 integrin.[326] Finally, prevalence of Vimentin, a mesenchymal marker, is evident in cells treated with TGF-β1 indicating a transition to a mesenchymal phenotype. Selected channels treated with the highest concentration of TGF-β1 (i.e., 200 pM) are imaged at high magnification **(Fig. 14.4B)**. These images demonstrate localization of β-catenin and E-cadherin to the cell-cell contact areas. A noticeable feature in some of the images is the striated pattern formed by the cells arranging themselves along fabrication artifacts. These are the result of machining marks left by the CNC machine during the channel fabrication and can be removed by utilizing other fabrication methods such as injection molding. All channels are stained with both the Alexa 488 and Alexa 568 dyes to detect non-specific binding. Importantly, we demonstrate that KOALA-HD can – in the footprint of a glass slide – cover a broad range of treatments and readouts, providing high content microscopy images at a high throughput scale, without a need for automation or trained personnel. In future applications, this platform could be imaged with a scanner for higher throughput analysis.[143,312]

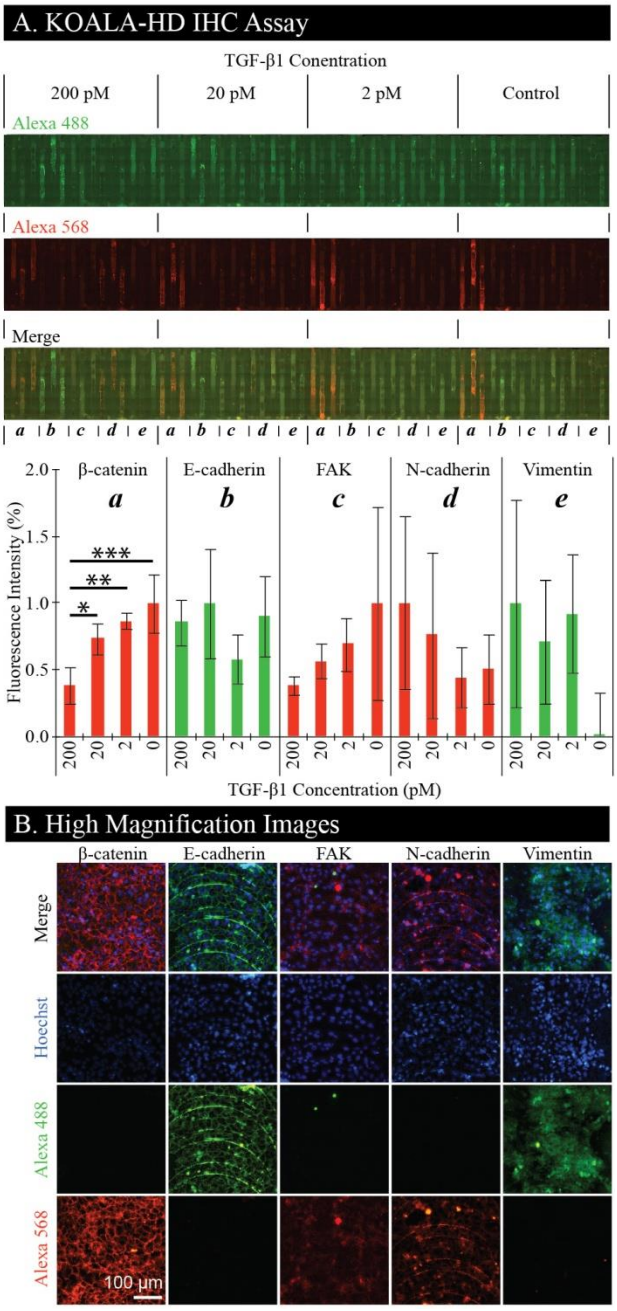

Fig. 14.4 Cell based assays and applications using KOALA-HD. (A) NMuMG cells are cultured in KOALA-HD channels and treated in 15 channel segments with varying concentrations of TGF-β1. Within each segment, channels are stained with primary/secondary antibodies for (a) β-catenin/Alexa-568, (b) E-cadherin/Alexa-488, (c) FAK/Alexa-568, (d) N-cadherin/Alexa-568, and (e) Vimentin/Alexa-488 (Hoechst not shown). The bar graph demonstrates average fluorescence intensities for each of the treatment conditions and antibody stains (n = 3). Error bars represent standard deviation. Analysis of Variance (ANOVA) indicated significant differences within B-catenin data ($p<0.01$). P-values are indicated for protected Fisher's Least Significant Difference (LSD) test as follows: * $p\leq0.05$, ** $p\leq0.01$, *** $p\leq0.001$. (B) High magnification images of each antibody stain taken from channels treated with 200 pM concentration of TGF-β1. Each channel is imaged for Hoechst, Alexa 488, and Alexa 568.

14.4 Conclusion

The KOALA-HD platform is a microscale fluidic handling technology that simplifies cell-based assays such that anyone can perform them. The only operation is to place a lid onto a base. KOALA-HD enables: reagent prepackaging and cryopreservation – acting to reduce preparation time and waste, lower demands on infrastructure or trained personnel – expanding access of cell-based assays to more labs, and enable high-throughput microfluidic applications through the scalability offered by parallelized fluidic handling procedures. We demonstrate how feature dimensions and geometry can be altered to accommodate close packing of microfluidic channels. In addition, we characterize the robustness simultaneously performing 60 assays within the footprint of one microscope slide. We demonstrate that the KOALA-HD would be suitable for toxicology, environmental pollutant, and natural product research by showing functional and advanced cellular readouts in the form of protein expression and morphology. However, due to the simplistic nature and device modularity it is possible that KOALA-HD could be expanded into other areas, including patient screening in clinics[19,20], water quality tests, or even food safety testing.

Chapter 15 Conclusions and Future Directions

The role of microfluidics in providing future treatment strategies, cures, and disease insight is eminent. Currently microfluidic technology development is expanding at exponential rates. As such, microfluidic technologies are poised to have a high impact in new clinical assays. However, commercialization of these technologies will be crucial to their utilization, distribution, and ultimately success. The preliminary chapters introduce microfluidic fabrication methods, which facilitate device fabrication in-house using methods compatible with commercial manufacturing. These techniques will enable researchers to fabricate with thermoplastics helping accelerate the rate at which prototypes can be made, reduce the costs of devices, accelerate the transition from an academic technology to a commercially viable product, and ultimately narrow the gap between academics and industry. Through three case studies, we then demonstrate how these fabrication techniques can be utilized to make a range of microfluidic technologies to address specific clinical needs, highlighting the design, manufacturing, and user simplicity. Conclusions and observations from the following case studies are listed below.

15.1 Case Study 1:

The potential role and importance of CTCs as biomarkers is well established. Yet, as our knowledge of CTCs continues to grow, so do the demands for more information; this requires the development of new technologies. We designed and characterized a series of easy-to-use, versatile sample preparation technologies to maximize utility to the end-user by enhancing assay flexibility and expanding the range of integrated endpoints. These technologies leverage commercially available magnetic beads allowing users to isolate nearly any analyte for which there is a capture mechanism, including: RNA, DNA, proteins, and cells. For CTC based applications, cells can be isolated, stained for intra- and extracellular markers, imaged for enumeration or protein localization, and subsequently processed for additional markers. The assays integrate both positive and negative selection into a single assay to improve sensitivity and specificity. While the versatility is great for research-based applications, a clinical

application would require defined procedures and protocols, as well as demonstration of purity and consistency. To facilitate the integration into clinical applications, we automated CTC extraction.

While these technologies have been introduced to the field, each carries its own limitations and challenges, which must be considered before broadly applying a technology to a problem. In the CTC field, technologies are constantly challenged by patient-to-patient heterogeneity, both within the target CTC population and in the background populations. The recent automated platform developed from SLIDE has the greatest potential moving forward, as arguably, it is one of the most versatile platforms, able to tailor to the user's needs by integrating serial combinations of positive and negative selection. The ability to capture multiple selection markers in series and deplete out contaminant populations may prove useful in heterogeneous samples, where CTCs may not fit the traditional EpCAM-positive profile. To determine just how effective the automated platform will be moving forward, more extensive patient-centric studies will need to be performed.

15.2 Case Study 2:

The inability to easily prescreen cancer drugs prior to systemic administration greatly limits our ability to combat cancer. Recent publications have demonstrated the ability to inject/implant small dosages of drug (so there is minimal to no systemic effects) directly in to a tumor, enabling direct assessment of the tumoral response to that drug. While a step forward, these technologies remain limited by histological endpoints as they only provide a snapshot into the drug's impact on the tumor; histological endpoints are inherently limited in the number of analytes and lack quantitative readouts. In this section, an alternative technology is introduced, which goes one step further. The presented device is capable of delivering drug locally for extended periods of time (weeks as opposed to days) to expand the range of drugs that can be tested. We also demonstrated the device's ability to sample soluble factors directly from the tumor microenvironment; this is the first technology that we are aware of that is capable of in situ sampling. From this sample, we are able to acquire a range of downstream protein endpoints utilizing

MAGPIX assays, which are capable of quantifying 100 analytes simultaneously. Further, this technology has the potential of collecting alternative analytes including: RNA, DNA, or exosome collection.

While ensuring functionality both in drug delivery and in situ sampling, a simplistic design, able to be fabricated in house was maintained. The simplistic design allows the user to tailor the device as needed, to change delivery or sampling rates and ultimately to enable a broad range of applications. To date, the device has only been tested in localized tumor environments. However, this is, fundamentally, a simultaneous delivery and sampling technology. Because it is easy to alter the design, and easy to implant, it is conceivable that this could be used for monitoring environments outside of tumor. Within the scope of the presented project, additional animal tests will be required to move forward with this device prior to human trials.

With this technology, we aim to expand our knowledge base as to dynamics occurring within the tumor during treatment through continued sampling from within the tumor. Using this technology, we may gain insight into proteomic response or protein signatures that are indicative of treatment or predictive of treatment success. Furthermore, this technology, along with others in its field, will help clinicians move away from untested systemic treatment and directly asses therapeutic options, measure tumoral then administer a pre-tested successful treatment systemically.

15.3 Case Study 3:

Neutrophils are the most prominent leukocyte in the blood stream. Investigating their function – such as diapedesis/migration or the formation of neutrophil extracellular traps (NETs) – has the potential to identify new neutrophil-based biomarkers for immune related diseases, including: asthma, rheumatoid arthritis, sleep apnea, and even cancer. One area neutrophils may play an important role is in pre-symptomatic diagnosis of the aforementioned diseases, especially in infants and children. Due to our limited knowledge of the potential power of neutrophils in diagnosing disease, it is important that technologies are able to elucidate numerous features, including commonly used metrics (i.e., percent migrated, directionality) and new metrics. KOALA is uniquely positioned as a technology to identify the

role of neutrophils in these diseases. KOALA requires only a single drop of blood (a lancet puncture instead of venipuncture) making it amenable to a wide range of subjects, including children. KOALA operates directly from whole blood, meaning time from blood draw to assay operation is low, limiting the chance of biasing the neutrophil's response due to prolonged processing steps. Additionally, and possibly most importantly, we can perform short term studies to look at temporal effects of neutrophil and elucidate the potential impact of lifestyle factors (e.g., caffeine, alcohol, exercise) on neutrophil migration; ultimately these factors may play an important role if neutrophils are eventually used as biomarkers. Furthermore, we developed new analytic techniques in quantifying migratory response. By separating the tracks into segments – pre-migration, during, and post migration –significantly different results are observed as well as reduced variation between the cells.

Lastly, in order to expand the use of KOALA and get the technology into other labs and eventually into clinics, we will need to ensure the device is both user friendly and identify ways to package and ship the reagents within KOALA. For this reason, we have developed the KOALA fluid handling technology. This platform enables prepackaging and storage of reagents and cells along with maintained easy operation. Further testing will be necessary for each individual assay and reagent; however, the technology exists to facilitate nearly any cell-based assays.

In summary, we believe that integrating thermoplastic fabrication techniques into academic labs will help facilitate the transition from academic institutions to commercial production. However, more work will be necessary to get technologies into the hands of the users. A major hurdle that many microfluidic technologies face is that they still require analytic equipment, such as a microscope. This may not be prohibitive for academic labs, since many of them have access to the necessary equipment, but creates a challenge for implementation into clinics. To achieve widespread implementation of a microfluidic technology, researchers must be cognizant, take into consideration the numerous factors from sample acquisition to result. Early in the design phase, researchers must evaluate all of the steps

necessary to perform the assay, and keep these in consideration throughout testing and validation to assure that the technology is both manufacturable and implementable.

Appendix A – Micromilling: a method for ultra-rapid prototyping of plastic microfluidic devices [14]

A.1 Micromilling: General Setup

Proper setup and alignment of the workpiece and tool are critical for ensuring accurate high quality milling, and are especially important for the small features found in microscale devices. Most microfluidic devices are constructed from thin (and thus pliable) sheets of plastic, and this flexibility can often lead to errors if the material is not properly secured during fabrication. Tool misalignment can also lead to downstream misalignment and inaccuracies of all microfeatures in the fabricated device. Some CNC mills provide specialized workpiece holding systems and automated tool alignment hardware that help reduce issues associated with setup, but these systems are usually part of higher-end milling systems, and thus come with a significant jump in cost. Here, we discuss simple methods and strategies that will enable workpiece and tool alignment with any CNC mill, thus improving feature accuracy without significantly higher cost.

A.2 Workpiece Setup

To secure a workpiece for machining while also ensuring accuracy, we recommend following some simple steps while working with the most common milling and machining hardware available **(Fig. A.1).** The first and simplest method is to clamp the workpiece directly to the worktable by using strap clamps **(Fig. A.1a)**. To minimize warpage of thin flexible materials, the strap clamps should be positioned as close to the cutting region as possible. Rigid bars can be placed below the clamps, or span multiple clamps, to help distribute forces and improve support for the workpiece. An underlying layer of "sacrificial" material can be placed below the workpiece to protect the worktable from potential damage. This sacrificial material is intended to accommodate accidental impact from cutting tools in place of the worktable, but if this material is itself too compliant, it can lead to machining inaccuracies, especially in

14 This chapter has been adapted from the supplemental materials from the following publication: "Micromilling: a method for ultra-rapid prototyping of plastic microfluidic devices" David J. Guckenberger, Theodorus E. de Groot, Alwin M. D. Wan, David J. Beebe, and Edmond W. K. Young. Lab on a Chip 2015.

the vertical z-direction. Any rigid plastic, such as polycarbonate, poly(methylmethacrylate) (PMMA), or polystyrene (PS), is suitable as the sacrificial layer. Aluminum can provide a more rigid sacrificial material, but can cause more damage to small endmills. This method works best for rigid materials (i.e., metals, or thick plastics), and while amenable to thin plastics, it provides little support between the clamps, and thus requires that the machinist check for warpage and vibrations between the clamps.

The second method employs the use of common workshop vises, which can be used to secure thick or rigid workpieces, such as a micro-mold or a large microfluidic device **(Fig. A.1b)**. Vises are not well-suited for thin plastics because they often induce significant warpage in the workpiece. However, they deserve mention because they are readily available, and commonly used in machining.

The third method is best suited for high resolution machining, and involves the use of adhesives to secure the workpiece to a rigid substrate **(Fig. A.1c)**. The rigid substrate is secured to the mill stage and levelled using strap clamps, relying on compliant pads to allow for adjustment. The workpiece is then adhered to the rigid substrate using a double-sided adhesive. This technique provides a precise, flat surface that will not vibrate or warp during milling operations, and is not limited to sheet- like planar workpieces. It is worth mentioning that vacuum tables are also available as a means to secure a workpiece (and come standard on some mills), and provide similar characteristics to the adhesive technique discussed above.

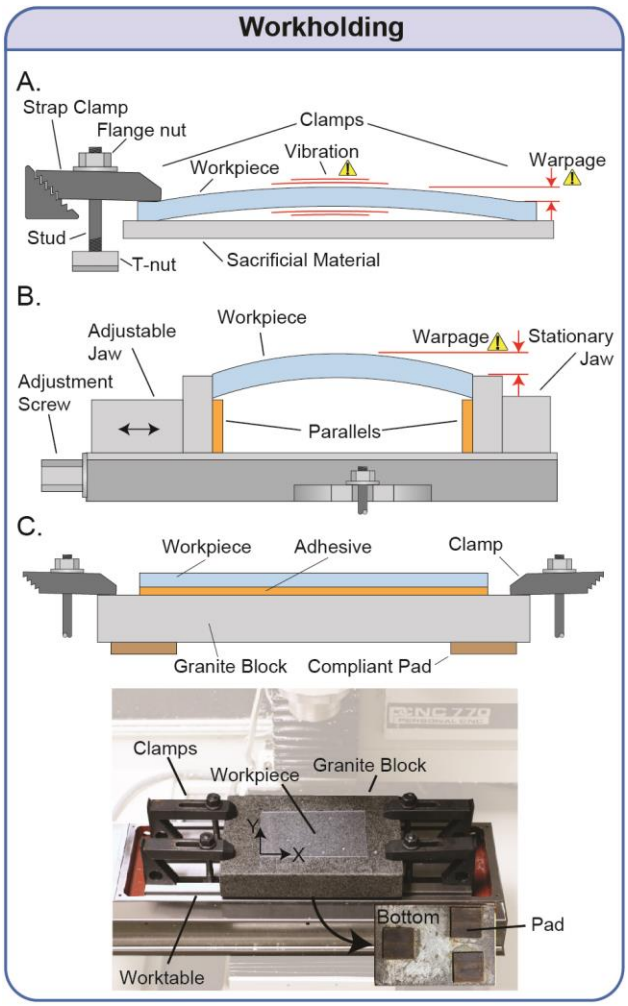

Fig. A.1 Simple low-cost workholding techniques. (a) Strap clamps can be used to secure the workpiece directly to the worktable. Use of sacrificial material will prevent damage to the worktable when milling through the workpiece. It is important to check for warpage when clamping thin materials, and to minimize vibrations when milling the device. (b) A vise is advisable for large objects. Parallels are often used to offset the object from the floor of the vise. Warpage can occur in thin materials, or from over-tightening. (c) Using adhesives to secure the workpiece to a known flat surface can reduce warpage and vibrations. A granite block is secured to the table using strap clamps at each of the four corners. Soft conformable pads below the granite block allow height adjustment via the clamps to level the block.

A.3 Tool Alignment

After the workpiece has been secured to the stage, the cutting tool must be properly aligned to ensure accurate cutting. Several simple methods to align the tool are discussed here, and are divided into methods for alignment along the Z-axis **(Fig. A.2a)**, and the X-Y-axes **(Fig. A.2b)**, respectively. For the Z-axis, four simple methods can be used. First, one can slowly lower or "step" the tool toward the surface while watching the tool contact the surface. When using reflective surfaces, it is often easier to watch the reflection of the tool coming into contact. Second, while running the spindle (i.e., rotating the tool), the

tool can be slowly stepped towards the surface. As soon as the tool contacts the surface, a chip will form, thus allowing the machinist to set the surface as the "zero" position. This method can be difficult to use with small endmills or ball endmills because the chip can be difficult to see. Third, with the spindle not running, one can lower the tool while sliding a piece of paper (of known thickness) back and forth underneath the tool, and between the tool and surface. The cutting tool, once in contact, will resist motion of the paper, at which point the position of the tool can then be offset from the surface by the thickness of the paper. Fourth, the tool can be left loose in the collet, and then tightened after it contacts the surface. This method is best suited for tool holders that secure the tool from the side via a setscrew. Additionally, no material is actually removed in this case, and the chance of user-induced tool damage is significantly reduced compared to the first three methods. However, because the endmill is held from the side in these holders, there will be a small lateral offset or *eccentricity* of the tool, with respect to the spindle axis. Upon completion of these methods (except for the paper method), the Z-axis position should be set to zero. If the paper method is used, the Z-axis position should be set to the thickness of the paper (e.g., ~0.003" / 0.075 mm). The accuracy of the first three methods is equivalent to the Z-step distance used during alignment. Drop test indicators are useful tools for levelling surfaces, and for checking surface flatness. One can simply lower the indicator to the surface, and traverse the XY-plane to measure variations in sample height.

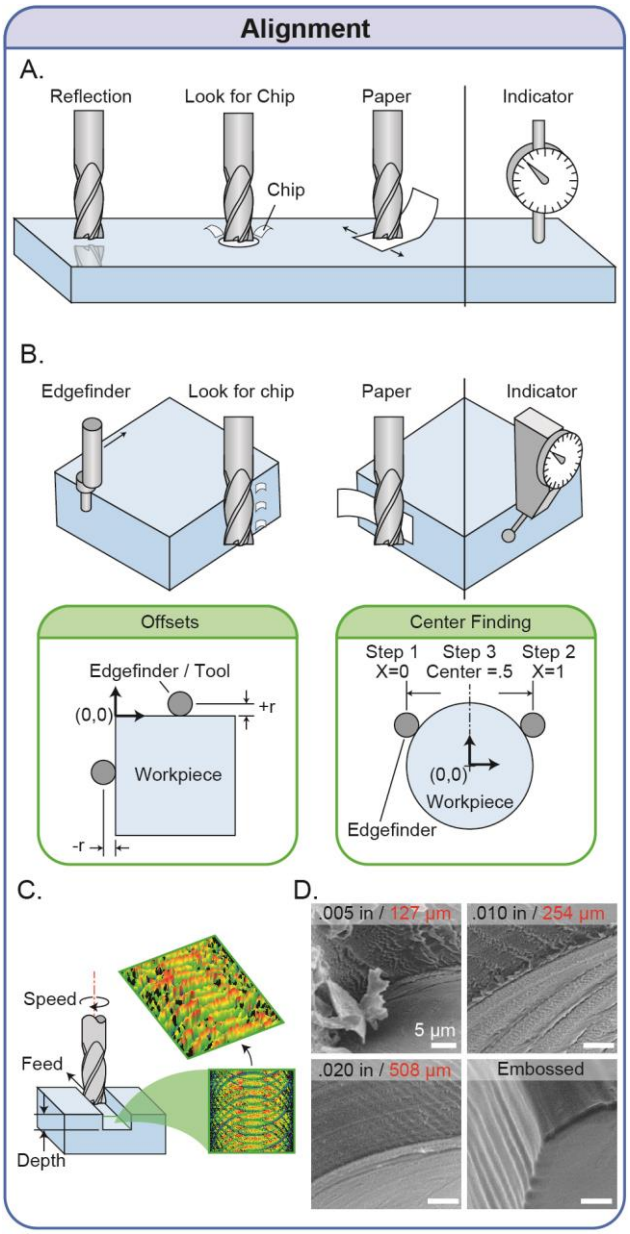

Fig. A.2 Tool alignment tips and tricks. (a) Methods for aligning the tip of the cutting tool to the surface, including visually verifying contact by reflection, looking for a chip of material, and using a piece of paper. (b) Methods for aligning the spindle axis to the edge of the part, including using an edgefinder, looking for a chip, or using a piece of paper. Green inset boxes represent: (i) the offsets from the tool edge to the spindle axis (left box) and (ii) a method to find the center of a workpiece (right box). Note that dial indicators can be used to detect the flatness of a surface or align a surface to an axis (a and b). (c) A milling operation is often defined by speed, feed, and depth of cut. The inset image was obtained from a profilometer measurement of surface roughness. (d) SEM micrographs of channels milled in PS with .005", .010", and .020" endmills, and an embossed channel. The object in the viewfield of the .005" endmill milled channel is a chip generated from the cut.

Alignment of the X and Y-axes may not be necessary for applications where the device is being milled from a large workpiece. In these cases, the X and Y-axis zeroes can be set at nearly any location on the workpiece. However, if the workpiece is already cut to the desired size, then the alignment of the X and Y-axes becomes critical **(Fig. A.2b)**. Three simple techniques are available for aligning the X and Y-axes. First, while the spindle is running, one can slowly step an *edgefinder* tool toward the surface of interest. An edgefinder is a two-part cylindrical tool where the top part is fixed in a tool holder, and the bottom part is initially eccentric, but connected to the top part. While continuously stepping the edgefinder toward the edge of interest, the bottom part will become concentric with the top part. Once the bottom part jumps to a side, the edge has been located. Second, while running the spindle, one can slowly step the cutting tool toward the surface of interest until contact is made, often indicated audibly or by the formation of a chip. Third, while running the spindle, one can slowly step the endmill toward the surface of interest while loosely holding a piece of paper against the surface. Upon contact, the endmill will pull the paper. ***Caution***: It is very important to use extreme care to prevent personal injury when employing this method. The second and third methods work well for large endmills, but are less suitable for micro-endmills because they produce chips that can be difficult to see, and they tend to cut through the paper, instead of pulling it. Nevertheless, when any of these alignment methods are correctly completed, the current position of the spindle axis (with respect to the XZ- or YZ-face) is offset from the face by the radius of the tool/edgefinder. These techniques can be employed to find the center of a workpiece, by simply setting one edge to zero, moving to the opposite edge to measure its position, and then determining the center by moving halfway between the two edges. Indicator probes are useful tools for helping the machinist align an edge of the workpiece with an axis of the CNC machine. This can be achieved by positioning the indicator probe on the side edge of interest, and traversing it along the parallel machine axis, while checking the indicator dial for orthogonal variation. Electronic probes are also now commercially available, and provide even higher precision and automated workflows, although they will add to the cost of the system. Overall, these techniques can achieve an accuracy equivalent to the minimum discrete step distance of the CNC.

A.4 Milling Techniques

Climb milling and conventional milling can yield drastically different results **(Fig. A.3a).** Beyond issues discussed in the main text (Section 4.2), deflection of the tool can cause loss in dimensional accuracy. As a result of conventional milling the tool will deflect into the bulk material, causing over removal. On the other hand, the tool will deflect away from the part when climb milling. While these deflections may be negligible, they should be considered, especially when using extended endmills, high feed rate, or difficult to cut materials.

Internal corners are not possible with and endmill, but various milling strategies can circumvent the inability to create internal corner **(Fig. A.3b)**. Internal corners are often needed when mating two components – such as a glass slide into a milled device. The rounded corner can be easily mitigated by milling the out the rounded portion of the corner.

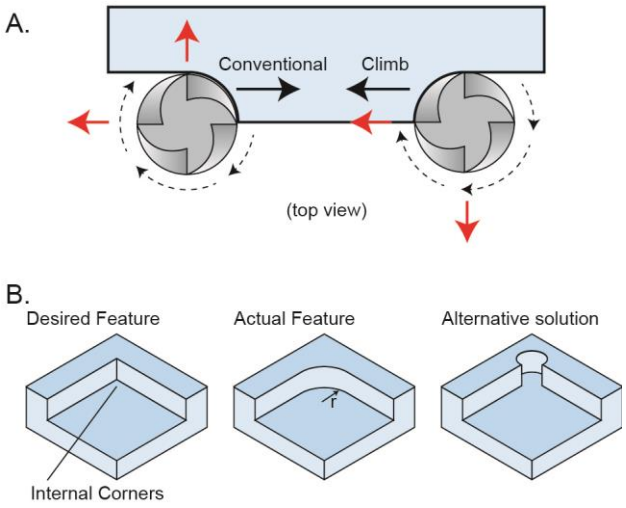

Fig. A.3 Milling strategies for surface finish and internal corners. (a) A comparison between climb milling and conventional milling. Black arrow represent direction of travel, dashed arrows represent direction of rotation, red arrows represent tool deflection. (b) A strategy to circumvent rounded internal corners.

A.5 Materials and Methods

A.5.1 CNC Fabrication

All CNC milled parts were fabricated with a Tormach PCNC 770 vertical milling machine (Tormach, Waunakee, WI). Microchannels and microfeatures (patterned on microdevices) were modelled with Solidworks (Dassault Systemes, Velizy-Villacoublay, France). The computer numerical control (CNC) program was created using SprutCAM (SprutCAM, Naberezhnye Chelny, Russia). Devices were milled into 1.2 or 2.0 mm thick polystyrene (PS) (#ST313120 and #ST313200, Goodfellow Cambridge Ltd., Huntingdon, England) using four flute carbide Accupro endmills in sizes of 0.005" (127 μm), 0.010" (254 μm), and 0.020" (508 μm) (#37289840, #37289857, and #37289840, MSC Industrial Supply Co., Melville, NY). To secure the PS workpiece to the machine worktable, a 6" x 12" x 2" Grade AA granite block (Standridge, Santa Fe Springs, CA) was first secured to the worktable using one clamp (#32580, Tormach) at each of the four corners **(Fig. A.1c)**. Soft, compliant material (i.e., foam padding) attached to the bottom of the granite block allowed fine adjustment via the clamps to level the block. Using a dial indicator (#24-315-4, SPI, Garden Grove, CA), the block was levelled to within ±0.00025" (6.4 μm) across 10" (250 mm) in the X-axis and 5" (125 mm) in the Y-axis. PS sheets were adhered directly to the block (with the manufacturer's protective film left on the PS sheet) using an adhesive transfer tape (#9472LE, 3M, St. Paul, MN). The levelness of the sheets was verified using a dial indicator.

Prior to milling, the manufacturer's top protective film covering the PS was removed, and the endmill was zeroed on the top surface of the PS via reflection method **(Fig. A.2a)** (variability of < .0005", or 12.7 μm). The devices were machined with varying feed rates, spindle speeds, and depths of cut. Feed rates (feed) were 1, 2.5, 5, 7.5, and 10 inches per min (ipm) (25, 64, 127, 190, and 250 mm/min, respectively); spindle speeds (speed) were 2500, 5000, 7500, and 10,000 rpm; and depths of cut (depth) were 25%, 50%, 100%, 200%, and 300% the diameter of the endmill. During milling, chips were cleared with a flood coolant of DI water mixed 20:1 with a synthetic coolant (#31750, Tormach). After machining, parts were rinsed with 70% ethanol in DI water, and dried with compressed air.

A.5.2 Hot Embossing

Polystyrene (PS) devices were embossed via epoxy molds fabricated as described by Young et al.[38] Devices without through-holes were embossed into 1.2 mm thick PS. Features with through-holes were embossed into a stack of 125- and 190-µm thick PS sheets (#ST311125 and #ST311190, Goodfellow), adding up to 80 to 125 µm less than the height of the tallest features. The embossing process was then set up as described by Young et al.[38]

A.5.3 Bonding

PS devices were bonded by one of two methods: (i) thermal bonding or (ii) solvent bonding. Devices were thermally bonded using techniques previously described by Young *et al*.[38] Devices were solvent-bonded based on established acetonitrile techniques.[74, 75, 315] Briefly, a hot plate was preheated to 70°C and covered with a sheet of lint-free lab wipe (#TX1109, ITW Texwipe, Kernersville, NC). Both halves of the PS device were placed on the hot plate and heated for 1 min. Acetonitrile (#271004, Sigma Aldrich) was dispensed drop wise onto one half of the device, and the second half was then promptly aligned and pressed onto the first half. After pressing by hand for 15 seconds, excess acetonitrile was aspirated from the channels, and pressure was reapplied to the device until all remaining acetonitrile evaporated (~30 seconds). All embossed devices were thermally bonded, while all milled devices were solvent bonded. Embossed devices, and one configuration of the milled devices, were bonded to a 125-µm thick PS cover layer. In the second configuration of milled devices, channels and ports were milled in separate sheets of 1.2 mm thick PS and the two sheets were bonded together.

A.5.4 Test Feature Design

Three different device designs were used to characterize (1) surface roughness, (2) resolution, and (3) cell-culture capabilities. To characterize surface roughness PS, PMMA (#63388722, MSC Industrial Supply Co.), or COC (#1420R, Zeonor, Louisville, KY) test pieces were first prepared by milling two parallel trenches (0.0625” wide by 0.0625” deep; 1.59 mm x 1.59 mm) separated by 0.5” (12.7 mm). Twelve individual test channels were then machined orthogonal to and spanning the two large trenches.

Each individual channel was machined in one tool pass, with varying parameters of feed, speed. Depth of cut was 100% and radial engagement was 50%. Trenches served to eliminate entrance effects in the Z-axis direction by allowing the endmill to enter freely, and then cut solely in the XY-plane.

To characterize spatial resolution for both the milling and embossing processes, square, circular, and rectangular features were milled or embossed into 1.2 mm PS. The height of the features were 100% the diameter of the endmill and the width for all features (diameter for the circular features) was 125 μm, 250 μm, 500 μm, 1 mm, and 2 mm. For rectangular features, the length was 10 mm. These features were replicated for all three endmill sizes with the following operational parameters: 2.5 ipm (63 mm/min), 5000 rpm, 100% (feed, speed, depth) for the 0.005" endmill; 1.5 ipm (38 mm/min), 5000 rpm, 100 % for the 0.010" endmill; and 0.25 ipm (6.3 mm/min), 5000 rpm, 100 % for the 0.020" endmill. The embossed features had the same dimensions as the machined features.

For cell culture experiments (see Section S2.6), milled channels were fabricated in two different configurations: (1) ports and channels were milled into one substrate, and (2) ports and channels were milled into separate substrates. In both cases, the microchannels were 10 mm long, 1.5 mm wide and 250 μm tall, with a 1 mm and 3 mm diameter port on opposing ends. Channels were milled with a .020" (508 μm) endmill at a speed, feed, and maximum depth set to .25 ipm, 5000 rpm, and 100%, respectively. Embossed channels had the same size as the milled channels, and were embossed as previously described.

A.5.5 Surface and Feature Analysis

Machined and embossed features were characterized by white light interferometry (NewView 7300, Zygo, Middlefield, CT) and imaged via scanning electron microscopy (SEM) (S-570 LaB6, Hitachi, Chiyoda, Tokyo, Japan). Samples were prepared for interferometry and SEM by sputtering gold and gold/palladium alloy. Surface roughness, feature size (i.e., width and length), and feature depth/height were measured with the Zygo NewView software. Surface roughness was quantified as the root-mean-square of the surface roughness along the length of the channel. Feature width was measured by drawing

a line from the edges of the feature and reporting the length. The depth was measured by taking a peak-to-valley measurement of a line drawn across the channel edge (i.e., a cross-sectional profile).

To characterize the XY accuracy and precision of the features, the parts were imaged with a stereoscope (#SZX12, Olympus Corp. Tokyo, Japan) and measurements were made against a ruler using ImageJ. Measurements made with the stereoscope were compared to those made with the interferometer. Measurements of features fabricated with the same endmill were pooled and analyzed together.

A.5.6 Vapor Polishing

The PS microchip was milled using a 1/8" diameter carbide ball endmill (#CCMG-404-B, Melin Tool Company, Cleveland, Ohio). The speed was 5000 rpm, the feed rate was 610 mm/min, and the depth of cut was 1% the diameter of the endmill. The acetone bath was created by placing a petri dish filled with acetone on a hot plate heated to 40° C. Once the acetone bath was heated, the microchip was flipped upside down, allowing the vapor to access the features, and held in the vapor for 90 seconds.

A.5.7 Cell Culture, Channel Preparation, and Analysis

To validate and demonstrate cell viability and image quality we cultured three cell lines: (1) human umbilical vein endothelial cells (HUVECs) cultured in EBM-2 media (#CC-3156 and #CC-4176, Lonza, Basel, Switzerland) with 10% FBS and 1% penicillin/streptomycin (P/S) (#15140-122, Gibco, Life Technologies, Carlsbad, CA); (2) PC-3 (stromal prostate cancer) cells cultured in RPMI (#10-040-CV, Cellgro, Manassas, VA) with 10% FBS, 1% P/S, 1% sodium pyruvate (#25-000-CL, Cellgro), and 1% MEM non-essential amino acids solution (NEAA; #11140-050, Gibco); and (3) HS-5 (bone marrow stromal) cells cultured in high glucose DMEM (#10-017-CV, Cellgro) with 10% FBS and 1% P/S. To promote cell adhesion, the microchannels and the PS substrates were treated with oxygen plasma (45 seconds, 50 W, 2.2 mbar) (Femto, Diener, Thierry Corporation, Royal Oak, MI) prior to bonding.[126, 191] To promote adhesion for HUVECs, these channels were also coated with bovine fibronectin at a concentration of 0.1 mg/mL for 15 min at room temperature.

Channels were assembled in three configurations: (1) embossed and thermally bonded to a PS cover layer; (2) milled into a PS workpiece, and then solvent-bonded to a PS cover layer; and (3) were milled into separate workpieces for channels and ports, respectively, and then solvent-bonded together. A tissue culture-treated 96-well microtiter plate (#353072, Corning Life Sciences, Corning, NY) was used as a control. The cells were seeded into the channels or wells at a surface density of ~25 cells/mm^2, and cultured at 37° C. Media was replaced after 24 hours of culture, and a LIVE/DEAD assay was performed at 48 hours using calcein AM (#C3100MP, Life Technologies) and ethidium homodimer (#L3224, Life Technologies), respectively. Each channel was imaged on an inverted epifluorescent microscope (TI Elcipse, Nikon, Tokyo, Japan), using 4, 10, and 20x objectives. Images were stitched together using Photoshop CS3 (Adobe, San Jose, CA), and cells were counted with ImageJ using the "find maxima" function in a region that was 1.25 x 9 mm. For each cell type and each assembly configuration, three channels/wells were cultured, counted, and averaged together. The average viability represents the percent of viable cells compared to the total cells present in each analyzed region, and the error bars represent one standard deviation.

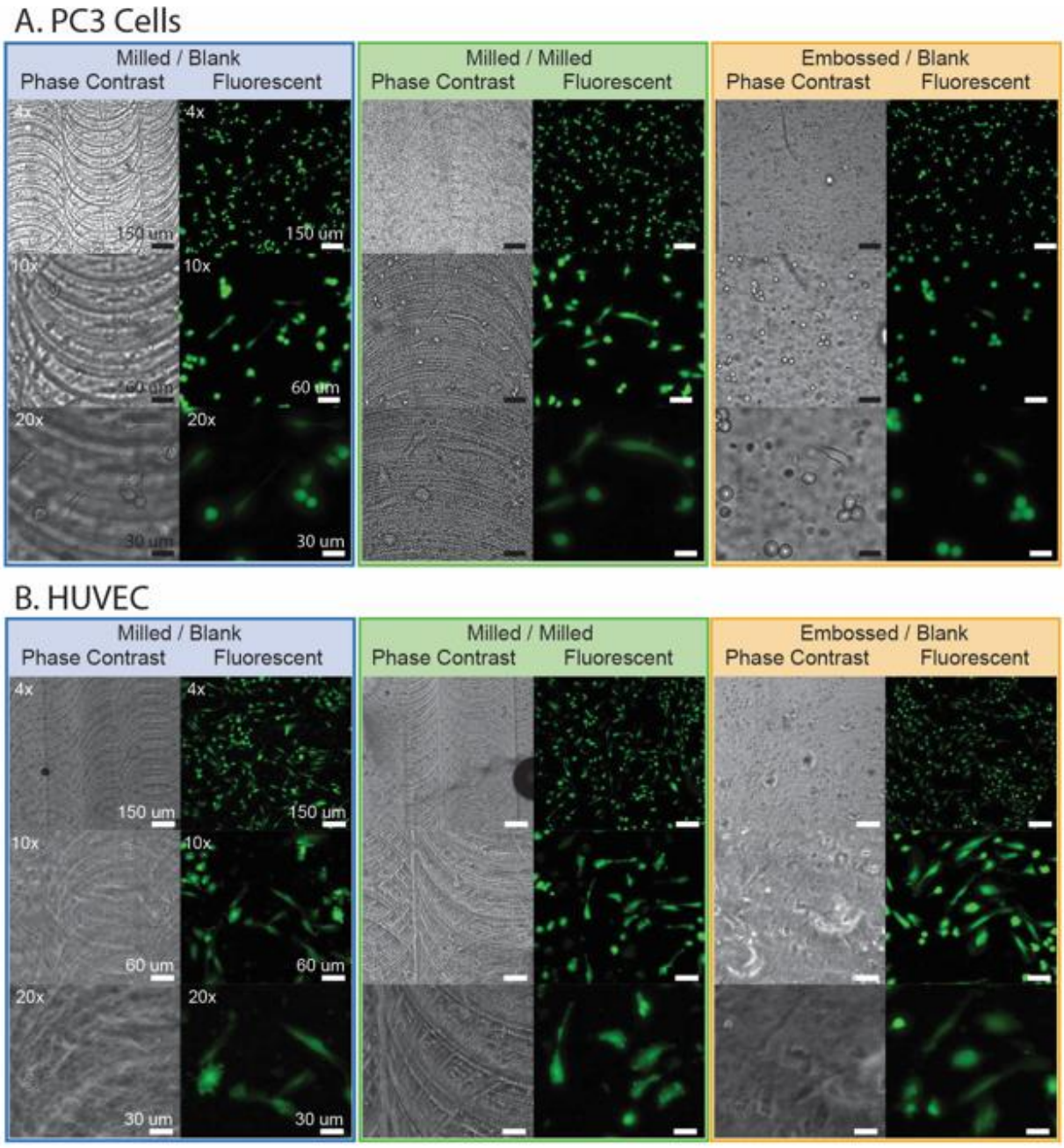

Fig. A.4 Cell culture and image analysis in milled and embossed microchannels. (a) PC3 and (b) HUVEC cells have been cultured in milled milled micrchannels bonded to a flat substrate (blue), milled ports bonded to a milled microchannel (green), and embossed microchannels bonded to a flat substrate (yellow). Each channel configuration was imaged using 4, 10, and 20×.

A.6 Supplemental Data

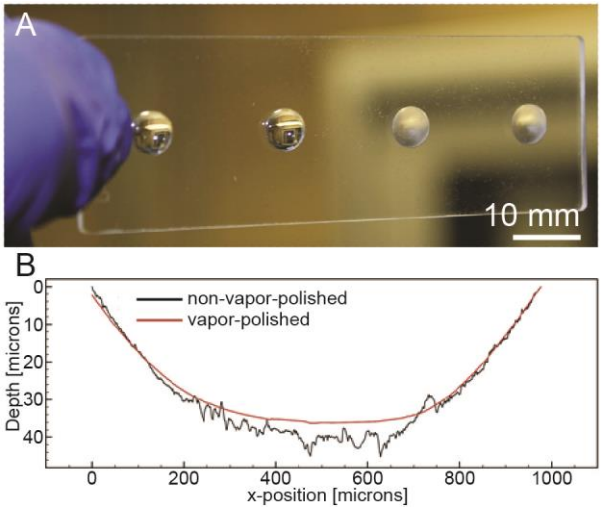

Fig. A.5 Vapor polishing milled devices. (a) Photograph of polystyrene (PS) slide with micromilled round-bottom wells. Two wells on the left were vapor-polished by placing the rough features directly above an acetone bath for 90 seconds. The two wells on the right were not vapor-polished. Note the lens-like surface finish of the two curved wells on the left. (b) Surface roughness of vapor-polished (red line) and non-vapor-polished (black line) wells as measured by surface profilometry.

A.7 CNC Programming

A.7.1 Computer Aided Design (CAD)

Both 2D and 3D CAD programs can be used in concert with downstream CNC milling process, each having its own advantages. 2D CAD programs include DraftSight (Dassault Systemes) and AutoCAD (Autodesk), and are advantageous for creating simple 2D sketches of parts *where the lines in the sketch itself are used as toolpaths for the milling operation* (see section C.2, Computer Aided Manufacturing). 3D CAD programs include Solidworks (Dassault Systemes), Inventor (Autodesk), and Pro/ENGINEER (PTC), and is more convenient to use with more complex parts involving multiple heights or contoured features. OpenSCAD is a 3D CAD software that uses text-based scripts, but is amenable to Windows, Mac, and Linux operating systems. The CAD work done in this paper was all performed with Solidworks.

A.7.2 Computer Aided Manufacturing (CAM)

Computer aided manufacturing (CAM) programs translate 2D sketches or 3D solid models from CAD into programming language that can be processed by the CNC mill. Note that CAD/CAM is

essentially CAM software integrated with CAD capabilities. CAM programs enable the user to define the material and the coordinate system, and use features to create and parameterize *toolpaths*, i.e., paths that the cutting tool follows to create the device. Many CAM software packages are available, including Mastercam (CNC Software Inc.), which integrates directly with the Solidworks design software, and SprutCAM, which is free for academic institutions. Here, we provide the basic knowledge for writing your own code, with a simple example to illustrate the process.

A.7.3 Origin Selection

While setting the toolpaths, the CAM software will require the user to define an origin, i.e., the point at which all axes (X, Y, and Z) are zeroed. The location of the origin is chosen by the machinist at their own discretion, but general strategies can simplify workflow and repeatability. In general, when setting the origin it is easiest to define a location that is accessible for measurement. For example, if the workpiece is significantly larger in the X- and Y-axis then the final component, then the X- and Y-axis origins can be arbitrarily chosen; however, if the workpiece is close to or the same size as the final component it is advisable to set the X and Y zeroes at the edges or center of the workpiece. For the Z-axis, it is often easiest to zero it at the top of the workpiece in either case. When using a vise, efficiency can be improved by setting an origin at the location of the stationary jaw. This allows the machinist to insert new workpieces without needing to re-zero the perpendicular axis. Keep in mind that once a surface is removed, that surface can no longer be used to reference the tools. In cases where re-referencing a workpiece is necessary (such as a tool change) and removing the reference point is unavoidable, it is easier to reference off an alternative object (such as the vise) instead of the workpiece itself. For information on locating the origin on the mill, we direct the reader to Section A.2 (Tool Alignment).

A.7.4 G-Code Basics

G-code is a subcategory of numerical control (NC) programming language, and is the code that controls the CNC machines. Postprocessors in the CAM software write and tailor the G-code specifically for the CNC controller in the machine. While this process is fairly reliable, the user may occasionally

need to intervene in a process, or double-check that the transfer of code was completed successfully. Having an understanding of the G-code will enable the user to check that the code has been written properly and to troubleshoot any issues that arise during milling. Furthermore, a basic understanding will enable the user to write custom G-codes by hand (in .txt file format) for simple tasks, which would otherwise be complicated by CAD/CAM programs.

Syntax

A list of NC codes can be easily found online; here we provide a shortened list with commonly used commands – that will work with any CNC mill – to give an understanding of syntax **(Fig. A.6a)**. G-code commands are alphanumeric, where the letter dictates the classification and the number specifies a classification subtype or location. In general, M classifications correspond to machine control – such as starting or stopping or spindle, whereas G classification correspond motion – such as moving the stage. In this section, we provided a detailed description of how these commands are used and structured **(Fig. A.6b)**.

M-Commands:

M1 – optional stop – will pause the program, allowing the user to check the part, manually change a tool, or re-align the axis. Once finished, the program will restart at the point it left of. Notice, the M1 will only stop the axis motions and will not stop the spindle or the coolant. The spindle and coolant can be stopped and started either manually or automatically using the following 'M' commands.

M3/M4 – start spindle in the clockwise/counter clockwise direction - will start the spindle. The speed at which the spindle turn, is specified using the 'S' command, described later. Most cutting tools cut in the clockwise (M3) direction, however users should check the tools to verify the cutting direction.

M5 – spindle stop – will turn the spindle off

M8/M9 – coolant start/stop – will turn the coolant on or off. Word of advice, it is sometimes advantageous to turn the coolant on prior to starting the spindle. This start up time will allow the coolant pump to start running, and reduce the chances of cutting before the coolant makes it too the tool.

G-commands:

G20/G21 – These commands are used to define metric or imperial unit systems. The units for distance will be either mm or inches and the units for speed will be either millimetres/minute or inches/minute, respectively. Only one of these commands can be active, and it should be specified at the beginning of the program. No additional syntax is associated with these commands.

G90/G91 - These commands define the coordinate system to either absolute or increment. As an example, if we want to move from starting location of (2, 3) to a new location of (4, 1) then we would specify X4 Y1 when using absolute coordinates but X2 Y-2 for incremental coordinates **(Fig. A.6b)**. In essence, G90 bases the coordinates off an origin while G91 resets its current location as an after each movement. Only one of these commands can be active, and it should be specified at the beginning of the program. No additional syntax is associated with these commands.

G0-G3 – These commands control the motion of the CNC. Each of these commands are followed by an X, Y, and Z, which specify the coordinates to which the tool will move. The G# simply specifies the path by which the tool will go to those coordinates.

G0 – linear interpolation – will move to the coordinates in a straight line at maximum speed

G1 – linear interpolation (Feed rate controlled) – will move to the coordinates in a straight line using a user defined feed rate set using the 'F' command (see below).

G2/G3 – Clockwise/Counter-clockwise Circular Interpolation – will move to the defined coordinates using an arced path. The center point of the arc is defined using I (for the X-axis location) and J (for the Y-axis position), which will succeed the X, Y, and Z. Some software will use a defined radius 'R' instead of and defined center point. Like G1, the feed rate is defined using the 'F' command.

The general structure for these commands is G# X# Y# Z# I# J#. However, any coordinates that do not change between the current position and the newly defined location do not need to be defined. For example, if the tool is set to move from position (2,3) to (2,1) we would write G1 X2 Y1 Z#; but, because the tool need only move in the Y-direction, we can truncate the command to G1 Y2 (using absolute (G90) coordinates). In fact, the only time two or more variables should be specified is when two or more of the axis need to move simultaneously. For example, if the tool is to move from position (2,3) to (4,1), directly, the truncated command would be G1 X4 Y1 (using absolute (G90) coordinates)

A.

Assorted Commonly Used G - Code

M1	*Optional Stop*	**G0**	*Rapid Motion*	G0 X# Y# Z#
M3	*Start Spindle*	**G1**	*Linear Motion*	G1 X# Y# Z#
M5	*Stop Spindle*	**G2**	*CW Arc*	G2 X# Y# Z# I# J#
M6	*Tool Change*	**G3**	*CCW Arc*	G3 X# Y# Z# I# J#
M8	*Start Coolant*	**N**	*Line Number*	N#
M9	*Stop Coolant*	**T**	*Tool Number*	T#
G20	*Inches*	**F**	*Feed Rate*	F#
G21	*Millimeters*	**S**	*Spindle Speed*	S#
G90	*Abs. Coord.*	**;**	*Comment*	
G91	*Incr. Coord.*			

B.

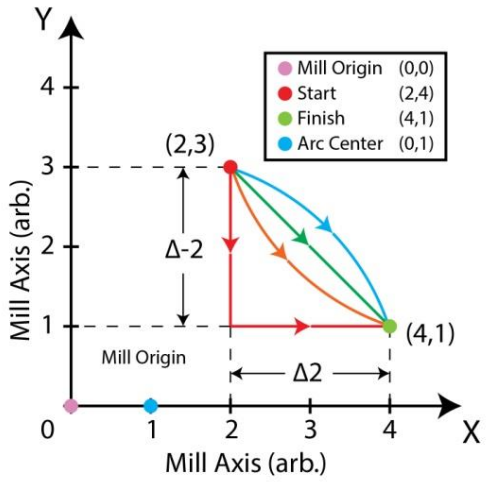

Start / Finish	Absolute (G90)	Incremental (G91)
	G1 X4 Y1	G1 X2 Y-2
	G1 Y1 G1 X4	G1 Y-2 G1 X2
	G2 X4 Y1 I1 J0	G2 X2 Y-2 I-1 J-4 (R4.5)
	G3 X4 Y1 I1 J0	G3 X4 Y1 I1 J0

Fig. A.6 G-code basics. (a) Simplified list of G-code commands sufficient to create a handwritten program. (b) Example of specific G-based commands and their associated motion profile, shown both in absolute and incremental coordinates. Axis scales are arbitrary but would be in either inch (G90) or mm (G91) units.

Other Commands:

T – Tool Number – sets the tool number and should be set at the beginning of the program or every time a tool is changed (Syntax: T#). This command is not necessary if tools are being manually changed by hand.

S – Spindle Speed – defines a speed (in RPM) for the spindle (Syntax: S#). Once a speed is defined, that speed will be utilized until a new speed is defined, even if the spindle is turned off then on again.

F – Feed Rate – defines the rate at which the tool will move relative to the material (Syntax: F#). Feed rate will have units of in/min (G20) or mm/min (G21). Once a feed rate is defined, that feed will be utilized until a new feed is defined. New feed rates, if needed, can be assigned for each 'G' command.

N – Line Number – is would be positioned at the beginning of every line of code (Syntax: N#). Each line can contain multiple commands consisting of: 'M', 'G20/G21', 'G90/G91', T, S, and F commands. However, 'G0 – G3' shall be listed on independent lines.

';' or '( )' – comments – enclosing code in parenthesis or preceding it with a semicolon will render that portion of the code to be a comment. Comments have no effect of operation of the mill and use of comments allows the user to temporarily block of portions or code, add reminders, or label steps.

A.7.5 Building a Code: An Example

Using the basic commands previously described, we provide a G-code example and go through it step by step to help the reader understand how to write their own code **(Fig. A.7)**. To start, we define our origin at the top-left-front corner of the workpiece. In N2 (line 2) we specify absolute coordinates (G90) and inch units (G20). In N3, we specify "Tool Number One", although this is only necessary if you are using an automatic tool changer or tool offsets. In N4, we start the coolant (M8), set the spindle speed (S#), and start the spindle (M3). From our experience, it is advantageous to start the coolant prior to starting the spindle, because this allows some time for the coolant pump to start, allowing the coolant to reach the tool prior to milling. N5 rapidly moves from where the tool is currently located (G0) to a location that is close to the starting location. N6 sets the feed rate (F#) and linearly plunges (G1) into the part. N7 moves linearly in the X-axis. Note that because a G1 command was defined in N6, it is not necessary to redefine the motion type. The machine will stay in G1 until a new motion type is specified. N8 mills an arc in the counterclockwise direction (G3) about a center located at (2,-1). N9 – N12 are

linear motions, but importantly, N10 moves in the X and Y directions simultaneously. N13 removes the tool from the part, and finally N14 stops the spindle (M5) and the coolant (M9).

Many G-codes are often significantly longer and more complex than the example shown here. It is at the discretion of the machinist to decide whether writing the code manually would be advantageous. However, the ability to write code manually can enable mill users to expand the utility of their mill. Keep in mind that a mill is a programmable machine with X Y and Z axes, and that the machinist can use this programming for other applications besides milling. [2,329, 330]

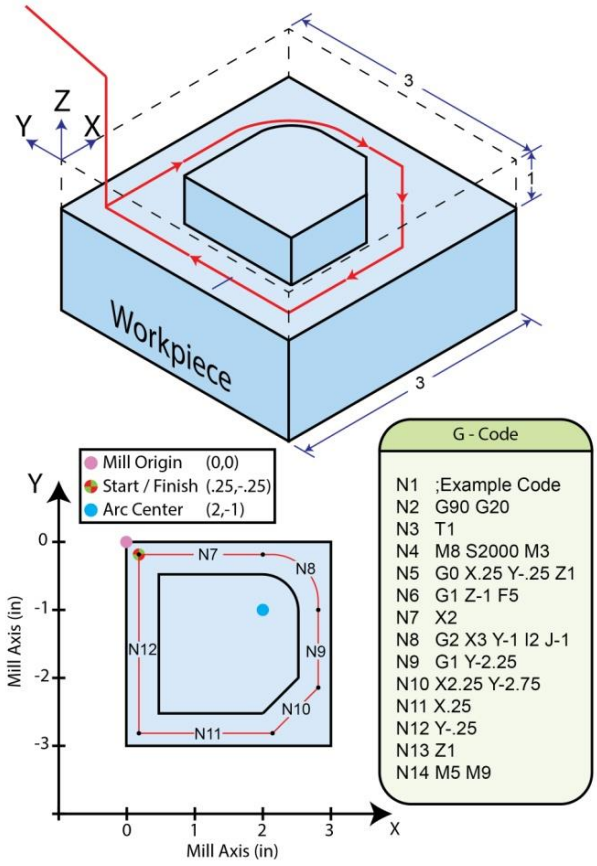

Fig. A.7 An example of a G-code demonstrating basic commands. The toolpath (red line) is shown in segments marked by the corresponding line number of code. The origin is set to the top-left-front corner of the workpiece.

Appendix B Fluorescence-based Assessment of Plasma-induced Hydrophilicity (FAPH) in Microfluidic Devices via Nile Red Adsorption and Depletion[15]

B.1 Results and Discussion

B.1.1 Cell Adhesion: The Need for in situ Measurements

The need to develop a fast, convenient, and informative method for determining surface hydrophilicity within microchannels was motivated in part by observations of inadequate cell adhesion and spreading in microchannels in cases when the plasma treatment was not optimized. Further, little is known about how plasma treatment occurs in confined environments though plasma in microchannels has been used to perform analog computing[331]. To illustrate how surface conditions, after oxygen plasma treatment, can affect cell adhesion, we cultured two established adherent cell types in microchannels with PS substrates, human umbilical vein endothelial cells (HUVECs) **(Fig. B.4A)**, and NIH-3T3 fibroblasts (FBs) **(Fig. B.4B)**, quantified the number of adhered cells and the cell spreading area **(Fig. B.4C)**, and normalized this data against their respective control conditions **(Fig. B.4D)**, as a metric of compatibility with the surface. For HUVECs, the control surface was PS with fibronectin (FN) coating at 0.1 mg/mL, and for FBs, the control surface was untreated PS.

15 This appendix has been adapted from the supplemental materials from the following publication: "Fluorescence-based Assessment of Plasma-induced Hydrophilicity (FAPH) in Microfluidic Devices via Nile Red Adsorption and Depletion" David J. Guckenberger, Erwin Berthier, Edmond W. K. Young, and David J. Beebe. Analytical Chemistry, 2015.

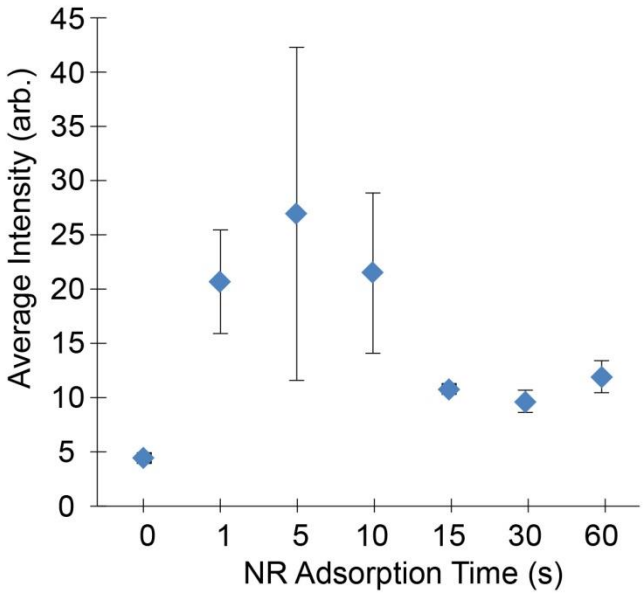

Fig. B.1 Fluorescent characterization of Nile Red. Fluorescence intensity is a function of adsorption time, and longer adsorption times yield better coating homogeneity (lower variability in intensity between images) (n = 3).

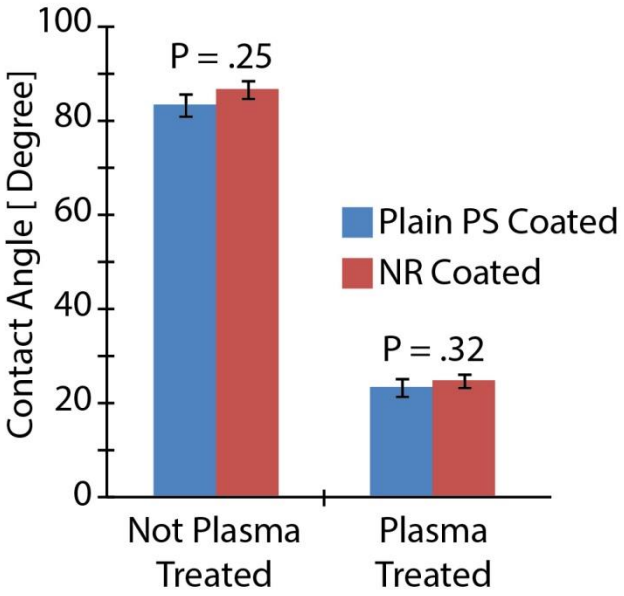

Fig. B.2 Impacts of NR on contact angle. The NR applied to the PS surface does not significantly affect the contact angle for non-plasma treated PS (p = .25) or plasma treated PS (p = .32) (Student T-test, n = 3).

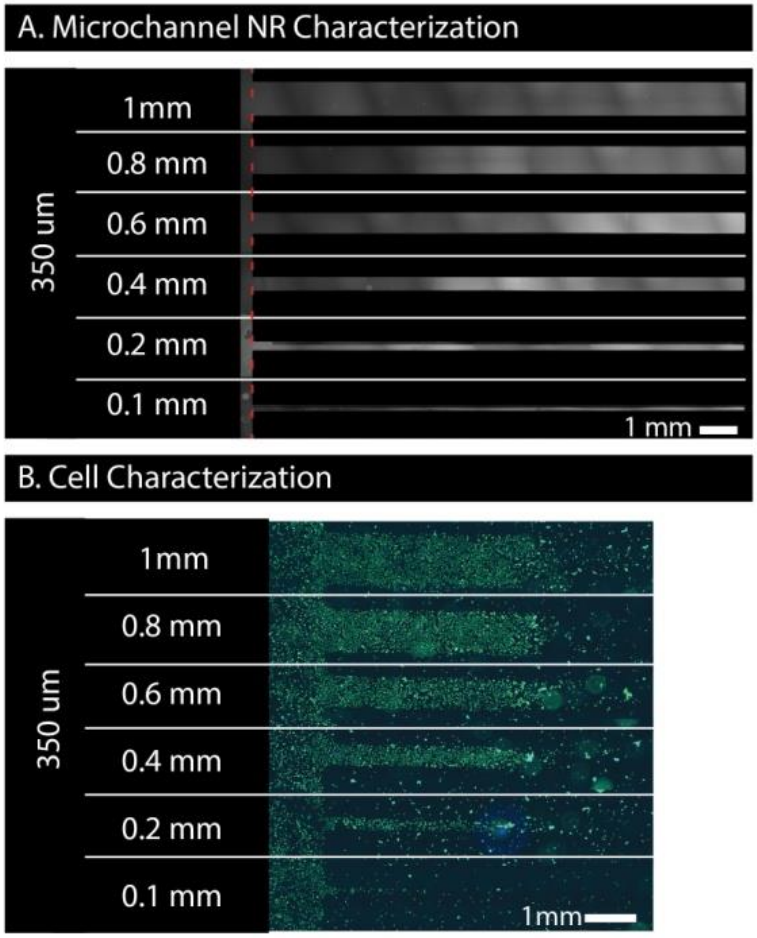

Fig. B.3 Impacts of channel dimesion of plasma treatment. (A) Nile Red characterization of 350-µm tall microchannels. There was significant variability in the fluorescent output after plasma treatment. (B) HUVECs cultured on a PS substrate after plasma treatment with 350-µm tall microchannels. Channels wider than 0.4 mm had a δ of ~4 mm, while the 0.1 and 0.2 mm wide channels had a δ of 0.2 and 1.2 mm, respectively.

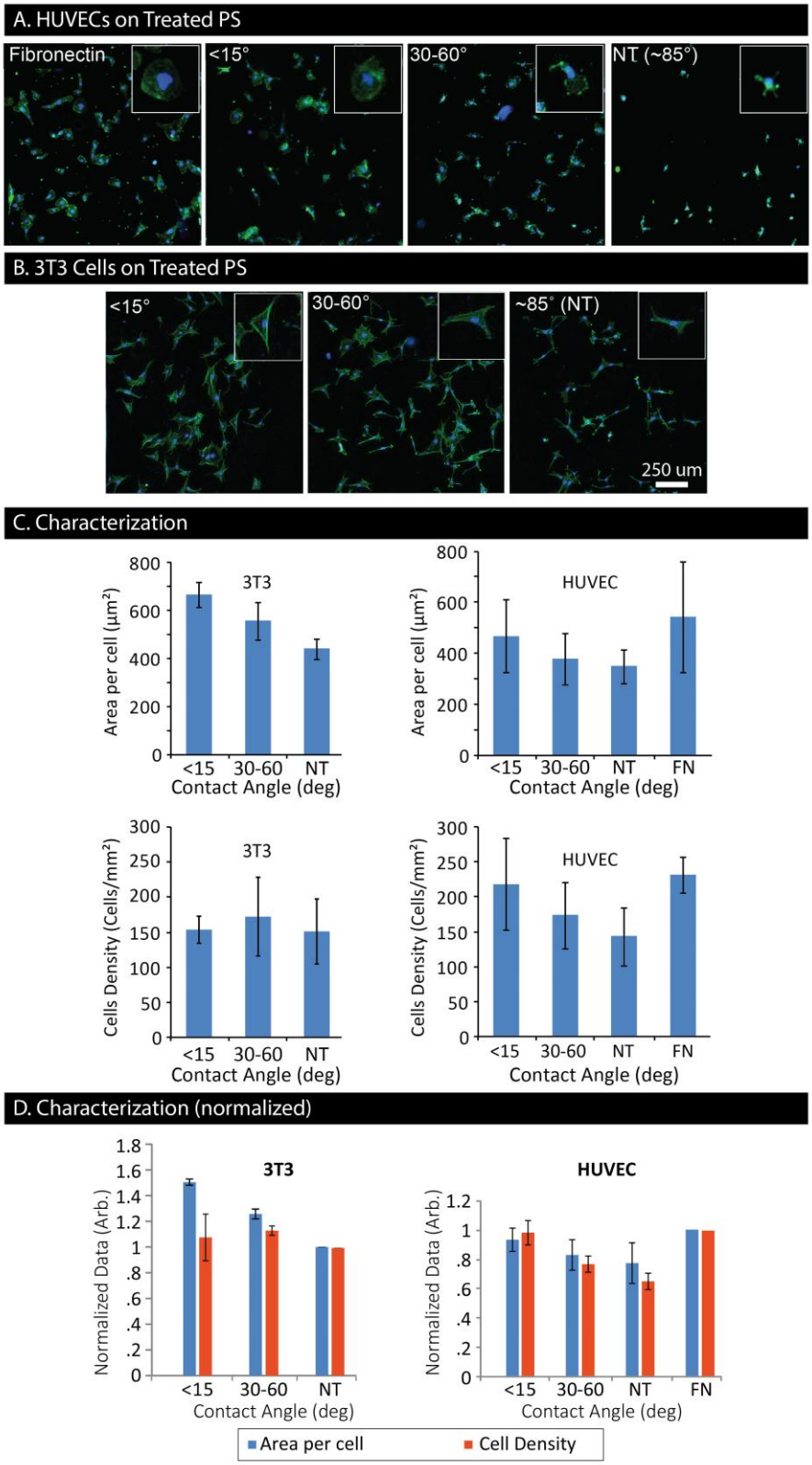
A. HUVECs on Treated PS
Fibronectin
<15°
30-60°
NT (~85°)
B. 3T3 Cells on Treated PS
<15°
30-60°
~85° (NT)
250 um
C. Characterization
3T3
HUVEC
Area per cell (μm²)
Cells Density (Cells/mm²)
<15
30-60
NT
FN
Contact Angle (deg)
D. Characterization (normalized)
3T3
HUVEC
Normalized Data (Arb.)
Area per cell
Cell Density

Fig. B.4 Impact of surface treatment on cell density and morphology. Culturing (A) HUVECs and (B) FBs on non-NR-coated PS samples demonstrate the effect of hydrophilicity on morphology and cell adhesion. (C) Average area per cell, and number of cells per unit area (cell density) were quantified for both HUVECs and FBs. (D) Normalized data for average area per cell, and number of cells per unit area. FBs were normalized to the untreated PS surface, and HUVECs were normalized to the fibronectin (FN) treated surface (n = 9). Both cell types follow the trend of decreasing average area per cell as the level of plasma treatment decreases.

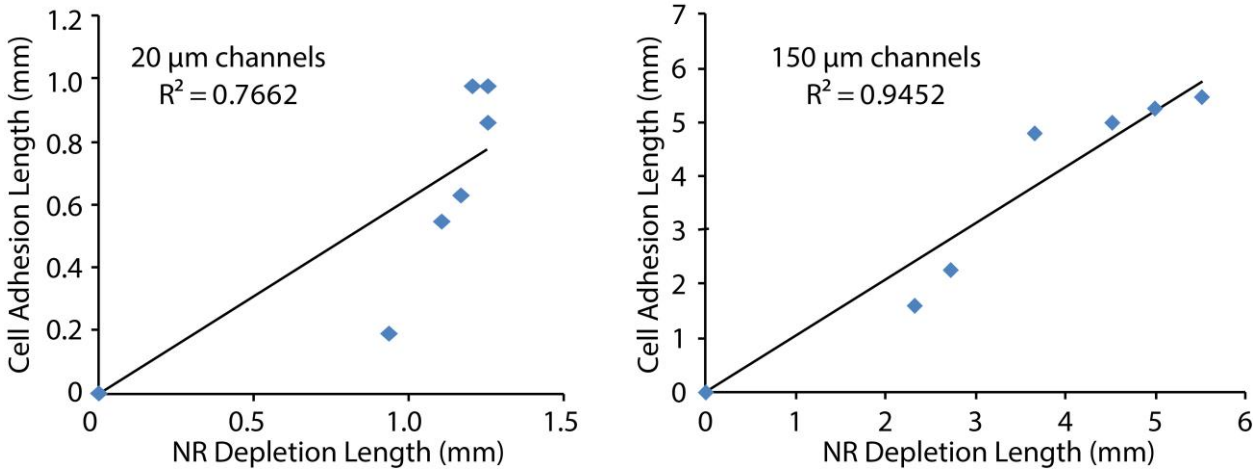

Fig. B.5 Correlation between FAPH and cell culture. Comparison between penetration distances based on the half maximums for NR-depletion and cell culture in 20 µm and 150 µm tall plasma treated microchannels.

Fig. B.6 Impacts of multiple ports (access points) on microchannels. Comparison between plasma treated channels with one open (top) verse two open ends (bottom). Penetration distance of the channel with one open end is 3.67 mm and penetration distance into the channel with two open ends is 3.77 mm.

Appendix C The VerIFAST: An integrated method for cell isolation and extracellular/intracellular staining [16]

C.1 Method Comparison

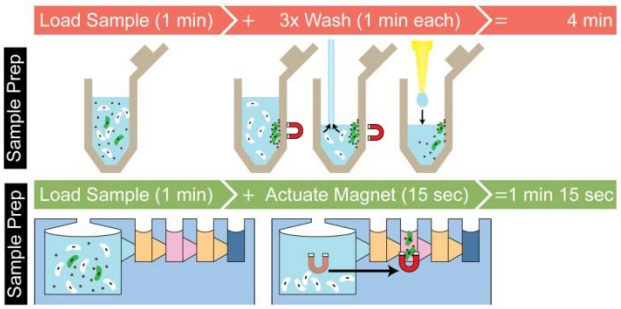

Fig. C.1 Workflow diagram comparing tube-based techniques and the VerIFAST. Sample Prep includes whole blood applications, and refers to preparation via density separation.

C.2 Benchmarking

	Veridex	CTC Chip	Filter	VerIFAST
Short assay time	✗	✗	✓	✓
Cells are viable	✗	✓	✓	✓
Cell removal	✗	✗	✗	✓
Simple to use	✗	✗	✓	✓
Multiple analytes	✓	✓	✗	✓
Easy to image	✓	✗	✗	✓
Clinically proven	✓	✓	?	?
Negative selection	✗	✗	✓	✗

✓ = Yes ✗ = No ? = To be determined

Fig. C.2 Benchmarking VerIFAST. Comparison between the VerIFAST and other methods of cellular isolation - including commercially available methods.

16 This appendicy has been adapted from the supplemental materials from the following publication: "The VerIFAST: An integrated method for cell isolation and extracellular staining" Benjamin P. Casavant*, David J. Guckenberger*, Scott M. Berry, Jacob T. Tokar, Joshua M Lang, and David J. Beebe. Lab on a Chip 2012

* Authors contributed equally

C.3 Oil Comparison

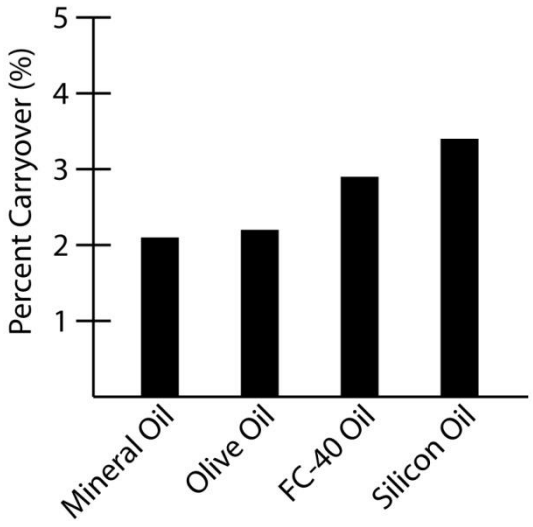

Fig. C.3 Comparison of oils used in the VerIFAST. The percent carryover was characterized by loading a fluorescent die into the input, and measuring the level of fluorescence carried through the oil and into the output well.

C.4 Staining Protocol

Step	Reagent	Time for step	Temperature
Fixation	4% PFA in PBS	10 minutes	22.5C
Wash (3x)	0.1% BSA in PBS	1 minute	22.5C
Permeabilization	1% Tween-20 in PBS	30 minutes	22.5C
Primary Antibody	1:50 primary antibody in PBS with 0.1% BSA	24 hours	4C
Wash (3x)	0.1% BSA in PBS	1 minute	22.5C
Secondary Antibody	1:500 secondary antibody in PBS with 0.1% BSA	2 hours	22.5C
Wash (3x)	0.1% BSA in PBS	1 minute	22.5C

Fig. C.4 List of the steps required for the intracellular staining. This entire process can be performed in the VerIFAST, without the risk of significant cell loss through the membrane. Furthermore, the VerIFAST enable beads to be removed from the cells prior to this staining process.

Appendix D Rapid and efficient sample preparation from complex biological samples using a Sliding Lid for Immobilized Droplet Extractions (SLIDE)[17]

D.1 Cam Mechanism

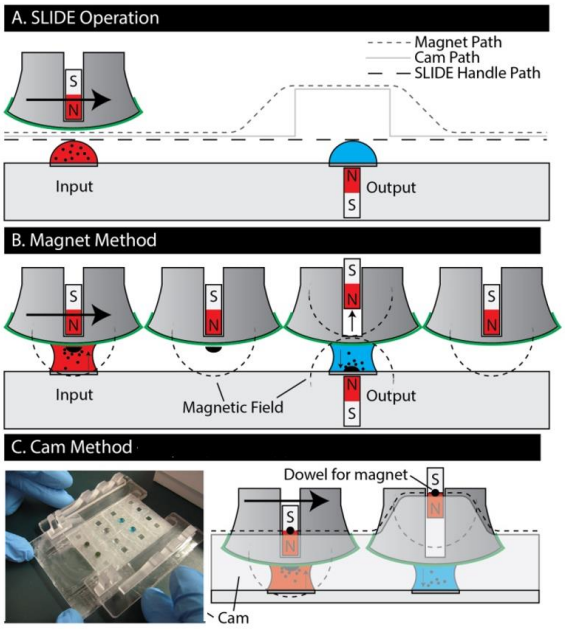

Fig. D.1 The SLIDE cam versus magnet method. (a) SLIDE operation showing either a CAM path to move the magnet or the magnetic displacement force. (b) Detailed description of the magnetic method to move PMPs from the top surface to the bottom drop. (c) The cam-based SLIDE is shown (left) with the physical motion (right).

17 This chapter has been adapted from the following publication: "Efficient Sample Preparation from Complex Biological Samples Using a Sliding Lid for Immobilized Droplet Extractions" Benjamin P. Casavant*, David J. Guckenberger*, David J. Beebe, and Scott M. Berry. Analytical Chemistry 2014.

* Authors contributed equally

D.2 Wax Patterning

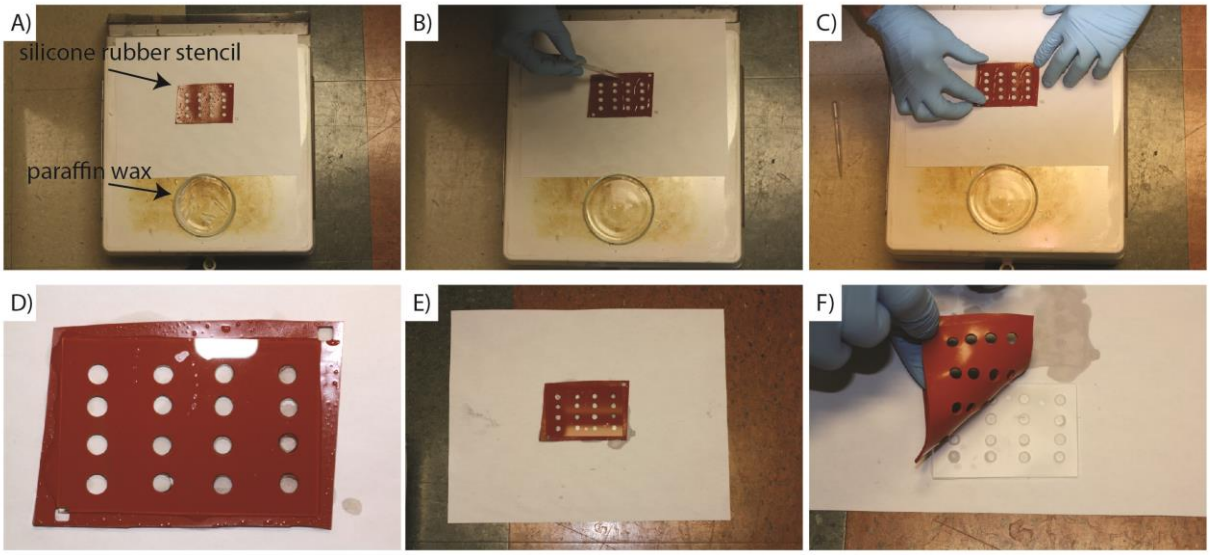

Fig. D.2 The method for making the SLIDE disposables. (a) paraffin wax is melted on a hot plate. (b) Paraffin wax is pipetted onto the silicone stencil. (c) A glass slide is placed onto the silicone stencil. (d) A close-up showing the melted wax spreading to coat the glass surface where the stencil contacts the glass. (e) The stencil and glass are removed from the hot plate and allowed to cool at room temperature. (f) The stencil is peeled from the glass disposable, showing the patterned paraffin on the disposable glass part.

D.3 Viscosity Results

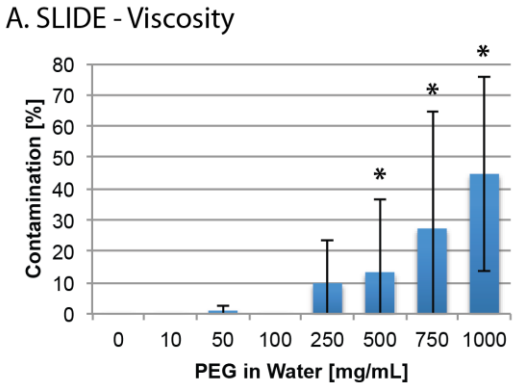

Fig. D.3 Impacts of viscosity on carryover. The amount of carryover from various viscosity fluids was evaluated in the SLIDE. * bars represent failure of the PMPs to be removed from the liquid, as the fluid acts as a ferrofluid.

Appendix E Automated Exclusion-based Sample Preparation Platform for Rare Cell Isolation [18]

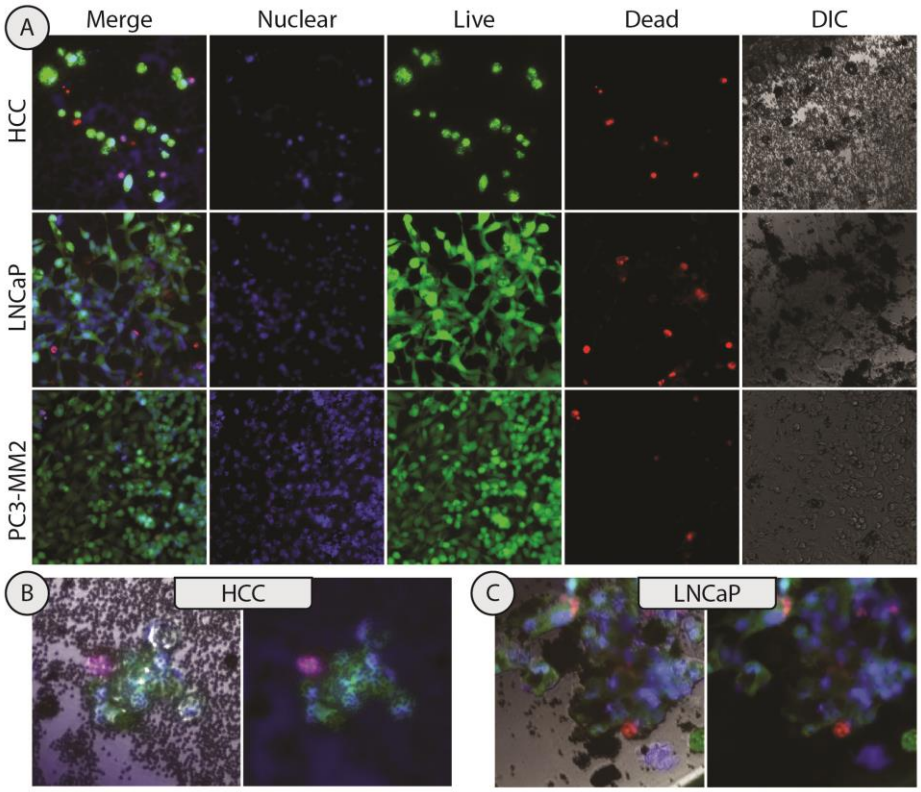

Fig. E.1 Culture of bead-captured cells. Live/dead assay of cells cultured with beads, for 10 days (or to confluency), following isolation from a contrived sample. (a) Combined brightfield and fluorescent images of the cells being cultured despite the presence of anti-EpCAM M270 PMPs. (b) Image of HCC cells cultured with beads. (c) Image of LNCaPs cultured with beads.

18 This appendix has been adapted from the supplemental materials from the following manuscript in preparation: "Automated Exclusion-based Sample Preparation Platform for Rare Cell Isolation" Hannah M. Pezzi*, David J. Guckenberger*, Jennifer Scherer, Scott M. Berry, Jacob Rothbauer, Sacha Horn, Jamie Sperger, Josh Lang, and David J. Beebe

* Authors contributed equally

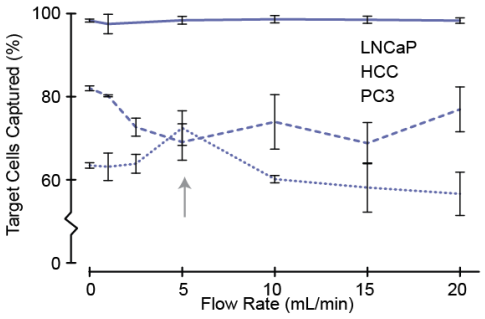

Fig. E.2 Impact of mixing flow rates on cell capture. A mixing rate of 5 mL/minute was chosen to minimize captured contaminant cells while maximize target cell capture.

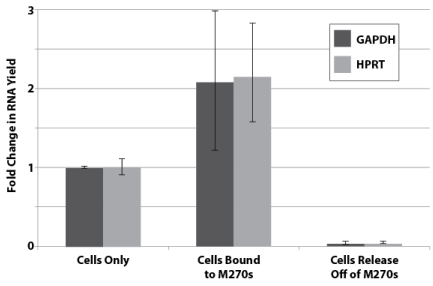

Fig. E.3 Impact of M270s on RNA extraction. M270s appear to improve RNA yields slightly when included in with the RNA extraction PMPs. GAPDH is the target gen and HPRT is a housekeeping gene. M270s might bind RNA which helps yield – cells, cells+M270+RNA bead, cell-M270 then RNA bead.

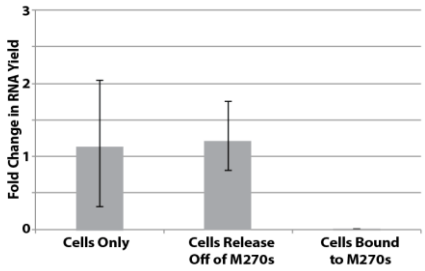

Fig. E.4 Impact of M270s on DNA extraction. If left in the sample for the DNA isolation protocol developed, DNA extraction is severely impaired. If a pre-lyse step is first performed, the M270 PMPs removed, and DNA lysis buffer and PMPs added, DNA yields are consistent with the DNA yields of cells alone.

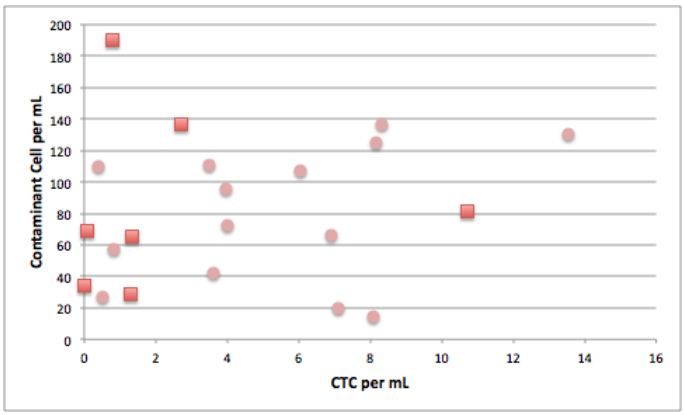

Fig. E.5 Comparison between contaminant and number of CTCs. No correlation observed between CTC population and contaminant cell population

Appendix F In vivo breast tumor sampling via a needle-implantable microdevice [19]

F.1 Materials and Methods (cont'd)

F.1.1 Design and Fabrication of the Implantation Device (cont'd)

The implantation device is comprised of an 18 gauge blunt end needle acting as a push-rod, and a 16 gage hypodermic needle acting as an implantation needle **(Fig. F**.1**)**. A hole is drilled into the front of the syringe to allow air to escape. The capsule is urged from the implantation needle by pressing on the plunger of the syringe.

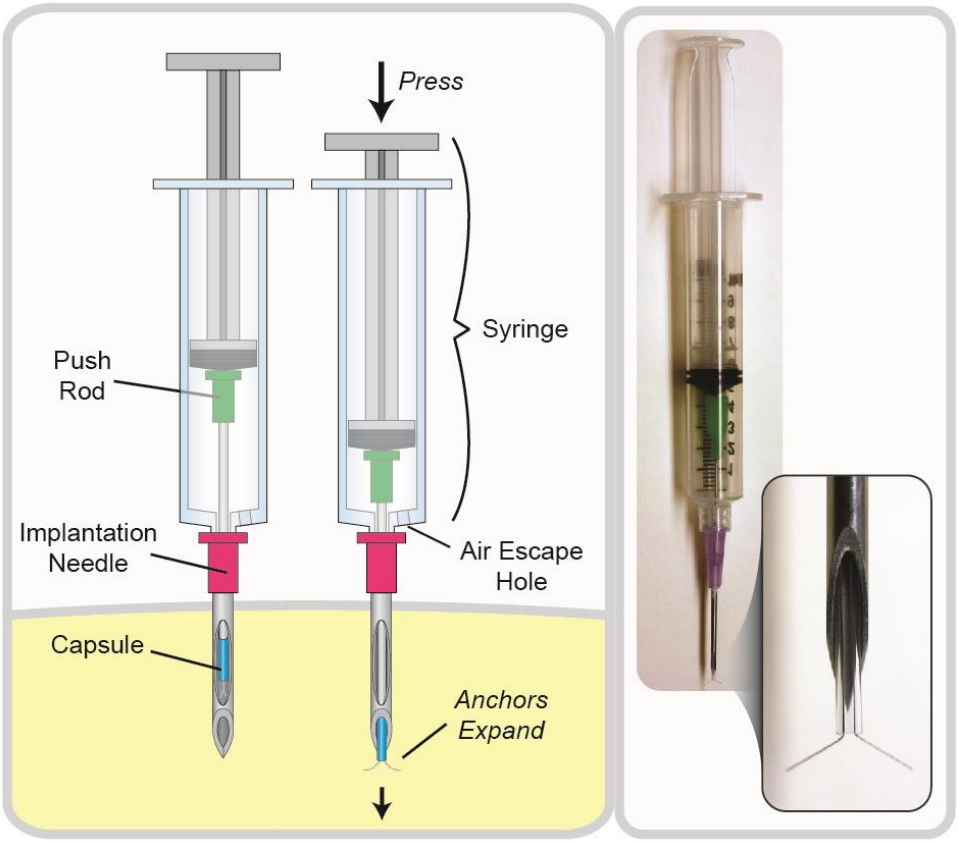

Fig. F.1 Design of the implantation device

19 This chapter has been adapted from supplemental materials intended for a manuscript in preparation for publication: "In vivo breast tumor sampling via a needle-implantable microdevice" David J. Guckenberger, Jay W. Warrick, Alka Choudhary, Amanda Schulman, Jennifer Mirrielees, Lee Wilke, Mark E. Burkard, and David J. Beebe.

F.1.2 Computational Modeling:

COMSOL modeling is used to estimate the boundaries of device behavior and the influence of various system parameters such as device geometry. The first use is to sample concentrations of analytes in the tumor microenvironment (TME). We focus only on modeling the protein lactase dehydrogenase (LDH). LDH is released upon cell death and is used in clinical and research settings to detect efficacy of cytotoxic chemotherapeutic agents such as Dox.[332]

F.1.3 Parameters, Constants, and Equations

Table F.1 Common parameters used to model Dox delivery and sampling of LDH in the tumor microenvironment

Variable Name	Value	Units	Description	Notes
Rad_{cell}	7.6 e^{-6}	m	Radius of the cell	-
Rad_{tumor}	7.5 e^{-3}	m	Radius of the model tumor	-
A_{cell}	4 π Rad_{cell}^2	m^2	Surface Area of each cell	-
Vol_{cell}	4/3 π Rad_{cell}^3	m^3	Volume of each cell	-
$D_{LDH,Water}$	5 e^{-11}	$m^2\ s^{-1}$	Diffusion rate of the LDH in water	Based on MW
$D_{LDH,tissue}$	DiffRatio * $D_{LDH,Water}$	$m^2\ s^{-1}$	Diffusion rate of the LDH in tissue. Roughly 10x slower than water.	333
$k_{LDH,production}$	1	s^{-1}	Nominal baseline production rate constant of LDH	-
$k_{LDH,clearance}$	$C_{LDH,out}$/ Vol_{cell}	s^{-1}	Calculated rate of clearance of LDH to produce steady state baseline concentration of 1	-
$C_{LDH,in}$	0	mol m^{-3}	Initial LDH concentration in the device	-
$C_{LDH,out}$	1	mol m^{-3}	Steady-state concentration of LDH in the tumor outside the device	-
$C_{cell,max}$	1/ Vol_{cell}	mol m^{-3}	Concentration of cells in the tumor	-

Table F.2 Constitutive Equations used to model the sampling.

$$\frac{dC_{LDH}}{dt} = -k_{clearance,LDH} * C_{LDH} + K_{baseline,LDH} * C_{cell} \quad (1)$$

F.1.4 Model Overview

The general process being modeled is diffusion of LDH into the capsule as a result of constitutive or baseline release rate of LDH. The geometrical parameters of the model are as follows **(Fig. F.2)**. The reservoir has a length, $L_{reservoir}$, and diameter, $Ø_{reservoir}$. The orifice of the device is placed in the center of the spherical 'tumor', which has a diameter, $Ø_{tumor}$, and a volumetric cell density of $C_{cell,max}$ where the volume of a cell is based upon a cell radius of Rad_{cell} = 7.5e-6 [m]. Multiple assumptions are made to simplify the model. Cells are modeled as a continuous entity as a concentration variable instead of discretely. Proliferation and associated tumor volume changes are ignored. The tumor is considered homogeneous in terms of cell density and diffusion coefficients yet, in reality, diffusivity of an analyte could potentially depend upon the concentration of live cells and dead tissue, which has been seen to alter blood perfusion and tissue permeability. The diffusion coefficients of cells is considered to be negligible, while the diffusion coefficient of LDH in tissue is considered to be 10% of that observed in water based on observations of other molecules in tissue.[334] The production rate of LDH in live cells is chosen to be a nominal value of 1 [1/s] which represents a scenario where the flux of LDH into the device can be easily supplied by adjacent cells without locally depleting the tissue. The clearance of LDH (e.g., via the blood stream) is modeled continuously and is calculated relative to the production rate to achieve a nominal baseline concentration of 1 mol/m^3. Although this concentration is not physiologically relevant, it simplifies interpretation of modeling results. Thus, concentrations of LDH are normalized by the baseline concentration and expressed as a percentage. Analyte concentration in the tumor is initially at 100% and diffuses into the reservoir, which is initially at 0%, with a rate based on the diffusion coefficient, D_{LDH}.

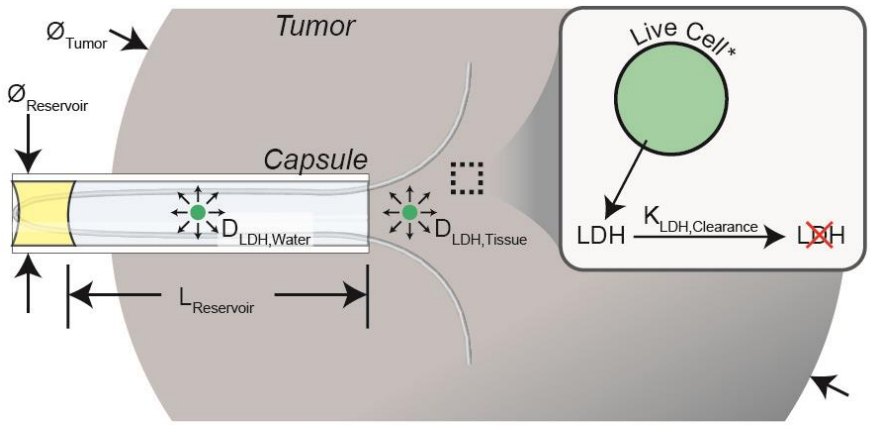

Fig. F.2 Setup of the computational models. Production, degradation, and diffusion of LDH from cells.

F.1.5 Model Setup

A highly idealized tumor is used to first estimate the timescale of diffusion of analyte (LDH) into the device from the surrounding tissue as a function of device geometry. In this model, the open end of the capsule is positioned in the tumor to allow diffusion into the capsule **(Fig. F**.1**)**. Live cells constitutively produce LDH and LDH is cleared from the tumor at rates provided in the literature, $k_{LDH,clearance}$ **(term 1 of Eq 2)).** The ambient cells maintain a constant basal concentration of LDH, which is modeled by balancing the parameters for $k_{LDH,production}$ and $k_{LDH,clearance}$. The ratio of $k_{LDH,production}$ and $k_{LDH,clearance}$ dictates the steady-state baseline concentration of LDH in the tissue, $C_{baseline,LDH}$. Further, the magnitude of $k_{LDH,production}$, or equivalently $k_{LDH,clearance}$ dictates whether diffusion of the analyte into the device will be cell production limited or, in the opposite case, diffusion limited (i.e., local concentrations of analyte are not significantly depleted by the device as analyte diffuses into the capsule). Which scenario is appropriate for a given analyte can be estimated by comparing the characteristic diffusion time of the device as the characteristic clearance time of the analyte in tissue. In the case of LDH, tissue clearance time is ~30-60 minutes [3] compared to the characteristic diffusion time of the device which is geometry dependent, but generally >7 days ($\tau = L_{Reservoir}^2/(2*D_{LDH,Water})$). Thus, all simulations were performed under the assumption that LDH sampling is diffusion limited instead of cell-production limited. This assumption raised the concentration of sampled LDH in this first set of simulations from ~83% to 90% at 14 days (i.e., ~7% at any given timepoint). Thus, the effect of the assumption was rather

minimal. An additional benefit of this assumption is that the simulations provide a bounding case for extrapolating results to other scenarios instead of being specific to the baseline production rate of LDH. The average concentration of analyte in the capsule is calculated and graphed, where 100% would indicate complete equilibrium between the reservoir and the TME.

F.2 Supplementary Results

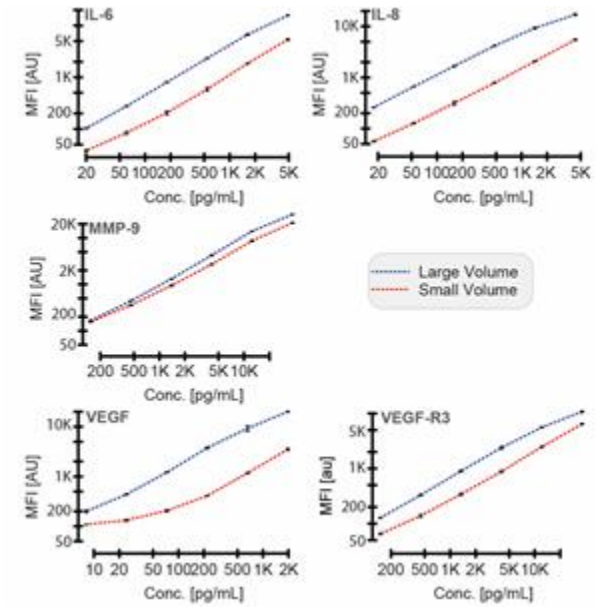

Fig. F.3 Magpix assay validation. The Magpix assay was validated by comparing the traditional (50 µL) assay volume to an assay performed using the ~3 µL sample volume obtained via the capsule.

Appendix G Integrated drug delivery and tumor sampling via a needle-implantable microdevice [20]

G.1 Materials and Methods

G.1.1 Design and Fabrication of the Implantation Device (cont'd)

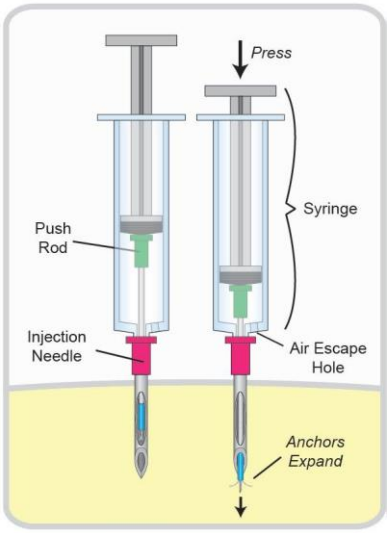

Fig. G.1 Schematic of the implantation device. (Left panel) The implantation device is comprised of a syringe, an 18 gauge blunt end needle acting as a push-rod, and a 16 gauge hypodermic needle acting as an implantation needle. The capsule is loaded into the implantation needle with the anchors completely contained. The capsule is urged from the implantation needle by pressing on the plunger of the syringe, during which the anchors automatically expand. A hole drilled into the front of the syringe allows air to escape, preventing air from being injected or expelling the capsule.

G.1.2 Computational Modeling

COMSOL modeling is used to estimate the boundaries of device behavior and the influence of various system parameters such as device geometry. Three different uses of the device are modeled. The first use is to sample concentrations of analytes in the tumor microenvironment (TME). The second is to deliver local concentrations of drug within a tumor. The third is to simultaneously deliver drug and sample soluble factor concentrations in the TME. The models increase in complexity, allowing us to address and discuss added complexity as it arises. We focus only on modeling the drug doxorubicin (Dox)

20 This chapter has been adapted from a manuscript in preparation for publication: "Integrated drug delivery and tumor sampling via a needle-implantable microdevice" David J. Guckenberger, Jay W. Warrick, Alka Choudhary, Amanda Schulman, Jennifer Mirrielees, Ross Vitek, Brian Johnson, Lee Wilke, Mark E. Burkard, and David J. Beebe

and the protein lactase dehydrogenase (LDH). LDH is released upon cell death and is used in clinical and research settings to detect efficacy of cytotoxic chemotherapeutic agents such as Dox.

G.1.3 Parameters, Constants, and Equations

Table G.1 Common parameters used to model Dox delivery and sampling of LDH in the tumor microenvironment

Variable Name	Value	Units	Description	Citations
Rad_{cell}	$7.6\ e^{-6}$	m	Radius of the cell	[cite]
Rad_{tumor}	$7.5\ e^{-3}$	m	Radius of the model tumor	-
A_{cell}	$4\ \pi\ Rad_{cell}^2$	m^2	Surface Area of each cell	-
Vol_{cell}	$4/3\ \pi\ Rad_{cell}^3$	m^3	Volume of each cell	-
$D_{negligible}$	$1\ e^{-30}$	$m^2 s^{-1}$	A nominal negligible diffusion coefficient used to model dox trapped within cells and cells within the tumor	-
DiffRatio	0.1	-	Approximate raio of diffusion trhough tissue vs water (based upon literature value for ($D_{Dox,tissue,out}/D_{Dox,Water}$)	[Cite]
$D_{Dox,Water}$	$5\ e^{-9}$	$m^2 s^{-1}$	Diffusion coef. of dox in tissue	-
$D_{Dox,tissue,out}$	DiffRatio * $D_{Dox,Water}$	$m^2 s^{-1}$	Diffusion coef. of Dox in tissue outside of cell	-
$D_{Dox,tissue,in}$	$D_{negligible}$	$m^2 s^{-1}$	Diffusion coef. of Dox inside of cell (i.e., negligible due to con- finement within the cell)	-
$D_{LDH,Water}$	CHECK ME	$m^2 s^{-1}$	Diffusion rate of the LDH	[Cite]
$D_{LDH,tissue}$	DiffRatio * $D_{LDH,Water}$	$m^2 s^{-1}$	Diffusion rate of the LDH	[Cite]
P	$7.4\ e^{-7}$	$m\ s^{-1}$	Permeability coefficient of Dox through cell membranes	[Cite]
$K_{Dox,clearance}$	$0.58\ e^{-4}$	s^{-1}	Clearance rate of dox	-
K_{factor}	$1\ e^{-3}$	$m^3\ s^{-1}\ mol^{-1}$	Factor (LDH) production rate	-
$K_{proliferation}$	$6.63\ e^{-6}$	s^{-1}	Rate of proliferation ((dN/N)/dt). Calculated based upon a 41 hr doubling time.	-
K_{ratio}	0.1	-	Ratio phys. relevant concentration and the reservoir concentration of drug	-
$K_{LDH,production}$	1	s^{-1}	Nominal baseline production rate constant of LDH	-
$K_{LDH,clearance}$	$LDH_{baseline}$ / Vol_{cell}	s^{-1}	Calculated rate of clearance of LDH to produce steady state baseline concentration of 1	-
K_{death}	$1.73\ e^{11}$ * Vol_{cell}	$m^3\ s^{-1}\ mol^{-1}$	Rate of death per cell	[Cite]
$IC50_{Dox}$	0.005	$mol\ m^{-3}$	IC50 of dox	-
$LDH_{perDeath}$	$1\ e^{6}$	-	Tuned parameter representing the number of molecules of LDH released per cell death. Tuned to achieve maximum of ~6 fold increase in LDH concentration of LDH release over the nominal baseline concentration of 1	-

$C_{LDH,in}$	0	mol m^{-3}	Initial Value for LDH concentration in the device	-
$C_{cell,max}$	1/ Vol_{cell}	mol m^{-3}	Volume of each cell	-
$C_{Dox,in}$	0	mol m^{-3}	Initial Concentration of Dox in the capsule	-
$C_{Dox,out}$	1000* $IC50_{Dox}$	mol m^{-3}	Initial Concentration of Dox outside of the capsule	-

Table G.2 Constitutive Equations used to model the sampling and delivery.

Eq. G.1 $$\frac{dC_{cell}}{dt} = k_{proliferation}(C_{cell,max} - C_{cell}) - k_{death} * C_{dox,in} * C_{cell}$$

Eq. G.2 $$\frac{dC_{LDH}}{dt} = -k_{clearance,LDH} * C_{LDH} + K_{baseline,LDH} * C_{cell} - k_{death} * C_{drug,in} * C_{cell} * LDH_{perDeath}$$

Eq. G.3 $$\frac{dC_{drug,out}}{dt} = -k_{clearance,drug} * C_{drug,out} - P * (C_{drug,out} - C_{drug,in}) * A_{cell} * C_{cell}$$

Eq. G.4 $$\frac{dC_{drug,in}}{dt} = P * (C_{drug,out} - C_{drug,in}) * A_{cell} * C_{cell}$$

G.1.4 Model Overview

The general process being modeled is the diffusion of drug (Dox) out of the capsule and into the tumor tissue, entrance of drug into cells, cell death due to intracellular dox, and subsequent release of lactase dehydrogenase (LDH) due to cell death, and diffusion of LDH into the device capsule. As part of this model we also include cell proliferation given the system is modeled for 2 weeks. There is also a constitutive or baseline release rate of LDH in the absence of drug.

The geometrical parameters of the model are as follows. The reservoir has a length, $L_{reservoir}$, and diameter, $Ø_{reservoir}$. The orifice of the device is placed in the center of the spherical `tumor', which has a diameter, $Ø_{tumor}$, and a volumetric cell density of $C_{cell,max}$ where the volume of a cell is based upon a cell radius of Rad_{cell} = 7.5e-6 [m].

Multiple assumptions are made to simplify modeling. Cell concentration is modeled as a continuous variable instead of discretely. Likewise, clearance of drug and excess LDH via the vasculature and degradation processes are modeled continuously and using a single lumped parameter for each of the analytes based upon the literature, $k_{LDH,clearance}$ and $k_{Dox,clearance}$. Intracellular drug is given a negligible diffusion

coefficient ($D_{Dox,in} = D_{negligible}$) to model the limited mobility within the tumor while inside the cell. Although tumor volume would be expected to increase over 2 weeks, the tumor is modeled with a fixed diameter to simplify the model. Accordingly, proliferation is limited by cell density to avoid unrealistic cell densities. Diffusivity of drug could also potentially depend upon the concentration of live cells as dead tissue has been seen to alter blood perfusion and tissue permeability. However, diffusivity of tissue was modeled as a constant based upon literature values for doxorubicin.

Regarding presentation of results, concentrations of LDH are normalized by the basal concentration and expressed as a percentage. Thus, analyte concentration in the tumor is initially at 100% and diffuses into the reservoir, which is initially at 0%, with a rate based on the diffusion coefficient, D_{LDH}. Similarly, drug concentrations are normalized by tissue IC50 value. Thus, values of 2 and 0.25 represent 2 times and 0.25 times the IC50 value for dox in tissue.

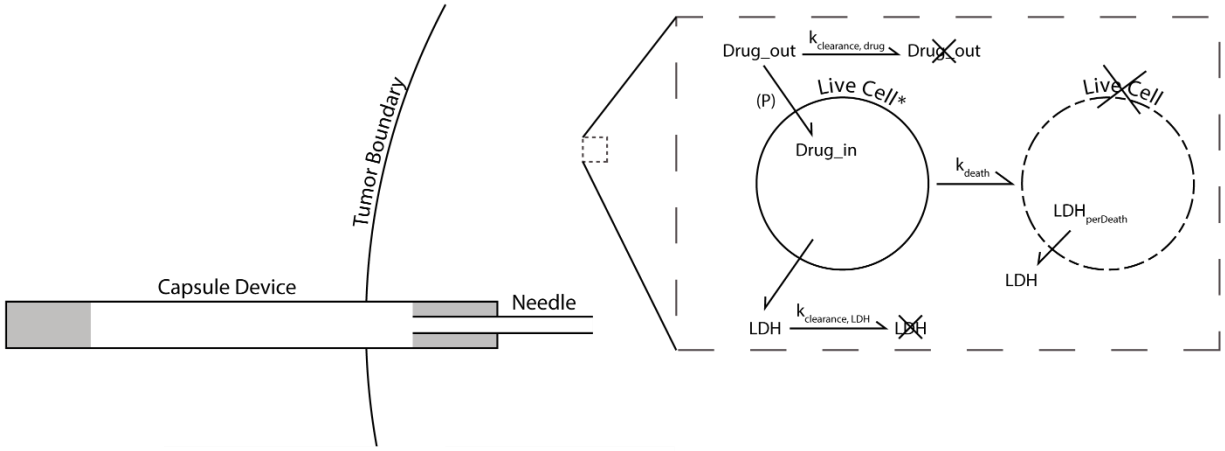

Fig. G.2 Setup of the computational models. The transport of drug from outside to inside of the cell is modeled using two species of drug, intracellular and extracellular. The process is modeled using a literature value of cell membrane permeability, P, for Dox (term 2 of Eq. G.3 and Eq. G.4). Drug and LDH are cleared from the tumor at rates provided in the literature, kDox,clearance and kLDH,clearance (term 1 of Eq. G.2 and Eq. G.3)). Live cells constitutively produce LDH (term 2 of Eq. G.2). Cells die at a rate dependent upon the intracellular concentration of drug (term 2 of Eq. G.1). Additional release of LDH results from cell death/lysis and, thus, is proportional to the rate of cell death (term 3 of Eq. G.2). (*) Cell proliferation is not depicted here; however it is included in the model via term 1 of Eq. G.1 to allow more cells to repopulation regions where cell death has occurred and is considered a cell density dependent process to avoid overcrowding of the tissue.

G.1.5 Case 1: Sampling soluble factor concentrations in the TME

A highly idealized tumor is used to first estimate the timescale of diffusion of analyte (LDH) into the device from the surrounding tissue as a function of device geometry in the absence of any drug effects. In this model, an open orifice capsule (i.e., just the reservoir component with one closed end, one open end, and no regulation needle) is placed into a tumor, where analyte is allowed to diffuse into the capsule. The ambient cells maintain a constant basal concentration of LDH. This is modeled by balancing the parameters for $k_{baseline}$ and $k_{LDH,clearance}$. The ratio of $k_{baseline}$ and $k_{LDH,clearance,LDH}$ dictates the steady-state baseline concentration of LDH in the tissue, $C_{baseline,LDH}$. Further, the magnitude of $k_{baseline}$, or equivalently $k_{LDH,clearance,LDH}$ dictates whether diffusion of the analyte into the device will be cell production limited or, in the opposite case, diffusion limited (i.e., local concentrations of analyte are not significantly depleted by the device as analyte diffuses into the capsule). Which scenario is appropriate for a given analyte can be estimated by comparing the characteristic diffusion time of the device as the characteristic clearance time of the analyte in tissue. In the case of LDH, tissue clearance time is ~30-60 minutes compared to the characteristic diffusion time of the device which is geometry dependent, but generally >7 days ($\tau = L_{Reservoir}^2/(2*D)$). A realistic clearance rate could be used but causes modeling instability due to effects of cell death from drug in subsequent simulations. The instability could be eliminated in subsequent simulations by assuming LDH sampling to be diffusion limited instead of cell-production limited. Thus, all simulations were performed using this assumption, including this first set. This assumption raised the concentration of sampled LDH in this first set of simulations from ~83% to 90% at 14 days (i.e., ~7% at any given timepoint). Thus, the effect of the assumption was rather minimal. An additional benefit of this assumption is that the simulations provide a bounding case for extrapolating results to other scenarios instead of being specific to the baseline production rate of LDH. The average concentration of analyte in the capsule is calculated and graphed, where 100% would indicate complete equilibrium between the reservoir and the TM.

G.1.6 Case 2: Localized delivery of Doxorubicin within a tumor

To model delivery, the device consisted of a reservoir with defined length, $L_{reservoir}$, and diameter, $Ø_{reservoir}$, and a regulation needle with a defined length, L_{needle}, and diameter, $Ø_{needle}$. The orifice of the device is placed in the center of the spherical 'tumor', which has a diameter, $Ø_{tumor}$, and a cell density of $C_{cell,max}$. In this model, the reservoir is filled with an initial concentratoin of drug which is 1000 fold higher than the IC50 of the drug, k_{ratio}. The drug is allowed to diffuse (at a rate of $D_{dox,\ water}$ from the reservoir, through the regulation needle, and into the surrounding tissue. Cellular uptake of the drug was regulated by the cellular permeability, P, and the drug was expelled by the cells at rate of $k_{clearance,drug}$. Cell death occurred when the local drug concentration exceeded the IC50 value. As the reservoir depleted and the localized drug diffused into the surrounding tissue, the cells proliferated, $k_{proliferation}$, back into the dead region. Cells were modelled as molecules (hence the use of moles as units) with a low diffusion rate, D_{cell}, that corresponds to a low cellular motility. The diffusion characteristics and impacts of dimensional change are detailed in the following subsections.

Reservoir Depletion and Drug Delivery

In this study, dimensions of the regulation needle were altered to assess the temporal impacts on reservoir depletion. In addition, either solely the reservoir length or both reservoir and needle length were changed to maintain either constant volume or constant resistance, respectively. We investigate needle sizes of 20, 22, 24, 26, 28, 30, 32, and 34 gauge, which correspond to diameters of 0.60, 0.41, 0.31, 0.26, 0.18, 0.16, 0.11, and 0.08 mm, respectively. This range was selected because a device made with a 20 g needle would require an implantation needle larger than 16 g, and a 34 gauge is near the lower limit of commercially available hypodermic needles. Needle lengths had nominal sizes of 2, 3, 4, and 6.5 mm, however the modeled length was reduced by ~0.73 mm to account the distance between the orifice and the tip of the bevel. Reservoir length ranged from 3.50 to 6.14 mm, which roughly corresponds to a tube length of 10 mm with two glue plug of 2 mm each.

IC50 radius calculation

In this study, we use the identical capsule parameters to model 1.2.2b to model the temporal effects on the radius between the needle orifice and the location at which the drug concentration is equivalent to the IC50 value. These values are plotted with respect to time. For comparison, we plot the region where the concentration is 2 times the IC50 value and half the IC50 value.

G.1.7 Case 3: Simultaneous delivery and detection

In this study, we investigate captured analyte in response to delivered drug. All of the dimensional an initial concentration values are recycled for this study. Here, as drug diffuses from the capsule, it is collected by the cells. Once cells reach a specific concentration, K_{death}, they die and release a set amount of LDH, $LDH_{perDeath}$. The LDH is free to diffuse throughout the tissue, some of which will diffuse into the capsule. As cell death subsides, the cells begin to proliferate back into the dead region. As this occurs, the LDH levels return to the baseline production. In each of the models, we calculate the average concentration of analyte in the capsule for each time point.

G.2 Supplementary Results

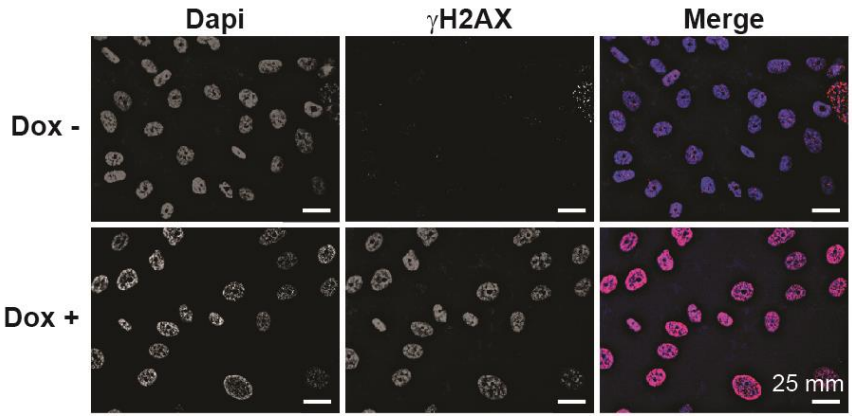

Fig. G.3 Efficacy of $\boldsymbol{\gamma}$H2AX staining in vitro. $\boldsymbol{\gamma}$H2AX was used to assess DNA damage in MDA-MB-231 cells after 50 nM Dox treatment for 48 hrs. Equal number of cells were grown on glass coverslips. When 60-70% confluent, cover slips were treated with 50 nM Dox for 48 hrs. Cover slips were fixed with 4% PFA, then stained for $\boldsymbol{\gamma}$H2AX and DAPI. Coverslips were imaged on a microscope at 40X magnification and identical exposure.

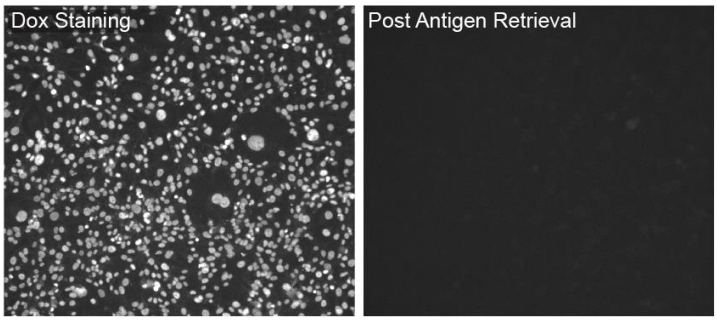

Fig. G.4 Impacts of histological processes on treatment validation. Our MDA-MD-231 cells cultured on a glass slide, treated with Dox, fixed with formalin (same as histology), sent to Tripp lab for staining (mock staining protocol). One slide went through antigen retrieval and the other didn't. The bright image didn't. Images are identically treated.

Appendix H Introduction[21]

H.1 Mechanical Validation:

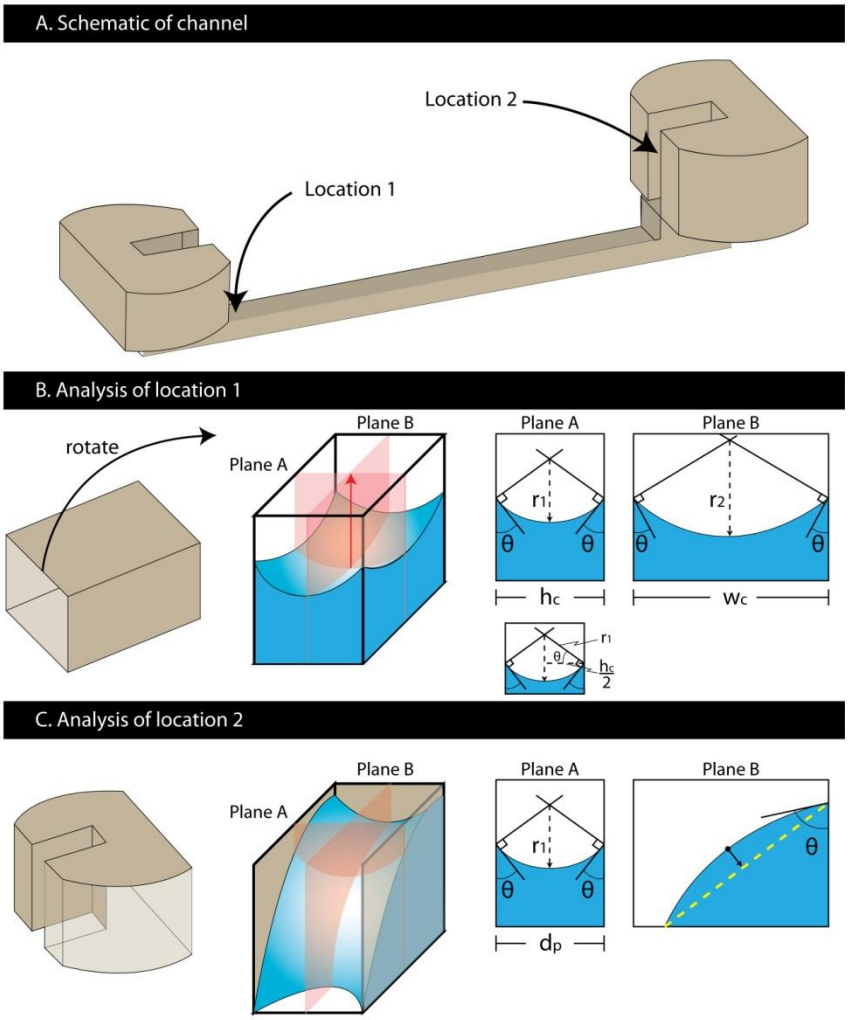

Fig. H.1 Key design features for proper function. (a) Schematic view of the microchannel and posts, identifying key locations of analysis. (b and c) Detailed cross-sections of location 1 and 2, demonstrating general fluidic shape and pertinent angles.

The design and dimensions of the microchannel and posts are key components to ensuring that the fluid remains in the channel and does not wick out **(Fig. H.1a).** As indicated in the figure, there are 2 locations that govern the proper function of the channel. The first location, location 1, is of smaller

21 This chapter has been adapted from the supplemental materials from the following publication: "Kit-On-A-Lid-Assays for accessible self-contained cell assays." Erwin Berthier*, David J. Guckenberger*, Peter Cavnar, Anna Huttenlocher, Nancy P. Keller, and David J. Beebe. Lab on a Chip, 2012.

* Authors contributed equally

dimensions then the second location, location 2, such that the differential pressure of the channel dominates the differential pressure of the post. The differential pressure, P, is characterized by the surface tension of the liquid, γ, and the two radii of curvature, r_1 and r_2.

Eq. H.1 $$\Delta P = \gamma \left(\frac{1}{r_1} + \frac{1}{r_2}\right)$$

In a rectangular channel with four sides, the radii of curvature are calculated for two perpendicular planes, which intersect the lowest portion of the meniscus. **(Fig. H.1b)** By simple trigonometry, the contact angle of the liquid, θ, and the width of the cross section, h_c and w_c, can be used to calculate the radius of curvature:

Eq. H.2 $$\cos\theta = \frac{\frac{h_c}{2}}{r_1}$$

Eq. H.3 $$\cos\theta = \frac{\frac{w_c}{2}}{r_2}$$

Reorganizing **Eq. H.2** and **Eq. H.3** provides:

Eq. H.4 $$r_1 = \frac{h_c}{2\cos\theta}$$

Eq. H.5 $$r_2 = \frac{w_c}{2\cos\theta}$$

The equation for the differential pressure is then achieved by substituting **Eq. H.4** and **Eq. H.5** into **Eq. H.1**:

Eq. H.6 $$\Delta P_{channel} = 2\,\gamma\, cos\theta \left(\frac{1}{h_c} + \frac{1}{w_c}\right)$$

The pressure differential of the post is calculated in a similar fashion, but differs since only three walls are present in the channel. **(Fig. H.1c)** Like the channel, two cross sectional planes are created. The radius of curvature, r_1, of the first plane, plane A, is calculated with the contact angle, θ, and the width of the channel, d_p:

Eq. H.7 $$r_1 = \frac{d_p}{2\cos\theta}$$

However, because there is only one wall present in plane B, the liquid will obtain a negative radius of curvature.

Eq. H.8 $r_2 < 0$

This negative radius of curvature will assist in keeping liquid in the channel, and can be removed from the pressure analysis. By removing **Eq. H.7** from the pressure analysis, and substituting **Eq. H.6** into **Eq. H.1** the equation for the differential pressure of the post becomes:

Eq. H.9 $\Delta P_{post} = \frac{2\,\gamma \cos\theta}{d_p}$

H.2 Alternative KOALA bases and lids:

To expand the KOALA platform as well as enable and accelerate alternative assays we have developed a variety of alternative lids and bases. The first base, as presented in the paper, is a comb type of channel that enables filling a variety of wells in one simple step **(Fig. H.2a)**. The base is formed in polystyrene and houses a variety of wells which are interconnected by a channel. When liquid is flowed into the channel, the liquid successively fills each of the wells. Once the liquid reaches a pad at the end of the channel, the pad wicks the excess fluid out of the channel, thereby disconnecting each of the wells from one another, and leaving a series of wells with a precise volume of liquid. This base is then used with a standard KOALA lid in the same, in the same fashion as described in the main article.

The second base is designed to enable a series of dilutions in two simple pipetting steps **(Fig. H.2b)**. The first channel functions in the same manner as the previously described, where the liquid goes in the channel, fills a series of wells, then is wicked into the pad. However, each well on the first side varies in size, to control to level of dilution. After the first well is filled, and the channel is empty, liquid is flowed into the second channel. As the fluid flows through the main channel, it fills each adjacent well, and pins at a constriction, adjacent to that of the first liquid. Next, fluid flows through a small channel, which fluidically connects the second liquid with the first liquid. As the fluid continues through the small channel, it creates a short between the fluid of the first well, and the floor of the larger circular well. This allows both liquid 1 and liquid 2 to flow into the larger well, and mix into solution. Ultimately, the

volume is controlled by the size of the larger well, and the levels of dilution are controlled by the size ratio of the smaller wells.

Finally, we developed a lid to perform neutrophil chemotaxis, to demonstrate the amenability of the KOALA platform to alternative channel designs and alternative assays **(Fig. H.2c)**. This lid uses the same channel and post format as the lid described in the main article. However, in this case, each device utilizes two inlet ports and one outlet port. The first step is to apply the lid to a base containing media in alternating wells. This will preload the channel with media, from one inlet port, to assure the entire channel is filled and no bubble are trapped in the migration channel. The second step is to apply the lid to a base containing a chemoattractant in alternate channels. In this case, the chemoattractant was mixed into a hydrogel to reduce convective mixing and unwanted flow. The third step is to apply the lid to a base containing neutrophils which are in alternating wells, opposite that of the chemoattractant. A gradient of chemoattractant then formed in the cross migration channel, and migration was observed over a 30 min time period. The KOALA platform enables simultaneous loading of the microchannels, which is beneficial to ensure that the gradient is consistent between each channel.

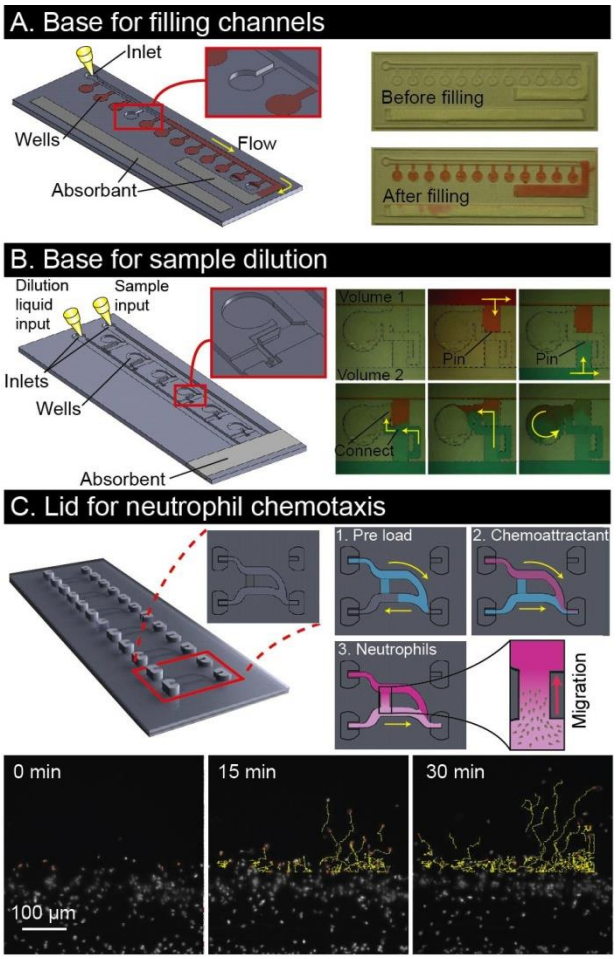

Fig. H.2 Alternative KOALA channel designs. (a) A KOALA base designed to automatically fill each well. (b) A KOALA base that automatically fills each well in specific serial dilutions. (c) A KOALA lid/channel designed for neutrophil migration assays.

Appendix I High-density self-contained microfluidic KOALA kits for use by everyone [22]

I.1 KOALA-HD Design and Dimensions:

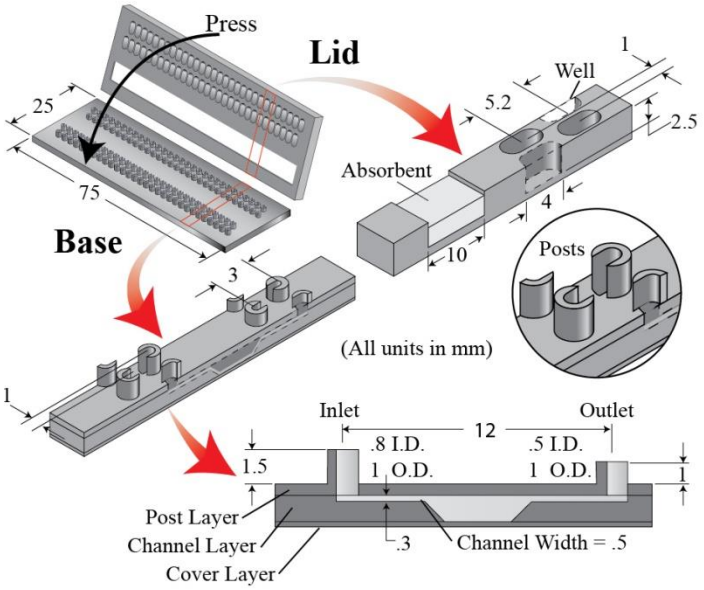

Fig. I.1 A dimensioned schematic of the KOALA-HD platform (all units in mm)

I.2 KOALA-HD Common Rail Designs:

Two common rail designs were tested. In the first design (Figure S2, top), common rail consists of several ports with fins on each side. When mated with a lid, the fins were designed to reach into the half eliptical wells to wick out the fluid. Two issues arose. First the fins were not large enough to collect all of the fluid, and second the the concus-finn filaments cause liquids to go into the regions between the fins ("A"). In attempt to mitigate this issues a second design was tested wherein the fins were (1) elevated from the surface to prevent contamination from concus-finn filaments ("B") and (2) enlarged to reach further into well ("C") and (Figure S2, bottom). However, this design still had several issues via displacement of fluid causing wells to spill into adjacent wells.

22 This appendix has been adapted from the supplemental materials from the following publication: "High-Density Self-Contained Microfluidic KOALA Kits for Use by Everyone" David J. Guckenberger, Erwin Berthier, and David J. Beebe. Journal of Laboratory Automation, 2014.

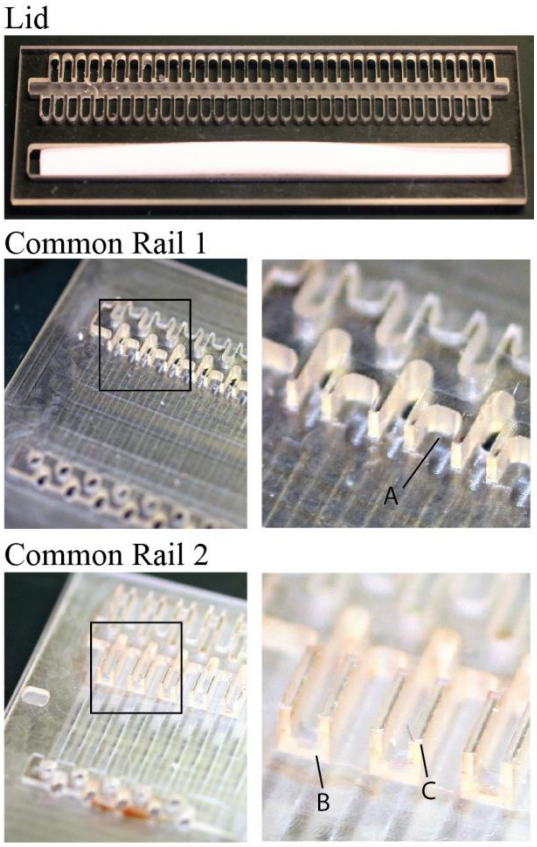

Fig. I.2 Alternative designs to the horseshoe posts.

I.3 Post Orientation Effects on Dead Volume:

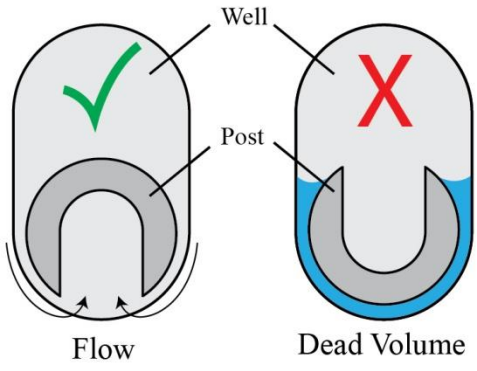

Fig. I.3 Impacts of post orientation. This schematic demonstrates the impacts of post orientation. Rotating the open side of the post enables capture of all of the fluid. If the post opens towards the center of the well, fluid gets trapped between the post and the wall.

Appendix J Supplemental Publications

J.1 Overview

This appendix includes a list of publications that used the technologies described in this dissertation.

J.2 New Technologies

J.2.1 Air Jump: a new ESP technology for sample preparation

"AirJump: Using Interfaces to Instantly Perform Simultaneous Extraction." Berry, S. M.; Pezzi, H. M.; LaVanway, A. J.; **Guckenberger, D. J.**; Anderson, M.; Beebe, D. J. *Applied Materials & Interfaces*, **2016.**

Air Jump is a new type of "exclusion-based" sample preparation technology that leverage phase interphases (in this case, air-liquid) to purify analytes. Much of the contaminant carryover stems from interactions with the sample vessel surface (e.g., pipetting residue, wetting). To eliminate this, AirJump isolates PMP-bound analyte by "jumping" analyte directly out of a free liquid/air interface. Further, AirJump has been validated for three important independent biological isolations, including: protein immunoprecipitation, viral RNA isolation, and cell culture gene expression analysis.

J.2.2 Magnetic technology to facilitate automation of ESP

"A magnetic system for automated manipulation of paramagnetic particles." Guckenberger DJ, Pezzi HM, Regier MC, Berry SM, Fawcett K, Barrett K, Beebe DJ. Analytical Chemistry. 2016

Here, we introduce a new, mechanically and operationally simplistic magnetic manipulation system for integration with the SLIDE technology to expand capabilities. This magnetic system is compatible with nearly any plate design, can be integrated into automated workflows, enables high-throughput formats, simplifies mechanical requirements, and is amenable to a range of analytes. Using this magnetic system, PMPs can be collected, released, and resuspended throughout multiple wells regardless of proximity. We demonstrate this system's capabilities to isolate whole cells, mRNA, and DNA, demonstrating up to a 28-fold improvement of purity via the multiwash protocols enabled by this magnetic technology.

J.3 Sieve Device for organoid staining

"High rates of chromosome missegregation suppress tumor progression without inhibiting tumor initiation." Zasadil, L. M.; Britigan, E. M. C.; Ryan, S. D.; Kaur, C.; Guckenberger, D. J.; Beebe, D. J.; Moser, A. R.; Weaver, B. A. Molecular Biology of the Cell. (Accepted, January 2015).

Organoids recapitulate multiple features of intact gut and can interrogated through immunostaining and fluorescent microscopy. The challenge with many staining protocols, such as staining the cells in a microtube, is the risk of losing (accidently aspiration, loss to tube wall) or overly agitating the organoid, which could be catastrophic to the outcome of the assay. Here, a sieve device (a modified version of the sieve well[76, 77]) was used to simplify staining protocol. The use of a membrane eliminated the need for centrifuagation and contained the organoid in a confined well to mitigate the potential loss of the organoid.

J.4 Implementing wax fabrication

"HIV Viral RNA Extraction in Wax Immiscible Filtration Assisted by Surface Tension (IFAST) Devices."Berry, S. M.; LaVanway, A. J.; Pezzi, H. M.; **Guckenberger, D. J.**; Anderson, M. A.; Loeb, J. M.; Beebe, D. J. *The Journal of Molecular Diagnostics*, **2014.**

The monitoring of viral load is critical for proper management of antiretroviral therapy for HIV-positive patients. Unfortunately, in the developing world, significant economic and geographical barriers exist, limiting access to this test. The complexity of current viral load assays makes them expensive and their access limited to advanced facilities. We attempted to address these limitations by replacing conventional RNA extraction, one of the essential processes in viral load quantitation, with a simplified technique known as immiscible filtration assisted by surface tension (IFAST). Furthermore, these devices were produced via the embossing of wax, enabling local populations to produce and dispose of their own devices with minimal training or infrastructure, potentially reducing the total assay cost. Using this technology, we have demonstrated accurate and repeatable measurements of viral load on samples with as low as 50 copies per milliliter of sample.

"Using Exclusion-based Sample Preparation (ESP) to Reduce Viral Load Assay Cost." Berry, S. M.; Pezzi, H. M,; Williams, E. D.; Kityo, C. M.; Mugyenyi, P. N.; Loeb, J. M.; **Guckenberger, D. J.**; Lavanway, A. J.; Puchalski, A. A.; Graziano, F. M.; Beebe, D. J. *PloS One*, **2015.**

Viral load (VL) measurements are critical to the proper management of HIV in developing countries. However, access to VL assays is limited by the high cost and complexity of existing assays. While there is a need for low cost VL assays, performance must not be compromised. Thus, new assays must be validated on metrics of limit of detection (LOD), accuracy, and dynamic range. Patient plasma samples from the Joint Clinical Research Centre in Uganda were de-identified and measured using both an existing VL assay (Abbott RealTime HIV-1) and our assay, which combines low cost reagents with a simplified method of RNA isolation termed Exclusion-Based Sample Preparation (ESP). 71 patient samples with VLs ranging from <40 to >3,000,000 copies/mL were used to compare the two methods. We demonstrated equivalent LOD (~50 copies/mL) and high accuracy (average difference between methods of 0.08 log, R^2= 0.97). Using expenditures from this trial, we estimate that the cost of the reagents and consumables for this assay to be approximately $5 USD. As cost is a significant barrier to implementation of VL testing, we anticipate that our assay will enhance access to this critical monitoring test in developing countries.

J.5 Neutrophil Extracellular Traps (NETs)

"Microfluidic Device for Simultanesou Analysis of Neutrophil Extracellular Traps and Production of Reactive Oxygen Species." Moussavi-Harami, S.F.; Mladinich, K. M.; Sackmann, E. K.; Shelef, M. A.; Starnes, T. W.; **Guckenberger, D. J.**; Huttenlocher, A.; Beebe, D. J. *Journal of Integrative Biology*, **2015.**

J.6 Circulating Tumor Cell (CTC) Isolation

"High Specificity in Circulating Tumor Cell Identification is Required for Accurate Evaluation of Programmed Death-Ligand 1." Schehr, J. L.; Schultz, Z.; Warrick, J. W.; **Guckenberger, D. J.**; Pezzi, H. M.; Sperger, J. M.; Heninger, E.; Saeed, A.; Leal, T.; Mattox, K.; Traynor, A.; Campbell, T.; Berry, S. M.; Beebe, D. J.; Lang, J. M. *PloS one,* **2016**.

The automated CTC platform was used to isolate circulating tumor cells, and facilitated this study.

"Integrated analysis of multiple biomarkers from circulating tumor cells enabled by exclusion-based analyte isolation." Sperger, J.; Strotman, L; Welsh, A.; Casavant, B. P.; Chalmers, Z.; Sacha, H.; Heninger, E.; Theide, S. M.; Tokar, J.; Gibbs, B. K.; **Guckenberger, D. J.**; Carmichael, L. L.; Stephens, P.; Berry, S. M.; Beebe, D. J.; Lang, J. M. *Clinical Cancer Research,* **2016.**

The automated CTC platform and VerIFAST were used to isolate circulating tumor cells, and facilitated this study.

References:

1. M. Friedman, H. Tanyeri, M. La Rosa, R. Landsberg, K. Vaidyanathan, S. Pieri and D. Caldarelli, *The Laryngoscope*, 1999, **109**, 1901-1907.
2. V. Majithia and S. A. Geraci, *The American Journal of Medicine*, 2007, **120**, 936-939.
3. E. R. Sutherland, W. W. Busse and N. Heart, *Journal of Allergy and Clinical Immunology*, 2014, **133**, 34-38. e31.
4. H.-L. Tan, L. Kheirandish-Gozal and D. Gozal, *Thorax*, 2014.
5. C. L. Marcus, L. J. Brooks, S. D. Ward, K. A. Draper, D. Gozal, A. C. Halbower, J. Jones, C. Lehmann, M. S. Schechter, S. Sheldon, R. N. Shiffman and K. Spruyt, *Pediatrics*, 2012, **130**, e714-e755.
6. H.-L. Tan, D. Gozal and L. Kheirandish-Gozal, *Nature and Science of Sleep*, 2013, **5**, 109-123.
7. D. C. Danila, M. Fleisher and H. I. Scher, *Clinical Cancer Research*, 2011, **17**, 3903-3912.
8. J. M. Lang, B. P. Casavant and D. J. Beebe, *Science translational medicine*, 2012, **4**, 141ps113-141ps113.
9. A. Sav, S. Adem, M. A. King, J. A. Whitty, K. Elizabeth, S. S. McMillan, K. Fiona, H. Beth and A. J. Wheeler, *Health Expect.*, 2013, **18**, 312-324.
10. E. K. Sackmann, A. L. Fulton and D. J. Beebe, *Nature*, 2014, **507**, 181-189.
11. E. M. Purcell, *Am. J. Phys*, 1977, **45**, 3-11.
12. D. J. Beebe, G. A. Mensing and G. M. Walker, *Annu Rev Biomed Eng*, 2002, **4**, 261-286.
13. T. M. Keenan and A. Folch, *Lab on a Chip*, 2008, **8**, 34-57.
14. G. M. Walker and D. J. Beebe, *Lab on a Chip*, 2002, **2**, 131-134.
15. P. C. Thomas, L. N. Strotman, A. B. Theberge, E. Berthier, R. O'Connell, J. M. Loeb, S. M. Berry and D. J. Beebe, *Anal Chem*, 2013, **85**, 8641-8646.
16. A. L. Paguirigan and D. J. Beebe, *BioEssays*, 2008, **30**, 811-821.
17. E. W. K. Young and D. J. Beebe, *Chemical Society Reviews*, 2010, **39**, 1036-1048.
18. M. Domenech, H. Yu, J. Warrick, N. M. Badders, I. Meyvantsson, C. M. Alexander and D. J. Beebe, *Integrative biology*, 2009, **1**, 267-274.
19. E. K. Sackmann, E. Berthier, E. W. Young, M. A. Shelef, S. A. Wernimont, A. Huttenlocher and D. J. Beebe, *Blood*, 2012, **120**, e45-53.
20. E. K.-H. Sackmann, E. Berthier, E. A. Schwantes, P. S. Fichtinger, M. D. Evans, L. L. Dziadzio, A. Huttenlocher, S. K. Mathur and D. J. Beebe, *Proceedings of the National Academy of Sciences*, 2014.
21. K. V. Christ, K. B. Williamson, K. S. Masters and K. T. Turner, *Biomedical Microdevices*, 2010, **12**, 443-455.
22. S. F. Moussavi-Harami, K. M. Mladinich, E. K. Sackmann, M. A. Shelef, T. W. Starnes, D. J. Guckenberger, A. Huttenlocher and D. J. Beebe, *Integrative Biology*, 2016, **8**, 243-252.
23. K. Domansky, W. Inman, J. Serdy, A. Dash, M. H. Lim and L. G. Griffith, *Lab on a chip*, 2010, **10**, 51-58.
24. K. E. Sung, N. Yang, C. Pehlke, P. J. Keely, K. W. Eliceiri, A. Friedl and D. J. Beebe, *Integrative Biology*, 2011, **3**, 439-450.
25. L. L. Bischel, E. W. K. Young, B. R. Mader and D. J. Beebe, *Biomaterials*, 2013, **34**, 1471-1477.
26. L. L. Bischel, K. E. Sung, J. A. Jiménez-Torres, B. Mader, P. J. Keely and D. J. Beebe, *The FASEB Journal*, 2014, **28**, 4583-4590.
27. J. A. Jiménez-Torres, S. L. Peery, K. E. Sung and D. J. Beebe, *Advanced healthcare materials*, 2016, **5**, 198-204.
28. D. Huh, B. D. Matthews, A. Mammoto, M. Montoya-Zavala, H. Y. Hsin and D. E. Ingber, *Science*, 2010, **328**, 1662-1668.
29. P. Yager, G. J. Domingo and J. Gerdes, *Annu. Rev. Biomed. Eng.*, 2008, **10**, 107-144.
30. C. D. Chin, V. Linder and S. K. Sia, *Lab on a Chip*, 2012, **12**, 2118-2134.
31. G. M. Whitesides, *Nature*, 2006, **442**, 368-373.
32. L. R. Volpatti and A. K. Yetisen, *Trends in biotechnology*, 2014, **32**, 347-350.
33. E. Berthier, E. W. Young and D. Beebe, *Lab Chip*, 2012, **12**, 1224-1237.
34. E. Verpoorte and N. De Rooij, *Proceedings of the IEEE*, 2003, **91**, 930-953.
35. Y. Xia and G. M. Whitesides, *Annual review of materials science*, 1998, **28**, 153-184.
36. G. M. Whitesides, E. Ostuni, S. Takayama, X. Jiang and D. E. Ingber, *Annual review of biomedical engineering*, 2001, **3**, 335-373.
37. D. J. Guckenberger, T. E. de Groot, A. M. D. Wan, D. J. Beebe and E. W. K. Young, *Lab on a Chip*, 2015.

38. E. W. K. Young, E. Berthier, D. J. Guckenberger, E. Sackmann, C. Lamers, I. Meyvantsson, A. Huttenlocher and D. J. Beebe, *Anal Chem*, 2011, **83**, 1408-1417.
39. M. Thalgott, B. Rack, T. Maurer, M. Souvatzoglou, M. Eiber, V. Kreß, M. M. Heck, U. Andergassen, R. Nawroth and J. E. Gschwend, *Journal of cancer research and clinical oncology*, 2013, **139**, 755-763.
40. V. Müller, S. Riethdorf, B. Rack, W. Janni, P. A. Fasching, E. Solomayer, B. Aktas, S. Kasimir-Bauer, K. Pantel and T. Fehm, *Breast Cancer Research*, 2012, **14**, 1.
41. E. Ozkumur, A. M. Shah, J. C. Ciciliano, B. L. Emmink, D. T. Miyamoto, E. Brachtel, M. Yu, P.-i. Chen, B. Morgan, J. Trautwein, A. Kimura, S. Sengupta, S. L. Stott, N. M. Karabacak, T. A. Barber, J. R. Walsh, K. Smith, P. S. Spuhler, J. P. Sullivan, R. J. Lee, D. T. Ting, X. Luo, A. T. Shaw, A. Bardia, L. V. Sequist, D. N. Louis, S. Maheswaran, R. Kapur, D. A. Haber and M. Toner, *Science Translational Medicine*, 2013, **5**, 179ra147.
42. S. L. Stott, C.-H. Hsu, D. I. Tsukrov, M. Yu, D. T. Miyamoto, B. A. Waltman, S. M. Rothenberg, A. M. Shah, M. E. Smas, G. K. Korir, F. P. Floyd, Jr., A. J. Gilman, J. B. Lord, D. Winokur, S. Springer, D. Irimia, S. Nagrath, L. V. Sequist, R. J. Lee, K. J. Isselbacher, S. Maheswaran, D. A. Haber and M. Toner, *Proc. Natl. Acad. Sci. U. S. A.*, 2010, **107**, 18392-18397.
43. W. Harb, A. Fan, T. Tran, D. C. Danila, D. Keys, M. Schwartz and C. Ionescu-Zanetti, *Translational oncology*, 2013, **6**, 528-IN521.
44. C. Schindlbeck, J. Stellwagen, U. Jeschke, U. Karsten, B. Rack, W. Janni, J. Jückstock, A. Tulusan, H. Sommer and K. Friese, *Clinical & experimental metastasis*, 2008, **25**, 233-240.
45. S. L. Werner, R. P. Graf, M. Landers, D. T. Valenta, M. Schroeder, S. B. Greene, N. Bales, R. Dittamore and D. Marrinucci, 2015.
46. C. Alix-Panabières and K. Pantel, *Nature Reviews Cancer*, 2014, **14**, 623-631.
47. O. Jonas, H. M. Landry, J. E. Fuller, J. T. Santini, J. Baselga, R. I. Tepper, M. J. Cima and R. Langer, *Science Translational Medicine*, 2015, **7**, 284ra257-284ra257.
48. R. A. Klinghoffer, S. B. Bahrami, B. A. Hatton, J. P. Frazier, A. Moreno-Gonzalez, A. D. Strand, W. S. Kerwin, J. R. Casalini, D. J. Thirstrup, S. You, S. M. Morris, K. L. Watts, M. Veiseh, M. O. Grenley, I. Tretyak, J. Dey, M. Carleton, E. Beirne, K. D. Pedro, S. H. Ditzler, E. J. Girard, T. L. Deckwerth, J. A. Bertout, K. A. Meleo, E. H. Filvaroff, R. Chopra, O. W. Press and J. M. Olson, *Science Translational Medicine*, 2015, **7**, 284ra258-284ra258.
49. L. M. Coussens and Z. Werb, *Nature*, 2002, **420**, 860-867.
50. P. Libby, P. M. Ridker and A. Maseri, *Circulation*, 2002, **105**, 1135-1143.
51. M. A. Shelef, J. Sokolove, L. J. Lahey, C. A. Wagner, E. K. Sackmann, T. F. Warner, Y. Wang, D. J. Beebe, W. H. Robinson and A. Huttenlocher, *Arthritis & Rheumatology*, 2014, **66**, 1482-1491.
52. *National Institutes of Health - National Heart, Lung, and Blood Institute*, 2014.
53. K. Malmstrom, G. Rodriguez-Gomez, J. Guerra, C. Villaran, A. Piñeiro, L. X. Wei, B. C. Seidenberg and T. F. Reiss, *Annals of Internal Medicine*, 1999, **130**, 487-495.
54. P. Phelps and D. Stanislaw, *Arthritis & Rheumatism*, 1969, **12**, 181-188.
55. K. Somersalo, O. P. Salo, F. Björkstén and K. K. Mustakallio, *Analytical Biochemistry*, 1990, **185**, 238-242.
56. D. E. Chenoweth, J. G. Rowe and T. E. Hugli, *Journal of Immunological Methods*, 1979, **25**, 337-353.
57. L. Glasser and R. L. Fiederlein, *Am J Clin Pathol*, 1979, **72**, 956-962.
58. A. Böyum, *Scand J Clin Lab Invest Suppl*, 1968, **97**, 77-89.
59. C. C. Silliman, G. W. Thurman and D. R. Ambruso, *Vox Sanguinis*, 1992, **63**, 133-136.
60. N. Agrawal, M. Toner and D. Irimia, *Lab on a Chip*, 2008, **8**, 2054-2061.
61. R. Mukhopadhyay, *Anal Chem*, 2007, **79**, 3248-3253.
62. H. Becker and L. E. Locascio, *Talanta*, 2002, **56**, 267-287.
63. K. Ren, Y. Chen and H. Wu, *Current Opinion in Biotechnology*, 2014, **25**, 78-85.
64. G. Julien, C. Thierry and M. Patrice, *Journal of Micromechanics and Microengineering*, 2007, **17**, R96.
65. R. R. Gattass and E. Mazur, *Nat Photon*, 2008, **2**, 219-225.
66. K. Sugioka, Y. Hanada and K. Midorikawa, *Laser & Photonics Reviews*, 2010, **4**, 386-400.
67. S.-C. Wang, C.-Y. Lee and H.-P. Chen, *Journal of Chromatography A*, 2006, **1111**, 252-257.
68. A. K. Au, W. Lee and A. Folch, *Lab on a Chip*, 2014, **14**, 1294-1301.
69. A. Waldbaur, H. Rapp, K. Lange and B. E. Rapp, *Analytical Methods*, 2011, **3**, 2681-2716.
70. H. Becker and C. Gärtner, *ELECTROPHORESIS*, 2000, **21**, 12-26.
71. H. Becker and C. Gärtner, *Anal Bioanal Chem*, 2008, **390**, 89-111.

72. A. Kummrow, J. Theisen, M. Frankowski, A. Tuchscheerer, H. Yildirim, K. Brattke, M. Schmidt and J. Neukammer, *Lab on a Chip*, 2009, **9**, 972-981.
73. M. E. Wilson, N. Kota, Y. Kim, Y. Wang, D. B. Stolz, P. R. LeDuc and O. B. Ozdoganlar, *Lab on a Chip*, 2011, **11**, 1550-1555.
74. E. Berthier, D. J. Guckenberger, P. Cavnar, A. Huttenlocher, N. P. Keller and D. J. Beebe, *Lab on a Chip*, 2013, **13**, 424-431.
75. D. J. Guckenberger, E. Berthier and D. J. Beebe, *Journal of Laboratory Automation*, 2014.
76. B. P. Casavant, D. J. Guckenberger, S. M. Berry, J. T. Tokar, J. M. Lang and D. J. Beebe, *Lab on a Chip*, 2013, **13**, 391-396.
77. L. Strotman, R. O'Connell, B. P. Casavant, S. M. Berry, J. M. Sperger, J. M. Lang and D. J. Beebe, *Anal Chem*, 2013, **85**, 9764-9770.
78. L. L. Bischel, B. R. Mader, J. M. Green, A. Huttenlocher and D. J. Beebe, *Lab on a Chip*, 2013, **13**, 1732-1736.
79. C. M. Carney, J. L. Muszynski, L. N. Strotman, S. R. Lewis, R. L. O'Connell, D. J. Beebe, A. B. Theberge and J. S. Jorgensen, *Biology of Reproduction*, 2014, **91**, 85, 81-13.
80. R. S. Woodbury and S. Kobayashi, 1974, vol. 96, pp. 110-110.
81. J. C. Aurich, I. G. Reichenbach and G. M. Schüler, *CIRP Annals - Manufacturing Technology*, 2012, **61**, 83-86.
82. C. R. Friedrich and M. J. Vasile, *Microelectromechanical Systems, Journal of*, 1996, **5**, 33-38.
83. Y.-b. Bang, K.-m. Lee and S. Oh, *Int J Adv Manuf Technol*, 2005, **25**, 888-894.
84. P. I. Okagbare, J. M. Emory, P. Datta, J. Goettert and S. A. Soper, *Lab on a Chip*, 2010, **10**, 66-73.
85. C. Chi-Hsiang, W. Yung-Cheng and L. Bean-Yin, *Int J Adv Manuf Technol*, 2013, **68**, 165-173.
86. T. Moriwaki, *CIRP Annals - Manufacturing Technology*, 2008, **57**, 736-749.
87. P.-C. Chen, C.-W. Pan, W.-C. Lee and K.-M. Li, *Int. J. Precis. Eng. Manuf.*, 2014, **15**, 149-154.
88. U. Attia, S. Marson and J. Alcock, *Microfluid Nanofluid*, 2009, **7**, 1-28.
89. S. Tanzi, M. Matteucci, T. L. Christiansen, S. Friis, M. T. Christensen, J. Garnaes, S. Wilson, J. Kutchinsky and R. Taboryski, *Lab on a Chip*, 2013, **13**, 4784-4793.
90. H. Becker and U. Heim, *Sensors and Actuators A: Physical*, 2000, **83**, 130-135.
91. P. Abgrall, L.-N. Low and N.-T. Nguyen, *Lab on a Chip*, 2007, **7**, 520-522.
92. F. P. W. Melchels, J. Feijen and D. W. Grijpma, *Biomaterials*, 2010, **31**, 6121-6130.
93. Y. Morimoto, W.-H. Tan and S. Takeuchi, *Biomedical Microdevices*, 2009, **11**, 369-377.
94. K. C. Bhargava, B. Thompson and N. Malmstadt, *Proceedings of the National Academy of Sciences*, 2014, **111**, 15013-15018.
95. G. Kumar, H. X. Tang and J. Schroers, *Nature*, 2009, **457**, 868-872.
96. T. Rabe, P. Kuchenbecker, B. Schulz and M. Schmidt, *International Journal of Applied Ceramic Technology*, 2007, **4**, 38-46.
97. T. Childs, *Metal machining: theory and applications*, Butterworth-Heinemann, 2000.
98. A. J. L. Shih, Jie; Lewis, Mark A.; Sternkowski, John S., *Journal of Manufacturing Science and Engineering*, 2004, **126**, 124-130.
99. E. W. K. Young, E. Berthier and D. J. Beebe, *Anal Chem*, 2012, **85**, 44-49.
100. A. Lamikiz, L. N. López de Lacalle, O. Ocerin, D. Díez and E. Maidagan, *Int J Adv Manuf Technol*, 2008, **37**, 122-139.
101. J. H. Kim, J. W. Park and T. J. Ko, *Computer-Aided Design*, 2008, **40**, 324-333.
102. M. B. L. Jun, Xinyu; DeVor, Richard E.; et al., *Journal of Manufacturing Science and Engineering*, 2006, **128**, 893-900.
103. A. Aramcharoen, P. T. Mativenga, S. Yang, K. E. Cooke and D. G. Teer, *International Journal of Machine Tools and Manufacture*, 2008, **48**, 1578-1584.
104. J. L. Endrino, G. S. Fox-Rabinovich and C. Gey, *Surface and Coatings Technology*, 2006, **200**, 6840-6845.
105. P. J. Agnew, *Mold Making Technology magazine*, 2004, 17-18.
106. E. Brinksmeier, R. Gläbe, O. Riemer and S. Twardy, *Microsyst Technol*, 2008, **14**, 1983-1987.
107. C.-S. Chen, D. N. Breslauer, J. I. Luna, A. Grimes, W.-c. Chin, L. P. Lee and M. Khine, *Lab on a Chip*, 2008, **8**, 622-624.
108. H. Klank, J. P. Kutter and O. Geschke, *Lab on a Chip*, 2002, **2**, 242-246.
109. M. B. Wabuyele, S. M. Ford, W. Stryjewski, J. Barrow and S. A. Soper, *ELECTROPHORESIS*, 2001, **22**, 3939-3948.

110. J. Steigert, S. Haeberle, T. Brenner, C. Müller, C. P. Steinert, P. Koltay, N. Gottschlich, H. Reinecke, J. Rühe, R. Zengerle and J. Ducrée, *Journal of Micromechanics and Microengineering*, 2007, **17**, 333.
111. G. Kiswanto, D. L. Zariatin and T. J. Ko, *Journal of Manufacturing Processes*, 2014, **16**, 435-450.
112. J. Zhang and J. Chen, *Int J Adv Manuf Technol*, 2007, **31**, 877-887.
113. K. Lee and D. A. Dornfeld, *Precision Engineering*, 2005, **29**, 246-252.
114. S. Dimov, D. T. Pham, A. Ivanov, K. Popov and K. Fansen, *Proceedings of the Institution of Mechanical Engineers, Part B: Journal of Engineering Manufacture*, 2004, **218**, 731-736.
115. C. K. Toh, *Journal of Materials Processing Technology*, 2004, **152**, 346-356.
116. P. G. Benardos and G. C. Vosniakos, *Robotics and Computer-Integrated Manufacturing*, 2002, **18**, 343-354.
117. L. K. Gillespie, *Burrs produced by end milling*, Report BDX-613-1503 United States10.2172/7259917Wed Dec 05 12:47:11 EST 2012Dep. NTISERA-02-007467; EDB-77-002691English, 1976.
118. C.-H. Chu and D. Dornfeld, *Journal of Manufacturing Processes*, 2005, **7**, 182-195.
119. K. Anselme, M. Bigerelle, B. Noel, E. Dufresne, D. Judas, A. Iost and P. Hardouin, *Journal of Biomedical Materials Research*, 2000, **49**, 155-166.
120. K. Kieswetter, Z. Schwartz, T. W. Hummert, D. L. Cochran, J. Simpson, D. D. Dean and B. D. Boyan, *Journal of Biomedical Materials Research*, 1996, **32**, 55-63.
121. K. Hatano, H. Inoue, T. Kojo, T. Matsunaga, T. Tsujisawa, C. Uchiyama and Y. Uchida, *Bone*, 1999, **25**, 439-445.
122. D. D. Deligianni, N. D. Katsala, P. G. Koutsoukos and Y. F. Missirlis, *Biomaterials*, 2000, **22**, 87-96.
123. C. Xu, F. Yang, S. Wang and S. Ramakrishna, *Journal of Biomedical Materials Research Part A*, 2004, **71A**, 154-161.
124. K. Mustafa, A. Odén, A. Wennerberg, K. Hultenby and K. Arvidson, *Biomaterials*, 2005, **26**, 373-381.
125. K. Anselme, P. Davidson, A. M. Popa, M. Giazzon, M. Liley and L. Ploux, *Acta Biomaterialia*, 2010, **6**, 3824-3846.
126. D. P. Dowling, I. S. Miller, M. Ardhaoui and W. M. Gallagher, *Journal of Biomaterials Applications*, 2011, **26**, 327-347.
127. R. A. Gittens, T. McLachlan, R. Olivares-Navarrete, Y. Cai, S. Berner, R. Tannenbaum, Z. Schwartz, K. H. Sandhage and B. D. Boyan, *Biomaterials*, 2011, **32**, 3395-3403.
128. I. R. G. Ogilvie, V. J. Sieben, C. F. A. Floquet, R. Zmijan, M. C. Mowlem and H. Morgan, *Journal of Micromechanics and Microengineering*, 2010, **20**, 065016.
129. R. N. Wenzel, *Industrial & Engineering Chemistry*, 1936, **28**, 988-994.
130. F. F. Ouali, G. McHale, H. Javed, C. Trabi, N. Shirtcliffe and M. Newton, *Microfluid Nanofluid*, 2013, **15**, 309-326.
131. F. J. M. Ruiz-Cabello, M. A. Rodríguez-Valverde and M. A. Cabrerizo-Vilchez, *Journal of Adhesion Science and Technology*, 2011, **25**, 2039-2049.
132. D. C. Duffy, J. C. McDonald, O. J. Schueller and G. M. Whitesides, *Anal Chem*, 1998, **70**, 4974-4984.
133. D. J. Beebe, G. A. Mensing and G. M. Walker, *Annual Review of Biomedical Engineering*, 2002, **4**, 261-286.
134. A. Folch and M. Toner, *Annual review of biomedical engineering*, 2000, **2**, 227-256.
135. C. Moraes, K. Wyss, E. Brisson, B. A. Keith, Y. Sun and C. A. Simmons, *Cellular and Molecular Bioengineering*, 2010, **3**, 319-330.
136. K. i. Ohno, K. Tachikawa and A. Manz, *Electrophoresis*, 2008, **29**, 4443-4453.
137. E. W. Young and C. A. Simmons, *Lab on a Chip*, 2010, **10**, 143-160.
138. Y. S. Heo, L. M. Cabrera, J. W. Song, N. Futai, Y.-C. Tung, G. D. Smith and S. Takayama, *Anal Chem*, 2007, **79**, 1126-1134.
139. K. J. Regehr, M. Domenech, J. T. Koepsel, K. C. Carver, S. J. Ellison-Zelski, W. L. Murphy, L. A. Schuler, E. T. Alarid and D. J. Beebe, *Lab on a Chip*, 2009, **9**, 2132-2139.
140. M. W. Toepke and D. J. Beebe, *Lab on a Chip*, 2006, **6**, 1484-1486.
141. E. Verneuil, A. Buguin and P. Silberzan, *EPL (Europhysics Letters)*, 2004, **68**, 412.
142. D. T. Eddington, J. P. Puccinelli and D. J. Beebe, *Sensors and Actuators B: Chemical*, 2006, **114**, 170-172.
143. A. L. Paguirigan and D. J. Beebe, *Integrative Biology*, 2009, **1**, 182-195.
144. C.-W. Tsao and D. L. DeVoe, *Microfluid Nanofluid*, 2009, **6**, 1-16.
145. L. Brown, T. Koerner, J. H. Horton and R. D. Oleschuk, *Lab on a Chip*, 2006, **6**, 66-73.
146. L. Martynova, L. E. Locascio, M. Gaitan, G. W. Kramer, R. G. Christensen and W. A. MacCrehan, *Anal Chem*, 1997, **69**, 4783-4789.

147. M. B. Wabuyele, S. M. Ford, W. Stryjewski, J. Barrow and S. A. Soper, *Electrophoresis*, 2001, **22**, 3939-3948.
148. J. Greener, W. Li, J. Ren, D. Voicu, V. Pakharenko, T. Tang and E. Kumacheva, *Lab on a Chip*, 2010, **10**, 522-524.
149. D. Ogończyk, J. Węgrzyn, P. Jankowski, B. Dąbrowski and P. Garstecki, *Lab on a Chip*, 2010, **10**, 1324-1327.
150. G. Mehta, J. Lee, W. Cha, Y.-C. Tung, J. J. Linderman and S. Takayama, *Anal Chem*, 2009, **81**, 3714-3722.
151. C. Tsao, L. Hromada, J. Liu, P. Kumar and D. DeVoe, *Lab on a Chip*, 2007, **7**, 499-505.
152. B.-H. Jo, L. M. Van Lerberghe, K. M. Motsegood and D. J. Beebe, *Journal of microelectromechanical systems*, 2000, **9**, 76-81.
153. W. Maszara, G. Goetz, A. Caviglia and J. McKitterick, *Journal of Applied Physics*, 1988, **64**, 4943-4950.
154. M. Bevilacqua and M. GIMBRONE JR, of Endothelial-Leukocyte Adhesion, 2012.
155. E. Berthier, J. Surfus, J. Verbsky, A. Huttenlocher and D. Beebe, *Integrative Biology*, 2010, **2**, 630-638.
156. J. W. Warrick, W. L. Murphy and D. J. Beebe, *IEEE reviews in biomedical engineering*, 2008, **1**, 75-93.
157. E. Berthier and D. J. Beebe, *Lab on a Chip*, 2007, **7**, 1475-1478.
158. P. C. Powell and A. I. Housz, *Engineering with polymers*, CRC Press, 1998.
159. W. Knoff, I. Hopkins and A. Tobolsky, *Macromolecules*, 1971, **4**, 750-754.
160. M. Narkis, I. Hopkins and A. Tobolsky, *Polymer Engineering & Science*, 1970, **10**, 66-69.
161. M. Worgull, *Hot embossing: theory and technology of microreplication*, William Andrew, 2009.
162. J. T. Borenstein, M. M. Tupper, P. J. Mack, E. J. Weinberg, A. S. Khalil, J. Hsiao and G. García-Cardeña, *Biomedical Microdevices*, 2010, **12**, 71-79.
163. A. Bhattacharyya and C. M. Klapperich, *Lab on a Chip*, 2007, **7**, 876-882.
164. G. M. Walker, H. C. Zeringue and D. J. Beebe, *Lab on a Chip*, 2004, **4**, 91-97.
165. S. M. Berry, K. J. Regehr, B. P. Casavant and D. J. Beebe, *J Lab Autom*, 2013, **18**, 206-211.
166. A. W. Jekelis, *Biomedical Instrumentation & Technology*, 2005, **39**, 232-236.
167. T. Pang and R. W. Peeling, *T Roy Soc Trop Med H*, 2007, **101**, 856-857.
168. F. Rouet, D. K. Ekouevi, M.-L. Chaix, M. Burgard, A. Inwoley, T. D. A. Tony, C. Danel, X. Anglaret, V. Leroy and P. Msellati, *J Clin Microbiol*, 2005, **43**, 2709-2717.
169. T. Peter, A. Badrichani, E. Wu, R. Freeman, B. Ncube, F. Ariki, J. Daily, Y. Shimada and M. Murtagh, *Cytometry Part B: Clinical Cytometry*, 2008, **74**, S123-S130.
170. S. M. Berry, E. T. Alarid and D. J. Beebe, *Lab Chip*, 2011, **11**, 1747-1753.
171. P. J. Weidle, S. Malamba, R. Mwebaze, C. Sozi, G. Rukundo, R. Downing, D. Hanson, D. Ochola, P. Mugyenyi and J. Mermin, *The Lancet*, 2002, **360**, 34-40.
172. V. DeGruttola, L. Dix, R. D'Aquila, D. Holder, A. Phillips, M. Ait-Khaled, J. Baxter, P. Clevenbergh, S. Hammer and R. Harrigan, *Antiviral therapy*, 2000, **5**, 41-48.
173. C. Zhang, J. Xu, W. Ma and W. Zheng, *Biotechnology advances*, 2006, **24**, 243-284.
174. D. Vuckovic, E. Cudjoe, D. Hein and J. Pawliszyn, *Anal Chem*, 2008, **80**, 6870-6880.
175. Z. Zhang, M. J. Yang and J. Pawliszyn, *Anal Chem*, 1994, **66**, 844A-853A.
176. A. F. Véronique, C. Marie-Laure, B. Stéphane, B. Marianne, F. Corinne, T. Kadidia, A. Marie-Christine, W. Josiane and R. Christine, *J Med Virol*, 2009, **81**, 217-223.
177. T. M. Squires and S. R. Quake, *Reviews of modern physics*, 2005, **77**, 977.
178. K. Tsougeni, D. Papageorgiou, A. Tserepi and E. Gogolides, *Lab on a Chip*, 2010, **10**, 462-469.
179. L. Tang and N. Y. Lee, *Lab on a Chip*, 2010, **10**, 1274-1280.
180. J.-P. Frimat, H. Menne, A. Michels, S. Kittel, R. Kettler, S. Borgmann, J. Franzke and J. West, *Anal Bioanal Chem*, 2009, **395**, 601-609.
181. N. Patrito, C. McCague, P. R. Norton and N. O. Petersen, *Langmuir*, 2007, **23**, 715-719.
182. J. M. Grace and L. J. Gerenser, *Journal of dispersion science and technology*, 2003, **24**, 305-341.
183. N. M. Oliveira, A. I. Neto, W. Song and J. F. Mano, *Applied physics express*, 2010, **3**, 085205.
184. L. J. Millet, M. E. Stewart, J. V. Sweedler, R. G. Nuzzo and M. U. Gillette, *Lab on a Chip*, 2007, **7**, 987-994.
185. J. Berthier, *Norwick, NY*, 2008, 350.
186. K. Haubert, T. Drier and D. Beebe, *Lab on a Chip*, 2006, **6**, 1548-1549.
187. M. Focke, D. Kosse, C. Müller, H. Reinecke, R. Zengerle and F. von Stetten, *Lab on a Chip*, 2010, **10**, 1365-1386.
188. J. Zhou, A. V. Ellis and N. H. Voelcker, *Electrophoresis*, 2010, **31**, 2-16.

189. P. M. van Midwoud, A. Janse, M. T. Merema, G. M. Groothuis and E. Verpoorte, *Anal Chem*, 2012, **84**, 3938-3944.
190. E. A. Vogler, *Journal of Biomaterials Science, Polymer Edition*, 1999, **10**, 1015-1045.
191. S. Y. Yang, E.-S. Kim, G. Jeon, K. Y. Choi and J. K. Kim, *Materials Science and Engineering: C*, 2013, **33**, 1689-1695.
192. R. K. Jena, C. Yue and Y. Lam, *Microsyst Technol*, 2012, **18**, 159-166.
193. D. A. Mair, E. Geiger, A. P. Pisano, J. M. Fréchet and F. Svec, *Lab on a Chip*, 2006, **6**, 1346-1354.
194. C. Lee, H. W. Kim and S. Kim, *Applied surface science*, 2007, **253**, 3658-3663.
195. S. Guruvenket, G. M. Rao, M. Komath and A. M. Raichur, *Applied Surface Science*, 2004, **236**, 278-284.
196. S. L. Barker and P. J. LaRocca, *Methods in Cell Science*, 1994, **16**, 151-153.
197. D. J. Guckenberger, E. Berthier, E. W. K. Young and D. J. Beebe, *Lab on a Chip*, 2012, **12**, 2317-2321.
198. X. Su, E. W. Young, H. A. Underkofler, T. J. Kamp, C. T. January and D. J. Beebe, *Journal of biomolecular screening*, 2011, **16**, 101-111.
199. Y. Wang, J. Balowski, C. Phillips, R. Phillips, C. E. Sims and N. L. Allbritton, *Lab on a Chip*, 2011, **11**, 3089-3097.
200. E. W. Young, E. Berthier and D. J. Beebe, *Anal Chem*, 2012, **85**, 44-49.
201. A. Riaz, R. P. Gandhiraman, I. K. Dimov, L. Basabe-Desmonts, J. Ducrée, S. Daniels, A. J. Ricco and L. P. Lee, *Lab on a Chip*, 2012, **12**, 4877-4883.
202. E. W. Young, A. R. Wheeler and C. A. Simmons, *Lab on a Chip*, 2007, **7**, 1759-1766.
203. A. K. Dutta, K. Kamada and K. Ohta, *Journal of photochemistry and photobiology A: Chemistry*, 1996, **93**, 57-64.
204. J. A. Bohnert, B. Karamian and H. Nikaido, *Antimicrobial agents and chemotherapy*, 2010, **54**, 3770-3775.
205. J. Eden, S.-J. Park, J. Cho, M. Kim, T. Houlahan, B. Li, E. Kim, T. Kim, S. Lee and K. Kim, *IEEE Transactions on Plasma Science*, 2013, **41**, 661-675.
206. M. Al-Hajj, M. S. Wicha, A. Benito-Hernandez, S. J. Morrison and M. F. Clarke, *Proceedings of the National Academy of Sciences*, 2003, **100**, 3983-3988.
207. M. W. Schmitt, M. J. Prindle and L. A. Loeb, *Annals of the New York Academy of Sciences*, 2012, **1267**, 110-116.
208. H. Clevers, *Nature medicine*, 2011, 313-319.
209. D. Gothard, R. S. Tare, P. D. Mitchell, J. I. Dawson and R. O. Oreffo, *Lab on a Chip*, 2011, **11**, 1206-1220.
210. T. Kelly, L. J. Suva, K. M. Nicks, V. MacLeod and R. D. Sanderson, *Journal of Bone and Mineral Research*, 2010, **25**, 1295-1304.
211. U. Dharmasiri, M. A. Witek, A. A. Adams and S. A. Soper, *Annual review of analytical chemistry*, 2010, **3**, 409-431.
212. E. S. Lianidou and A. Markou, *Clinical chemistry*, 2011, **57**, 1242-1255.
213. L. E. Lowes, D. Goodale, M. Keeney and A. L. Allan, *Methods Cell Biol*, 2011, **102**, 261-290.
214. X. Cheng, D. Irimia, M. Dixon, J. C. Ziperstein, U. Demirci, L. Zamir, R. G. Tompkins, M. Toner and W. R. Rodriguez, *JAIDS Journal of Acquired Immune Deficiency Syndromes*, 2007, **45**, 257-261.
215. N. Daniele, M. C. Scerpa, F. Landi, M. Caniglia, M. J. Miele, F. Locatelli, G. Isacchi and F. Zinno, *Pathology-Research and Practice*, 2011, **207**, 209-215.
216. U. A. Gurkan, T. Anand, H. Tas, D. Elkan, A. Akay, H. O. Keles and U. Demirci, *Lab on a chip*, 2011, **11**, 3979-3989.
217. E. A. Warner, K. T. Kotz, R. F. Ungaro, A. S. Abouhamze, M. C. Lopez, A. G. Cuenca, K. M. Kelly-Scumpia, C. Moreno, K. A. O'Malley and J. D. Lanz, *Laboratory Investigation*, 2011, **91**, 1787-1795.
218. A. Y. Fu, H.-P. Chou, C. Spence, F. H. Arnold and S. R. Quake, *Anal Chem*, 2002, **74**, 2451-2457.
219. S. J. Tan, R. L. Lakshmi, P. Chen, W.-T. Lim, L. Yobas and C. T. Lim, *Biosensors and Bioelectronics*, 2010, **26**, 1701-1705.
220. H. Wu, A. Wheeler and R. N. Zare, *Proceedings of the National Academy of Sciences of the United States of America*, 2004, **101**, 12809-12813.
221. C. J. Easley, J. M. Karlinsey, J. M. Bienvenue, L. A. Legendre, M. G. Roper, S. H. Feldman, M. A. Hughes, E. L. Hewlett, T. J. Merkel and J. P. Ferrance, *Proceedings of the National Academy of Sciences*, 2006, **103**, 19272-19277.
222. H. K. Lin, S. Zheng, A. J. Williams, M. Balic, S. Groshen, H. I. Scher, M. Fleisher, W. Stadler, R. H. Datar and Y.-C. Tai, *Clinical Cancer Research*, 2010, **16**, 5011-5018.
223. A. Williams, M. Balic, R. Datar and R. Cote, in *Minimal residual disease and circulating tumor cells in breast cancer*, Springer, 2012, pp. 87-95.

224. A. Wolff, I. R. Perch-Nielsen, U. Larsen, P. Friis, G. Goranovic, C. R. Poulsen, J. P. Kutter and P. Telleman, *Lab on a Chip*, 2003, **3**, 22-27.
225. H. Bordelon, N. M. Adams, A. S. Klemm, P. K. Russ, J. V. Williams, H. K. Talbot, D. W. Wright and F. R. Haselton, *ACS applied materials & interfaces*, 2011, **3**, 2161-2168.
226. M. Yu, S. Stott, M. Toner, S. Maheswaran and D. A. Haber, *The Journal of cell biology*, 2011, **192**, 373-382.
227. H. Chen, A. Abolmatty and M. Faghri, *Microfluid Nanofluid*, 2011, **10**, 593-605.
228. K. Sur, S. M. McFall, E. T. Yeh, S. R. Jangam, M. A. Hayden, S. D. Stroupe and D. M. Kelso, *The Journal of Molecular Diagnostics*, 2010, **12**, 620-628.
229. M. Shikida, K. Takayanagi, H. Honda, H. Ito and K. Sato, *Journal of Micromechanics and Microengineering*, 2006, **16**, 1875.
230. J. Atencia and D. J. Beebe, *Nature*, 2005, **437**, 648-655.
231. B. Zhao, J. S. Moore and D. J. Beebe, *Science*, 2001, **291**, 1023-1026.
232. S. M. Berry, L. N. Strotman, J. D. Kueck, E. T. Alarid and D. J. Beebe, *Biomedical Microdevices*, 2011, **13**, 1033-1042.
233. Y. Huang, E. L. Mather, J. L. Bell and M. Madou, *Anal Bioanal Chem*, 2002, **372**, 49-65.
234. S. C. Tan and B. C. Yiap, *BioMed Research International*, 2009, **2009**.
235. R. Boom, C. Sol, M. Salimans, C. Jansen, P. Wertheim-van Dillen and J. Van der Noordaa, *J Clin Microbiol*, 1990, **28**, 495-503.
236. R. C. den Dulk, K. A. Schmidt, G. Sabatté, S. Liébana and M. W. Prins, *Lab on a Chip*, 2013, **13**, 106-118.
237. A. H. Ng, K. Choi, R. P. Luoma, J. M. Robinson and A. R. Wheeler, *Anal Chem*, 2012, **84**, 8805-8812.
238. Y. Zhang and T. H. Wang, *Advanced Materials*, 2013, **25**, 2903-2908.
239. M. K. Chaudhury and G. M. Whitesides, *How to make water run uphill*, DTIC Document, 1992.
240. R. T.-P. Chow, *Journal of Fluid mechanics*, 1983, **137**, 1-29.
241. A. Nakajima, *NPG Asia Materials*, 2011, **3**, 49-56.
242. S. P. Thampi, R. Adhikari and R. Govindarajan, *Langmuir*, 2013, **29**, 3339-3346.
243. B. M. Mognetti, H. Kusumaatmaja and J. Yeomans, *Faraday discussions*, 2010, **146**, 153-165.
244. T. W. Chun, L. Stuyver, S. B. Mizell, L. A. Ehler, J. A. Mican, M. Baseler, A. L. Lloyd, M. A. Nowak and A. S. Fauci, *Proc. Natl. Acad. Sci. U. S. A.*, 1997, **94**, 13193-13197.
245. J. L. Simpson and S. Elias, *JAMA*, 1993, **270**, 2357-2361.
246. T.-W. Chun, J. S. Justement, S. Moir, C. W. Hallahan, J. Maenza, J. I. Mullins, A. C. Collier, L. Corey and A. S. Fauci, *J. Infect. Dis.*, 2007, **195**, 1762-1764.
247. A. Seppo, V. Frisova, I. Ichetovkin, Y. Kim, M. I. Evans, A. Antsaklis, K. H. Nicolaides, T. Tafas, P. Tsipouras and M. W. Kilpatrick, *Prenat. Diagn.*, 2008, **28**, 815-821.
248. A. Saker, A. Benachi, J. P. Bonnefont, A. Munnich, Y. Dumez, B. Lacour and P. Paterlini-Brechot, *Prenat. Diagn.*, 2006, **26**, 906-916.
249. O. Lara, X. Tong, M. Zborowski and J. J. Chalmers, *Exp. Hematol.*, 2004, **32**, 891-904.
250. R. Königsberg, E. Obermayr, G. Bises, G. Pfeiler, M. Gneist, F. Wrba, M. de Santis, R. Zeillinger, M. Hudec and C. Dittrich, *Acta Oncol.*, 2011, **50**, 700-710.
251. A. J. Armstrong, M. S. Marengo, S. Oltean, G. Kemeny, R. L. Bitting, J. D. Turnbull, C. I. Herold, P. K. Marcom, D. J. George and M. A. Garcia-Blanco, *Mol. Cancer Res.*, 2011, **9**, 997-1007.
252. M. Mego, M. Mego, M. Mego, S. Mani, C. Li, E. Andreoupolou, S. Tin, S. Jackson, E. Cohen, H. Gao, M. Cristofanilli and J. Reuben, *Cancer Res.*, 2009, **69**, 3011-3011.
253. T. M. Gorges, I. Tinhofer, M. Drosch, L. Röse, T. M. Zollner, T. Krahn and O. von Ahsen, *BMC Cancer*, 2012, **12**, 178.
254. A. Gradilone, C. Raimondi, C. Nicolazzo, A. Petracca, O. Gandini, B. Vincenzi, G. Naso, A. M. Aglianò, E. Cortesi and P. Gazzaniga, *J. Cell. Mol. Med.*, 2011, **15**, 1066-1070.
255. G. Kallergi, K. Galatea, M. A. Papadaki, P. Eleni, M. Dimitris, G. Vassilis and A. Sophia, *Breast Cancer Res.*, 2011, **13**, R59.
256. C. A. Savary, M. L. Grazziutti, B. Melichar, D. Przepiorka, R. S. Freedman, R. E. Cowart, D. M. Cohen, E. J. Anaissie, D. G. Woodside, B. W. McIntyre, D. L. Pierson, N. R. Pellis and J. H. Rex, *Cancer Immunol. Immunother.*, 1998, **45**, 234-240.
257. C. L. Mackall, T. A. Fleisher, M. R. Brown, I. T. Magrath, A. T. Shad, M. E. Horowitz, L. H. Wexler, M. A. Adde, L. L. McClure and R. E. Gress, *Blood*, 1994, **84**, 2221-2228.
258. S. D. Mikolajczyk, L. S. Millar, P. Tsinberg, S. M. Coutts, M. Zomorrodi, T. Pham, F. Z. Bischoff and T. J. Pircher, *J. Oncol.*, 2011, **2011**, 252361.

259. B. P. Casavant, D. J. Guckenberger, D. J. Beebe and S. M. Berry, *Anal. Chem.*, 2014, **86**, 6355-6362.
260. S. M. Berry, H. M. Pezzi, A. J. LaVanway, D. J. Guckenberger, M. A. Anderson and D. J. Beebe, *ACS Appl. Mater. Interfaces*, 2016, **8**, 15040-15045.
261. S. M. Berry, E. T. Alarid and D. J. Beebe, *Lab Chip*, 2011, **11**, 1747-1753.
262. B. P. Casavant, D. J. Guckenberger, S. M. Berry, J. T. Tokar, J. M. Lang and D. J. Beebe, *Lab Chip*, 2013, **13**, 391-396.
263. D. J. Guckenberger, H. M. Pezzi, M. C. Regier, S. M. Berry, K. Fawcett, K. Barrett and D. J. Beebe, *Anal. Chem.*, 2016.
264. L. M. Zasadil, E. M. C. Britigan, S. D. Ryan, C. Kaur, D. J. Guckenberger, D. J. Beebe, A. R. Moser and B. A. Weaver, *Mol. Biol. Cell*, 2016, **27**, 1981-1989.
265. K. Schulze, C. Gasch, K. Staufer, B. Nashan, A. W. Lohse, K. Pantel, S. Riethdorf and H. Wege, *Int. J. Cancer*, 2013, **133**, 2165-2171.
266. S. J. Cohen, C. J. A. Punt, N. Iannotti, B. H. Saidman, K. D. Sabbath, N. Y. Gabrail, J. Picus, M. Morse, E. Mitchell, M. C. Miller, G. V. Doyle, H. Tissing, L. W. M. M. Terstappen and N. J. Meropol, *J. Clin. Oncol.*, 2008, **26**, 3213-3221.
267. N. Aceto, A. Bardia, D. T. Miyamoto, M. C. Donaldson, B. S. Wittner, J. A. Spencer, M. Yu, A. Pely, A. Engstrom, H. Zhu, B. W. Brannigan, R. Kapur, S. L. Stott, T. Shioda, S. Ramaswamy, D. T. Ting, C. P. Lin, M. Toner, D. A. Haber and S. Maheswaran, *Cell*, 2014, **158**, 1110-1122.
268. S. d. Wit, S. de Wit, G. van Dalum, A. T. M. Lenferink, A. G. J. Tibbe, T. J. N. Hiltermann, H. J. M. Groen, C. J. M. van Rijn and L. W. M., *Sci. Rep.*, 2015, **5**, 12270.
269. R. Fisher, L. Pusztai and C. Swanton, *Br. J. Cancer*, 2013, **108**, 479-485.
270. C. Holohan, H. Caitriona, S. Van Schaeybroeck, D. B. Longley and P. G. Johnston, *Nat. Rev. Cancer*, 2013, **13**, 714-726.
271. P. L. Bedard, A. R. Hansen, M. J. Ratain and L. L. Siu, *Nature*, 2013, **501**, 355-364.
272. M. A. Dawson and K. Tony, *Cell*, 2012, **150**, 12-27.
273. L. A. Diaz, Jr. and A. Bardelli, *J. Clin. Oncol.*, 2014, **32**, 579-586.
274. P. P. Provenzano, K. W. Eliceiri, J. M. Campbell, D. R. Inman, J. G. White and P. J. Keely, *BMC medicine*, 2006, **4**, 1.
275. P. J. Hung, P. J. Lee, P. Sabounchi, N. Aghdam, R. Lin and L. P. Lee, *Lab on a Chip*, 2005, **5**, 44-48.
276. M. C. Regier, L. J. Maccoux, E. M. Weinberger, K. J. Regehr, S. M. Berry, D. J. Beebe and E. T. Alarid, *Biomed. Microdevices*, 2016, **18**, 70.
277. S. B. Fox, K. C. Gatter, R. Bicknell, J. J. Going, P. Stanton, T. G. Cooke and A. L. Harris, *Cancer Res.*, 1993, **53**, 4161-4163.
278. E. A. Voigt and Y. John, *J. Interferon Cytokine Res.*, 2015, **35**, 734-747.
279. T. W. Orlikowsky, F. Neunhoeffer, R. Goelz, M. Eichner, C. Henkel, M. Zwirner and C. F. Poets, *Pediatr. Res.*, 2004, **56**, 804-809.
280. D. Kim and A. E. Herr, *Biomicrofluidics*, 2013, **7**, 41501.
281. C. Bock and T. Lengauer, *Nat. Rev. Cancer*, 2012, **12**, 494-501.
282. A. D. Cox, S. W. Fesik, A. C. Kimmelman, J. Luo and C. J. Der, *Nat. Rev. Drug Discov.*, 2014, **13**, 828-851.
283. K. H. Khoo, K. K. Hoe, C. S. Verma and D. P. Lane, *Nat. Rev. Drug Discov.*, 2014, **13**, 217-236.
284. H. J. Burstein, P. B. Mangu, M. R. Somerfield, D. Schrag, D. Samson, L. Holt, D. Zelman, J. A. Ajani and O. American Society of Clinical, *J. Clin. Oncol.*, 2011, **29**, 3328-3330.
285. D. J. Samson, *J. Clin. Oncol.*, 2004, **22**, 3618-3630.
286. D. Schrag, H. S. Garewal, H. J. Burstein, D. J. Samson, D. D. Von Hoff, M. R. Somerfield, A. W. G. o. C. Sensitivity and A. Resistance, *J. Clin. Oncol.*, 2004, **22**, 3631-3638.
287. M. A. Dobrovolskaia and S. E. McNeil, *J. Control. Release*, 2013, **172**, 456-466.
288. L. C. Wienkers and T. G. Heath, *Nat. Rev. Drug Discov.*, 2005, **4**, 825-833.
289. O. Jonas, H. M. Landry, J. E. Fuller, J. T. Santini, Jr., J. Baselga, R. I. Tepper, M. J. Cima and R. Langer, *Sci. Transl. Med.*, 2015, **7**, 284ra257.
290. R. A. Klinghoffer, S. B. Bahrami, B. A. Hatton, J. P. Frazier, A. Moreno-Gonzalez, A. D. Strand, W. S. Kerwin, J. R. Casalini, D. J. Thirstrup, S. You, S. M. Morris, K. L. Watts, M. Veiseh, M. O. Grenley, I. Tretyak, J. Dey, M. Carleton, E. Beirne, K. D. Pedro, S. H. Ditzler, E. J. Girard, T. L. Deckwerth, J. A. Bertout, K. A. Meleo, E. H. Filvaroff, R. Chopra, O. W. Press and J. M. Olson, *Sci. Transl. Med.*, 2015, **7**, 284ra258.
291. H. D. Chirra and T. A. Desai, *Small*, 2012, **8**, 3839-3846.

292. R. Farra, N. F. Sheppard, Jr., L. McCabe, R. M. Neer, J. M. Anderson, J. T. Santini, Jr., M. J. Cima and R. Langer, *Sci. Transl. Med.*, 2012, **4**, 122ra121.
293. A. C. R. Grayson, R. S. Shawgo, A. M. Johnson, N. T. Flynn, Y. Li, M. J. Cima and R. Langer, *Proc. IEEE*, 2004, **92**, 6-21.
294. D. A. LaVan, T. McGuire and R. Langer, *Nat. Biotechnol.*, 2003, **21**, 1184-1191.
295. J. Berthier, F. Loe-Mie, V. M. Tran, S. Schoumacker, F. Mittler, G. Marchand and N. Sarrut, *J. Colloid Interface Sci.*, 2009, **338**, 296-303.
296. L. Morosi, P. Spinelli, M. Zucchetti, F. Pretto, A. Carrà, M. D'Incalci, R. Giavazzi and E. Davoli, *PLoS One*, 2013, **8**, e72532.
297. L. Hernandez, H. Lorena, S. Tatiana, W. Jeffrey, C. John and J. E. Segall, in *Methods in Molecular Biology*, 2009, pp. 227-238.
298. J. B. Wyckoff, J. E. Segall and J. S. Condeelis, *Cancer Res.*, 2000, **60**, 5401-5404.
299. R. Pauwels, *Antiviral research*, 2006, **71**, 77-89.
300. C. Xiao and J. H. Luong, *Biotechnology progress*, 2003, **19**, 1000-1005.
301. Y. Wang, Z. Chen, L. Xiao, Z. Du, X. Han, X. Yu and Y. Lu, *Electrophoresis*, 2012, **33**, 773-779.
302. K. Blagovic, L. Y. Kim and J. Voldman, *PloS one*, 2011, **6**, e22892.
303. K. R. King, S. Wang, D. Irimia, A. Jayaraman, M. Toner and M. L. Yarmush, *Lab on a Chip*, 2007, **7**, 77-85.
304. N. M. Toriello, E. S. Douglas, N. Thaitrong, S. C. Hsiao, M. B. Francis, C. R. Bertozzi and R. A. Mathies, *Proceedings of the National Academy of Sciences*, 2008, **105**, 20173-20178.
305. D. Chen, M. Mauk, X. Qiu, C. Liu, J. Kim, S. Ramprasad, S. Ongagna, W. R. Abrams, D. Malamud and P. L. Corstjens, *Biomedical Microdevices*, 2010, **12**, 705-719.
306. M. A. Dineva, L. Mahilum-Tapay and H. Lee, *Analyst*, 2007, **132**, 1193-1199.
307. W. Du, L. Li, K. P. Nichols and R. F. Ismagilov, *Lab on a Chip*, 2009, **9**, 2286-2292.
308. J. Fu, Y.-K. Wang, M. T. Yang, R. A. Desai, X. Yu, Z. Liu and C. S. Chen, *Nature methods*, 2010, **7**, 733-736.
309. M. Théry, V. Racine, M. Piel, A. Pépin, A. Dimitrov, Y. Chen, J.-B. Sibarita and M. Bornens, *Proceedings of the National Academy of Sciences*, 2006, **103**, 19771-19776.
310. S. Takayama, J. C. McDonald, E. Ostuni, M. N. Liang, P. J. Kenis, R. F. Ismagilov and G. M. Whitesides, *Proceedings of the National Academy of Sciences*, 1999, **96**, 5545-5548.
311. J. Warrick, I. Meyvantsson, J. Ju and D. J. Beebe, *Lab on a Chip*, 2007, **7**, 316-321.
312. J. P. Puccinelli, X. Su and D. J. Beebe, *Journal of the Association for Laboratory Automation*, 2010, **15**, 25-32.
313. T. Thorsen, S. J. Maerkl and S. R. Quake, *Science*, 2002, **298**, 580-584.
314. M. Zimmermann, H. Schmid, P. Hunziker and E. Delamarche, *Lab on a Chip*, 2007, **7**, 119-125.
315. P. Zhou, L. Young and Z. Chen, *Biomed Microdevices*, 2010, **12**, 821-832.
316. E. Berthier, J. Warrick, H. Yu and D. J. Beebe, *Lab on a Chip*, 2008, **8**, 852-859.
317. Y. S. Song, S. Moon, L. Hulli, S. K. Hasan, E. Kayaalp and U. Demirci, *Lab on a Chip*, 2009, **9**, 1874-1881.
318. L. J. Itle and M. V. Pishko, *Biotechnology progress*, 2005, **21**, 1004-1007.
319. K. Bhadriraju and C. S. Chen, *Drug Discovery Today*, 2002, **7**, 612-620.
320. I. Barbulovic-Nad, H. Yang, P. S. Park and A. R. Wheeler, *Lab on a Chip*, 2008, **8**, 519-526.
321. E. Michelini, L. Cevenini, L. Mezzanotte, A. Coppa and A. Roda, *Anal Bioanal Chem*, 2010, **398**, 227-238.
322. K. Ewer, J. Deeks, L. Alvarez, G. Bryant, S. Waller, P. Andersen, P. Monk and A. Lalvani, *The Lancet*, 2003, **361**, 1168-1173.
323. X. Su, A. B. Theberge, C. T. January and D. J. Beebe, *Anal Chem*, 2013, **85**, 1562-1570.
324. J. Zavadil and E. P. Bottinger, *Oncogene*, 0000, **24**, 5764-5774.
325. E. Piek, A. Moustakas, A. Kurisaki, C. H. Heldin and P. t. Dijke, *Journal of Cell Science*, 1999, **112**, 4557-4568.
326. M. Wendt and W. Schiemann, *Breast Cancer Research*, 2009, **11**, R68.
327. N. A. Bhowmick, M. Ghiassi, A. Bakin, M. Aakre, C. A. Lundquist, M. E. Engel, C. L. Arteaga and H. L. Moses, *Molecular Biology of the Cell*, 2001, **12**, 27-36.
328. T. Vincent, E. P. A. Neve, J. R. Johnson, A. Kukalev, F. Rojo, J. Albanell, K. Pietras, I. Virtanen, L. Philipson, P. L. Leopold, R. G. Crystal, A. G. de Herreros, A. Moustakas, R. F. Pettersson and J. Fuxe, *Nat Cell Biol*, 2009, **11**, 943-950.

329. J. D. Beck, B. L. Canfield, S. M. Haddock, T. J. H. Chen, M. Kothari and T. M. Keaveny, *Bone*, 1997, **21**, 281-287.
330. R. F. Bigley, M. Singh, C. J. Hernandez, G. J. Kazakia, R. B. Martin and T. M. Keaveny, *Bone*, 2008, **42**, 212-215.
331. D. R. Reyes, M. M. Ghanem, G. M. Whitesides and A. Manz, *Lab on a Chip*, 2002, **2**, 113-116.
332. A. Shafiu Kamba, M. Ismail, T. A. Tengku Ibrahim and Z. A. B. Zakaria, *BioMed research international*, 2013, **2013**.
333. B. D. Weinberg, R. B. Patel, A. A. Exner, G. M. Saidel and J. Gao, *Journal of Controlled Release*, 2007, **124**, 11-19.
334. A. L. Notkins and C. Scheele, *Journal of the National Cancer Institute*, 1964, **33**, 741-749.